

NON-LINEAR ANALYSIS OF INFILLED FRAMES

(PART ONE)

VOL. I.

By

Abolghasem Saneinejad

A

THESIS

Submitted to the Department of
Civil and Structural Engineering,

in partial fulfilment of the

requirements for the

Degree of

Doctor of Philosophy

UNIVERSITY OF SHEFFIELD

May, 1990

SUMMARY

This thesis is concerned with the analysis of building frames acting compositely with infilling wall panels. The significance of the composite action is emphasized and previous work on infilled frames is reviewed. The existing methods of analysis are categorized and their analytical assumptions are highlighted. It is concluded that more accurate results may be obtained from the development of a non-linear finite element analysis. The finite element method is reviewed and new elements for representing beams, interfaces and loading are developed. Failure criteria for concrete under *multiaxial stress and* also failure criteria for masonry under uniaxial compression are developed. The non-linear elastoplastic behaviour of concrete is modelled using the concept of equivalent uniaxial strain and the model is extended for cracked materials. Elastoplastic models are also developed for ductile materials (steel) for secant and incremental changes of stresses and strains. These models and the newly developed elements are incorporated into the finite element analysis which is numerically implemented by a new computer program, NEPAL. A number of steel frames with concrete infills covering the practical range of beam, column and infill strengths and also wall panel aspect ratios, are analysed using this program. The finite element results are compared with the predictions of a range of existing methods of analysis and their limitations are discussed in detail. A new method of hand analysis is developed, based on a rational elastic and plastic analysis allowing for limited ductility of the infill and also limited deflection of the frame at the peak load. The new method is shown to be capable of providing the necessary information for design purposes with reasonable accuracy, taking into account the effects of strength and stiffness of the beams and columns, the aspect ratio for the infill, the semi-rigid joints and the condition of the frame-infill interfaces (co-efficient of friction and lack of fit). It is concluded that simple and economical design approaches can be established for frames with infilling walls.

ACKNOWLEDGEMENTS

The author would like to thank Mr. B. Hobbs for his continual support and encouragement which made this work possible.

TABLE OF CONTENTS

PART ONE

List of Tables	xvii
List of Figures	xix
Notations	xxvii
CHAPTER 1 Introduction	1
CHAPTER 2 Review of Previous Work	6
2.1 Introduction	6
2.2 Behaviour of Infilled Frames under Racking load	6
2.3 Early Work and the Concept of Diagonal Strut	9
2.4 Theories Based on Infill/Frame Stiffness Parameter.....	12
2.4.1 General	12
2.4.2 Stafford Smith Observations on the Behaviour of Infilled Frames Subjected to Racking Load	13
2.4.3 Stafford Smith's Theoretical Analysis	15
2.4.4 Lateral Strength of Infilled Frames	20
2.4.5 Lateral Stiffness of Infilled Frames	25
2.4.6 Behaviour of Masonry Infilled Frames under Racking Load	28
2.5 Empirical Method of Analysis Based on Stiffness Parameter, λh	30
2.5.1 Empirical Data and Analysis of Infill	30
2.5.2 Analysis of Frame	33

2.53	comments	34
2.6	Design Recommendations for Elastic Analysis of Infilled Steel Frames.....	37
2.6.1	General	37
2.6.2	The Basis of the Method	37
2.6.3	Infill Design	38
2.6.4	Design of Frame	41
2.6.5	Comparison	43
2.7	Theories Based on Frame/Infill Strength Parameter	44
2.7.1	General	44
2.7.2	Wood Classification for Collapse of Infilled Frame.....	45
2.7.3	Wood's Plastic Analysis of Infilled Frames.....	47
2.7.4	Axial and Shear Forces in Frame Members	53
2.7.5	Application of Wood Method for Analysis of Multi-bay and Multi-Storey Frames With or without Panels	53
2.7.6	Discussion of Wood Method	54
2.7.7	Plastic Analysis of Infilled Frames with Application of the Yield Line Method	55
2.8	Liauw et al Plastic Method	57
2.8.1	Finite Element Analyses	57
2.8.2	Collapse Modes and Loads	60
2.8.3	Comparison With Experimental Results	65
2.8.4	Using the Liauw et al Plastic Method for Analysis of Single-Bay Multi-Storey Infilled Frames	66
2.8.5	Discussion of Liauw et al Method	67
2.9	Conclusion from The Literature Review	69

CHAPTER 3	The Finite Element Technique	73
3.1	General	73
3.2	Finite Element Concept	73
3.3	Newton Raphson Iteration	74
3.4	Finite Element Formulation	76
3.4.1	General.....	76
3.4.2	Element Displacement Functions	77
3.4.3	Element Strain Functions	78
3.4.4	Stress-strain Relation	79
3.4.5	Element Stiffness Matrix	80
3.4.6	Element Equivalent Nodal Forces	91
3.5	Local Normalized Coordinates	82
3.5.1	Definitions	82
3.5.2	Evaluation of the Integrals in Terms of Local Normalized Coordinates	83
3.6	Numerical Integration	85
3.7	Contribution of Reinforcement to R.C Elements	87
3.7.1	General	87
3.7.2	Uniformly Distributed Reinforcement	88
3.7.3	A Single Bar Parallel to One of the Element Local Coordinates	89
3.8	Some Requirements of the F.E Discretization	91
3.9	Masonry Wall Discretization	95
3.9.1	General.....	95
3.9.2	Standard 3-D Element	95
3.9.3	Newly Developed 3-D Four-node Element.....	96
3.9.4	Plane-Stress Equivalent Elements.....	98
3.9.5	Plane-stress Equivalent Units and Laminar Joints.....	98

3.9.6	Plane-stress Masonry-Equivalent and Interface Elements	100
3.9.7	Super Element of Masonry	101
3.9.8	Conclusion on the Choices of Masonry Elements	101
3.10	Interface Discretization	103
3.10.1	General	103
3.10.2	Algorithm of Linkage Element	104
3.10.3	Newly Developed Interface Element	107
3.11	Frame Discretization	112
3.11.1	General	112
3.11.2	Non-conforming Rectangular element	114
3.11.3	Proposed Rectangular Beam Element	116
3.12	Choice Of Masonry Infilled Frame Subdivision	119
3.13	Choices of Concrete Infilled Frame Subdivision	122

CHAPTER 4 Constitutive Formulation of Materials 123

4.1	General	123
4.2	The Existing Fracture Models	124
4.3	Proposed Constitutive Formulation for Brittle Materials Under Uniaxial Compression	130
4.3.1	Stress-Strain Relation	130
4.3.2	Poisson's Ratio	134
4.3.3	Loading-Unloading-Reloading Behaviour	136
4.4	Brittle Materials Subjected to Uniaxial Tension	138
4.5	Failure Criteria	140
4.5.1	General	140
4.5.2	Proposed Failure Criterion of Brittle Materials under Triaxial Compression	144

4.5.3	Proposed Failure Criterion for Brittle Materials under Triaxial Compression-Tension	147
4.5.4	Proposed Failure Criterion for Brittle Materials under Tension-Compression	149
4.5.5	Proposed Failure Criterion for Brittle Materials Under Triaxial Tension	149
4.6	Proposed Constitutive Formulation for Brittle Materials Under Multiaxial Stresses	150
4.6.1	General	150
4.6.2	Equivalent Uniaxial Strains (EUS).....	153
4.6.3	Proposed Stress-EUS Relationship Formulation.....	153
4.6.4	EUS at Peak Load.....	156
4.6.5	Transformation of EUS to Real strains and Vice-versa	159
4.6.6	Proportional Unloading and Reloading	163
4.6.7	Proposed Incremental Stress-strain Relationship	168
4.7	Non-proportional Loading	171
4.7.1	Stress-strain Relationship.....	171
4.7.2	Poisson's Ratios under Non-proportional Loading.....	173
4.7.3	Proposed Incremental Stress-strain Relationship for Non-proportional Load Increment	174
4.8	Cracking and Cracked Materials	175
4.8.1	Cracking.....	175
4.8.2	Cracked Materials.....	176
4.8.3	Proposed Slip-dilatancy Crack Model	178
4.8.3.1	General Concept	178
4.8.3.2	Stress-strain Relationship for Cracked Materials under Plane Stress Conditions	179
4.8.3.3	Material with Open Cracks	181
4.8.3.4	Material with Closed Cracks	182

4.8.3.5	Material with Interlocked Cracks	182
4.8.4	Proposed Incremental Stress-strain Relationship for Cracked Materials	183
4.8.5	Proposed Model for Double Sets of Cracks	186
4.8.5.1	General Concept and Definitions	186
4.8.5.2	Material with Closed Minor Cracks	187
4.8.5.3	Materials with Open Minor Cracks	190
4.8.6	Proposed Incremental Stress-strain Relationship for Double Cracked Materials	194
4.9	Constitutive Formulation for Steel	196
4.9.1	General Characteristics of Steel	196
4.9.2	Proposed Model for Stress-Strain Relationship of Steel Material under Uniaxial Stress	198
4.9.3	Failure Criteria of Steel	199
4.9.4	Stress-strain Relationship of Ductile Material	201
4.9.4.1	Definitions and Basis of Elastic-Perfect Plasticity Theory	201
4.9.4.2	Stress-Strain Relationship under Multiaxial Stress Conditions	203
4.9.4.3	Stress-Strain Relationship for Plane Stress Loading	206
4.9.5	Incremental Stress-Strain Relationship for Ductile Materials	207
4.9.5.1	In Elastic State	207
4.9.5.2	In Elastoplastic State	209
4.9.5.3	Under Plane Stresses and in Elastoplastic State	211
4.9.6	Stress-strain Relationship for Reinforcement within a R.C Element	212
4.10	Constitutive Formulation for Mechanical Behaviour of Interfaces and Joints	213
4.10.1	General	213
4.10.2	Yielding, Slip and Separation Criteria	214

4.10.3	Stress-Relative Displacement Relationship of Interfaces	218
4.10.3.1	General	218
4.10.3.2	Proposed Model Based on Experimental Observations	219
4.10.4	Determination of the State of an Interface ...	223
4.10.4.1	General	223
4.10.4.2	New State of a Previously Fully Bonded Interface	224
4.10.4.3	New State of a Previously Partially Bonded Interface	227
4.10.4.4	<i>New State of a Totally Debonded Interface</i>	230
4.10.4.5	Proposed Incremental [D] Matrix	232
4.11	Constitutive Formulation for Masonry	234

CHAPTER 5 Numerical Implementation and Programming

236

5.1	General	236
5.2	Characteristics of Program NEPAL	236
5.3	Loading Procedure	237
5.4	Criteria for Convergence	240
5.5	Examination of The Proposed F.E Analysis.....	243
5.5.1	General	243
5.5.2	R.C Beam Without Shear Reinforcement	244
5.5.3	R.C. Beam with Shear Reinforcement	246
5.5.4	Square Steel Frame Subjected to Racking	248
5.5.5	Micro-concrete infilled Steel Frame Subjected to Racking	249
5.6	Conclusion	257

PART TWO

CHAPTER 6	Application of The Finite Element Analysis and Discussion	259
6.1	Aims and Scope	259
6.2	Infill Size and Proportion	259
6.3	Frame Members	261
6.4	Infill Material	261
6.5	Frame-Infill Interface	264
6.6	Infilled Frames Analysed	264
6.7	Open Frames	266
6.8	Infilled Frames	268
6.8.1	General	268
6.8.2	Load-Deflection Diagrams	268
6.8.3	Frame Forces	274
6.8.4	Infill Stresses	275
6.8.5	Frame-Infill Interaction	275
6.9	Discussion of Overall Behaviour of Infilled Frames	278
6.9.1	General	278
6.9.2	Elastic State	278
6.9.3	Elastoplastic State	278
6.9.4	Plastic State	279
6.9.5	Some Exceptions for Strong Frames	281
6.9.6	Comments	281
6.10	Discussion on Normal Force at Frame-infillInterface.....	281
6.10.1	General	281

6.10.2	Effect of Infill Aspect Ratio	283
6.10.3	Effect of Beam to Column Strength Ratio	283
6.10.4	Effect of Frame/Infill Strength Ratio	283
6.10.5	Effect of Diagonal Cracking	284
6.10.6	Effect of Coefficient of Friction	284
6.11	Discussion on Shear Force at Frame-infill Interface	284
6.12	Discussion on Infill Stress Distribution	286
6.12.1	General	286
6.12.2	Loaded Corners	286
6.12.3	Central Region	287
6.13	Discussion on Frame Forces	290
6.13.1	General	290
6.13.2	Axial Forces	290
6.13.3	Shear Forces	291
6.13.4	Bending Moment	293

CHAPTER 7 Proposed Method of Analysis and Comparison

		296
7.1	Introduction	296
7.1.1	General	296
7.1.2	Basis of The Analysis	298
7.2	Frame-infill Interaction	299
7.3	Frame-infill Contact Lengths	304
7.4	Infill Boundary Stresses	306
7.5	Lateral Deflection	310
7.6	Frame Bending Moments	312
7.7	Frame Forces	313
7.8	Peak Horizontal Load	314
7.9	Modes of Displacement and Failure	315

7.9.1	Frame Failure	315
7.9.2	Infill Failure	315
7.9.3	Infilled Frame Failure	318
7.10	Cracking Load	319
7.11	Stiffness	323
7.12	Special cases with Square Infills	323
7.13	Balancing Friction at Infill Boundary	325
7.14	Design Chart	326
7.15	Frames Without Plastic Hinge at the Peak Load	330
7.16	Comparison Programme	331
7.17	Results used in The Comparison Programme	332
7.17.1	The Finite Element Analysis Results	332
7.17.2	Experimental Results	332
7.18	The Methods of Analysis Involved in Comparison	335
7.19	Comparison of Peak Racking Load, H_c	338
7.19.1	General	338
7.19.2	Methods Based on Stiffness Parameter l_h	341
7.19.3	Wood Method (W)	345
7.19.4	Liauw Method (L)	347
7.19.5	Proposed Method (P)	349
7.20	Comparison of the Estimated Cracking Load, H_t	352
7.21	Comparison of the Estimated Initial Stiffness, K_0	354
7.22	Comparison of Estimated Frame Bending Moments	357
7.23	Comparison of the Predicted Frame Axial Forces	360
7.24	Comparison of Estimated Frame Shear Forces ...	361
7.25	Comments	362

CHAPTER	8	Conclusions and Recommendations	364
8.1		Conclusions	364
8.1.1		Investigation Approach	364
8.1.2		Present Finite Element Analysis	365
8.1.3		General Behaviour of Infilled Frames	367
8.1.4		Methods Based on Infill/Frame Stiffness Parameter	371
8.1.5		Wood's Plastic Method	372
8.1.6		Liauw et al Plastic Method	373
8.1.7		New Hand Method of Analysis	374
8.2		Recommendations for Future Work	375
8.2.1		Extension of Program NEPAL	375
8.2.2		Experimental Investigation	376
8.2.3		Application of Finite Element Analysis	376
8.2.4		Design Procedure	377

REFERENCES 378

APPENDIX A	Input Data for Program NEPAL	A1
A.1	General	A1
A.2	Input Data	A2
A.2.1	Structure Geometry	A2
A.2.2	Zone Properties	A2
A.2.3	Zone Topology	A3
A.2.4	Nodal Displacement Output Data	A3
A.2.5	Properties of The Materials	A3
A.2.6	Reinforcement Properties	A4
A.2.7	Reinforcement Geometry.....	A5
A.2.8	Structural Restraint	A5
A.2.9	Loading	A5

A.2.10	Material Non-linearity	A6
A.2.11	Deflection Increment Characteristics	A6
A.2.12	Output Results Characteristics	A6
A.2.13	Iterations Characteristics	A6
A.3	Notes	A7
A.3.1	Note 1	A7
A.3.2	Note 2	A7
A.3.3	Note 3	A8
A.3.4	Note 4	A9
A.4	Infilled Frame Examples	A9
A.4.1	Masonry Infilled R.C. Frame	A9
A.4.2	Micro Concrete Infilled Steel Frame	A9

APPENDIX B Structure of Program NEPAL B1

APPENDIX C Proposed 3-D Equivalent
4-Node Element C1

APPENDIX D Proposed Beam Element D1

D.1	General	D1
D.2	Proposed Rectangular C1 Beam Element.....	D3
D.2.1	The General Concept	D3
D.2.2	Shape Functions for Horizontal Nodal Displacements	D5
D.2.3	Shape Functions for Vertical Nodal Displacements	D9
D.2.4	Proposed Shape Functions for Shear Deformation	D12
D.2.5	Proposed Shape Function for Relative Displacement of the Centre Line of the Beam ..	D17
D.2.6	The Proposed Beam Element Stiffness Matrix ...	D19

APPENDIX E Comparison Tables E1

APPENDIX F Constitutive Formulation For Masonry F1

F.1 GeneralF1

F.2 Masonry under Uniaxial CompressionF2

F.2.1 Mechanics of Masonry in CompressionF2

F.2.2 Compressive Strength of Masonry
using the Stiffness Parameters of
Masonry MaterialsF4

F.2.3 Compressive Strength of Masonry using the
Strength Parameters of Masonry MaterialsF6

F.2.4 Proposed Generalized Approach for predicting
the Compressive Strength of MasonryF7

F.2.5 Stress-strain Relationship of Masonry
under Uniaxial CompressionF12

F.3 Masonry Subjected to In-plane StressesF14

F.3.1 Historical ReviewF14

F.3.2 General ConsiderationsF14

F.3.3 Masonry under Compression and ShearF16

F.3.4 Masonry under Biaxial CompressionF22

F.4 Examination of the Proposed
Failure CriteriaF23

F.5 Determination of the Stiffness Properties
of Masonry ComponentsF24

;

;

;

LIST OF TABLES

TABLE NO	TABLE TITLE
1.1	Racking Tests on Encased Steel Frames with Various Wall-Panel Infillings(after Wood(7))
2.1	comparison of Compressive Strength and Frame's moments(after Wood(20))
2.2	Criteria for a Non-linear F.E. Analysis Program
3.1	Comparison of Different Types of Beam Element
3.2	Choice of Infill Subdivision
4.1	The Possible Major and Minor Crack State Combinations
4.2	Experimental Data for Interfaces, Joints and Cracks
5.1	Properties of The Materials Related to Fig 5.5
6.1	F.E. Subdivision And Dimensions of Infilling Wall
6.2	Geometry and Mechanical Properties of Frame Members
6.3	Mechanical Properties of Assumed Materials
6.4	Mechanical Properties of Frame-Infill Interface
6.5	Stiffness and Strength Parameters of The Infilled Frames Considered
6.6	Elastic and Plastic Horizontal Load Capacity Of Open frames
6.7	Normal Stress Distribution at Infill-Frame Interface
6.8	Shear Transferred at Frame Infill Interface.
6.9	Stress Combination at Centre of Infill Resulted from Finite Element Analysis
6.10	Frame Thrust, Shear and Moment Distribution

- 7.1 Frame Forces
- 7.2 Comparison of The Collapse Racking load, H_c
- 7.3 Deviation of H_c (%) for Frames with Low α_c Value
- 7.4 Comparison of diagonal Tension Load, H_t
- 7.5 Comparison of Stiffness, K_0
- 7.6 Comparison of Bending Moment at Loaded Corners
- 7.7 Comparison of Bending Moment at the Unloaded Corners
- 7.8 Comparison of Column Bending Moment, M_{3c}
- 7.9 Comparison of Column Axial Force, N_{c1}
- 7.10 Comparison of Column Shear Force, S_{c1}

- A.1 Data Listing for R.C Frame with Masonry Infill.
- A.2 Data Listing for Steel Frame with Concrete infill
- B.1 The Structure Charts of Program 'NEPAL'
- B.2 List Of Variable Names Used in Program 'NEPAL'
- C.1 Strain Distribution in The Proposed Plane
3-D Equivalent Element
- E.1 to 12 Finite Element Analysis of Infilled Frames.
- E.13to 39 Hand Analysis of Infilled frames
- F.1 Comparison of The Proposed Calculated and
Experimental Compressive Strength of Brickwork

LIST OF FIGURES

FIGURE NO	FIGURE TITLE
2.1	Notations
2.2	Behaviour of Infilled Frame.
2.3	Infilled Frame Under Diagonal Loading.
2.4	Diagonally Loaded Infilled Frame and Interactive Forces (after Stafford Smith(12))
2.5	Typical Load-Deflection Curve for Concrete Infilled Steel Frame
2.6	Length of Contact as Function of λh (after Stafford Smith(12))
2.7	Infill Theoretical Stress Diagram for $a/h'=3/8$ (after Stafford Smith(12))
2.8	P/R as Function of λh (after Stafford Smith(12))
2.9	Infilled Frame
2.10	Diagonal Strength of Concrete Infill as a Function of λh
2.11	Comparison of Experimental and Theoretical Diagonal Strength of Infill as Function of λh (after Stafford Smith(12))
2.12	Experimental and Theoretical Effective Width of Diagonal Strut as Function of Length of Contact (after Stafford Smith(12))
2.13	Equivalent Strut Width as Function of λh for Stiffness Proposes (after Stafford Smith and Carter(12))
2.14	Shear Failure Criterion for Masonry Under Vertical Compression and Horizontal Shear.
2.15	Shear Strength of Infill as a Function of λh (after Stafford smith and Carter(13))

FIGURE NO	FIGURE TITLE
2.16	Variation of Strength of Infills of Model and Full-scale Brickwork (after Mainstone(9))
2.17	Variation of Strength of Infills of Micro Concrete (after Mainstone(9))
2.18	Variation of Stiffness of Infills of Model and Full-Scale Brickwork (after Mainstone(9))
2.19	Variation of Stiffness of Infills of Micro Concrete (after Mainstone(9))
2.20	Comparison of Various Methods of Analysis of Infilled Frame Based on λh
2.21	Idealized Plastic Failure Modes for Infilled Frames (after Wood(20))
2.22	Perspective View of Nielsen's(21) Square Yield Criterion for Unreinforced Wall, after Wood(20)
2.23	Infilled Frame Shear Mode of Collapse, Mode 'S'; (after Wood(20))
2.24	Infilled Frame Shear Rotation Mode of Collapse, Mode 'SR' (after wood(20))
2.25	Infilled Frame Diagonal Compression Mode of Collapse, Mode 'DC' (after Wood(20))
2.26	Design Chart for Determination of Optional Correction to f_s (after Wood(20))
2.27	Appropriate Penalty Factor (after Wood(20))
2.28	Variation of γ_p against aspect ratio of panel.
2.29	Finite Element and Experimental Results of Liauw et al(24)
2.30	Results of F.E. Analysis(24) in The Third Story of The Model Before and After Peak Load.
2.31	Mode 1 - Corner crushing with Failure in Columns (after Liauw et al(25))
2.32	Mode 2 - Corner Crushing with Failure in Beams (after Liauw et al(25))

FIGURE NO	FIGURE TITLE
2.33	Mode 3 - Diagonal Crushing (Span Greater than Height) (after Liauw et al(25))
2.34	Comparison of Liauw et al(25) estimated load with Experimental Results.
2.35	Failure Modes of Multistorey Infilled Frames. (after Liauw et al(25))
3.1	Newton Raphson Iteration
3.2	Geometry of a Quadrilateral Element.
3.3	Numerical Integration
3.4	Reinforcement Modelling.
3.5	The Most Used Isoparametric Elements
3.6	Masonry 3.D F.E Subdivision
3.7	3.D Equivalent 4-node Element
3.8	2-D Masonry F.E Subdivision Using Laminar Joints
3.9	2-D Masonry F.E Subdivision Using Masonry Equivalent Elements and Zero Thick Interfaces
3.10	The Modes of Joint Failure in a Masonry super-Element
3.11	Modelling of an Interface by Linkage Elements
3.12	Modelling of an Interface Segment by The Proposed 4-node Element
3.13	Wilson et al(44) Non-Conforming Beam Element.
3.14	Linear Elastic Analysis of Infilled Frame with Various F.E Subdivision Mesh
3.15	Effect of Scaling The Size of Masonry Elements on The Typical Infill Crack Pattern
4.1	Linear Elasticity Fracture Model
4.2	Non-Linear Elasticity Fracture Model
4.3	Elastic Perfect Plasticity Fracture Model
4.4	Elastic Work-Hardening Plasticity Fracture Model

FIGURE NO	FIGURE TITLE
4.5	The Elastoplastic Fracture Model of Darwin and Peknold(47)
4.6	Comparison of the Proposed Formulation with Experiments of Kupfer et al(55)
4.7	Comparison of Actual and Proposed Complete Stress-strain Curves of Concrete.
4.8	Comparison of the Proposed Value for Poisson's Ratio with the Experimental Results(55)
4.9	Concrete Under Unloading and Reloading
4.10	Stress strain Curve of Concrete in Tension
4.11	Drucker-Prager and Von Mises Yield Surfaces in Principal Stress Space.
4.12	Mohr-Coulomb and Tresca Yield Surface in Principal Stress Space (after Zienkiewicz(36))
4.13	Comparison of the Proposed Failure Criteria for Concrete under Biaxial Compression with the Experimental Results of Kupfer et al(55)
4.14	Typical Triaxial Test Arrangements
4.15	Comparison of the Proposed Failure Criteria with Experimental Results of Kupfer et al(55)
4.16	Experimental Stress-strain Relationship of Concrete under Biaxial Loading.
4.17	Equivalent Uniaxial Stress-strain Curves
4.18	Comparison of The Proposed Analytical Prediction of Equivalent Uniaxial Strains at Peak Load with Some Experimental Data
4.19	Comparison of the Proposed Prediction of The Poisson's Ratio at Peak Stress with Experimental Results of Kupfer et al(55)
4.20	Comparison of the predicted and actual Stress-strain Diagrams for concrete under biaxial Compression; $\sigma_1=0$, $\sigma_2/\sigma_3=0.52$
4.21	Comparison of the predicted and actual Stress-strain Diagrams for concrete under Biaxial Compression and tension; $\sigma_2=0$, $\sigma_1/\sigma_2=-0.052$

FIGURE NO	FIGURE TITLE
4.22	Stress and Equivalent Uniaxial Strain Relationship of Concrete under Proportional Multiaxial Unloading and Reloading
4.23	Proposed Model for Relationship of Normalized Values of Stress and Equivalent Uniaxial Strain of Concrete under Proportional loading
4.24	Comparison of The Proposed Prediction of Unloading Modulus of Elasticity with Karsan and Jersa(60) Formula.
4.25	Proposed Model for Non-Proportional Triaxial Load Increment
4.26	Different Fracture Criteria for Concrete in Tension
4.27	Crack Modelling.
4.28	Possible States of a Single Cracked Material.
4.29	Determination of One Co-efficient for both Crack Dilatancy and friction
4.30	Double Cracked Material
4.31	Possible States of Double Cracked Materials.
4.32	Stress-strain Curves for Steel(after Chen(39));
4.33	Proposed Stress-strain Relationship Models for Steel.
4.34	Von Mises Yield Criterion on The Co-ordinate Plane $\sigma_3=0$
4.35	Criteria for Inelastic Behaviour of an Interface
4.36	Concrete-on-steel Shear-relative Displacement Relationship
4.37	Behaviour of Bed-Joints of Grouted Concrete Block Masonry under Precompression
4.38	Typical Shear Stress-Tangential Displacement Curves for Interfaces under Constant Normal Stress
4.39	Proposed Constitutive Model for Fully bonded Interfaces

FIGURE NO	FIGURE TITLE
4.40	Proposed Constitutive Model for Partially Bonded Interface
4.41	Proposed Constitutive Model of Totally Debonded Interface
5.1	Proposed Load Application.
5.2	F.E Analysis of RC Beam under Centre Point Load.
5.3	Comparison of The F.E Analysis of RC Beam With Experimental Results of Bresler et al (95)
5.4	Comparison of The F.E Analysis of an Open Steel Frame with Experimental Values (29)
5.5	Comparison of The F.E Analysis of Model Steel Concrete Infilled Frame With Experimental Results (29)
5.6	F.E Results at Station 1 ($\Delta h=0.382\text{mm}$). (a)Frame, (b)Interface and (c)Infill
5.7	F.E Results at Station 2 ($\Delta h=0.678\text{mm}$); (a)Frame, (b)Interface and (c)Infill
5.8	F.E Results at Station 3 ($\Delta h=0.934\text{mm}$); (a)Frame, (b)Interface and (c)Infill
5.9	F.E Results at Station 4 ($\Delta h=1.54\text{mm}$); (a)Frame, (b)Interface and (c)Infill
6.1	Infilled Frame Under Diagonal Loading
6.2	Typical Open Frame Load-Deflection Diagram
6.3 to 7	Load-Deflection Diagrams, Results of F.E Analysis
6.8	F.E. Analysis Results of Infilled Frame MMUR2 at Working Stress Load Level.
6.9	F.E. Analysis Results of Infilled Frame MMUR2 at Peak Load Level
6.10	Typical Progressive Failure Stages of Infilled Frame under Racking
6.11	Biaxial Stress Combinations of Infill in Highly Stressed Regions Leading to Crushing or Cracking

FIGURE NO	FIGURE TITLE
7.1	Proposed Frame-Infill Interaction Forces; a)wall, b)column, c)moment diagram
7.2	Deformation of Infilled Frames; a)columns only, b)beams only
7.3	Proposed Infill Boundary Stresses; a)boundary stresses, b)at column interface c)at beam interface
7.4	Frame forces; a)Horizontal Forces Equilibrium, b) Column forces, c) Column Bending Moment Diagram
7.5	Upper Limit for Length of Contact
7.6	Graphical Representation of Failure Modes
7.7	Chart for adjusting μ_c , β_c and α_c
7.8	Application of The Chart; a)high μ_c b)low μ_c
7.9	Comparison of Various Methods of Analysis with Finite Element and Test Results of Horizontal Collapse Load, H_c .
7.10	Comparison of Various Methods of Analysis with Finite Element and Test Results of; a)Cracking load, H_t , b)Stiffness, K_0 .
A.1	Code Number for Geometry of Interface
A.2	R.C Masonry-infilled Frame Subdivision Lay-out.
A.3	Reinforcement Data of The Frame Tested by Samai(8)
A.4	Steel Concrete-infilled Frame Subdivision Lay-out
D.1	Deformation of a Beam Segment under Arbitrary Forces
D.2	Modes of Deformation of the Proposed Beam Element Resulting from Nodal Displacements.
D.3	Deformation of the Proposed Beam Element Due to Displacement of the Proposed 5th Node
D.4	Displacement of Centre Line of a Beam Due to Effect of the Poissin's Ratio

FIGURE NO

FIGURE TITLE

- F.1 Proposed Constitutive Model for Partially Bonded Interface
- F.2 Proposed Constitutive Model of Totally Debonded Interface
- F.3 Stress Distribution within the Components of Masonry under Uniaxial Compression.
- F.4 Charts to Estimate the Compressive Strength of Masonry.
- F.5 Comparison of the Proposed Masonry Failure Criteria with Experimental Data; $\theta=45$.
- F.6 Comparison of the Proposed Masonry Failure Criteria with Experimental Data; $\theta=67.5$.
- F.7 Comparison of the Proposed Masonry Failure Criteria with Experimental Data; $\theta=67.5$.

;

NOTATIONS

- a = Length of contact between column and infill
- a = Vector of nodal displacements
- a = Length of element
- A = A constant controlling failure criteria of brittle material under biaxial compression-tension
- b = Height of element
- [B] = Element strain function matrix
- c = A constant value used in failure criteria of brittle material under multiaxial compression
- d = Diagonal length of a panel
- D = A parameter controlling the falling branch of stress-strain curve
- [D] = Stress-strain relation matrix
- [D_t] = Tangent stress-strain relation matrix
- e = Normalized EUS; $e = \epsilon_{iuc} / \sigma_{iuc}$
- e_E = Normalized EUS on the envelope stress-strain curve
- e_p = Normalized plastic EUS
- E = Secant modulus
- E₀ = Initial tangent modulus
- E_b = Modulus of elasticity of beams of a frame
- E_c = Modulus of elasticity of columns of a frame
- E_c = Secant modulus at peak unconfined uniaxial compression
- E_f = Modulus of elasticity of frame members
- E_i = Initial modulus of elasticity of infill
- E_s = Secant modulus at peak stresses
- E_{st} = Secant modulus at peak uniaxial tension

E_t = Tangent modulus
 E_{u1} = Tangent modulus in proportional unloading
EUS = Equivalent Uniaxial Strain
 f_c' = Standard cylinder strength of concrete
 f_{cu} = Standard cube strength of concrete
 f_{bc} = Equal biaxial compression strength
 \bar{f}_{bc} = f_{bc}/σ_c
 f_{ij} = A parameter related to variation of poisson's ratio
F = Diagonal load transferred by frame alone
 f_t = Direct tensile strength of concrete
 f_{tb} = Joint tensile bond strength
 f_{sb} = Joint shear bond strength
 f_m = Mortar compressive strength on cylinder
 f_{pr} = Masonry prism strength
g = A parameter controlling EUS curves
 h' = Height of infill
h = Height of column measured o/c of beams
H = Weighting coefficient in numerical integration
H = Horizontal load carried by an infilled frame; index u indicates the ultimate load and indices t and c signify the tensile and compressive failure modes respectively
I = Moment of inertia
 I_f = Moment of inertia of frame members
 I_b = Moment of inertia of the beams in a frame
 I_c = Moment of inertia of the columns in a frame
[K] = Structure stiffness matrix
 $[K_t]$ = Structure tangent stiffness matrix
 $[K]^e$ = Element stiffness matrix
 $[K_t]^e$ = Element tangent stiffness matrix

k = Material constant controlling the Poisson's ratio
 l' = Length of infill
 l = Length of beams measured o/c of columns
 m = Strength parameter in Wood's Theory
 M_p = Plastic resisting moment of frame members
 $[N]$ = Strain/stress relation matrix
 N = Shape function
 P = Total diagonal load transferred by infilled frame
 $\{P\}$ Vector of external loads
 q = A constant controlling the failure criterion of brittle material under multiaxial compression
 $\{q\}$ Vector of equivalent nodal forces
 $\{q\}^e$ = Vector of element equivalent nodal forces
 R = Diagonal load transferred by an infilled frame; index u indicates the ultimate load and indices t and c signify the tensile and compressive failure modes respectively
 $\{R\}$ = Vector of out-of-balanced nodal forces
 s = Normalized principal stress
 t = Wall or element thickness
 t_i = Thickness of infill
 t_s = Thickness of equivalent steel layer
 $[T]$ = Transformation matrix
 u, v = Total displacement components along x and y coordinate respectively
 w = Overall change in thickness
 w = width of opening of a crack or an interface
 w_s = An specified width of diagonal strut of infilled frame
 w_e = Effective width of diagonal strut of infill (indices k, c and t denote the values corresponding to the diagonal compressive strength and diagonal cracking load respectively)
 x, y, z = Structure coordinates

γ_p = Penalty factor in Wood's method
 $\{\epsilon\}$ = Vector of total strain.
 $\{\epsilon_p\}$ = Vector of total plastic strain
 $\{\epsilon_{sl}\}$ = Vector of total equivalent-joint-slip strain in joint material
 $\{\epsilon_{sp}\}$ = Vector of total equivalent-joint-separation strain in joint material
 $\{\epsilon_u\}$ = Vector of EUS
 ϵ_{iu} = EUS in principal coordinates
 ϵ_{iuc} = Equivalent uniaxial strain at peak stress
 ϵ_c = Strain corresponding to σ_c in uniaxial unconfined loading
 ϵ_t = Strain corresponding to σ_t in uniaxial direct tension
 $\{\epsilon_{uE}\}$ = Vector of projection of equivalent uniaxial strain on equivalent uniaxial envelope curves
 ϵ_{iuE} = The component of $\{\epsilon_{uE}\}$ corresponding to the principal coordinate
 $\{\epsilon_{up}\}$ = Vector of equivalent uniaxial plastic residual strain after full unloading
 ϵ_{iup} = The component of $\{\epsilon_{up}\}$ corresponding to i th principal direction
 λ = Stiffness parameter in Stafford Smith method
 ν = Poisson's ratio
 ν_0 = Initial Poisson's ratio
 ν^*, ν = Incremental Poisson's ratio
 μ = Coefficient of friction of interface
 i = Volumetric steel ratio of its equivalent layer
 σ_n, τ = Normal and shear stresses respectively.
 σ = Vector of stress in structure coordinates
 $\{\sigma\}^T = [\sigma_x, \sigma_y, \sigma_z, \gamma_{xy}, \gamma_{yz}, \gamma_{zx}]$
 σ_c = Unconfined uniaxial compressive strength. (-ve)
 $\sigma_c = -(0.90 \text{ to } 0.96) f_c'$ (-ve)

$\rho\sigma', \tau'$ = Normal and shear stresses on yield surface;

they appear with various suffixes:-

σ_1', σ_2' and σ_3' (for principal directions),

$\sigma_x', \sigma_y', \sigma_z', \tau_{xy}', \tau_{yz}', \tau_{zx}'$ (for an arbitrary directions)

σ_{dt} = Diagonal tensile stress at centre of the infill to cause tensile failure

ξ, η Normalized coordinates

CHAPTER ONE

Introduction

Framed buildings normally contain wall panels whose prime function is to either separate spaces within the building or to complete the building envelope. The properties of these walls and their position within the structural frame may be so chosen that they can also have a significant influence on the response of the structure subjected to side sway. Such structural configurations are termed "Infilled Frames" and have been investigated by a number of researchers.

The history of work on infilled frames dates back to the mid 1950's when the design of rigid-jointed multi-storey frames was being revolutionized as a result of work done by Wood et al (1,2), Beaufoy et al (3) and Chandler (4) and Livesley et al (5), wherein "The degree of restraint method" and application of the critical load in the new elastoplastic design of these structures were being developed. According to the new design method, which was reported later by "The Joint Committee (6)", the stability of rigid multistorey framed structures would significantly improve and considerable economy would be achieved if side sway is resisted separately by walls and floors or bracing. However, in this method no allowance was given for the contribution of the infilling walls in limiting side sway of

framed structures due to the lack of understanding of the behaviour of infilled frames. Wood⁽⁷⁾, 1958, concluded that "there had been a neglect in the past to study the stiffening effect of cladding of tall buildings." He listed a series of in-plane racking tests, Table 1.1, on encased steel frames with various wall panel infillings. This table shows the significance of the infilling walls in reducing side sway of multistorey buildings.

Since then even though the potential economy and efficiency of infilled frame construction has always been evident, its use still has not been widely accepted, primarily due to lack of theory. During the last three decades a few analytical approaches have been developed. A summary of previous work is **given** in Chapter 2. These methods can generally be classified into the following categories:

- i) The approaches based on linear elasticity theories.
- ii) The approaches using perfect plasticity theories.

The assumptions made in these approaches vary widely, and the predictions of strength and stiffness also vary widely.

Attempts to verify these approaches using experimental results have not been totally successful because the experimental data are significantly affected by variations in the properties of the materials. It is not feasible to measure all the necessary information, such as stresses in the infill and also in the frame members.

The finite element method, however, as a powerful and fast growing technique, has become a popular method for

solving highly indeterminate problems. Therefore, quite a few finite element analyses have been developed for infilled frames during the past ten years mainly using either pure elasticity or perfect plasticity theories with allowance for separation and slip of the joints. The results of these analyses have been used to examine the aforementioned elastic and plastic methods. These are reviewed in Chapter 2. The rather large discrepancy between the two groups of approaches indicates that study of infilled frames still lacks a rational analysis accounting for both elastic and plastic behaviour of the structure.

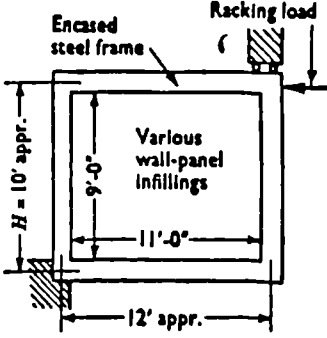
The prime objective of this study has therefore, been to develop a finite element program particularly written for the analysis of infilled frames and examine the existing methods. It was desirable that such a program should be capable of simulating the non-linear behaviour of frame, infill and their interfaces as accurately as possible. In order to satisfy these requirements it was necessary to investigate the materials behaviour in detail and to develop suitable mathematical models for their mechanical response. This work is covered in Chapter 4. In order to improve the accuracy and economy of the finite element analysis, new elements such as beam, interface and loading elements needed to be developed. These elements and also the basis of the finite element method are described in Chapter 3. These efforts led to the finite element analysis computer program "NEPAL" written by the author. This program is introduced in Chapter 5. This chapter also reports the tests carried out to examine the performance of

the program in solving some non-linear structural problems.

The next phase of the work was to study the behaviour of infilled frames within practical ranges of beam, column and infill strength and also the infill aspect ratio. Computation and results of analysis of these frames are described and discussed in Chapter 6 leading to the necessity of proposing a new hand method of analysis based on both elastic and plastic behaviour of the materials and limited infill strain at collapse load. Development of such a method is described in Chapter 7. This chapter also deals with comparison of the results of the newly developed method with the results of the finite element analysis and previously existing experiments and methods.

The final chapter presents the conclusions drawn from the present investigation and recommendations and suggestions to carry on the work in the future.

Table 1.1 Racking Tests on Encased Steel Frames with Various Wall-Panel Infillings (after Wood⁷)

Type of frame and infill	First visible crack			Ultimate load: tons	Horizontal deformation at ultimate load: inches
	Load: tons	Horizontal deformation ΔH : inch	Approximate ratio deformation/height: $\Delta H/H$		
					
<p><i>Frame Type 1</i> Horizontal girders 10 in. \times 4½ in. (I 25) Vertical stanchions 10 in. \times 8 in. (I 55) (weak way) 6-in. \times 4-in. \times ½-in. bolted cleat connexions to top and bottom flanges of each beam</p>					
Open bare frame	7	1.0 {First yield}	—	9.3	6.0
Encased frame	14	1.0	1/100	20	2.3
Encased frame with 4½-in. brick panel	35	0.3	1/350	49	2.5
(Repeat test) with 4½-in. brick panel	30	0.28	1/400	56	2.8
Brick-on-edge infilling	21	0.27	1/400	40	2.0
3-in. clinker block	22	0.25	1/450	35	0.8
(Repeat test) 3-in. clinker block.	24	0.28	1/400	36	0.8
3-in. hollow clay block	22	0.40	1/275	30	1.5
13½-in. brick	110	0.26	1/425	135	0.6
4½-in. brick, with door opening .	13	0.11	1/1000	38	2.1
<p><i>Frame Type 2 (somewhat stiffer than Type 1)</i> Horizontal girders 13 in. \times 5 in. (I 35) Vertical stanchions 10 in. \times 8 in. (I 55) (strong way) 6-in. \times 4-in. \times ½-in. cleat connexions</p>					
Encased frame	17	1.0	1/100	23	2.2
4½-in. brick infilling	37	0.28	1/400	75	1.5

CHAPTER TWO

Review of Previous Work

2.1 Introduction

The composite behaviour of an infilled frame is a complex statically indeterminate problem. Since 1958 this topic has been the subject of several separate investigations at various institutions throughout the world. The approaches to the problem have varied widely. Considering the different assumptions made, it is not surprising that the predictions of stiffness and strength have also varied widely. A detailed review of previous experimental and theoretical investigations has been given by Samai⁽⁸⁾. In this chapter the intention is to briefly review the behaviour of infilled frame and to summarize the main stages in the development of its analysis and understanding of its behaviour.

2.2 Behaviour of Infilled Frames under Racking Load

Fig 2.1 shows a rectangular single bay single storey infilled frame under racking load, **H**.

Mainstone⁽⁹⁾ described the behaviour of this composite structure as follows:

If, before loading, the infill fits the frame perfectly, its initial behaviour will lie somewhere between the extremes illustrated in Figs 2.2(a) and 2.2(b). The

maximum possible contribution to resisting the load will be achieved by a state of uniform shear throughout, calling for continuous transfer of shear along the interfaces with the frame plus continuous tension on beams and continuous compression on columns for non-square frames, Fig 2.2(a). Considered as a diagonal strut, the infill may then be said to have an effective width, w' , Fig 2.1(b).

At the other extreme, the interface reactions will be concentrated to the corners and the distribution of stress will be highly non-uniform, leading to a behaviour equivalent to that of a much narrower strut Fig 2.2(b).

Between the two extremes the interface reactions will always be distributed over finite lengths of the beams and columns i.e, **BF** and **BG** in Fig 2.4, unlike the concentrated reactions of a true diagonal strut, Fig 2.2(b). Some changes in the mode of deformation of the frame will be induced leading to a further increase in the composite stiffness. Diagonal cracking, if it precedes crushing of the infill, will modify this initial behaviour by creating, in effect, two or more struts in place of the original one, Figs 2.2(c), 2.2(d). Quite marked changes in the mode of deformation of the frame may then result from redistributions of the interface reactions.

If, before loading, the infill does not fit perfectly, the interface reactions and the resulting behaviour will be further modified. A continuous gap at the top, for instance, will mean that load can be transmitted to the infill only by compression and shear on the vertical faces. The alignment of the effective strut will then be

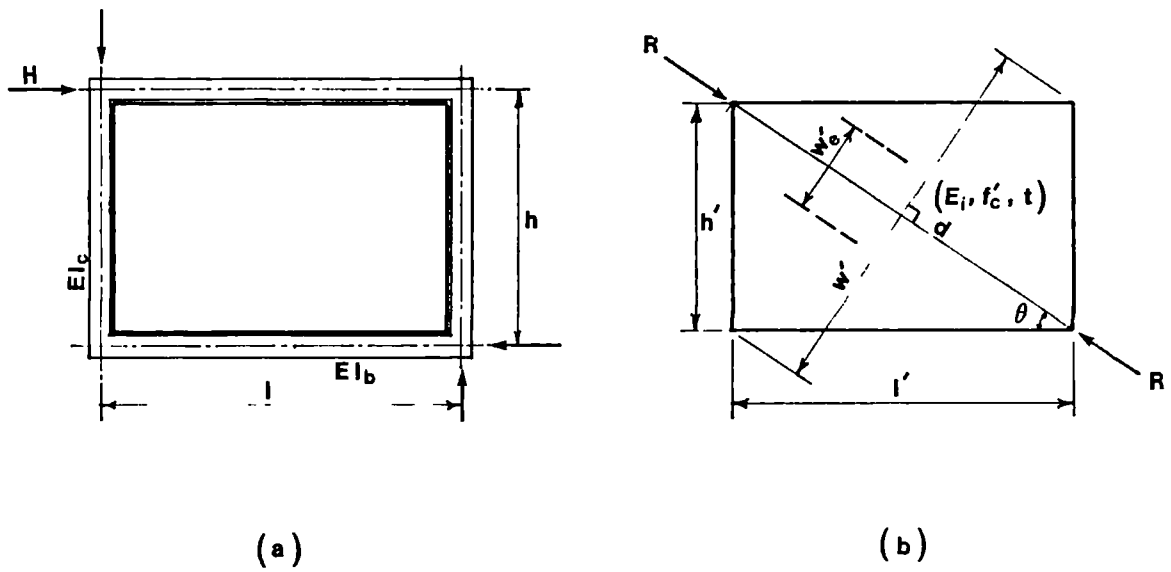


Figure 2.1 Notations

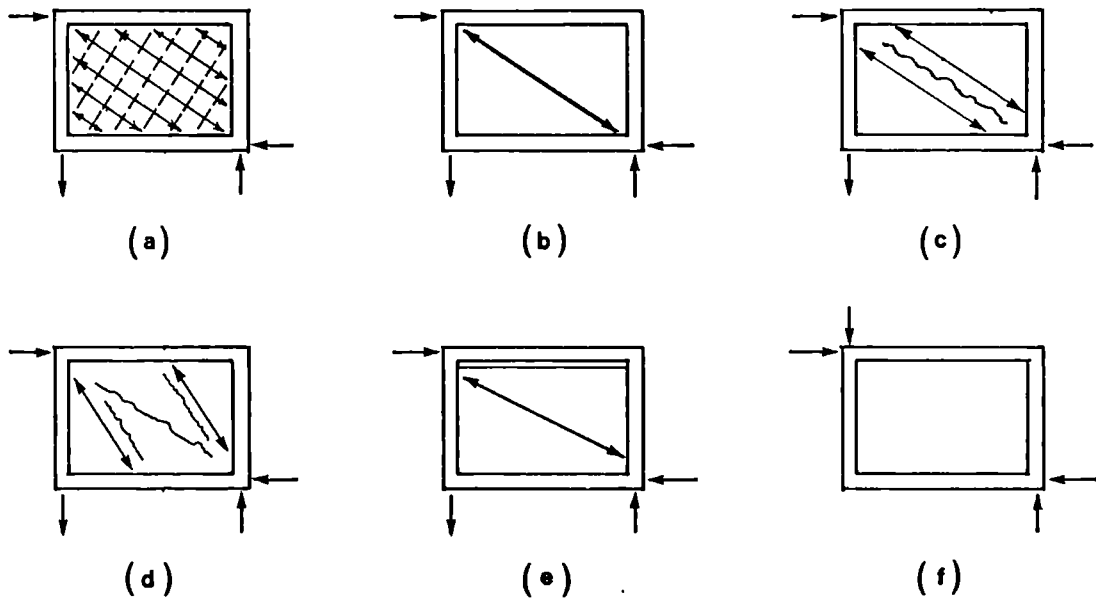


Figure 2.2 Behaviour of Infilled Frame; (a)infill under uniform shear, (b)infill as a diagonal bracing, (c and d)infill as behaving between (a) and (b), (e)infill with lack of fit and (f)infilled frame loaded diagonally (after Mainstone⁽⁹⁾)

somewhat different initially, Fig 2.2(e), and there will be a tendency for the infill to slip and rotate until it bears on the beam and column at the loaded corners.

An infilled frame may be loaded diagonally as shown in Fig 2.2(f). This type of loading produces compression in the windward column in place of tension that would arise in practice as shown in Fig 2.2(a) to (e).

The real behaviour of an infill in resisting a racking load is more complex than that of a simple diagonal strut. However the early work on the subject was based on idealization of the infill as a simple diagonal strut

2.3 Early Work and the Concept of Diagonal Strut

Serious experimental and analytical investigation on infilled frames was started in 1958 by Polyakov(10). He suggested the possibility of considering the effect of the infilling wall in each panel as equivalent to diagonal bracing Fig 2.3(b). This suggestion was later taken up by Holmes(11), 1961. He represented the infill by a pin-jointed strut connecting the loaded corners as shown in Fig 2.3(b). He also concluded that, at failure, the deflection of the composite wall and frame is small in comparison with the **deflection** of the bare frame. Therefore, the frame members remain in ^{the} elastic stage up to failure load. Accordingly, he calculated the change in the frame diagonal, δd , as:

$$\delta d = \frac{H-R(h')^3 \cos\theta}{24EI_c} \left[1 + \frac{I_c}{I_b} \cot\theta \right] \cos\theta \quad (2.1)$$

The shortening of the equivalent strut at failure was also calculated as:

$$\delta d = \epsilon_c d \quad (2.2)$$

$$\delta d = \epsilon_c h' / \sin \theta \quad (2.3)$$

where ϵ_c denotes the strain in the infill at failure.

The value of ϵ_c was taken as 0.002 as a safe limiting value for concrete infill. From Eq 2.1 and 2.3 the horizontal load at failure, H , was derived by Holmes(11) as follows:

$$H = \frac{24EI_c \epsilon_c}{h'^2 \left[1 + \frac{I_c}{I_b} \cot \theta \right] \sin \theta \cos \theta} + A f_c \cos \theta \quad (2.4)$$

Where R is replaced by the product of the cross sectional area, A , of the equivalent strut and the crushing strength of the infill, f_c . Holmes(11) showed that, for strength purposes, $td/3$ best represents the value of A for the infilled frames tested. However, the theoretical deflections at the ultimate load, corresponding to the proposed value of A , were generally much lower than those of the companion experimental deflections.

The Holmes one third rule for determining the width of the diagonal strut is independent of infill/frame strength and stiffness parameters. However, as will be seen later in this chapter, the behaviour of an infilled frame is highly dependent on these parameters.

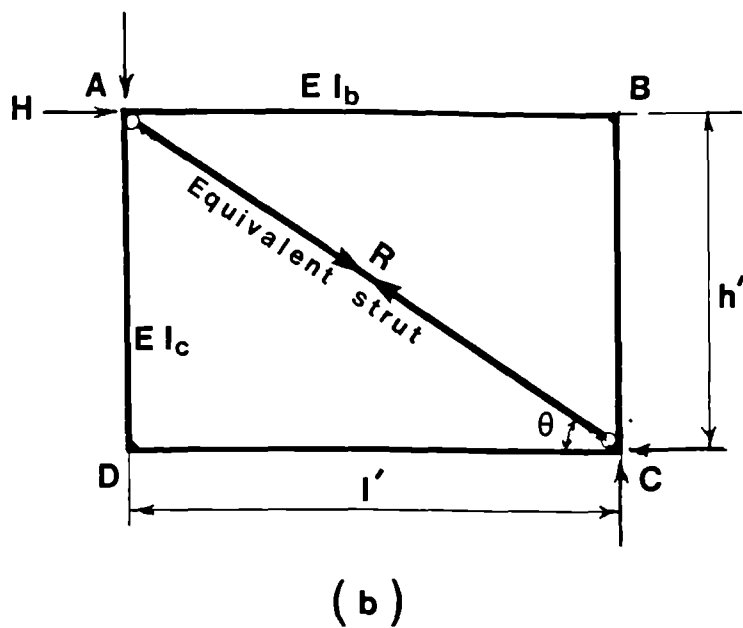
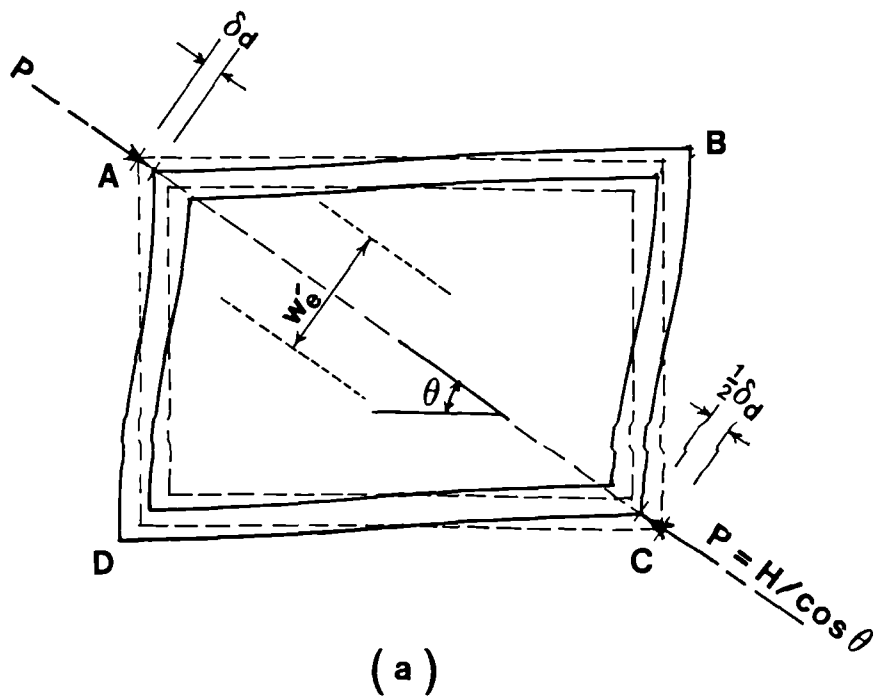


Figure 2.3 Infilled Frame Under Diagonal Loading; (a) frame deformation and (b) idealization of infill as diagonal strut (after Holmes⁽¹¹⁾)

Holmes(11)' approximation, although crude, may be considered as the basis for later work especially the work done by Stafford Smith(12), 1966, which is summarized in the following sections.

2.4 Theories Based on Infill/Frame Stiffness Parameter

2.4.1 General

Stafford Smith(12), 1966, carried out a wide range of tests on 150mm square micro-concrete model infills bounded by steel frames subjected to diagonal load, Fig 2.4. According to his observation, he adopted the equivalent

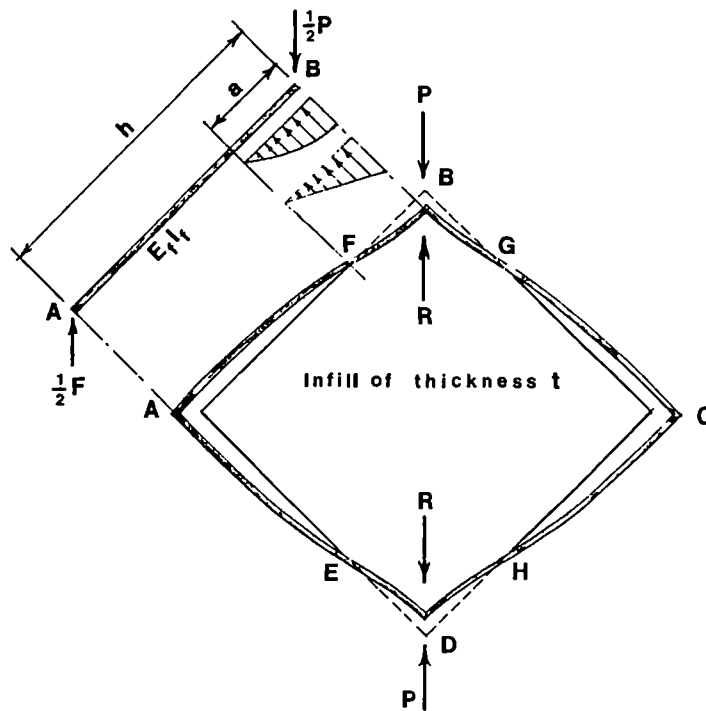


Figure 2.4 Diagonally Loaded Infilled Frame and Interactive Forces (after Stafford Smith(12))

diagonal strut in representing the effect of infill. However, Stafford Smith did not share the view of the one third rule proposed by Holmes⁽¹¹⁾ which is described in Section 2.3. Instead, he pointed out that the width of the equivalent diagonal strut is determined by the finite lengths of contact between the frame and the infill at the loaded corners, Fig 2.4.

Stafford Smith and Carter⁽¹³⁾, 1969, expanded the work of Stafford Smith to deal with rectangular and multistorey infilled frames. Also they further studied the stiffness of such structures. A review of their work is given in the following sections.

2.4.2 Stafford Smith Observations on the Behaviour of Infilled Frames Subjected to Racking Load

When an infilled frame is under either horizontal or diagonal load, Fig 2.4, the infill and the frame separate over a large part of the length of each side and contact remains only adjacent to the corners at the ends of the compression diagonal. As the load is increased, failure occurs eventually in either the frame or the infill as follows:

- i) frame failure results from tension in the windward column or from shearing of the columns or beams.
- ii) Infill failure is initially by cracking along the compressive diagonal. The final failure results from crushing near one of loaded corners or, in the case of a comparatively very stiff frame, crushing over a more

general interior region of the infill. However, if the infill is of brick masonry an alternative possibility of shearing failure along the plane of the bed-joints may arise.

Typical load deflection curves obtained by Stafford Smith⁽¹²⁾ for cracking and non-cracking concrete infills are shown in Fig 2.5.

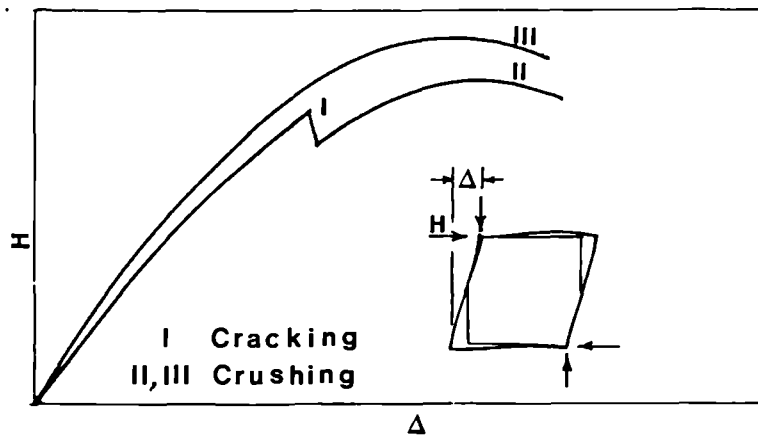


Figure 2.5 Typical Load-Deflection Curve for Concrete Infilled Steel Frame (after Stafford Smith and Carter⁽¹³⁾)

2.4.3 Stafford Smith's Theoretical Analysis

Stafford Smith⁽¹²⁾ carried out extensive theoretical work using elasticity theory to derive the length of contact and strength and stiffness of infilled frames as follows.

Fig 2.4 shows a square infill frame subjected to diagonal load illustrating the model infilled frames tested by Stafford Smith⁽¹²⁾. Consider the side **AFB**, in Fig 2.4, of which **FB** remains in contact with the infill. Assuming a triangularly distributed reaction along **FB**, the bending and equilibrium equations were derived for the separate lengths, **AF** and **FB**; these then were related by the continuity conditions at point **F**. A further equation for the energy of **AB** and one-quarter of the infill, allowed Stafford Smith to reduce the whole set to a single equation in terms of λh and a/h' where:

$$\lambda h = h \sqrt[4]{\frac{E_i t_i}{4E_f I_f h'}} \quad (2.5)$$

represents the infill/frame stiffness parameter. A similar analysis was carried out, using a parabolic distribution of the reaction along **FB** to produce an alternative equation relating a/h' and λh . The solutions of these equations yielded the two curves given in Fig 2.6 which also shows the Stafford Smith's experimental results for length of contact. The close alignment of the two curves, and the satisfactory agreement of the experimental results, could lead to the

adoption of either curve. However, the third curve shown in Fig 2.6 also agreed closely with the experimental results and the two other curves. This additional curve is given by:

$$\frac{a}{h'} = \frac{\pi}{2\lambda h} \quad (2.6)$$

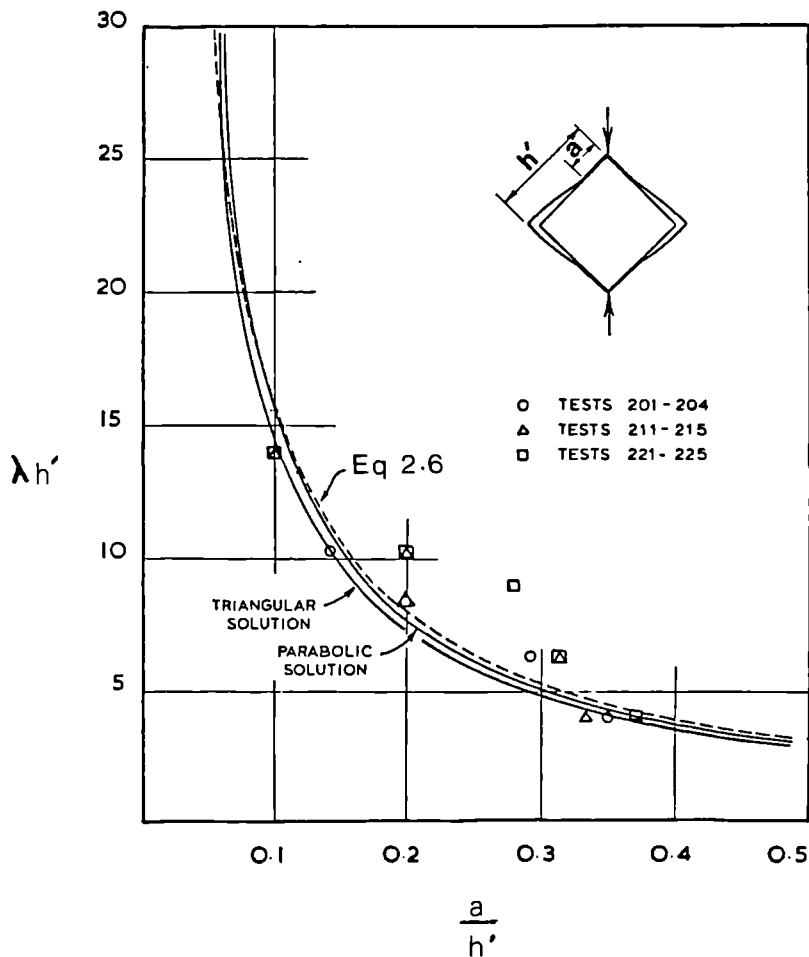


Figure 2.6 Length of Contact as Function of λh (after Stafford Smith(12))

which was adapted from the equation for the length of contact of a free beam on an elastic foundation subjected to a concentrated load, following the analysis of Hetenyi et al(14). Because the third curve was more conveniently expressed algebraically than the other two, and in other respects was equally acceptable, it was adopted by Stafford Smith for later use in the analysis.

The stiffness parameter, λh , was later generalized by Stafford Smith and Carter(13) to allow for rectangular walls as follows:

$$\lambda h = h \sqrt[4]{\frac{E_i t_i}{4 E_c I_{ch'}} \sin 2\theta} \quad (2.7)$$

Since an elastic theory was used in the analysis, the length of contact remained constant during the course of loading.

Having derived the length of contact, it became possible to isolate the infill from the frame, Fig 2.4, and to represent the frame-infill interaction forces, R , by only a set of normal forces distributed triangularly over the length of contact as shown in Fig 2.4 i.e, no frictional force was allowed for at the frame infill interface. Thence for various lengths of contact ranging between 1/8 to 5/8 of the height of infill, Stafford Smith(12) developed a set of two dimensional finite difference analyses and plotted the corresponding stress diagrams to relate the interior stresses to the boundary forces of the infill, as typically shown in Fig 2.7.

In order to study the contribution of the frame, Stafford Smith, this time, represented the infill interaction forces by triangularly distributed normal forces acting over the length of contact on each side of the frame, Fig 2.4. Thence, he calculated the load carried by the frame alone, F , by developing an energy analysis of the redundant system which was repeated for various lengths of contact within the same range as above.

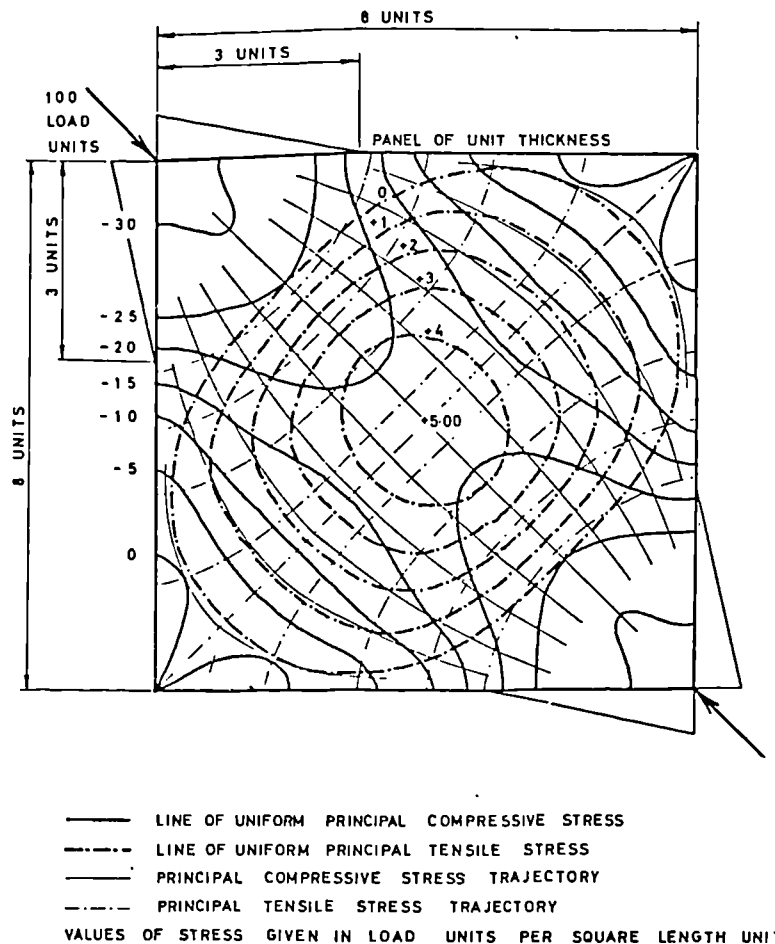


Figure 2.7 Infill Theoretical Stress Diagram for $a/h'=3/8$ (after Stafford Smith(12))

The above analysis for frame and infill allowed the total carrying load, P , of the infilled frame to be calculated as follows:

$$P = R + F$$

Fig 2.8 shows the variation of significance of the diagonal load carried by the frame, F , in comparison with the infill load, R , as a function of λh for square infilled frames. As shown, the contribution of F is less than only 5% of the infill carrying load, R , when λh , is more than 3.8. However, for infilled frames with λh , less than 3.8 (weak infill) the contribution of the frame to the total diagonal carrying load, R , rapidly becomes significant.

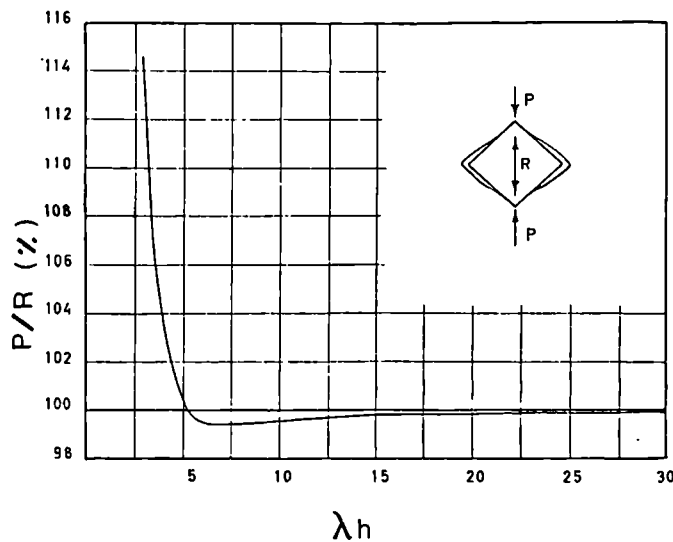


Figure 2.8 P/R as Function of λh (after Stafford Smith(12))

2.4.4 Lateral Strength of Infilled Frames

In order to simplify the analysis, Stafford Smith⁽¹²⁾ ignored the diagonal load transferred through the frame as shown in Fig 2.8 and as discussed in the last paragraph of Section 2.4.3. The lateral strength of infilled frames then can simply be obtained from static analysis of the frame in which the infills are replaced by equivalent diagonal pin-jointed struts as shown in Fig 2.9. It should be noted that, in reality, the above assumption does not necessarily mean that the flexural stiffness of the frame is neglected since the flexural stiffness of the frame has already allowed for in determination of the length of contact in Eqs 2.6 and 2.7.

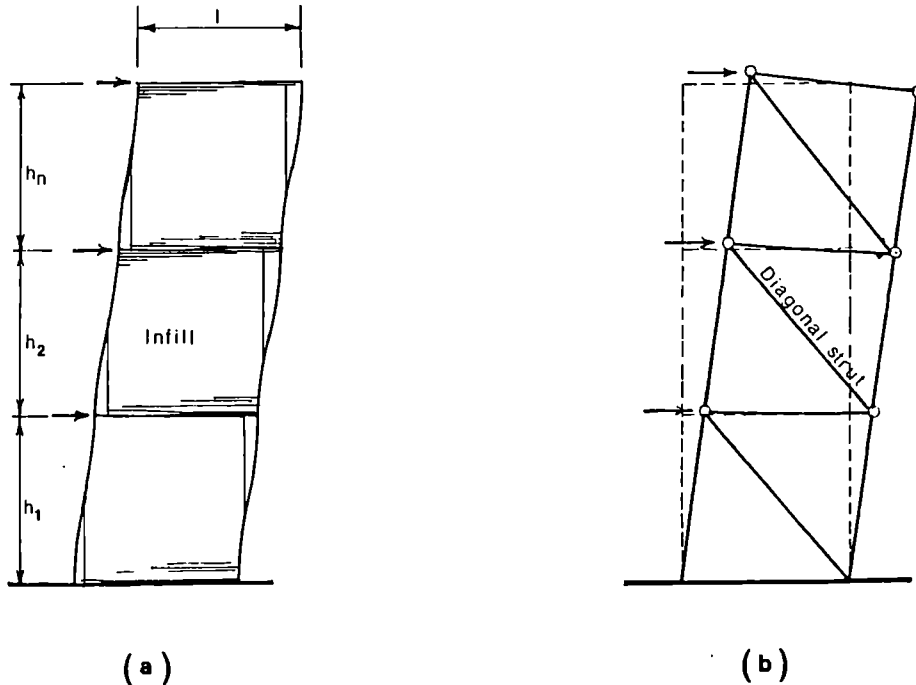


Figure 2.9 Infilled Frame; (a) laterally loaded infilled frame and (b) equivalent frame (after Stafford Smith and Carter⁽¹³⁾)

Collapse of an infilled frame may occur through failure either of the frame or of the infill. Failure of the frame can result from tension in windward columns or shear in the beams, columns or their connections. If however, the frame is adequately strong, collapse will eventually occur by compression failure of the infill propagating from one of the loaded corners or, in the case of a comparatively very stiff frame, crushing over a more general interior region of the infill. Compressive failure of infill may be preceded by a diagonal cracking along the compressive diagonal.

Infill failure modes and loads were formulated by Stafford Smith⁽¹²⁾ for square panels. The work was later generalized for masonry infills, rectangular panels and multi-storey infilled frames by Stafford Smith and Carter⁽¹³⁾. These are described as follows.

a) Diagonal Cracking of Infill

The diagonal force necessary to cause cracking of the infill, R_{ut} , is that which would produce a maximum principal tensile stress in the infill equal to the tensile failure strength of the infill material. From the maximum principal tensile stress values taken from the infill stress diagrams, Fig 2.7, and Eq 2.6 a series of curves were constructed by Stafford Smith and Carter⁽¹³⁾ to relate the diagonal cracking load, R_{ut} , to λh for various panel length/height proportions. Fig 2.10 shows these curves where F_t' is replaced by $0.1f_c'$, a reasonable value for concrete tensile strength, thus allowing the basic parameter

for expressing the cracking strength, $R_{ut}/(f_t'h't)$, to be converted to $R_{uc}/(f_c'h't)$ and thereby permitting a direct comparison of the cracking and compressive failure curves on the same graph. Fig 2.10 also shows that the greater is the length/height proportion of the infill, or the smaller is the value of λh , i.e the stiffer is the column relative to the infill, the greater is the diagonal cracking strength of infill.

b) Compressive Failure of Infill

The onset of this mode of failure is gradual. Therefore, the collapse may be assumed to be due to a plastic like failure within one of the loaded corners surrounded by lengths of contact, a . Allowing for a uniform crushing stress, f_c' , within this region, the diagonal compressive failure load, R_{uc} , was derived as follows.

$$R_{uc} = a t_i f_c' \text{Sec}\theta \quad (2.8)$$

Substituting for a from Eq 2.6 the above equation may be written in its non-dimensional form as:

$$\frac{R_{uc}}{f_c'h't} = \frac{\pi}{2\lambda h} \text{Sec}\theta \quad (2.9)$$

which is also plotted in Fig 2.10. The above theoretical tensile and compressive infill failure loads and the test results obtained by Stafford Smith⁽¹²⁾ are compared in Fig 2.11 showing a fairly good agreement.

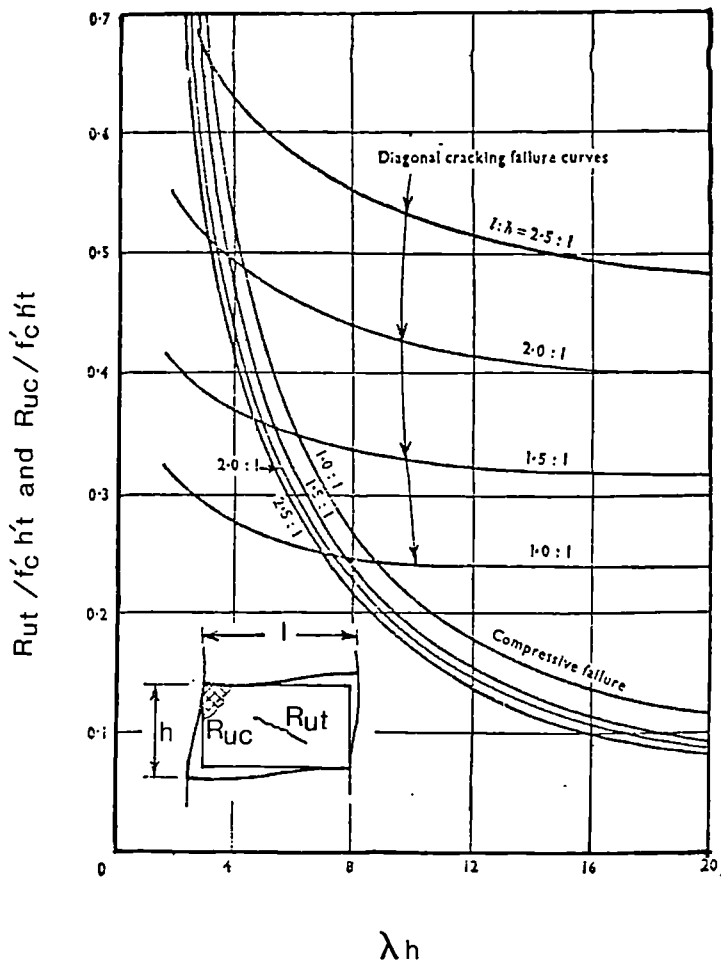


Figure 2.10 Diagonal Strength of Concrete Infill as a Function of λh (after Stafford Smith and Carter (13))

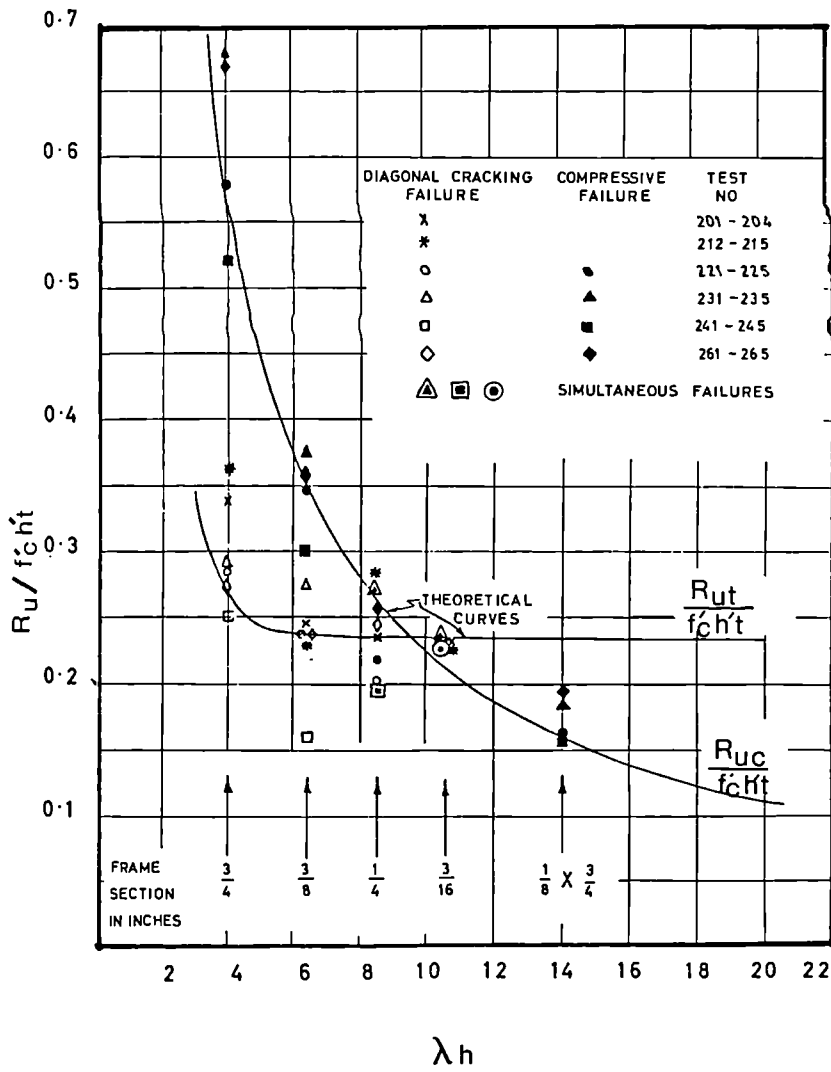


Figure 2.11 Comparison of Experimental and Theoretical Diagonal Strength of Infill as Function of λh (after Stafford Smith(12))

2.4.5 Lateral Stiffness of Infilled Frames

Using the typical infill stress diagrams shown in Fig 2.7, the strains along the loaded diagonal were computed by Stafford Smith⁽¹²⁾ and the equivalent strut width ratio, w_{ek}'/d , was deduced. For stiffness purposes the equivalent strut width ratio was plotted as a function of a/h' in Fig 2.12. As shown, the theoretical values of w_{ek}'/d are consistently higher than the experimental values. Stafford Smith first attributed this discrepancy to the non-linear behaviour of the infill around the loaded corners. However a further series of diagonal loading tests on steel frames with infills of epoxy resin- a relatively linear material- gave results similar to that with mortar infills. Therefore, Stafford Smith⁽¹²⁾ concluded that the excessive theoretical predictions were due partly to assuming a triangular interaction stress distribution which, perhaps, should have been more heavily loaded towards the corner, and partly due to the inexactness of the finite difference, method especially in the region near the application of the load.

Despite this conclusion, Stafford Smith and Carter⁽¹³⁾ concluded that the effective width of an infill acting as a diagonal strut is influenced by the following factors:

- i) the relative stiffness of the column and the infill
- ii) the length/height proportion of the infill
- iii) the stress-strain relationship of the infill material
- iv) the magnitude of the diagonal load acting on the infill

They modified the previous work of Stafford Smith(12) by allowing for non-linearity of the infill material and length/height proportion of the infill resulted in a series of curves shown in Fig 2.13.

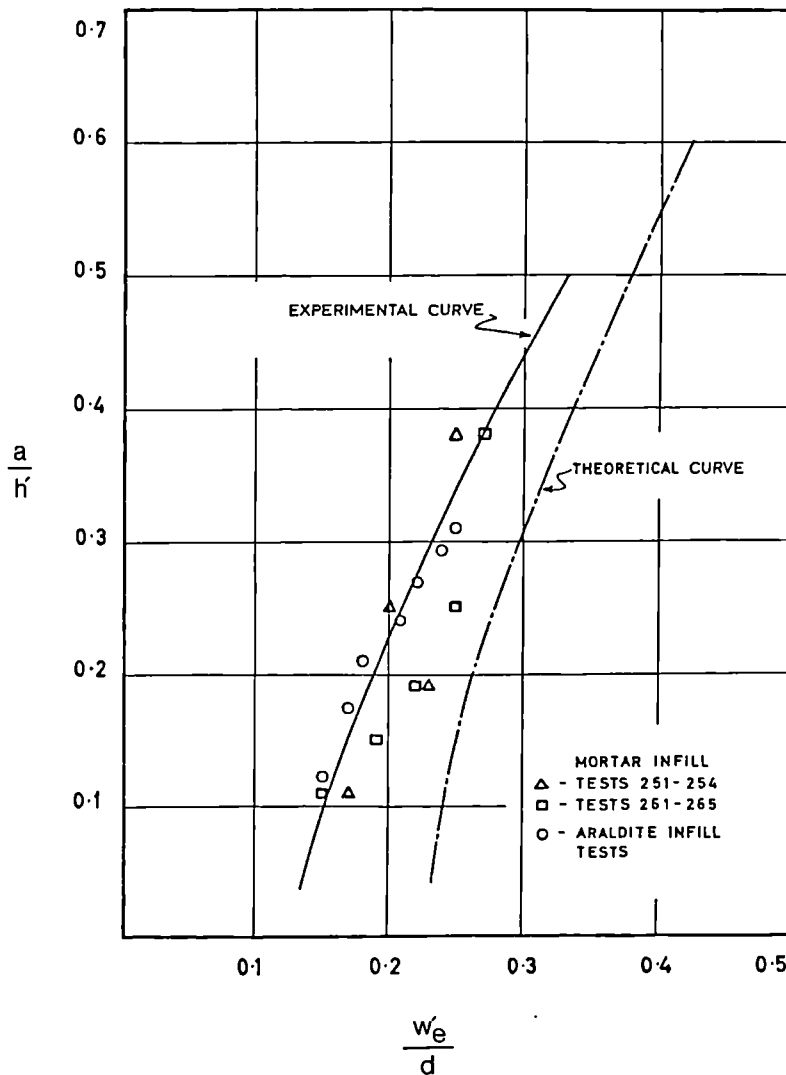


Figure 2.12 Experimental and Theoretical Effective Width of Diagonal Strut as Function of Length of Contact (after Stafford Smith(12))

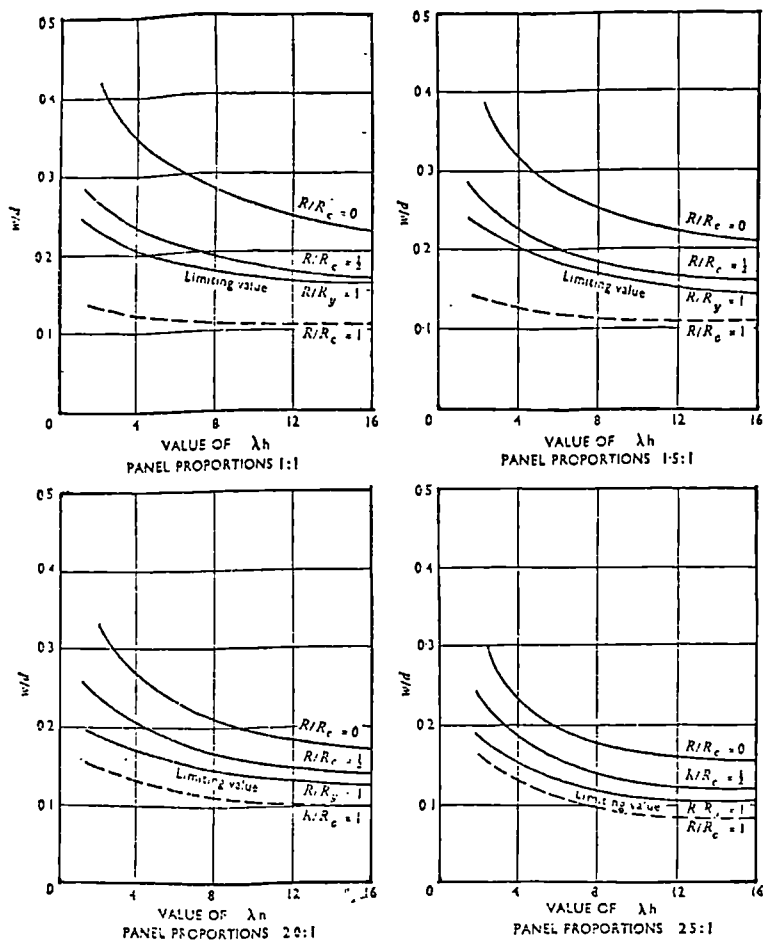


Figure 2.13 Equivalent Strut Width as Function of λh for Stiffness Proposes (after Stafford Smith and Carter (12))

2.4.6 Behaviour of Masonry Infilled Frames under Racking Load

The in-plane deformation and failure of masonry is influenced by the properties of its components, the units and the mortar. The influence of mortar joints is significant, as these joints act as planes of weakness. Experimental observations (13,15,16) have shown that when a masonry infilled frame is subjected to in-plane racking loads, failure of the infill may occur by one of the following modes:

- a) Shear cracking along the interface between the bricks and mortar
- b) Tension cracking through the mortar joints and the units
- c) Local crushing of the masonry or mortar in one of the loaded corners of the infill

Failure modes (b) and (c) are similar to those which occur in concrete panels. Therefore the infill/frame stiffness parameter, λh , can be used in the same manner to estimate the compressive failure and diagonal cracking loads. However the failure mode (a) is particular to masonry infillings. The load to cause such failure was calculated by Stafford Smith and Carter (13) as follows:

Fig 2.14 shows the commonly used masonry joint shear failure criterion (31). This criterion was incorporated into the finite difference stress analysis, carried out for different height/length ratio panels, and resulted in a series of curves relating the diagonal shear failure load, R_{us} , to λh as shown in Fig 2.15.

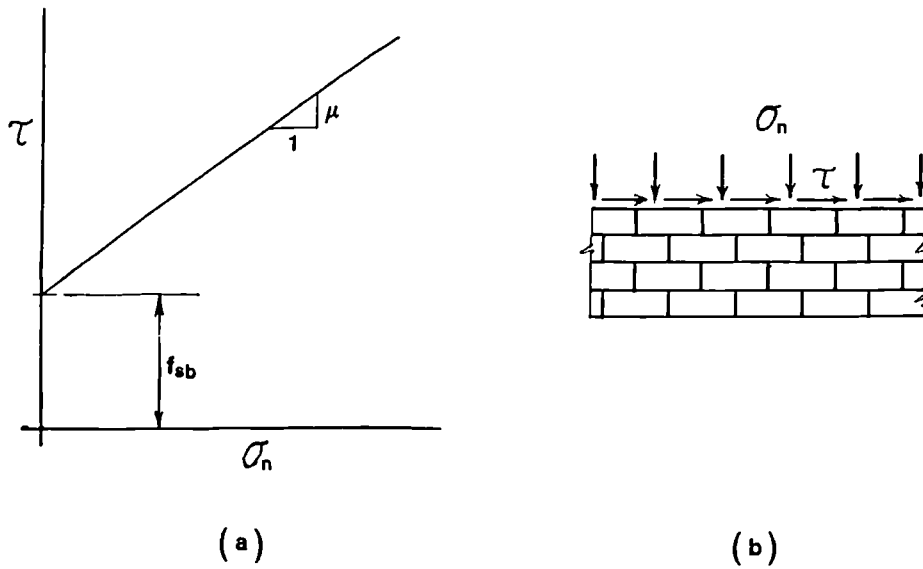


Figure 2.14 Shear Failure Criterion for Masonry Under Vertical Compression and Horizontal Shear; (a) the criterion and (b) applied stresses

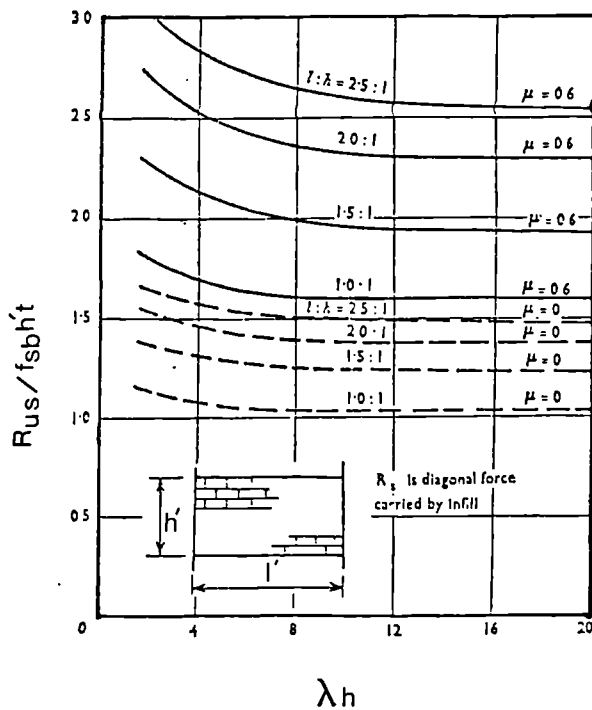


Figure 2.15 Shear Strength of Infill as a Function of λh (after Stafford smith and Carter (13))

2.5 Empirical Method of Analysis Based on Stiffness

Parameter λh

2.5.1 Empirical Data and Analysis of Infill

Mainstone⁽⁹⁾, 1971, discussed an extensive series of tests, carried out at the Building Research Station, on model frames with infills of model brickwork and micro-concrete and also a much smaller number of full-scale tests. He concluded that the range of possible behaviour of an infilled frame is much wider than that envisaged by any theoretical analysis that had been undertaken. Fairly wide variations may be observed even between nominally identical specimens as a result, presumably, of different local variations of elasticity and strength of the infill materials and slight variation in the initial fit of the infill. Therefore for design purposes, only a fairly simple method seems to be justified. In order to develop such a method, Mainstone⁽⁹⁾ adopted the idea of representing the infill by a pin-jointed equivalent diagonal strut, though he believed that it can be justified theoretically only for behaviour prior to cracking. He plotted the aforesaid test results against λh , Figs 2.16 to 2.19, and formulated, empirically, the equivalent diagonal strut widths W'_{ec} , W'_{et} , and W'_{ek} for compressive failure, tensile failure and stiffness of infilling wall respectively as follows:

For $\lambda h < 5$:	Concrete	Brickwork	
$\alpha_k = w'_{ek}/w' =$	$0.115(\lambda h)^{-0.4}$	$0.175(\lambda h)^{-0.4}$	(2.10, 11)
$\alpha_t = w'_{et}/w' =$	$0.255(\lambda h)^{-0.4}$	$0.170(\lambda h)^{-0.4}$	(2.12, 13)
$\alpha_c = w'_{ec}/w' =$	$0.840(\lambda h)^{-0.88}$	$0.560(h)^{-0.88}$	(2.14, 15)

For $5 < \lambda h < 8$:

$$\alpha_k = w'_{ek}/w' = 0.110 (\lambda h)^{-0.3} \quad 0.160 (\lambda h)^{-0.3} \quad (2.16, 17)$$

$$\alpha_t = w'_{et}/w' = 0.220 (\lambda h)^{-0.3} \quad 0.150 (\lambda h)^{-0.3} \quad (2.18, 19)$$

$$\alpha_c = w'_{ec}/w' = 0.780 (\lambda h)^{-0.8} \quad 0.520 (\lambda h)^{-0.8} \quad (2.20, 21)$$

The scatter ^{the} in results obtained, especially for α_k as shown in Fig 2.19, were due to variation of some other affecting factors such as shrinkage and lack of fit. It is worth mentioning that the equations given by Mainstone in the later paper, are identical to these equations but they have been presented in a different format.

For the above equations, the infill/frame stiffness parameter, λh , is defined as:

$$\lambda h = \sqrt{\frac{4 h^4 E_i t_i \sin 2\theta}{4 E_c I_{ch'}}} \quad (2.22)$$

Considering Fig 2.1, the diagonal failure load of infill can be calculated as follows:

$$R_i = w_e' t_i f_i \quad (\text{for concrete infill})$$

Substituting for w_e' gives:

$$R_i = \alpha w' t_i f_i$$

From the geometry of the infill, Fig 2.1, w' can be written in terms of h' as follows:

$$w' = 2h' \cos \theta$$

or
$$R_i = 2\alpha h' \cos \theta t_i f_i \quad (2.23)$$

The horizontal component of R_i leads to:

$$H_i = 2\alpha h' \cos^2\theta t_i f_i$$

The peak value of the racking load, H_{iu} , is then written as:

$$H_{iu} = 2\alpha h' \cos^2\theta t_i f_c' \quad (2.24)$$

where α takes the either value of α_t or α_c in order to correspond the cracking ^{and} compression failure loads, H_{iut} and H_{iuc} respectively.

Diagonal deflection of the infill can also be derived in terms of the infill diagonal load, R_i , as:

$$\Delta d = d \frac{R_i}{w e k' t_i E_i}$$

$$\Delta d = \frac{h' R_i}{\sin\theta w e k' t_i E_i}$$

Substituting for h' in terms of w' leads to:

$$\Delta d = \frac{w' R_i}{\sin 2\theta w e k' t_i E_i}$$

Substituting for R_i and Δd in terms of H_i and Δh using the geometry of the infill, Fig2.1, gives:

$$\Delta h = \frac{H_i}{K_i} \quad \text{where} \quad K_i = \alpha_k t_i E_i \sin 2\theta \cos^2\theta \quad (2.25)$$

K_i denotes the secant stiffness of the infill to either the cracking load or to 90% of the compressive failure load.

2.5.2 Analysis of Frame

Diagonal compression of the infill permits the frame to deform diagonally and resists a portion of the diagonal load, ie.

$$R = R_i + R_f$$

This relation for the horizontal loads is written as:

$$H = H_i + H_f$$

The stiffness of the composite structure becomes:

$$K = K_i + K_f \quad \text{where} \quad K_f = H_f/\Delta h$$

Mainstone (9) concluded that "provided that the peripheral joints between the infill and the frame are well filled, the composite elastic stiffness of the infilled frame will usually be that of the infill." He then suggested to neglect the frame contribution in calculation of the cracking load and stiffness. For the collapse load, however, he suggested either to neglect the frame contribution or allow for the full plastic strength of the frame while assuming no infill exists. In order to establish a consistent approach for the later references in this study, the author decided to account for the elastic contribution of the frame assuming that no infill exists. and the strength of the frame may not exceed the plastic collapse load of the bare frame. This modification is described below.

Using the elastic approach suggested by

Holmes⁽¹¹⁾, Eq 2.1 to 2.4, the frame contribution to diagonal load has been derived by the author as follows:

$$H_f = \Delta h / K_f \quad (2.26)$$

where K_f , the frame stiffness is written as:

$$K_f = \frac{24E_f I_c}{h'^3 [1 + (I_c / I_b) \cot \theta]}$$

Substituting for Δh from Eq 2.25 and replacing the appropriate terms of stiffness by λh in accord to Eq 2.22 the above relation can be arranged to give:

$$H_f = Q H_i \quad (2.27)$$

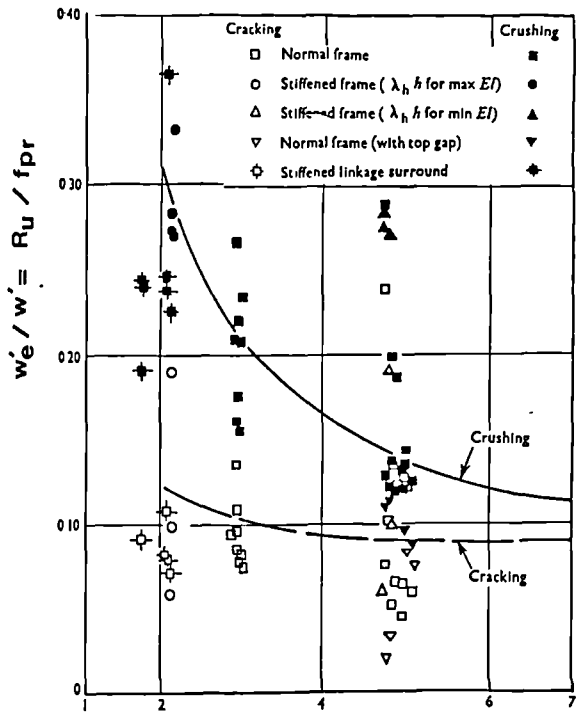
where:

$$Q = \frac{6(h/h')}{\alpha_k (\lambda h)^4 [1 + (I_b / I_c) \cot \theta] \cos^2 \theta}$$

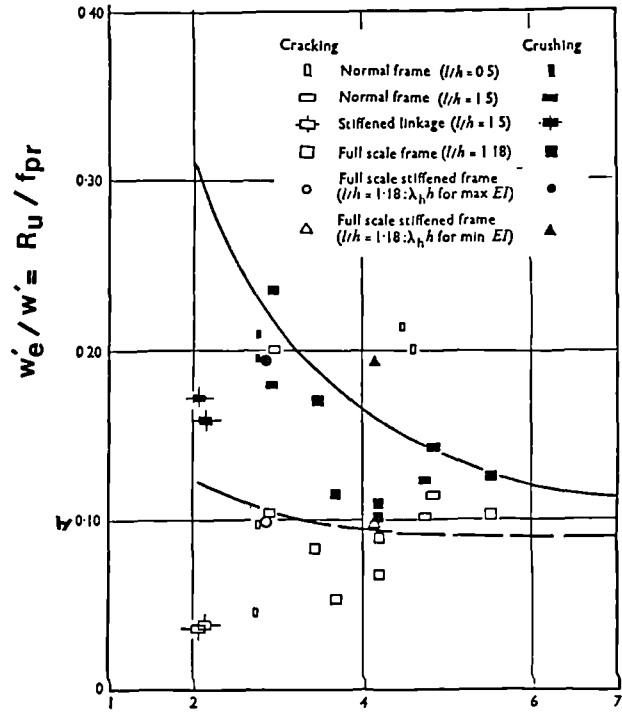
2.5.3 Comments

Fig 2.20 compares the Mainstone⁽⁹⁾ empirical equations and the theoretical method of Stafford Smith and Carter⁽¹³⁾. As seen the two methods generally follow the same trend. However for length/height ratios greater than unity, the predictions of the two methods for compressive failure of the infilled frame are quite different.

Later Stafford Smith and Riddington⁽¹⁸⁾ modified the theoretical method of Stafford Smith and Carter⁽¹³⁾ so as, presumably, to make it closer to the experimental results formulated by Mainstone⁽⁹⁾. This is described in the following section.

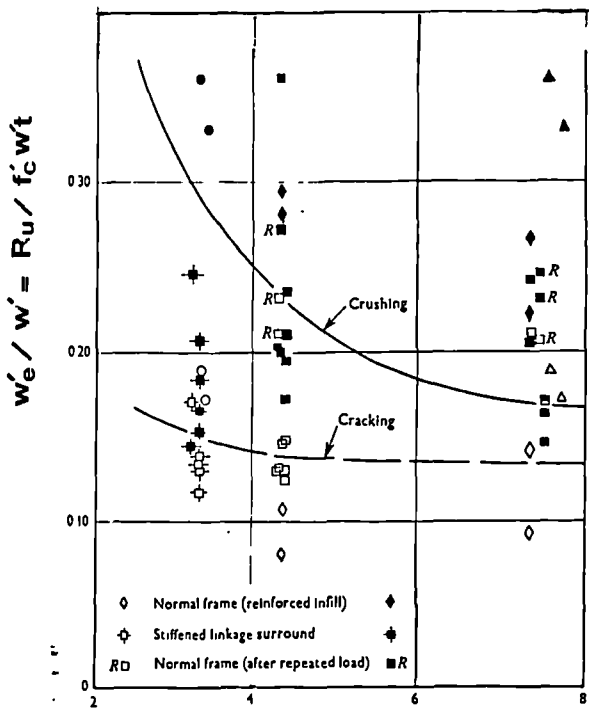


(a)

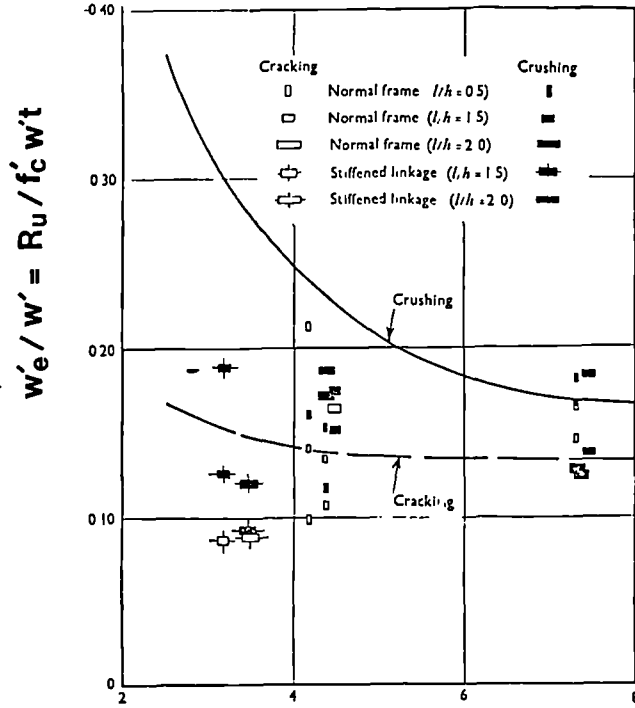


(b)

Figure 2.16 Variation of Strength of Infills of Model and Full-scale Brickwork; (a) square infill and (b) rectangular infill (after Mainstone(9))



(a)



(b)

Figure 2.17 Variation of Strength of Infills of Micro Concrete; (a) square infills and (b) rectangular infills (after Mainstone(9))

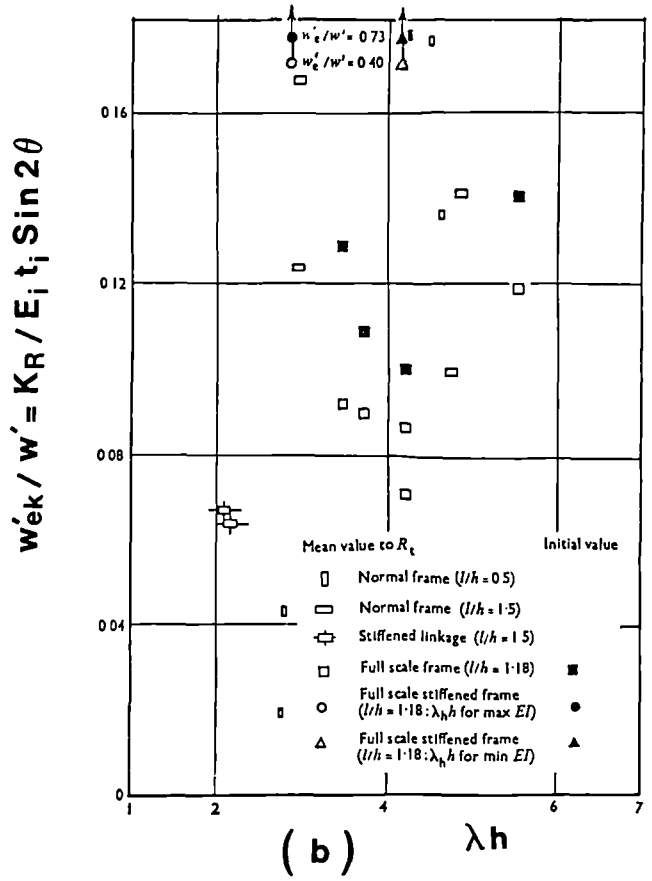
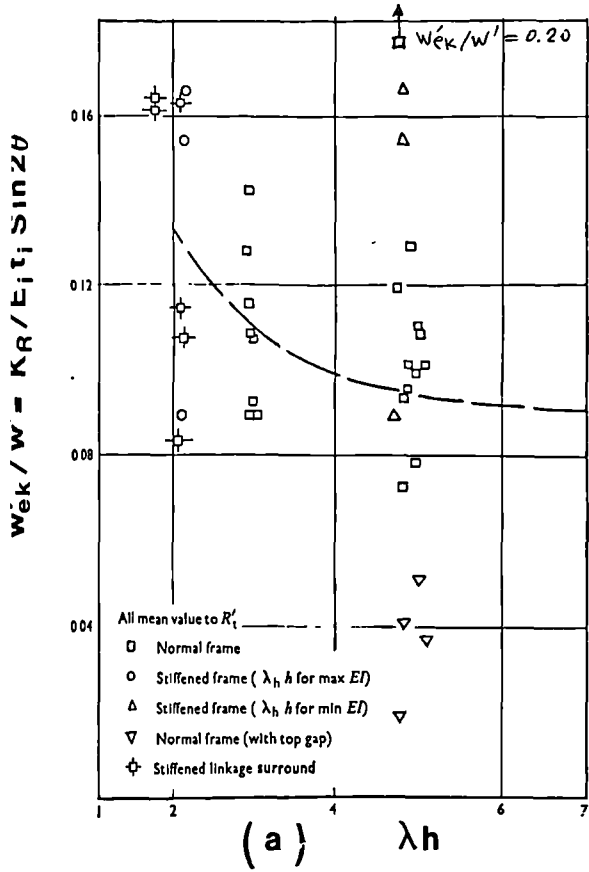


Figure 2.18 Variation of Stiffness of Infills of Model and Full-Scale Brickwork; (a) square infills and (b) rectangular infills (after Mainstone (9))

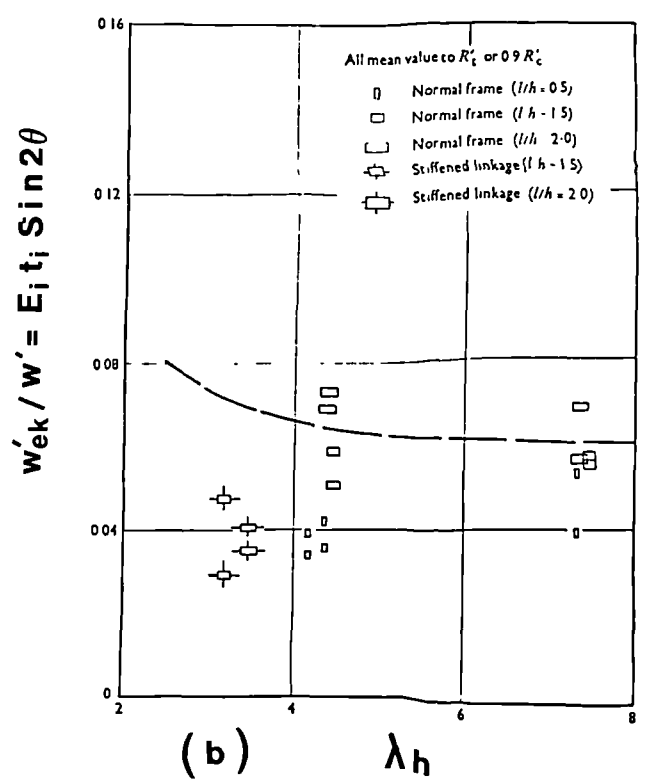
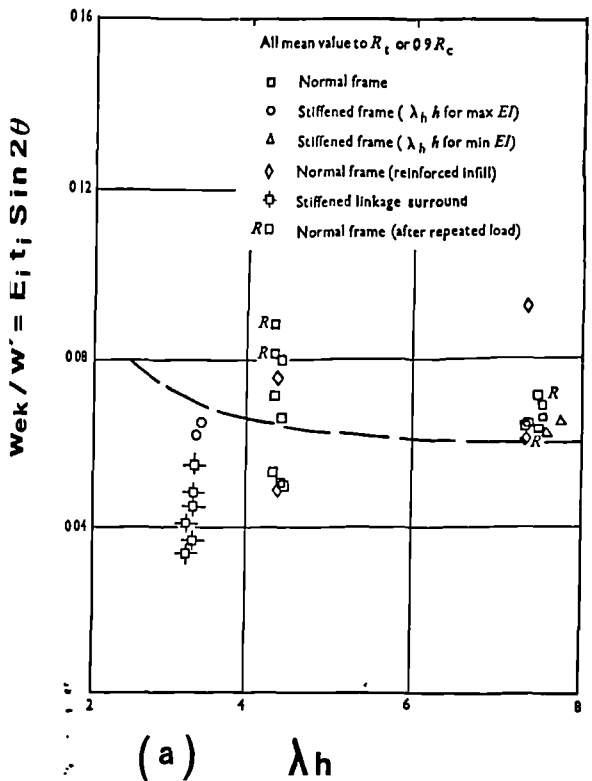


Figure 2.19 Variation of Stiffness of Infills of Micro Concrete; (a) square infills and (b) rectangular infills (after Mainstone (9))

2.6 Design Recommendations for Elastic Analysis of Infilled Steel Frames

2.6.1 General

Riddington and Stafford Smith⁽¹⁷⁾, further developed the elastic analysis of infilled frames using the finite element method. They allowed for frictional forces and slippage between the infill and the frame as well as multi-storey and multi-bay systems. No plasticity and non-linearity due to the materials were allowed for in the analysis. This work and the previous work of Stafford Smith and Carter⁽¹³⁾ and also the empirical equations of Mainstone⁽⁹⁾ were incorporated by Stafford Smith and Riddington⁽¹⁸⁾ to establish a method of analysis for commonly used masonry infilled frames. This method is described in detail in the following sections.

2.6.2 The Basis of the Method

A convenient procedure for the design of an infilled frame building is to initially design the frame to carry the vertical loads. The thickness of the walls which are to serve as bracing infills are then decided on the basis of acoustic or fire requirements whilst also having to satisfy the minimum requirements for stability as given in masonry codes of practice. The strength of the components working together as an infilled frame would then be checked against the estimated racking load and increased in size, if necessary. Consideration of the analogous structure in Fig 2.9 leads intuitively to the proposal that axial forces in the frame members and equivalent diagonal struts can be

estimated by a static analysis of the equivalent pin-jointed braced frame. The finite element analysis of infilled frames provided convincing support to this approach as shown in Table 1 of reference (18).

2.6.3 Infill Design

The development of a design method for a masonry infill requires consideration of the three possible modes of failure: by diagonal tension, by shear or by corner compressive failure (see also section 2.4.6). The stresses to cause these modes of failure are: σ_{dt} , σ_y and τ_{xy} , diagonal tension, normal and shear stress respectively at the centre of the infill and σ_{dc} , diagonal compressive stress caused by diagonal compression.

Stafford Smith and Riddington(18) found that the state of the material in the central region of the infill is linear-elastic. Therefore the stresses within this region were adapted from their finite element analysis which were approximated as follows:

$$\tau_{xy} = 1.43 H / l't \quad (2.28)$$

$$\sigma_{dt} = 0.58 H / l't \quad (2.29)$$

$$\sigma_y = (0.8 h'/l' - 0.2)H / (l't) \quad (2.30)$$

where τ_{xy} , σ_{dt} and σ_y are horizontal shear, diagonal tension and vertical compressive stresses respectively. Having these stresses, the corresponding failure loads were calculated as follows:

a) Shear failure:

Shear failure is assumed to be initiated in the infill along the joints at the centre of the infill. The shear strength of masonry can be represented by friction type equation of the form:

$$\tau_{xy}' = f_{sb} + \mu\sigma_y' \quad (2.31)$$

in which f_{sb} and μ are the shear bond strength and the coefficient of friction respectively of the unit-mortar interfaces. Combination of Eqs 2.28, 2.30 and 2.31 gives:

$$1.43H_{us}/l't = f_{sb} + 0.8(h'/l') - 0.2H_{us}/l't$$

Hence:

$$H_{us} = \frac{f_{sb}l't}{1.43 - \mu(0.8 h'/l' - 0.2)} \quad (2.32)$$

where H_{us} is shear failure load of the masonry infill. The values f_{sb} and μ may vary due to the type of mortar and masonry unit.

b) Diagonal tension failure:

Tensile failure in a masonry infill initiates from the centre of the infill as one or more diagonal cracks extending along the loaded diagonal passing through mortar joints and units. As there was little information available on the diagonal tensile strength of masonry Stafford Smith and Riddington⁽¹⁸⁾ estimated this value equal to the tensile strength of mortar. This was approximated as one-tenth of the mortar compressive strength i.e:

$$\sigma_{dt}' = 0.1f_m \quad (2.33)$$

Combination of Eqs 2.33 and 2.29 results in:

$$H_{ut} = 0.172 f_m l' t \quad (2.34)$$

Eq 2.34 estimates the diagonal cracking load, H_{ut} , for masonry infill.

c) Compressive failure of the infill corners:

Stafford Smith and Riddington⁽¹⁸⁾ found that unlike the stress within the central region of the infill, the compressive stresses occurred in the loaded corners were extremely sensitive to the λh value which was simplified for design purposes as follows:

$$\lambda h = \sqrt[4]{\frac{E_i t_i h'^3}{4 E_c I_c}} \quad (2.35)$$

It should be noted that, in the above equation the term $\sin 2\theta$ is omitted and the difference between h' and h is ignored as compared to Eq 2.7.

Since compressive failure occurs, presumably, in a plastic manner and the results obtained from the linear-elastic finite element analysis⁽¹⁷⁾ were not sufficiently accurate, Stafford Smith and Riddington⁽¹⁸⁾ adopted the empirical equation of Mainstone⁽⁹⁾, Eqs 2.15, to derive the horizontal compressive collapse load, H_{uc} , as follows:

w' and w'_{ec} may be substituted in Eq 2.15 as:

$$w' = 2h' / \cos \theta$$

$$w'_{ec} = R_{uc} / f_{prt}$$

to give:

$$\frac{(R_{uc}/f_{prt})}{(2h' \cos\theta)} = 0.56(\lambda h)^{-0.88}$$

The horizontal compressive failure load, H_{uc} , can be related to R_{uc} as:

$$H_{uc} = R_{uc} \cos\theta$$

Substituting for R_{uc} leads to:

$$H_{uc} = 1.12(\lambda h)^{-0.88} h' t f_{pr} \cos^2\theta \quad (2.36a)$$

This equation for concrete becomes:

$$H_{uc} = 1.68(\lambda h)^{-0.88} h' t f_c' \cos^2\theta \quad (2.36b)$$

2.6.4 Design of Frame

a) Axial forces in frame members:

The axial forces due to vertical loads should be calculated on the basis of the tributary areas. The axial forces in the members due to horizontal loading can be estimated by a simple static analysis of an equivalent frame with the columns pin-jointed at each storey level, the beams pin-jointed at their ends and the infills considered as diagonal pin-jointed bracing struts.

b) Bending moments and shear forces in frame members:

Frame members must be also able to withstand bending moments and shear forces induced as a result of inexactness of the assumption of the infill acting as a pin-jointed diagonal bracing. In reality the infill bears

against the beam and column members over part of their lengths. The finite element analysis⁽¹⁷⁾ showed that the bending moment in the frame members are not likely to exceed 5% the total horizontal force, H , times the height of the columns, h' . Therefore the columns must be able to resist a bending moment of $Hh'/20$ and a shear force equal to H .

The beams must also be designed for bending moments and shear forces in addition to the axial forces calculated as above. If an upper beam of an infilled panel is not restrained by an infill above, it should be designed to withstand a mid-span hogging moment of $Hh'/20$ in combination with the moment due to vertical dead loads. The beam and its connections must be able to carry an upwards shear force of $Hh'/1'$ in combination with the shear force due to vertical dead loads.

Where the beam below an infill is not restrained by an infill below, the beam must be able to withstand a mid-span sagging moment of $Hh'/20$ in addition to the moment due to dead and live loads. The beam and its connections must be able to carry a downwards shear force of $Hh'/1'$ in addition to the shear force due to dead and live loads.

c) Deflection of frame:

A crude but conservative, ie. excessive estimate of horizontal deflection of infilled frame, can be made by treating the frame as pin-jointed and each infill as a diagonal pin-jointed bracing strut with a cross-sectional area equal to one-tenth of its diagonal length times its thickness and an elastic modulus of $7 \times 10^3 \text{ N/mm}^2$.

2.6.5 Comparison

Fig 2.20 compares the calculated loads using the design method of Stafford Smith and Riddington(18) and those of the empirical equations of Mainstone(9). The results of the compressive failure load, R_{ut} , were obviously coincident since, the new method(18) uses the empirical equations(9).

The infill tensile cracking strength, R_{ut} , obtained from the design recommendations is rather unsafe for rectangular infills, Fig 2.20 (b). A Detailed comparison is made in Chapter 7.

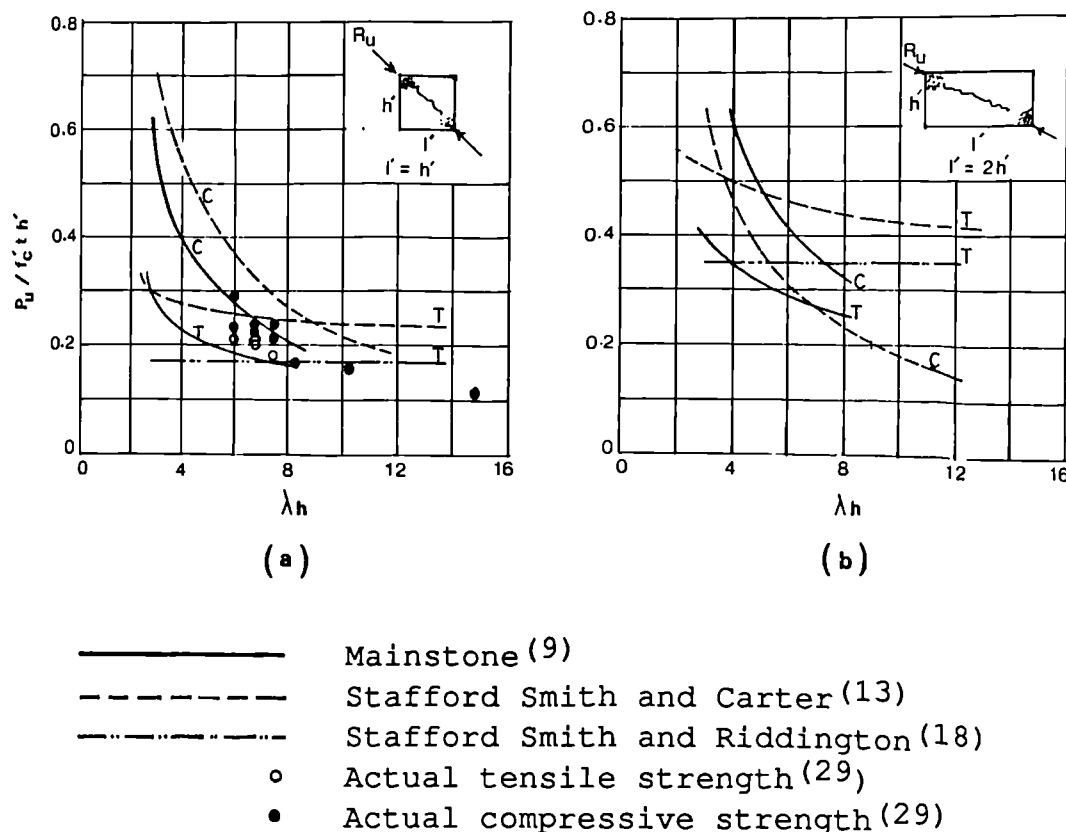


Figure 2.20 Comparison of Various Methods of Analysis Based on λh ; (a) square infill, (b) non-square infill.

Note: T = Tensile strength C = Compressive strength

2.7 Theories Based on Frame/Infill Strength Parameter

2.7.1 General

The theoretical investigations on the behaviour of infilled frames, up to 1978, were based generally on elasticity theories. However as discussed in Section 2.6.3(c) these theories fail to establish a rational criteria for compressive failure of the infill. Because such failure occurs gradually and is associated with distinct modes of distortion of the frame, it indicates the existence of particular mechanisms by which plastic like collapse occurs. This was well understood by Wood⁽²⁰⁾ who published his paper titled "Plasticity, Composite Action and Collapse Design of Reinforced Shear Wall Panels in Frames" and opened a new chapter in the analysis and understanding of the behaviour of infilled frames. He identified four possible modes of collapse as illustrated in Fig 2.21 and developed a rational plastic analysis based on a frame/infill strength parameter utilizing Nielsen⁽²¹⁾ square yield criterion within yielding zones.

Later, in 1981, an alternative treatment of the plastic analysis was given by May⁽²²⁾. He used the same principles as Wood except he used the yield line method of analysis in plasticity theories. The results were identical to those of Wood. This method was also capable of predicting the collapse loads and modes of infills with openings.

2.7.2 Wood Classification for Collapse of Infilled Frame

Wood(20) studied a large number of tests carried out at the Building Research Establishment by various investigators. The majority of the tests involved masonry panels. Four distinct types of plastic collapse modes were identified as follows:

a) Shear mode "S"

Fig 2.21(a) shows the collapse mode of a very strong frame and a weak wall where plastic hinges formed at the joints of the frame. The beams and the columns remained straight producing a pure shear strain in the wall. This referred to as the shear mode "S".

b) Shear rotation mode "SR"

Fig 2.21(b) shows the collapse mode of a relatively stronger wall where a plastic hinge appeared in each beam at the intersection of the discontinuity lines which clearly separate apparently unstrained rigid corner regions (top left and bottom right) from a central shear region where massive distortion has taken place. The unstrained corners merely undergo a rigid body rotation, and therefore, this mode is called the shear rotation mode "SR".

c) Diagonal compression mode "DC"

The stronger is the wall relative to the frame, the greater is the distance between the unstrained corner and the plastic hinge in the beam. With a very strong wall, or weak frame, the hinge appears nearer the opposite corner

and a similar plastic hinge appears in the columns as shown in Fig 2.21(c). This indicates a heavily stressed wall diagonal in compression. This mode is called the diagonal compression "DC".

d) Corner crushing mode "CC"

The special case when only the corner is crushed, Fig 2.21(d), (instead of a complete diagonal band) is called the corner crushing mode "CC".

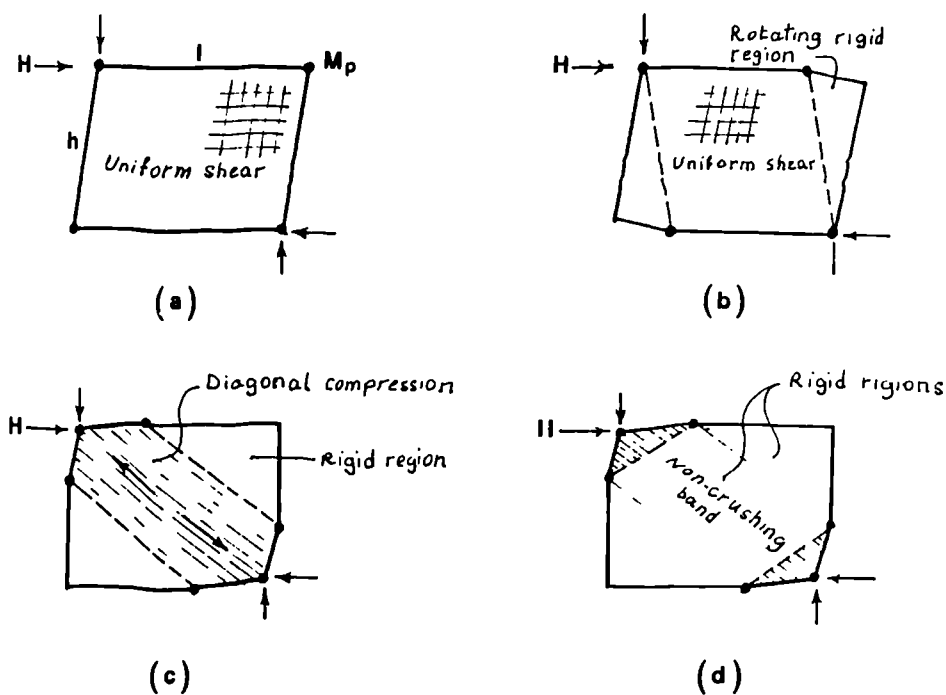


Figure 2.21 Idealized Plastic Failure Modes for Infilled Frames (after Wood(20)); (a) shear mode 'S' (b) shear rotation mode 'SR', (c) diagonal compression mode 'DC' and (d) corner crushing mode 'CC'

2.7.3 Wood's Plastic Analysis of Infilled Frames

Wood(20) stated that "the elastic analysis of Stafford Smith can only predict the starting width of an idealized compressive diagonal band. This is a crude approach to an equivalent plastic diagonal. No parameter from the theory of elasticity can predict changes of collapse modes". Wood concluded that "ideally, with many more test results, collapse modes should be plotted in terms of both plasticity and elasticity, as has already done for frame instability in tall buildings (e.g. the Merchant-Rankine(7) formula) with plasticity predominating. Meanwhile the Stafford Smith approach is useful for designers for predicting other limit states, such as cracking and working deflections, at working conditions." For collapse analysis, however, Wood proposed an analysis using the standard perfect plasticity theories as described below.

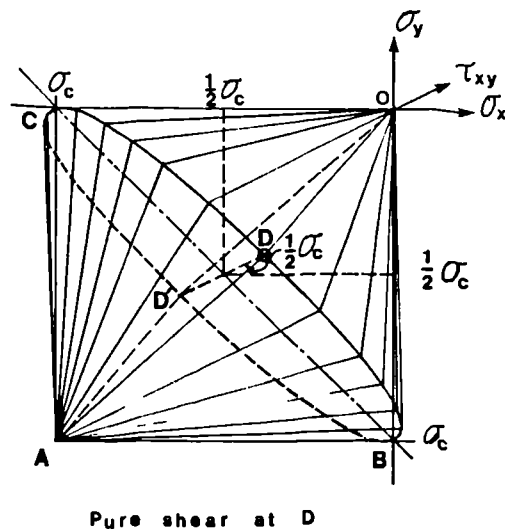


Figure 2.22 Perspective View of Nielsen's(21) Square Yield Criterion for Unreinforced Wall (after Wood(20))

Combining Nielsen(21) idealized plastic yield criterion, Fig 2.22, for membranes which either are crushed at a constant yield stress or cracked at zero (ie. constant) tensile stress, with standard plastic theory for frameworks, modes **S**, **SR** and **DC** were predicted in proper order of decreasing relative frame/infill strength ratio, **m**, as shown below:

Mode	Range of m	Stress Distribution
S	$1.0 < m$	Fig 2.23
SR	$0.25 < m < 1$	Fig 2.24 (2.37)
CC,DC	$0 < m < 0.25$	Fig 2.25

where the equilibrium of **stress fields** are shown in Fig 2.23 to 2.25 and **m** is defined as:

$$m = 8M_p / (\sigma_{ct} l'^2) \quad (2.38)$$

M_p is the minimum plastic moment of the frame members. The horizontal collapse load is given as:

$$H_u = f [4M_p/h' + 0.5\sigma_{ct} l'] \quad (2.39)$$

where: $f = 1$ (for **S** mode)

and $f = f_s + \Delta f$ (for modes **SR**, **CD**, **CC**) (2.40)

where:

$$f_s = \frac{2}{\sqrt{m} + 1/\sqrt{m}} \quad (2.41)$$

and Δf is a correction to f accounting for the effects of stronger beams or columns and rectangular panels. Δf is plotted in Fig 2.26 in terms of **m** for selected ratios of l/h and μ where $\mu = M_{pb}/M_{pc}$ and M_{pb} and M_{pc} are the plastic

resistance moments of beams and columns respectively. σ_c in Eq 2.38 and 2.39 is the effective yield strength of infill material and it is given as:

$$\sigma_c = \gamma_p f_c' \quad (\text{for concrete infill}) \quad (2.42)$$

$$\sigma_c = \gamma_p f_{pr} \quad (\text{for masonry infill}) \quad (2.43)$$

where f_c' and f_{pr} are standard uniaxial cylinder crushing strength of concrete and prism strength of masonry infilling walls respectively. γ_p is proposed as a penalty factor so as to lower the strength of the infill in order to cater for the discrepancy between the theoretical predictions and experimental results. Figs 2.27 plots the values of γ_p in terms of the nominal values of m and m_n , for masonry and micro-concrete infills respectively. The values of m_n can simply be calculated as follows:

$$m_n = 8M_p / (f_c' c t l'^2) \quad (\text{for concrete}) \quad (2.44)$$

$$m_n = 8M_p / (f_{pr} t l'^2) \quad (\text{for masonry}) \quad (2.45)$$

i.e, assume the wall is made of a perfect plastic material and the proposed yield criterion is exact.

The ranges of the nominal value of the strength parameter, m_n , for S, SR, DC and CC modes can be calculated by combining the corresponding γ_p curves to the ranges of m values given in Eq 2.37. These are shown in Fig 2.27 and are also summarized below.

S	$0.23 < m_n$	
SR	$0.075 < m_n < 0.23$	(2.46)
DC, CC	$0 < m_n < 0.075$	

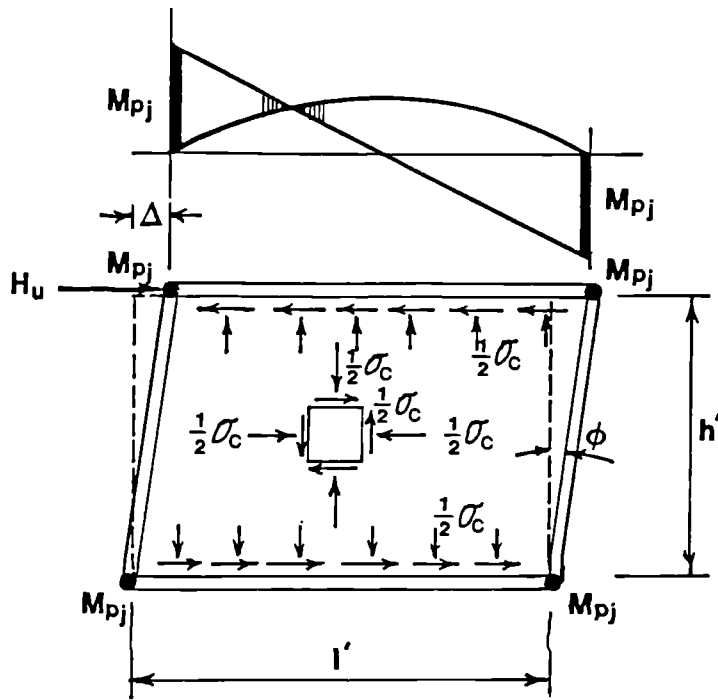


Figure 2.23 Infilled Frame Shear Mode of Collapse, Mode 'S'; Distortion Mechanism and Lower Bound Stress Field (after Wood(20))

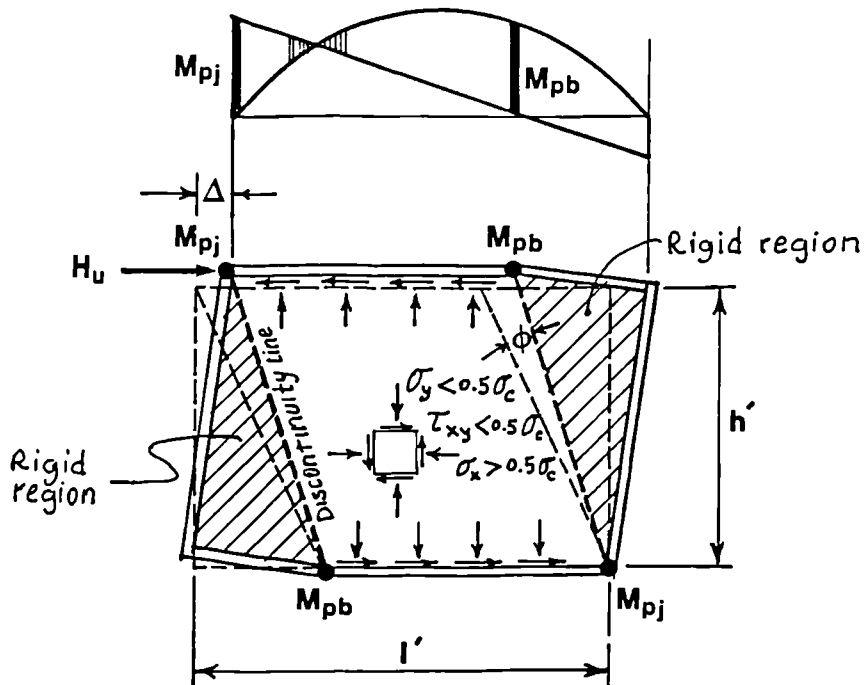


Figure 2.24 Infilled Frame Shear Rotation Mode of Collapse, Mode 'SR'; Distortion Mechanism and Lower Bound Stress Field (after wood(20))

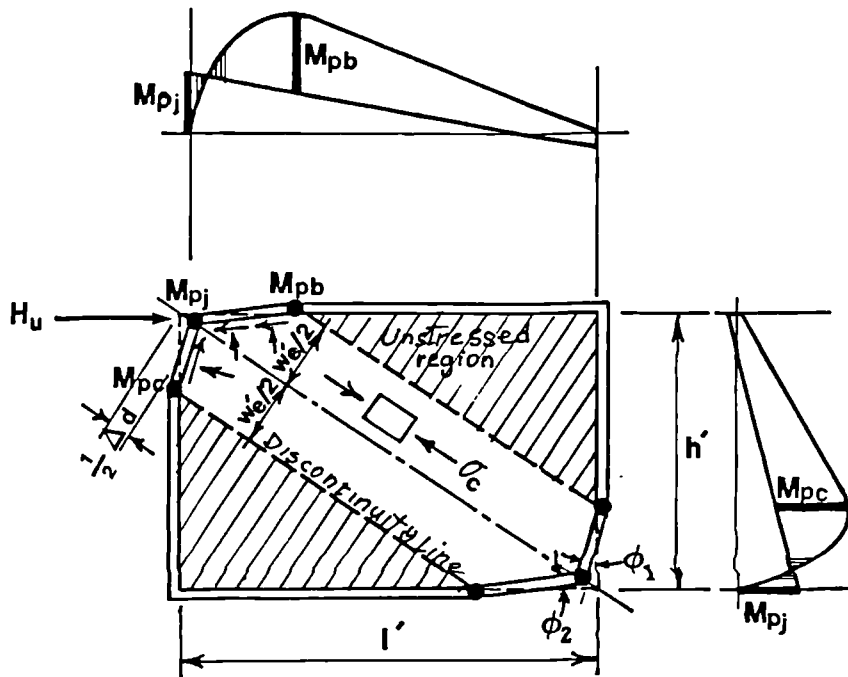
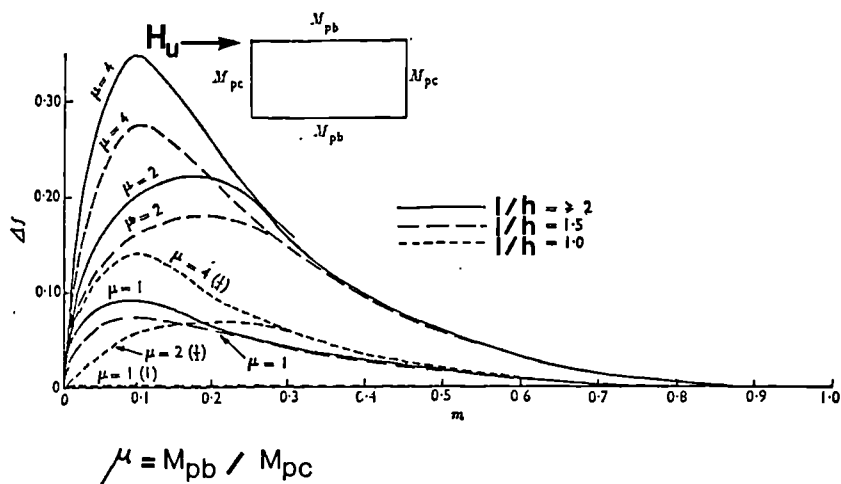
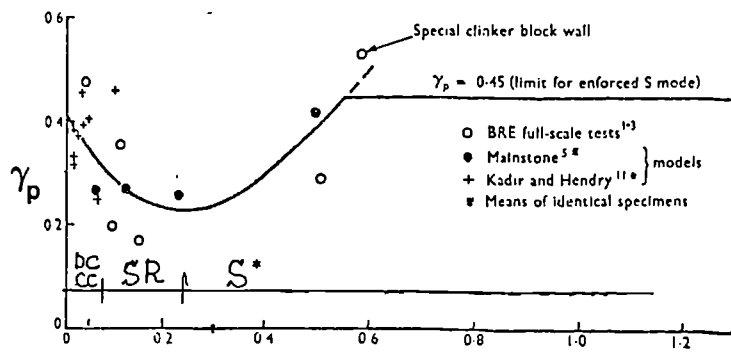


Figure 2.25 Infilled Frame Diagonal Compression Mode of Collapse, Mode 'DC'; Distortion Mechanism and Lower Bound Stress Field (after Wood(20))



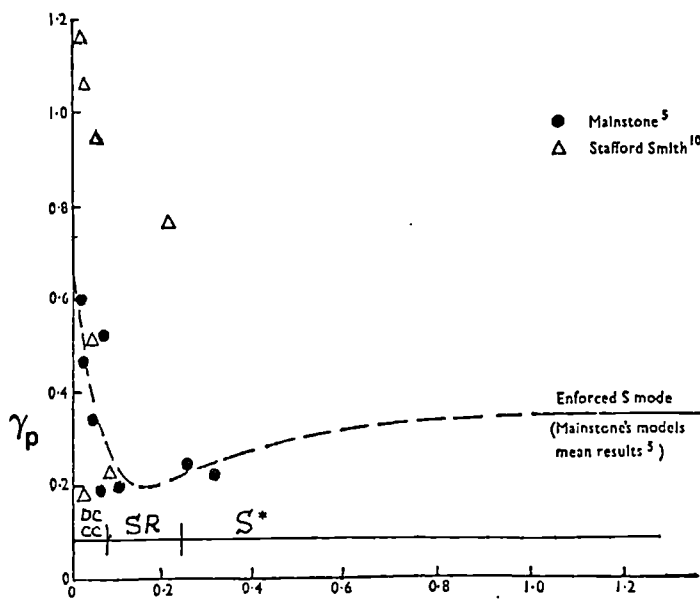
If $\mu \geq 1$ (strong beams), use chart direct
 If $\mu < 1$ (weak beams) and $|h|/h = 1$, use μ values in brackets
 If $\mu < 1$ (weak beams) and $|h|/h = 1.5$ or 2.0 , use $\mu = 1$ curve for all values of μ

Figure 2.26 Design Chart for Determination of Optional Correction to f_s (after Wood(20))



$$m_n = 8 m_p / \sigma_c t w l^2$$

(a)



$$m_n = 8 m_p / \sigma_c t w l^2$$

(b)

Figure 2.27 Appropriate Penalty Factor; (a) for brickwork infilled frames and (b) for micro-concrete model infilled frames (after Wood(20))

Note: the correction due to Sims' discussion(23) has been included.

2.7.4 Axial and Shear Forces in Frame Members

The plastic moments are altered by both axial and shear forces. For a simplified design, Wood(20) suggested that the axial forces in frame members may be calculated by assuming that infills act as bracing members, or diagonal strut. Shear forces in the frame members may approximately be calculated giving one half the diagonal force to beams and the other half to the columns.

Reinforced concrete frames are sensitive to high hydrostatic pressure from the wall (Figs 2.23 to 2.25) which may induce failure in the frame, particularly if there is tension in columns on the windward side. Wood(20) has shown γ_p as low as 0.05 for some tests subjected to tension and shear in windward column. He commented that this was obvious and makes it necessary for special safeguards for combined tension, shear and bending to be devised so that designers using reinforced concrete frames can avoid ruining composite action.

2.7.5 Analysis of Multi-bay and Multi-Storey Frames

If all adjoining bays and storeys are occupied by walls, this tends to enforce a pure shear failure (Mode S). However it is necessary to divide M_p between the two panels, sharing the element (beam or column) under consideration, to avoid including M_p twice in summing individual panel strength. If there are no walls above and below, the available plastic moment resisting of the beam equals the actual plastic moment resisting of the beam in question minus the required plastic moment for floor loads.

The columns completely free of wall panels are to be designed by any acceptable no-sway design method. Columns involved in shear panel design, must be relatively free of buckling effects. It is suggested⁽²⁰⁾ that P/P_{Euler} should not exceed 0.5 with rigid joints or 0.25 with pinned joints.

2.7.6 Discussion of Wood Method

Wood's plastic method was discussed by Mainstone, Stafford Smith and Sims⁽²³⁾. A summary of the major points of this discussion is given below.

Mainstone referred to the enforced shear mode tests (with weak frame joints) carried out in British Research Station. In these tests, infill strain was far from uniform, both when the panel reached its peak strength and subsequently. Therefore he suggested that the shear mode S to be regarded as an ideal limit rather than as a real material mode.

Sims felt that the role of γ_p is more complex than just being a penalty for the use of idealized plasticity theory for a material showing limited plasticity. In deriving it from test results, it must also contain effects from other parameters not considered in the basic theory, e.g. the effect of elastic deformations and the use of an idealized yield criterion.

Admitting the Sims' view⁽²³⁾, Wood himself stated that "The next important advance must come from finite element or similar analysis allowing for elastoplasticity of infilling wall with restricted plastic strain. Outstanding research now lies in determining an extra theory to deal

with plastic strain limitation -better than just γ_p - as Mr Sims suggested."

Table 2.1 evaluates the design example of Wood(20) using the methods proposed by various authors for the purpose of comparison of only their prediction of the compression collapse load. This comparison showed that the plastic methods enforce much greater frame bending moments. Detailed comparison is made in Chapter 7.

Table 2.1 Comparison of Compressive Strength and Frame's Moments. (after Wood(20))

Author	Horizontal load KN	Column Moment KNm
Stafford Smith and Carter(13)	466	0
Mainstone(9)	285	29
Stafford Smith Riddington(18)	285	36.4
Wood(20)	383	142 Mode SR
Liauw et al(26)*	240	142 Mode 3

* Added by the author, see also Section 2.8

2.7.7 Plastic Analysis of Infilled Frames with Application of the Yield Line Method

May(22) introduced a new type of yield line, termed "Rotational Yield Line" permitting linearly variable compressive and tensile plastic deformations normal to the yield line. He used this type of yield line to model the regional crushing and cracking normally observed in test. This method was used to reanalyse all the modes previously

examined by Wood(20) and was shown to give identical results.

As discussed in Section 2.7.6, May's work showed that although the infill strain is far from uniform, the shear mode **S** should be regarded as a real mode and not just as an ideal limit as Mainstone(23) suggested.

The yield line method was also used for design of square panels with centrally placed square opening. It was concluded(22) that the method can also be used for rectangular panels with opening located anywhere within the panel.

Ma(96) adapted bi-linear models for both the steel frame and concrete infill using, thus, a perfect-plastic material model implemented into the finite element analysis, mainly for the purpose of examining the results of the yield line method proposed by May(22). His analyses and experiments led him to suggest an empirical γ_p value relating to only the aspect ratio of the wall, Fig 2.28.

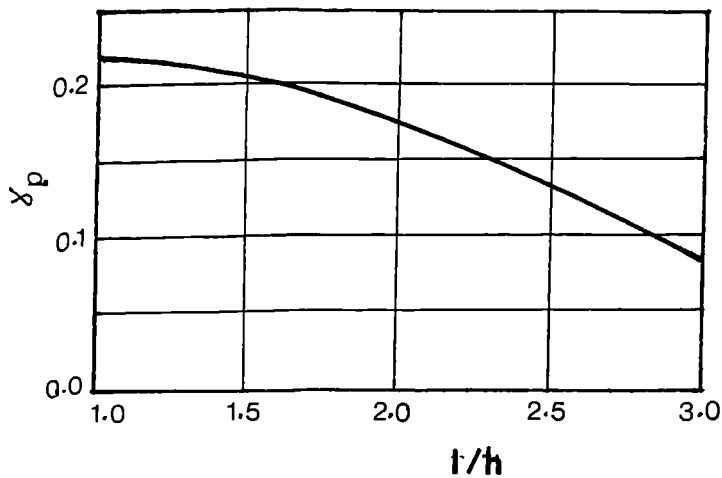


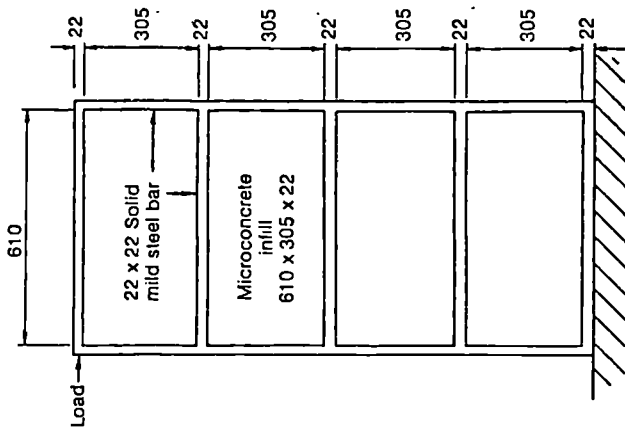
Figure 2.28 Variation of γ_p against aspect ratio of panel.
(after Ma(96))

2.8 Liauw et al Plastic Method

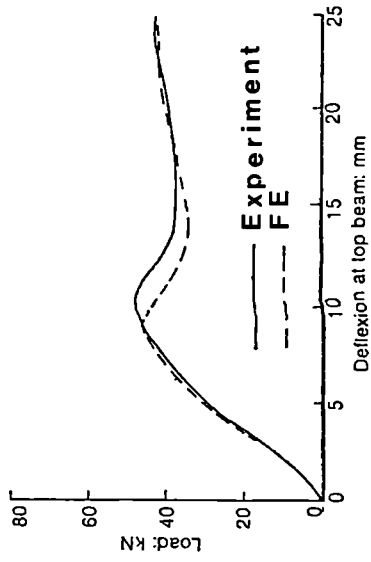
2.8.1 Finite Element Analyses

As discussed in Section 2.7.6, the plastic method of analysis of Wood⁽²⁰⁾ is highly dependent on the penalty factor, γ_p , which varies considerably in terms of the frame/infill strength ratio parameter, m . Yet γ_p is an empirical factor. In order to refine γ_p , Wood⁽²³⁾ suggested a Finite Element or similar analysis should be utilized. Such numerical analysis should allow for elastic-plastic stress-strain characteristic of both the frame and the infill materials.

Liauw et al⁽²⁴⁾, 1982, developed a F.E. analysis for infilled frames. To the knowledge of the author, this was the first attempt at development of a non-linear finite element analysis for infilled frames with allowance for limited plasticity of the infilling wall. Joint slip and separation criterion for the interface between the frame and infill and also crack modeling were also incorporated into the analysis. The biaxial behaviour of the infill was, however, simplified as for uniaxial case, i.e, a square yield criterion was adopted. The analysis example was a four-storey steel frame with micro-concrete infilling walls as shown in Fig 2.29(a). The results of F.E analysis were compared to the experimental values and showed fairly good agreement, Fig 2.29(b). The numerical analysis gave fairly detailed information about frame forces and infill stresses both before and after crushing of the infill, Fig 2.30.

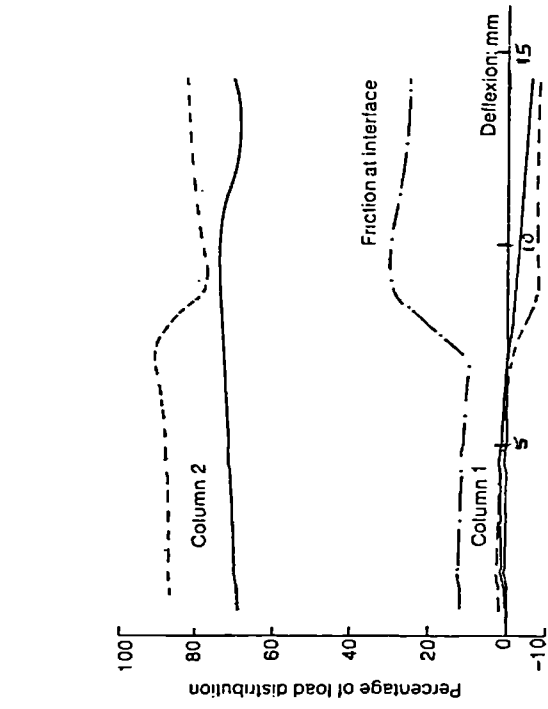


(a)

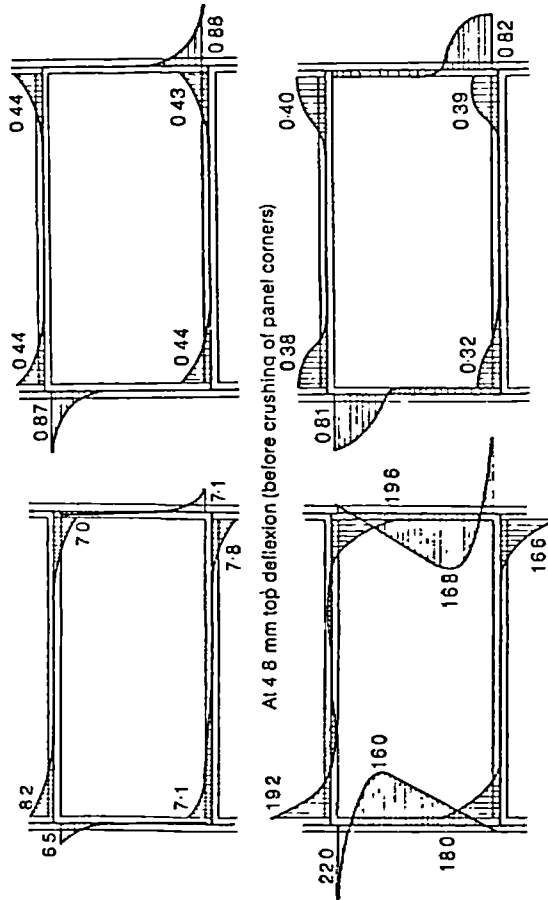


(b)

Figure 2.29 Finite Element and Experimental Results of Liauw et al (24);
 (a) geometry of the model and (b) load deflection curves



(c)



(b)

(a)

Figure 2.30 Results of F.E. Analysis (24) in The Third Story of The Model Before and After Peak Load; (a) bending moments, (b) frame shear forces and (c) distribution of lateral shear

Basing on the above F.E. analysis results(24), Liauw et al(25) pointed out that:

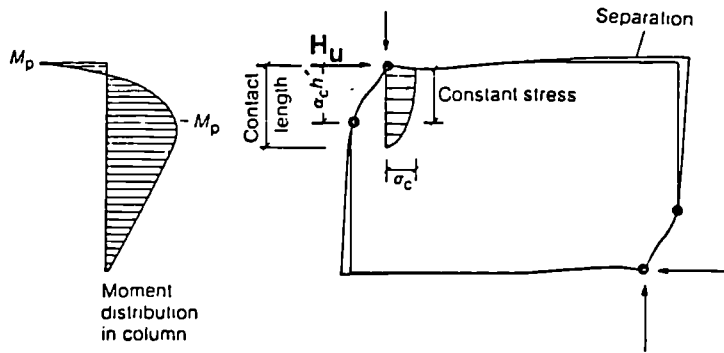
"the penalty factor γ_p in Wood's plastic method of analysis (described in Section 2.7.3) might not be due as much to the lack of plasticity of the infilling wall, but as a consequence of the excessive friction assumed at the frame infill interfaces and the negligence of separation in the composite shear mode (mode S in Wood failure mode classification)."

From the work of Liauw et al(25), it may be concluded that frame-infill separation occurs at early stages of loading, even though it might not be visible, or even might not be measurable in the experiment. Frictional force, at beam-infill interface was reported as small as 12% of the racking load initially but rapidly increased to 33% during and after crushing of the infill, Fig 2.30(c). This additional information allowed Liauw et al(25) to establish a new plastic method for design of infilled frames as outlined in the following section.

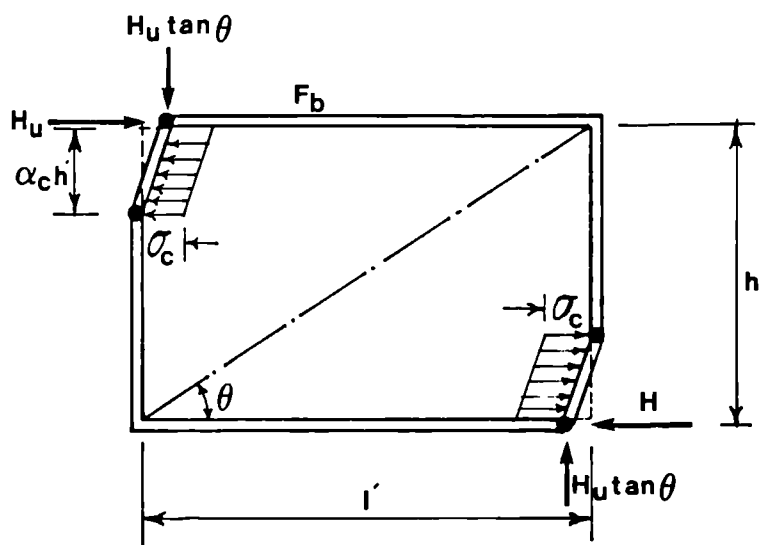
2.8.2 Collapse Modes and Loads

When a single-storey infilled frame is subjected to racking load, the mode of failure depends on the panel proportions and the relative strengths of the columns, beams and the infill. With relatively weak column and strong infill, failure occurs in the columns with subsequent crushing of the infill in the loaded corners. The most

compressive principal stress is directed almost normal to the column. Therefore, the small shear and normal forces at the beam interface may be neglected and regarded as strength reserve. This is referred to as "the corner crushing mode with failure in columns" (mode 1). Fig 2.31 shows the results of F.E analysis and the proposed collapse mechanism of mode 1. With relatively weak beams and strong infill, failure occurs in the beams with subsequent crushing of the infill in the loaded corners. The largest compressive stress is directed almost normal to the beam. Therefore, the small shear and normal forces at the column interface may be neglected and regarded as strength reserve. This mode of failure is termed "corner crushing mode with failure in beams" (mode 2). Fig 2.32 shows the results of F.E analysis and the proposed collapse mechanism of mode 2. With relatively strong frame and weak infill, failure occurs in the infill by crushing in the loaded corners with subsequent failure in the joints of the frame at the loaded corners. The most compressive principal stress is assumed to be directed normal either to the columns or beams depending on whether the height of the panel is smaller or bigger than its length respectively. Therefore, shear and normal forces of the contact length of the other two sides of the panel may be neglected. This mode of failure is termed "diagonal crushing mode" (mode 3). Fig 2.33 shows the results of F.E analysis and the proposed collapse mechanism of mode 3.

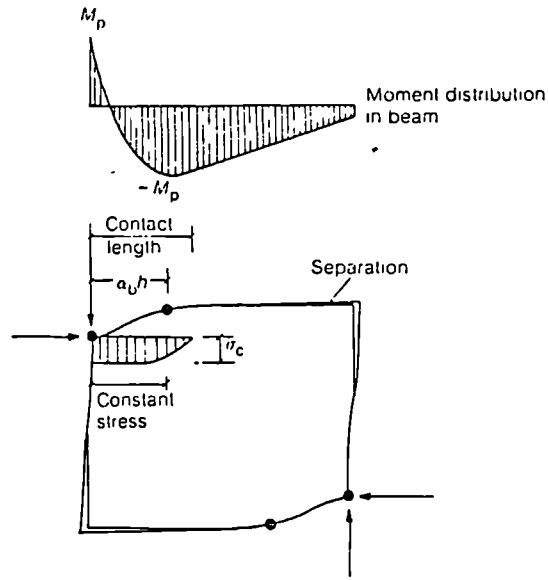


(a)

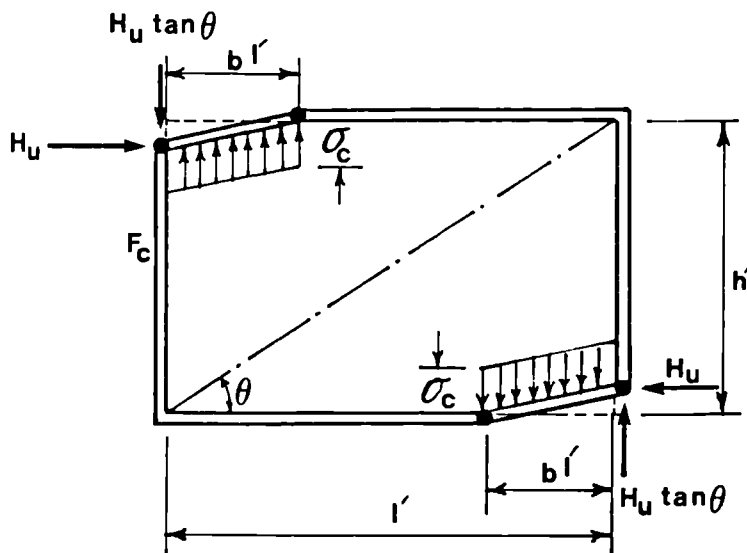


(b)

Figure 2.31 Mode 1 - Corner crushing with Failure in Columns; (a) results of finite element analysis (24), (b) theoretical idealization (25) (after Liauw et al (25))

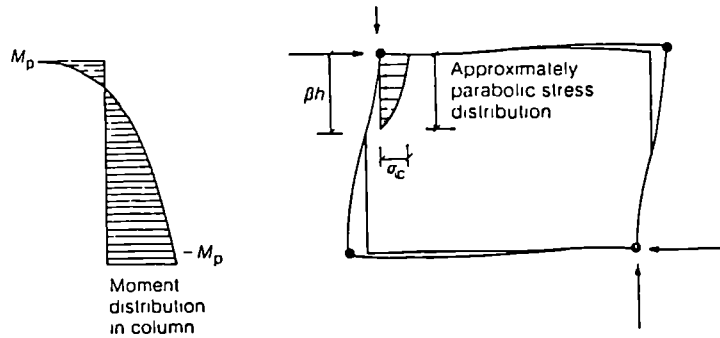


(a)

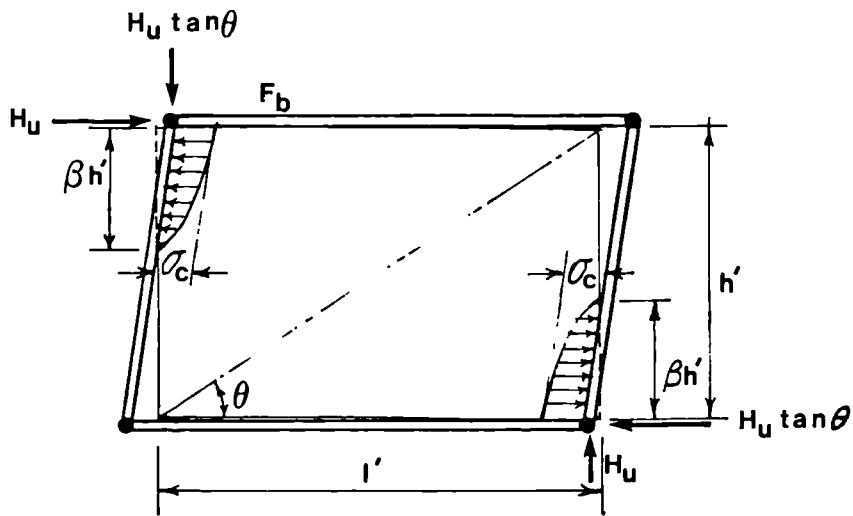


(b)

Figure 2.32 Mode 2 - Corner Crushing with Failure in Beams; (a) results of finite element analysis(24) and (b) theoretical idealization(25) (after Liauw et al(25))



(a)



(b)

Figure 2.33 Mode 3 - Diagonal Crushing (Span Greater than Height); (a) results of finite element analysis(24) and (b) theoretical idealization(25) (after Liauw et al(25))

Examination of upper and lower bound solutions (carried out by Liauw et al (25,33)) and minimization of the horizontal collapse racking load, H_u , led to the following relations:

$$H_u = m\sigma_c t h'$$

m is the minimum of the following values:

$$\text{For mode 1: } m_1 = m_{jc} = \left[2(M_{pj} + M_{pc}) / (\sigma_c t h'^2) \right]^{1/2} \quad (2.48)$$

$$\text{For mode 2: } m_2 = m_{jb} / \tan\theta = \left[2(M_{pj} + M_{pb}) / (\tan^2\theta \sigma_c t h'^2) \right]^{1/2} \quad (2.49)$$

$$\text{For mode 3: } m_3 = m_j^2 + k/6 = 4M_{pj} / (\sigma_c t h'^2) + k/6 \quad (2.50)$$

where k is given as:

$$\text{For } h'/l' < 1: \quad k = (2/3)\beta - (1/2)\beta^2 \quad (2.51)$$

$$\text{For } h'/l' > 1: \quad k = \left[(2/3)\beta - (1/2)\beta^2 \right] \cot^2\theta \quad (2.52)$$

β may be taken as 1/3 so as to match with the experimental results. The indexed m values are frame/infill strength parameters. The indices denote the part of the frame under consideration; b for beam, c for column and j for joint. σ_c is the compressive strength of the infill. Liauw et al (25) did not specify whether f_c' or f_{cu} was meant by σ_c , but it may reasonably be taken as f_c' for concrete and f_{pr} for masonry.

2.8.3 Comparison With Experimental Results

The experimental results of Barua and Mallick (26), Mallick and Severn (27), Mainstone (9) and Kadir and Hendry (28) were partly compared with the proposed method in

Fig 2.34 showing a fairly good agreement. Examination of the values of β ranging between 1/4 to 1/2 showed⁽²⁵⁾ that β equal to 1/3 gives reasonably accurate and also on the safe side results. Table 2.2 compares this method with all the other available methods for predicting the collapse load and column plastic moment of a masonry infilled frame.

2.8.4 Using the Liauw et al Plastic Method for Analysis of Single-Bay Multi-Storey Infilled Frames

The collapse modes of multi-storey infilled frames are basically the same as those of single-storey. However many different combinations are possible; some typical collapse modes are shown in Fig 2.35.

Liauw et al⁽²⁵⁾ proposed that the design of such structures should be carried out storey by storey based on simple design rules. They developed the standard energy approach and derived the m values for the top storey as:

$$\begin{aligned} m_1 &= m_{jc} \\ m_2 &= m_{jb}/\tan\theta \\ m_3 &= m_j^2 + (1/6)k \end{aligned} \tag{2.53}$$

and for other storeys as:

$$\begin{aligned} m_1 &= m_c \\ m_2 &= m_b/\tan\theta \\ m_3 &= m_j^2 + (1/6)k \end{aligned} \tag{2.54}$$

where:

$$\begin{aligned} m_c &= 4M_{pc}/(\sigma_c t h'^2) \\ m_b &= 4M_{pb}/(\sigma_c t h'^2) \end{aligned} \tag{2.55}$$

2.8.5 Discussion of Liauw et al Method

May, Ma, Wood and Sims(33) made a comprehensive discussion on the Liauw et al(25) method mainly in the area of upper and lower bound solutions of the proposed modes of distortion. Correspondingly, Liauw et al gave additional clarifications by carrying out both the upper and lower bound solutions for all the proposed modes of distortion. These solutions were identical for each mode. However, the significance of the major approximations, due to ignorance of the tangential forces on the contact surfaces and also neglecting the normal stress acting on the minor side of the loaded corners, deserve further verification especially for infilled frames having a height/length ratio different from those studied by Liauw et al(25), Fig 2.29.

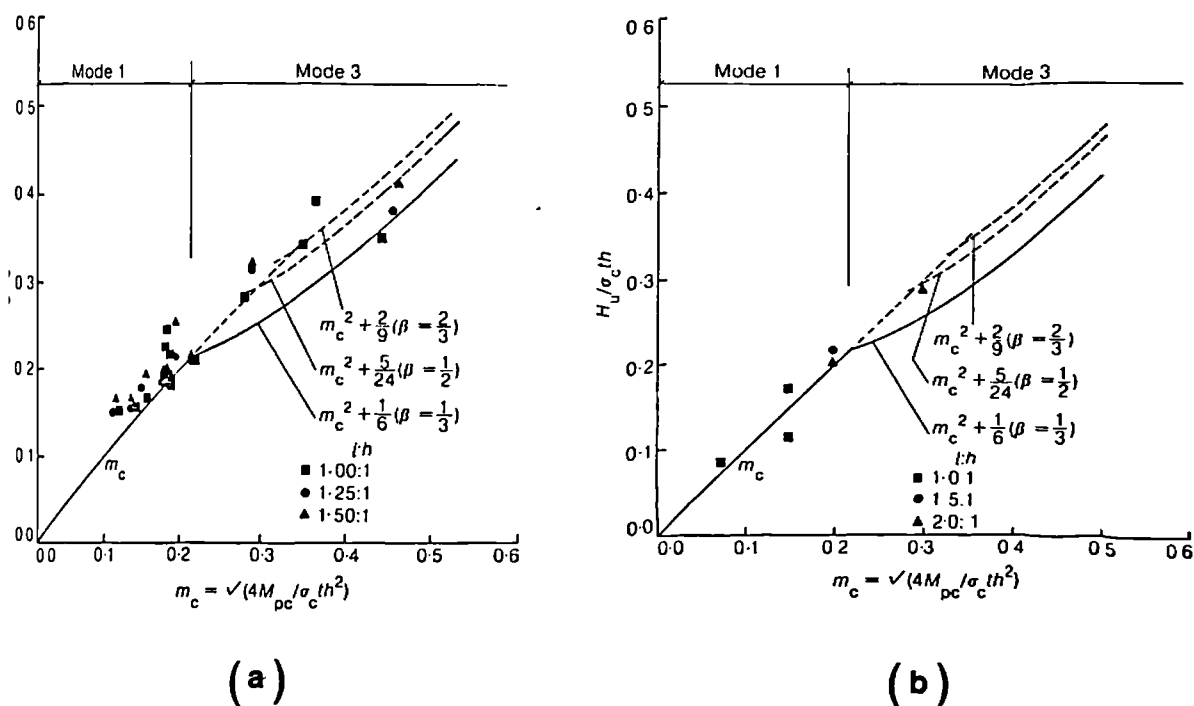
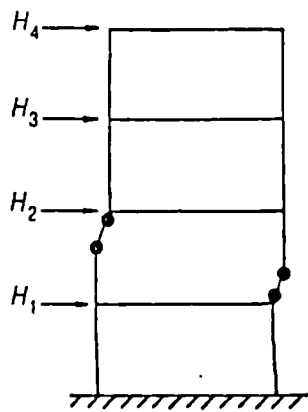
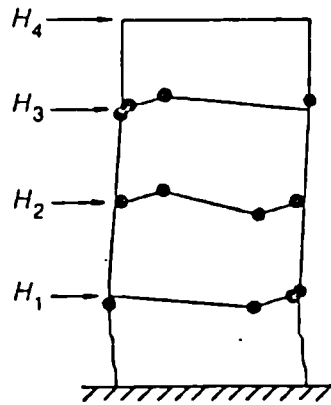


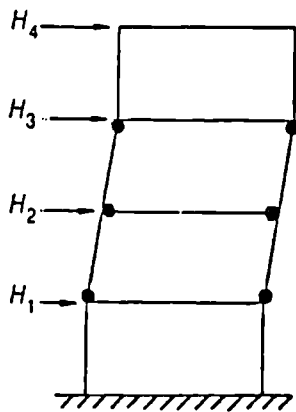
Figure 2.34 Comparison of Liauw et al Estimated Loads (25) with Experimental Results; (a) Barua et al(26), (b) Mallick et al(27) (after Liauw et al(25))



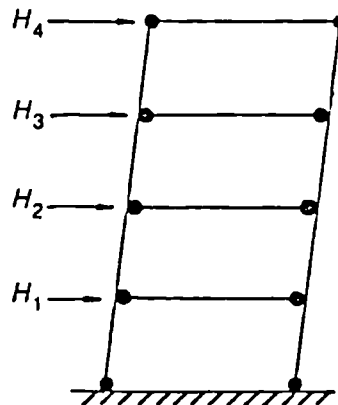
(a)



(b)



(c)



(d)

Figure 2.35 Failure modes of Multistorey Infilled Frames;
 (a) mode 1, (b) mode 2, (c) mode 3 and
 (d) mode 3, (after Liauw et al(25))

2.9 Conclusion From The Literature Review

Attempts at developing a design method for infilled frames have resulted in two distinct categories of methods;

- a) The methods based on the infill/frame stiffness parameter, λ_h , described in Sections 2.3 to 2.6 and
- b) The methods based on the frame/infill strength parameter, m , described in Sections 2.7 and 2.8.

The former methods assume the frame remains in an elastic state up to the peak load. The latter methods, however, use the plasticity theories, thus indicating that both the frame and the infill experience plasticity before the peak load ^{been} has reached when the frame undergoes a plastic collapse mechanism upon which the peak load can be calculated.

The current investigation, thus, may be extended to study the true behaviour of infilled frames. By an experimental approach, one may not discover whether the frame or infill experiences plasticity first. However, previous experiments (20,29) have proved ^{the} occurrence of the frame plasticity only after the peak load.

On the other hand, the Finite Element method has proved to be a powerful device in solving highly indeterminate problems. Wood (23), discussing his plastic method, stated that "The next important advance must come from Finite Element analysis, allowing for elastoplasticity of infilling wall with restricted plastic strain." Such a Finite Element analysis should simulate the infilled frame behaviour as truly and as accurately as possible.

Table 2.2 lists the features, which will enhance the analysis, if they can be incorporated with a finite element analysis.

Table 2.2 also lists those features (marked by x) that have been included in some previously developed Finite Element analysis programs, written particularly for infilled frame structures.

The main objective of this study is, thus, to develop a Finite Element analysis program, enhanced by as many as possible of the desired features listed in Table 2.2. Such a program may then be used to examine the degree of accuracy of the existing methods. Also, it is desirable to examine the significance of the effect of those parameters and variables that are not included in these methods. The next step, then, would be the inclusion of the variables and parameters, which have proven to have significant effects on the behaviour of infilled frames.

Having developed such a program, it is possible to carry out a parametric study and to examine the effects of the variables on the overall behaviour of infilled frames. Such variables include material properties, dimension of the frame or infill, vertical loading, lack of fit, precompression, order of application of loads, position and size of any opening, other frame combinations such as multi-storey and multi-bay panels and degree of restraint of frame connections (rigid, semi-rigid, hinge). Such a parametric study could provide a set of data for development of a code of practice for design of infilled frames.

The criteria for design of infilled frame structures can be established with respect to the following requirements:

- i) Limit states of serviceability such as: deflection, cracking, separation, slip (if desired to be prevented or limited for structures of particular purpose), and spalling of the infill material at the loaded corners, should it happen well before the peak load has reached.
- ii) Limit state of collapse; permitting an acceptable range of plastic strain for the material in question.

;

Table 2.2 Summary of The Effects That Are Desirable to be Accounted for in a Finite Element Computer Program for Analysis of Infilled Frames.

EFFECTS	ACCOUNTED FOR IN:					
	(REFERENCES)					
	17	24	34	35	96	P
<u>IN THE MATERIAL MODELING</u>						
Non-linearity of materials		X			X	X
Strain softening of infill material		X				X
Loading-unloading characteristics					X	X
Variation of the Poisson's ratio						X
Biaxial failure criterion				X		X
Crack modeling, opening and closing		X			X	X
The behaviour of interlocked cracks						X
Occurrence of secondary cracks						X
Biaxial failure criteria for masonry				X		
<u>IN THE INTERFACE MODELING</u>						
Lack of fit		X	X			X
Bond resistance		X		X		X
Friction-slip characteristics	X	X	X	X	X	X
Separation and recontacting		X	X	X	X	X
<u>IN THE FINITE ELEMENTS</u>						
Axial deformation of frame members	X		X			X
Shear deformation of frame members	X		X			X
Masonry bound in the subdivision mesh			X			X
Weight of the structure						X
<u>OTHER</u>						
Post-peak-load behaviour		X				X

P= The proposed finite element computer program, NEPAL

CHAPTER THREE

The Finite Element Technique

3.1 General

The review of previous work on the behaviour of infilled frames led to selection of The finite element technique for study of the non-linear behaviour of infilled frames in this investigation.

The finite element method is described in standard texts, eg. Zienkiewicz (36). In this chapter, only the principles will briefly be described in order to establish a notation for the later descriptions and developments.

In order to simulate the actual behaviour of infilled frames as close as possible, all the features listed in Table 2.2 will be regarded as the minimum requirements for the proposed finite element analysis computer program.

3.2 Finite Element Concept

The finite element method is a technique used for solving partial differential equations by discretizing these equations in their space dimensions to give finite elements. The regional matrix equations, written for nodal points of elements, are summed resulting in global matrix equations.

In structural engineering applications of this

method, the body of the structure is subdivided into elements being linked together by nodes. The global matrix equations take the form of:

$$\{P\} = [K]\{a\} \quad (3.1)$$

which relates the nodal forces vector, $\{P\}$, to the nodal displacements vector, $\{a\}$, where $[K]$ denotes the stiffness matrix of the structure under consideration. In a linear elastic analysis $[K]$ is a square ^{symmetric} matrix of constant terms resulting from the geometry and the mechanical properties of the materials of the structure. Eqs 3.1 are, thus, a set of linear simultaneous equations which can be solved directly. When non-linearity of material is desired to be accounted for, $[K]$ becomes a function of current nodal displacements causing the Eqs 3.1 to become non-linear. Such equations cannot be solved directly. However, there are numerical solutions to such equations as described in the following section.

3.3 Newton Raphson Iteration

The most frequently used iteration schemes for the solution of non-linear finite element equations are of the Newton Raphson type⁽³⁶⁾ illustrated in Fig 3.1. In this method, equilibrium conditions, at completion of each load increment, are satisfied by successive approximation of the form:

$$\{R_i(n)\} = \{P_i - q_i(n)\} = [K_i(n-1)]\{\Delta a_i(n)\} \quad (3.2)$$

in which $[K_i(n-1)]$ denotes the tangent stiffness matrix of the structure at completion of $(n-1)$ th iteration. $\{\Delta a_i(n)\}$ is the n th correction to the current nodal displacements vector and $\{P_i\}$ signifies the total externally applied loads vector at the load increment station i . $\{q_i(n)\}$ denotes the nodal forces vector corresponding to the current stresses, so called "equivalent nodal forces vector." $\{R_i(n)\}$ is termed "The vector of unbalanced nodal forces." The nodal displacement increment correction vector, $\{\Delta a_i(n)\}$, is used to obtain the next displacement approximation;

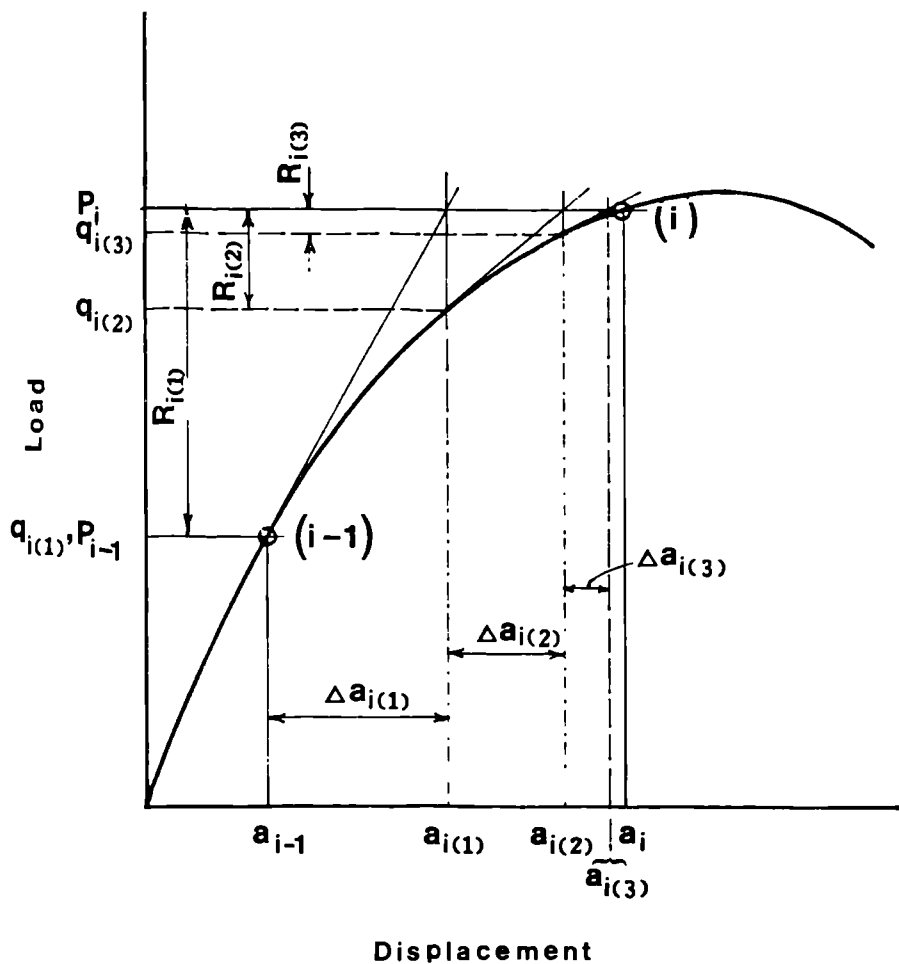


Figure 3.1 Newton Raphson Iteration

$$\{a_i(n)\} = \{a_i(n-1)\} + \{\Delta a_i(n)\} \quad (3.3)$$

Iterations are repeated, Fig 3.1, until an appropriate convergence criterion is satisfied. When such convergence is achieved the external loads vector, $\{P\}$, is increased to a higher level. The procedure is continued until a desired load level is reached or complete failure of the structure takes place.

3.4 Finite Element Formulation

3.4.1 General

Non-linear finite element analysis reduces to solution of linear tangential displacement equations, Eqs 3.2, involving the tangent stiffness matrix of the structure, $[K]$. $[K]$ is a matrix of currently constant terms which are computed by assembling the terms of the elements' tangent stiffness matrices, $[K]^e$. The technique of assembling is widely described in standard finite element texts (36, 37). An element tangent stiffness matrix, $[K]^e$, relates the element unbalanced nodal forces vector, $\{\Delta F\}$, to the element nodal displacements vector, $\{\Delta a\}^e$, as follows:

$$\{\Delta F\} = [K]^e \{\Delta a\}^e \quad (3.4)$$

The overall equivalent nodal forces vector, $\{q\}$, also results from assembling the elements equivalent nodal forces, $\{q\}^e$. Derivation of $[K]^e$ and $\{q\}^e$ are given in standard texts of finite element (36, 37) but it is convenient to review the principles in order to establish a notation for later descriptions. For the sake of

simplicity, in the following subsections, the superscript 'e' is omitted, and all the stiffness values are meant to be tangential unless otherwise specified.

3.4.2 Element Displacement Functions

Displacement components, \mathbf{u} and \mathbf{v} , of an arbitrary point within the area of an element may linearly be related to the element nodal displacements. For a two dimensional n-node element, such relationships may be expressed as follows:

$$\mathbf{u} = \sum_{i=1}^n (N_{uxi}X_i + N_{uyi}Y_i)$$

$$\mathbf{v} = \sum_{i=1}^n (N_{vxi}X_i + N_{vyi}Y_i)$$

Where N_{uxi} etc. are a set of independent functions of the co-ordinates of the point under consideration, so called the element shape functions, and, X_i and Y_i are displacement components of node i . The element displacement functions may be written in matrix form as follows:

$$\begin{bmatrix} \mathbf{u} \\ \mathbf{v} \end{bmatrix} = \begin{bmatrix} N_{ux1} & N_{uy1} & \dots & N_{uxn} & N_{uyn} \\ N_{vx1} & N_{vy1} & \dots & N_{vxn} & N_{vyn} \end{bmatrix} \begin{bmatrix} X_1 \\ Y_1 \\ \dots \\ X_n \\ Y_n \end{bmatrix} \quad (3.5a)$$

Or: $\{\mathbf{e}\} = [\mathbf{N}]\{\mathbf{a}\}$

where \mathbf{e} denotes the element displacement vector. For incremental values, the above relation becomes:

$$\{\Delta e\} = [N]\{\Delta a\} \quad (3.5b)$$

If, for all the values of i , $N_{uxi} = N_{vyi}$ and $N_{uyi} = N_{vxi} = 0$, $[N]$ reduces to:

$$[N] = \begin{bmatrix} N_1 & 0 & N_2 & 0 & \dots & N_n & 0 \\ 0 & N_1 & 0 & N_2 & \dots & 0 & N_n \end{bmatrix}$$

This form of displacement shape function matrix is common with all quadrilateral isoparametric C_0 elements (36).

3.4.3 Element Strain Functions

Components of strains vector at an arbitrary point within a plane structure, are given (38) as:

$$\{\epsilon\} = \{\epsilon_x = \partial u / \partial x, \epsilon_y = \partial v / \partial y, \gamma_{xy} = \partial u / \partial y + \partial v / \partial x\}^T$$

where $u(x, y)$ and $v(x, y)$ are displacement functions of the structure. The above relations can be written in matrix form as:

$$\begin{bmatrix} \epsilon_x \\ \epsilon_y \\ \gamma_{xy} \end{bmatrix} = \begin{bmatrix} \partial / \partial x & 0 \\ 0 & \partial / \partial y \\ \partial / \partial y & \partial / \partial x \end{bmatrix} \begin{bmatrix} u \\ v \end{bmatrix}$$

or: $\{\epsilon\} = [L]\{e\} \quad (3.6)$

Substituting for $\{e\}$ from Eqs 3.5, Eqs 3.6 become:

$$\{\epsilon\} = [L][N]\{a\}$$

Define:

$$[B] = [L][N] \quad (3.7)$$

hence:

$$\{\epsilon\} = [B]\{a\} \quad (3.8a)$$

For incremental changes of nodal displacements, the above relation becomes:

$$\{\Delta\epsilon\} = [B]\{\Delta a\} \quad (3.8b)$$

The [B] matrix is called "The element strain-displacement matrix" which is independent of the properties of the material.

3.4.4 Stress-strain Relation

In a non-linear elastoplastic material, for small variation of stress or strain components, the material is assumed to be linear elastic and the incremental stress-strain relation is expressed by the well known elasticity equations. These equations can be written in their matrix form as follows:

$$\{\Delta\sigma\} = [D_t]\{\Delta\epsilon\} \quad (3.9)$$

where the tangent elasticity matrix, $[D_t]$, is a matrix of constant terms corresponding to the current tangent mechanical properties of the material. The determination of the tangent elasticity matrix is discussed, in Chapter 4. For a plane stress isotropic continuous material, the elasticity matrix follows 'Hooke's law and is given as:

$$[D_t] = \frac{E_t}{(1-\nu^{*2})} \begin{bmatrix} 1 & \nu^* & 0 \\ \nu^* & 1 & 0 \\ 0 & 0 & (1-\nu^*)/2 \end{bmatrix} \quad (3.10)$$

where E_t and ν^* are the tangent values of modulus of elasticity and Poisson's ratio of the material respectively.

3.4.5 Element Stiffness Matrix

Since changes in internal stresses and strains are due to changes in element nodal forces and displacements, one of the energy methods may be used to derive the stiffness matrix of an element as shown below.

If the material behaviour is linear-elastic between the two stations, the total internal strain energy may be calculated as:

$$U = \frac{1}{2} \int_V \{\Delta \epsilon\}^T \{\sigma\} dV$$

Substituting for $\{\sigma\}$ from Eqs 3.9, gives:

$$U = \frac{1}{2} \int_V \{\Delta \epsilon\}^T [D_t] \{\Delta \epsilon\} dV$$

Substituting for $\{\Delta \epsilon\}$ from Eqs 3.8b, leads to:

$$U = (1/2) \{\Delta a\}^T \left[\int_V [B]^T [D_t] [B] dV \right] \{\Delta a\}$$

The work done by external nodal forces may also be calculated as:

$$W = (1/2) \{\Delta a\}^T \{\Delta F\}$$

where $\Delta \mathbf{F}$ denotes the changes in the nodal forces vector. Equating the internal and external energy, \mathbf{U} and \mathbf{W} , $\Delta \mathbf{F}$ can be derived as follows:

$$\{\Delta \mathbf{F}\} = \left[\int_{\mathbf{V}} [\mathbf{B}]^T [\mathbf{D}_t] [\mathbf{B}] d\mathbf{V} \right] \{\Delta \mathbf{a}\}$$

Comparison of the above equation with Eq 3.4 leads to the element tangent stiffness matrix as follows:

$$[\mathbf{K}]^e = \int_{\mathbf{V}} [\mathbf{B}]^T [\mathbf{D}_t] [\mathbf{B}] d\mathbf{V} \quad (3.11)$$

Note that the integration must be carried out over the volume of the element.

3.4.6 Element Equivalent Nodal Forces

Using the same energy method as used in previous section, the equivalent nodal forces vector, \mathbf{q} , may be derived in term of the stress vector as follows:

$$\mathbf{U} = 1/2 \int_{\mathbf{V}} \{\boldsymbol{\varepsilon}\}^T \{\boldsymbol{\sigma}\} d\mathbf{V}$$

Substituting for $\{\boldsymbol{\varepsilon}\}$ from Eqs. (3.8a), gives:

$$\mathbf{U} = (1/2) \{\mathbf{a}\}^T \int_{\mathbf{V}} [\mathbf{B}]^T \{\boldsymbol{\sigma}\} d\mathbf{V}$$

The work done by the nodal forces may be written as:

$$W = (1/2)\{a\}^T\{q\}^e$$

Equating U and W and solving for $\{q\}^e$, leads to:

$$\{q\}^e = \int_V [B]^T \{\sigma\} dV \quad (3.12)$$

3.5 Local Normalized Coordinates

3.5.1 Definitions

Fig 3.2 shows mapping of a quadrilateral element into normalized local coordinates, ξ and η . The origin of the normalized coordinates, $O(\xi=0, \eta=0)$, is located at the intersection of bisectors of opposite sides of the quadrilateral. Normalization of the local co-ordinates requires that,

$$\xi_1=-1, \quad \eta_1=-1$$

$$\xi_2=-1, \quad \eta_2=+1$$

$$\xi_3=+1, \quad \eta_3=+1$$

$$\xi_4=+1, \quad \eta_4=-1$$

It is convenient to convert Eqs 3.11 and 3.12 into local normalized coordinates because,

- a) The element shape functions are normally worked out in terms of local normalized coordinates in order to be independent of geometry and location of the element.
- b) Local normalized coordinates allow the integrations of

Eqs 3.11 and 3.12 to be carried out numerically using Gaussian quadrature over quadrilateral regions(36).

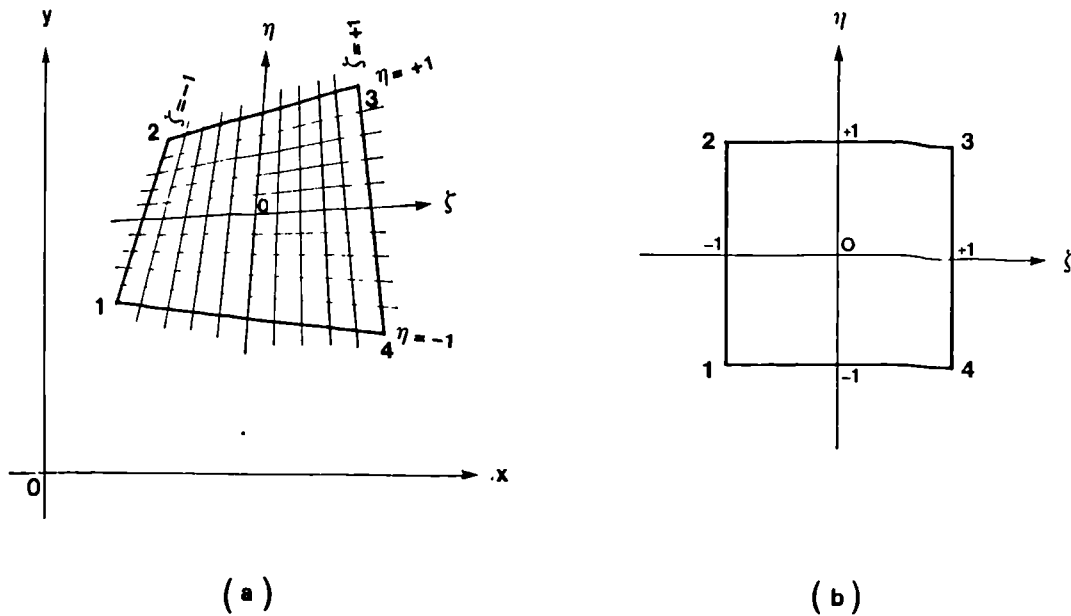


Figure 3.2 Geometry of a Quadrilateral Element;
 (a) in global co-ordinates and (b) mapped into
 normalized co-ordinates

3.5.2 Evaluation of the Integrals in Terms of Local Normalized Coordinates

Expressions 3.11 and 3.12 involve matrix [B] which depends on $\partial N_i / \partial x$ and $\partial N_i / \partial y$. These derivatives can be derived by the chain rule of partial differentiation as follows:

$$\begin{bmatrix} \partial N_i / \partial x \\ \partial N_i / \partial y \end{bmatrix} = [J]^{-1} \begin{bmatrix} \partial N_i' / \partial \xi \\ \partial N_i' / \partial \eta \end{bmatrix} \quad (3.13)$$

Or: $[DERIV] = [J]^{-1} [DER]$

where N_i' is the displacement shape function of the i th node of the element in terms of local normalized coordinates, ξ and η , and $[J]$ is the Jacobian matrix expressed as:

$$[J] = \begin{bmatrix} \partial x / \partial \xi & \partial y / \partial \xi \\ \partial x / \partial \eta & \partial y / \partial \eta \end{bmatrix} \quad (3.14)$$

The terms of $[J]$ matrix can be calculated only when coordinates of any arbitrary point in global coordinates are known in terms of the normalized coordinates, i.e. $x = P(\xi, \eta)$ and $y = Q(\xi, \eta)$. When the element is isoparametric (i.e. the shape functions defining geometry and function are the same), x and y are given (36) as follows:

$$x = N_1' X_1 + N_2' X_2 + \dots + N_n' X_n = \sum_{i=1}^n N_i' X_i$$

$$y = N_1' Y_1 + N_2' Y_2 + \dots + N_n' Y_n = \sum_{i=1}^n N_i' Y_i$$

where X_i and Y_i are coordinates of the nodal points of the element in global coordinates system. Substituting for x and y into relation 3.14, the $[J]$ matrix can be derived in terms of ξ and η and the coordinates of nodal points of the element as follows:

$$[J] = \begin{bmatrix} \partial N_1' / \partial \xi & \dots & \partial N_n' / \partial \xi \\ \partial N_1' / \partial \eta & \dots & \partial N_n' / \partial \eta \end{bmatrix} \begin{bmatrix} X_1 & Y_1 \\ \dots & \dots \\ X_n & Y_n \end{bmatrix} \quad (3.15)$$

Or; $[J] = [DER] [COORD]$

Even when the element is not isoparametric, the Jacobian matrix can still be calculated using a new set of shape functions, \mathbf{N}_i^* , (specially used for this purpose) being compatible with the geometry of the element.

The determinant of Jacobian matrix, $[\mathbf{J}]$, must also be evaluated for transformation of the integrals involving $dx dy$ as follows (39):

$$\mathbf{f}(\xi, \eta) dV = t \int_{-1}^{+1} \int_{-1}^{+1} \mathbf{f}(\xi, \eta) |\mathbf{J}| d\xi d\eta \quad (3.16)$$

Where t denotes the thickness of the element and $\mathbf{f}(\xi, \eta)$ signifies either functions of Eqs 3.11 or Eqs 3.12.

3.6 Numerical Integration

Calculation of ^{the} element stiffness matrix, $[\mathbf{K}]^e$, and equivalent nodal forces, $\{\mathbf{q}\}^e$, led to integrals of type:

$$\mathbf{I} = t \int_{-1}^{+1} \int_{-1}^{+1} \mathbf{f}(\xi, \eta) |\mathbf{J}| d\xi d\eta$$

Analytical evaluation of such integral at this form is impractical as far as applications of numerical analysis is concerned. Therefore, in practice, such integrals are evaluated numerically using gaussian quadrature over quadrilateral regions. The quadrature rules are all of the form:

$$I = t \sum_{G=1}^{G=n} H_i H_j f(\xi_j, \eta_i) |J|_{ij} \quad (3.17)$$

Where t denotes the thickness of the element. H_i and H_j are weights and ξ_i and η_j are abscissa of the region under consideration as shown in Fig 3.3. Values of weights and abscissas of the quadrilateral regions, in the gaussian quadrature rule, are available in standard finite element texts;

eg. Zienkiewicz (36). Such integration is an approximation. The exact solution may be obtained if the number of gaussian points is optimal; one for parabolic, two for cubic and three for quadratic functions (36,37).

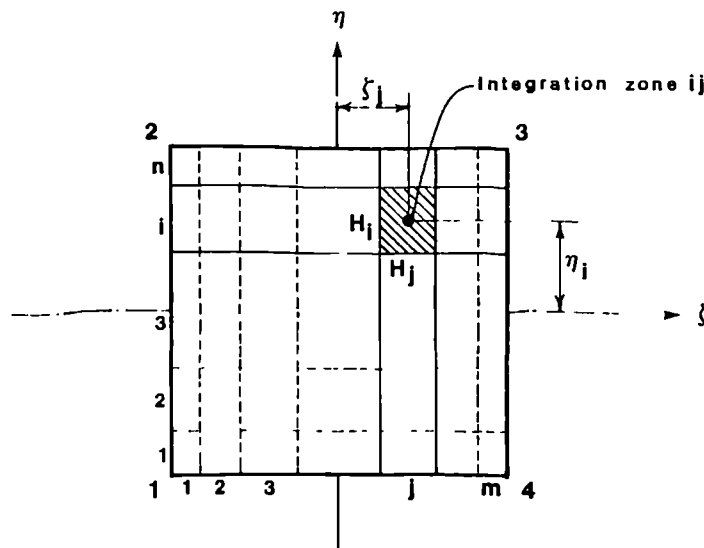


Figure 3.3 Numerical Integration

3.7 Contribution of Reinforcement to R.C Elements

3.7.1 General

It has been customary to consider the two constituents, concrete and steel reinforcement, as separate contributors to the overall stiffness and strength using the principle of superposition.

It is common to assume full kinematic continuity between concrete and steel, at least at nodal points on element boundaries. However, the two materials are highly unequal in their behaviour; Young's modulus for steel bar is one order higher than that of concrete, and unlike that of concrete, the stress-strain relation of steel is symmetric in tension and compression. The limited reinforcement-concrete bond strength results in:

- a) bond failure and sliding of reinforcing bars,
- b) local deformation of reinforcement in cracked concrete (doweling effect) and
- c) tension stiffening effect of uncracked concrete between cracks.

In order to reduce the errors due to such effects, various adjustments in properties of constituent materials have been specified, Chen⁽³⁹⁾. These are discussed in Chapter 4.

Having made such adjustments, reinforcement may be modeled as:

- a) two-node bar element or
- b) anisotropic equivalent solid layer stuck on the surface of the element where it is applicable or
- c) Single bar stuck on the surface of the element.

The choice of two-node bar element greatly increases the

size of the global stiffness matrix. Therefore, the other two models were adopted in this work.

Contribution of reinforcement is to be superimposed to that of the concrete as described in the following sections.

3.7.2 Uniformly Distributed Reinforcement

As shown in Fig 3.4(a, b), a uniformly distributed reinforcement with rate of r_s may be modeled by an anisotropic steel layer with thickness of $r_s t$ and having full strength and stiffness in direction of the reinforcement and zero strength and stiffness normal to this direction, where t is the thickness of the element.

The contribution of reinforcement of this type to the element properties may be computed in exactly the same way as described for the element itself. This contribution may be superimposed directly. i.e:

$$I = I_c + I_s \quad (3.18)$$

Where I denotes either integrals of Eqs 3.11 and 3.12 and subscripts c and s specify concrete and steel materials respectively.

In the particular case when reinforcement is uniformly distributed, the second integration, I_s , can be eliminated by including the mechanical properties of the steel layers into that of the concrete as follows:

$$[D] = [D_c] + r_{s1}[D_{s1}] + r_{s2}[D_{s2}] + \dots \quad (3.19)$$

$$\{\sigma\} = \{\sigma_c\} + r_{s1}\{\sigma_{s1}\} + r_{s2}\{\sigma_{s2}\} + \dots \quad (3.20)$$

where $[D_{si}]$ denotes the stress-strain relation matrix for i th layer of reinforcement. This will be studied in Section 4.9.6.

3.7.3 A Single Bar Parallel to One of the Element Local Coordinates

A single bar within an element is assumed to be stuck on the surface of the element and follows the displacement function of the element Fig 3.4(c, d). The contribution of such a bar can be computed by dividing it into parts and integrating the contribution of these parts numerically. When the reinforcing bar is extended parallel to one of the local co-ordinates, say ξ as shown in Fig 3.4(c), the numerical integration of its contribution can be computed as follows:

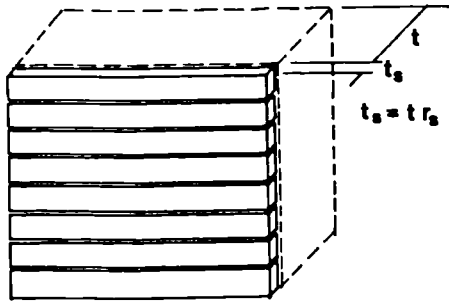
$$I_s = \sum 2tr_s H_j f(\xi_j, \eta_s) |J| s_j \quad (3.21)$$

The multiplier $2tr_s$ represents the integration of the rate of reinforcement, tr_s , between $\eta=-1$ to $\eta=+1$.

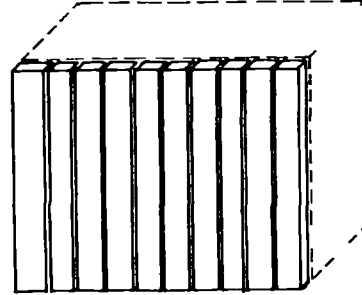
By altering the corresponding indices in Eq 3.21, Eq 3.22 can be written for a steel bar extended parallel to η as follows:

$$I_s = \sum 2tr_s H_i f(\xi_s, \eta_i) |J| i_s \quad (3.22)$$

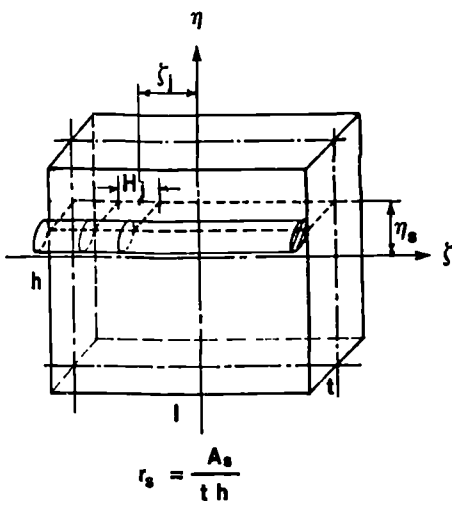
⋮
⋮
⋮



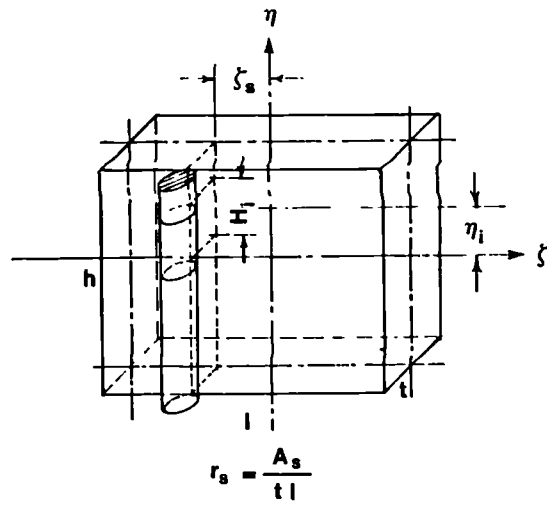
(a)



(b)



(c)



(d)

Figure 3.4 Reinforcement Modelling;
 (a) uniformly distributed horizontal reinforcement
 (b) uniformly distributed vertical reinforcement,
 (c) horizontal **single** reinforcement and
 (d) vertical **single** reinforcement.

3.8 Some Requirements of the F.E Discretization

The finite element method requires that the structure be discretized into finite elements. "The choice of elements depends on the particular application and the loading characteristics. In plane problems, isoparametric elements have proven to be the most versatile elements to model different problems in engineering mechanics, because the number of nodes and the order of integration are adjustable," Meyer and Bath⁽⁴⁰⁾. Fig 3.5 summarizes the most frequently used isoparametric elements in one dimensional truss, 2-D plane and 3-D solid structures. Displacement shape functions of these elements are available in standard texts; eg. Zienkiewicz⁽³⁶⁾.

The isoparametric 4-node plane element, Fig 3.5(b), has linear displacement shape functions of the form:

$$N_i = (1/4) (1 + \xi \xi_i) (1 + \eta \eta_i) \quad (3.23)$$

where N_i is the shape function of node i defined as the displacement component $u(\xi, \eta)$ or $v(\xi, \eta)$ of an arbitrary point within the element when node i is **given** a unit displacement in either ^{of the} co-ordinate directions of ξ or η respectively and ξ_i and η_i denote the position co-ordinates of node i ; eg, for $i=1$ $\xi_i=-1$ and $\eta_i=-1$. As can be seen, N_i is a linear function of the position co-ordinates of the point under consideration. The value of N_i becomes unity

when the point under consideration is located at node i and becomes zero when the point is located at any other nodal points. This is a necessary condition for a displacement shape function⁽³⁶⁾. For any element configuration, the sides of an isoparametric 4-node element remain straight. However, in an 8-node element, Fig 3.5(c), the sides follow a parabolic curve. Therefore, the shape functions of an 8-node plane element are to the second power of the position coordinates of the point under consideration as presented below.

$$\begin{aligned}
 i=1,3,5,7; \quad N_i &= (1/4) (1+\xi\xi_i) (1-\eta\eta_i) (\xi\xi_i+\eta\eta_i-1) \\
 i=2,6; \quad N_i &= (1/2) (1+\xi\xi_i) (1-\eta^2) \\
 i=4,8; \quad N_i &= (1/2) (1+\eta\eta_i) (1-\xi^2)
 \end{aligned}
 \tag{3.24}$$

Isoparametric 12-node (cubic) element, Fig 3.5(d), has yet more flexibility to follow the displacement variations. Nowadays there is a tendency to use more elaborate elements for the sake of economy and accuracy⁽³⁶⁾.

In non-linear finite element analyses of structures, the displacement equations must be solved several times, involving a considerable amount of computation time. The computation time for equation solving is approximately in proportion to N^2W . Where N and W are the total number of nodal displacement freedoms and the half-band-width of the global stiffness matrix respectively. Therefore, considerable care must be used in choosing the type of elements and the way the structure is subdivided and the

nodes are numbered in order that the size of the global stiffness matrix becomes as small as possible. The size of the stiffness matrix may considerably be reduced by a coarse subdivision of parabolic or even cubic elements. But the choice of element is also structure dependent. Therefore, the efficiency and compatibility of a selected element must be examined for the structure in question. For this purpose, the computer program "ELCO", which is the linear and elastic version of program "NEPAL", was used. Program "ELCO" is capable of solving linear problems with almost any type of element including some new proposed elements described in the following sections. Program "NEPAL" will be discussed in Chapter 5.

Application of the finite element method in the analysis of infilled frame structures requires specific considerations in:

- a) the finite element discretization of:
 - i) infilling wall,
 - ii) frame and
 - iii) wall/frame interfaces.
- b) the mechanical modeling of the materials.

These are studied in the rest of this chapter and Chapter 4.

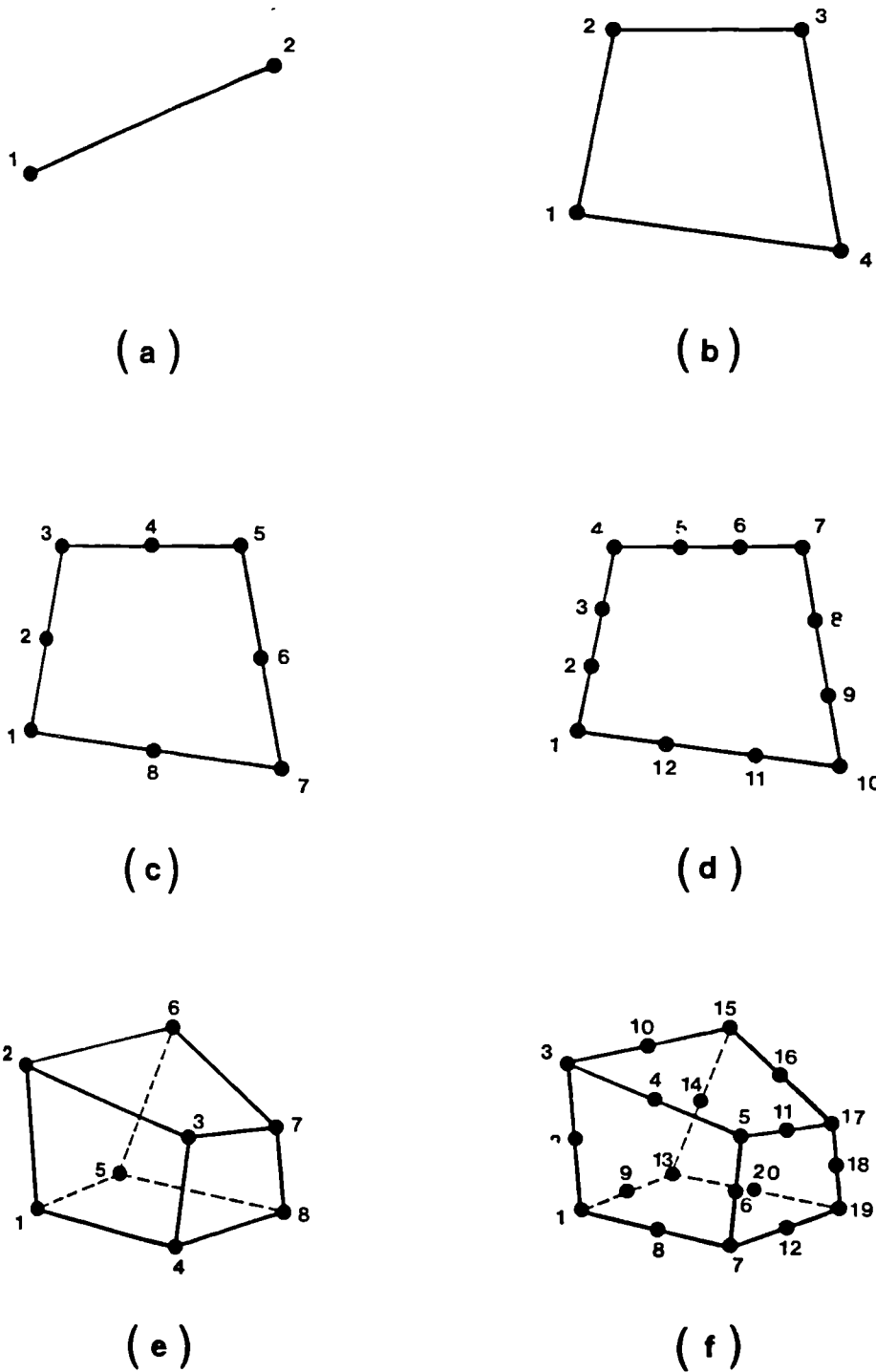


Figure 3.5 The Most Used Isoparametric Elements; (a) 2-node 1-D, (b) 4-node plane linear quadrilateral, (c) 8-node plane (parabolic quadrilateral), (d) 12-node plane (cubic quadrilateral), (e) 8-node 3-D solid and (f) 20-node 3-D solid

3.9 Masonry Wall Discretization

3.9.1 General

Masonry is made of mortar joints and masonry units with different mechanical properties. When masonry is subjected to in-plane loading, some out-of-plane interactive forces develop at interfaces of mortar joints and masonry units as a result of effects of the poisson's ratio and elasticity of the mortar joints. Therefore, the behaviour of masonry is three dimensional and elastoplastic.

3.9.2 Standard 3-D Elements

Standard finite element procedure suggests masonry be discretized into a set of 8-node and 6-node solid 3-D elements as shown in FIG 3.6. Also a set of 3-D interface elements with zero thickness must be included with the subdivision in order that the mechanical behaviour of unit/joint interfaces can be allowed for. This involves 72 nodal displacement freedoms per masonry unit. Such a high number of displacement freedoms demands a very expensive finite element analysis.

Therefore, the number of displacement freedoms should somehow be reduced. The following sections discuss some other choices with lesser number of displacement freedoms.

⋮
⋮
⋮

3.9.3 Newly Developed 3-D Four-node Element

A symmetry plane is attributed to any plane element having a uniform finite thickness. When a plane element is perfectly plane and subjected to a set of out of plane forces acting symmetrically about its symmetry plane, the induced out-of-plane displacements are also symmetric about the symmetry plane of the element. The symmetry plane does not move in the third direction. Therefore, it may be treated as a reference plane for all the out-of-plane displacements occurring within the thickness of the element.

Taking advantage of such a reference plane, an 8-node solid element may be assigned only four nodes located at the corners of the reference plane as shown in Fig 3.7. The algorithm of such element is given in detail in Appendix C.

The efficiency of the above element was examined by elastic analysis of a plate under laterally symmetric loading along the edges of the plate. The results showed that the out of plane displacement extends, effectively, only up to half of the thickness of the plate from its edge. Therefore, the thicker the elements are (relative to their area), the more accurately they simulate the actual out of plane deformation of the structure.

Use of this element reduces the number of nodes and consequently the number of displacement freedoms down to 36 per masonry unit. Since, to the knowledge of the author, a constitutive formulation for 3-D cracked material does not exist, the newly developed element may be used for the elements loaded only up to occurrence of the first crack.

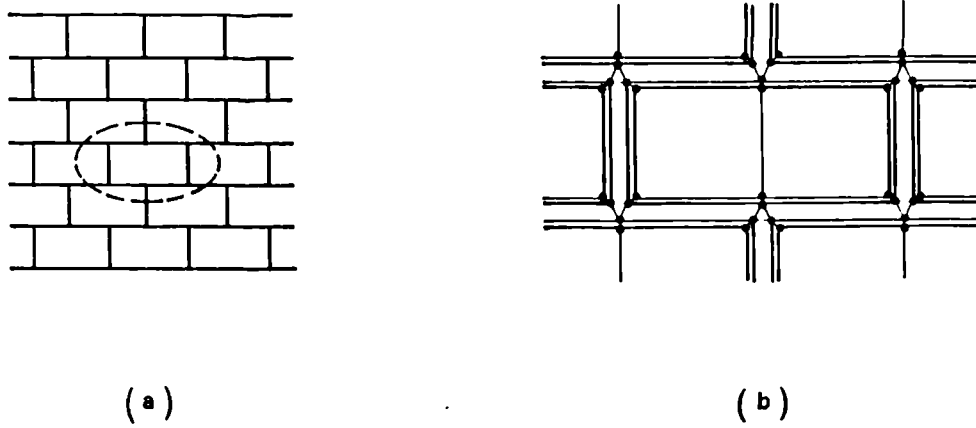


Figure 3.6 Masonry 3.D Finite Element Subdivision;
 (a) masonry bonds (b) subdivision mesh

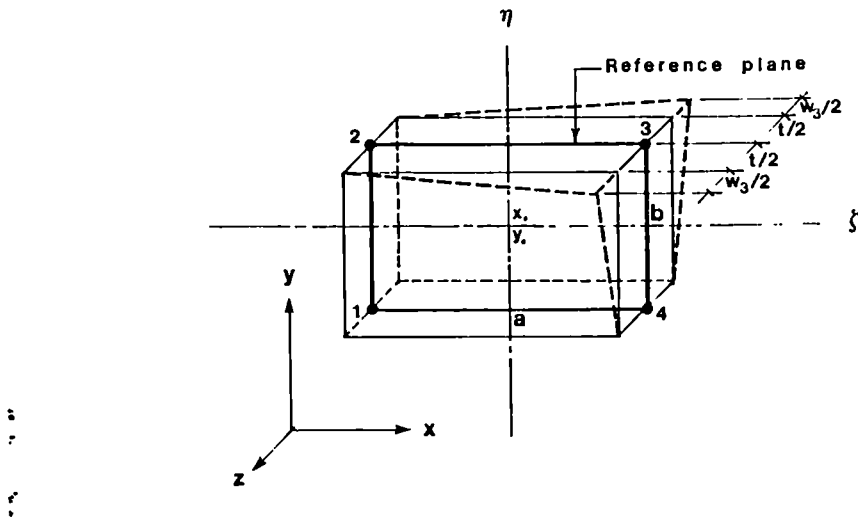


Figure 3.7 3.D Equivalent 4-node Element

3.9.4 Plane-Stress Equivalent Elements

A diagonally loaded masonry infilling wall usually cracks well before its ultimate strength is reached. Since a constitutive formulation for three dimensionally loaded cracked materials does not exist, the problem has to be reduced to two dimensions. In order to bring the problem into 2-D space, same finite element subdivision as shown in Fig 3.6 may be adopted provided that the mechanical properties of the mortar joints and masonry units are adjusted to allow for the effect of three- Dimensionality. The problem, then, involves 24 displacement freedoms per masonry unit, Fig 3.6.

The number of displacement freedoms can further be decreased by combining either the mortar joint and interface elements named "laminar joint elements" shown in Fig 3.8 or combining the masonry units and the adjacent mortar joint elements called "masonry equivalent elements" shown in Fig 3.9. These are described in the following sections.

3.9.5 Plane-stress Equivalent Units and Laminar Joints

In order to further reduce the number of nodes, The mechanical behaviour of the unit/mortar interfaces may be included into the bed and head joints eliminating the interface elements. By this device the joint elements become laminar, vide Zienkiewicz⁽³⁶⁾. Inclusion of laminar bed and head joints, brings the number of displacement freedoms down to 12 per masonry unit, Fig 3.8.

The element shape functions matrix, [N], and the strain

displacement matrix, $[B]$, are not influenced by such laminarity because these matrices are independent from the material properties. However, the weakening effect of laminarity must be included in the stress-strain relationship of the joint material. The author's effort led to the conclusion that, should the joint material crack in one or two directions and also slip or separate at the discontinuity planes of the material, an explicit constitutive formulation leading to a symmetric element stiffness matrix cannot be achieved. Therefore, laminar elements can only be used for uncracked materials.

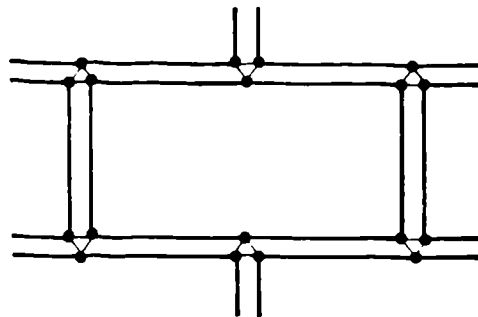


Figure 3.8 2-D Masonry finite element subdivision using laminar joint element

3.9.6 Plane-stress Masonry-Equivalent and Interface Elements

As discussed in Section 3.9.4, the number of nodes of a masonry subdivision mesh may further be reduced by combining the masonry units and the adjacent mortar joint elements called "masonry-equivalent element". This approach reduces the number of displacement freedoms per masonry unit down to 12. As shown in Fig 3.9, masonry is, therefore, assumed to be made of a single material with mechanical properties equivalent to those of masonry ignoring the weakening effect of interfaces. Whereas these effects are accounted for by the interface elements described in Section 3.10 and 3.11. The masonry equivalent material is discussed in Sections F.3.2 to F.3.4.

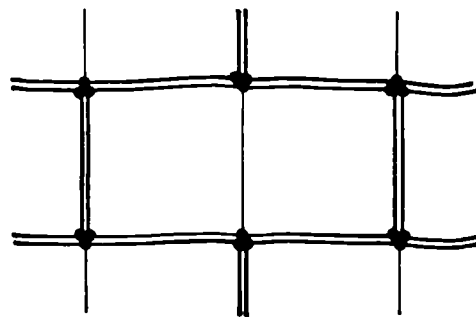


Figure 3.9 2-D Masonry Finite Element Subdivision Using Masonry-equivalent Elements and Zero Thickness Interfaces

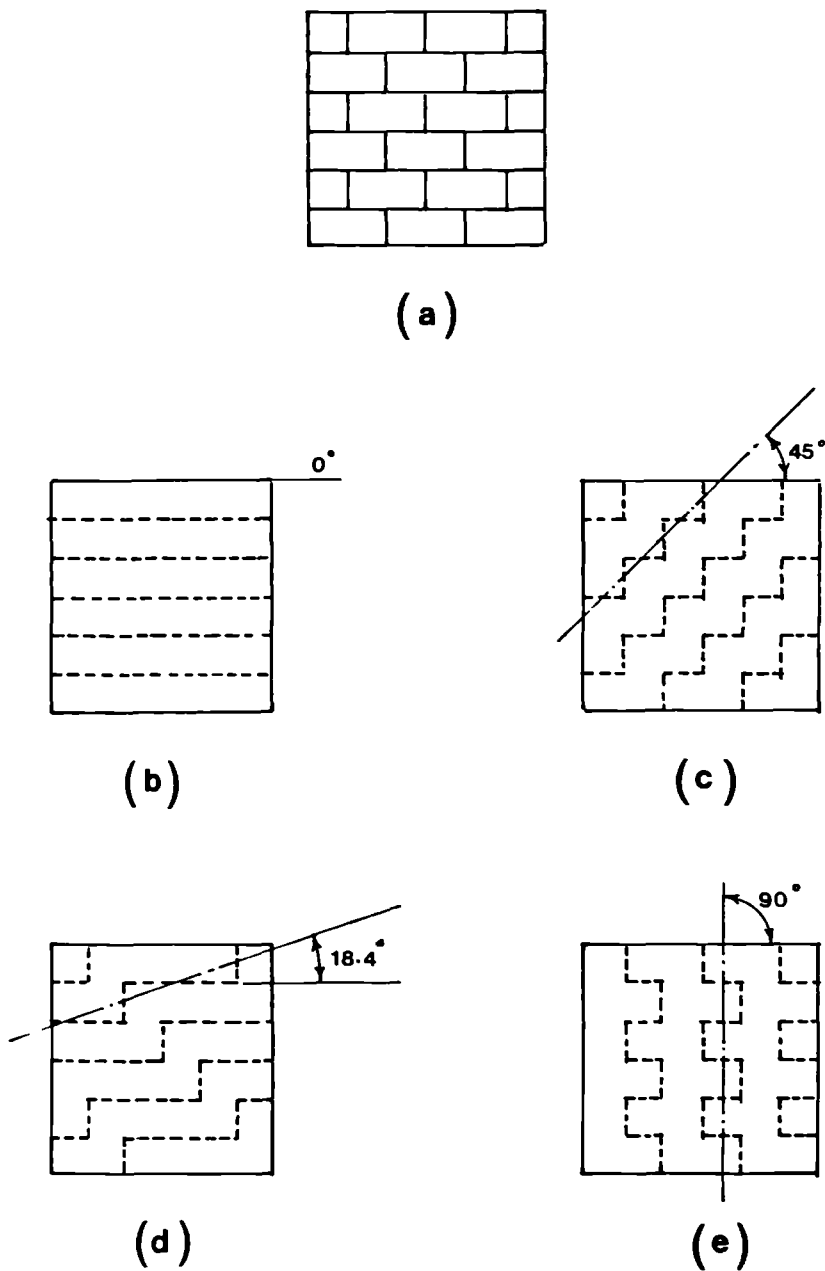
3.9.7 Super Element of Masonry

The size of the stiffness matrix could, be further reduced using a super element of masonry, provided that such an element can be developed. The idea is that, if the mechanical properties of interface elements can be included into the masonry-equivalent elements discussed in Section 3.9.6, a super element of masonry is created. Such an element must have a set of potential crack planes as shown in Fig 3.10.

Development of a super element of masonry was found to be rather complicated and was not pursued. It is worth attempting sometime in the future because masonry walls can then be subdivided into any type of isoparametric element providing a considerable economy to the finite element analysis of masonry structures.

3.9.8 Conclusions on the Choices of Masonry Elements

Comparison of the six choices discussed in Sections 3.9.2 to 3.9.7 shows that, should a non-linear elastoplastic analysis up to complete failure of masonry beyond cracking and joint failure be carried out, the choice of masonry-equivalent element surrounded by interface elements with only 12 degrees of freedom per masonry unit described in Section 3.9.6, appears to be a practical and economical finite element representation of masonry walls. This type of element and masonry subdivision has first been used by Page⁽⁸⁶⁾ in 1987.



Note: 2 more discontinuity angles exists; which are similar to (d) and (c) with -ve slope.

Figure 3.10 The Modes of Joint Failure in a Masonry Super Element; (a) concrete block masonry, (b) failure through bed joints and (c,d,e,) failure through bed and head joints

3.10 Interface Discretization

3.10.1 General

The significance of the behaviour of the frame-infill interface was discussed in section 2.2. The mechanical properties of interfaces are described in Chapter 4. In this section, only the geometry of the interfaces is discussed.

The geometry of interfaces was first modeled by Goodman⁽⁴¹⁾ in 1968 for finite element analysis of rocks. The Goodman's interface element consists of a four-node element having 8 degrees of freedom and zero thickness. Since the stiffness matrix of this element resulted from a direct algebraic integration rather than the standard numerical summation, such an element can be considered to have only one sampling point representing the whole length of the interface held by the element.

An equivalent element but much simpler element than that of Goodman, is the well known two-node linkage element with four degrees of freedom used by Riddington⁽¹⁷⁾ and also by Liauw et al⁽²⁴⁾. Linkage elements have a variety of applications in the finite element method; eg. reinforcement-concrete bond problems, cracking and rock joints. The stiffness matrix of a linkage element is given in Section 3.10.2 as to provide a basic notation to the subject.

In this study, however, the popular linkage element was not satisfactory, as so many elements were required to obtain a detailed stress distribution diagram

over the length of contact between frame and the infill. Instead, a new four-node element with eight degrees of freedom was developed. Unlike the linkage and Goodman interface elements, the proposed element uses the standard numerical integration procedure and is capable of handling as many sampling points as desired along the interface element leading to accurate and detailed results with only a small number of elements. The algorithm of this element is given in Section 3.10.3.

3.10.2 Algorithm of Linkage Element

The application of linkage element was briefly pointed out in Section 3.10.1. Fig 3.11 illustrates the geometry of this element. The vectors of nodal forces, $\{F\}$, nodal displacements, $\{a\}$, and relative displacements, $\{e\}$, are also shown in Fig 3.11 and are expressed in matrix form as follows:

$$\{F\} = \begin{bmatrix} F_{x1} \\ F_{y1} \\ F_{x2} \\ F_{y2} \end{bmatrix}, \quad \{a\} = \begin{bmatrix} x_1 \\ y_1 \\ x_2 \\ y_2 \end{bmatrix}, \quad \{e\} = \begin{bmatrix} s \\ w \end{bmatrix}$$

The stiffness matrix of this element may be derived as described below.

The external work done by the vector of the nodal forces may be calculated as:

$$W = (1/2)s(F_{x2}-F_{x1}) + (1/2)w(F_{y2}-F_{y1}) \quad (3.25)$$

The internal work done at the interface may be written as:

$$U = (1/2)A(\tau s + \sigma_n w)$$

Substituting for τ and σ_n from Eq 4.172 gives:

$$U = (1/2)A(K_s s^2 + K_n w^2) \quad (3.26)$$

where, A , denotes the area of the interface held by the linkage element and τ and σ_n are the tangential and normal

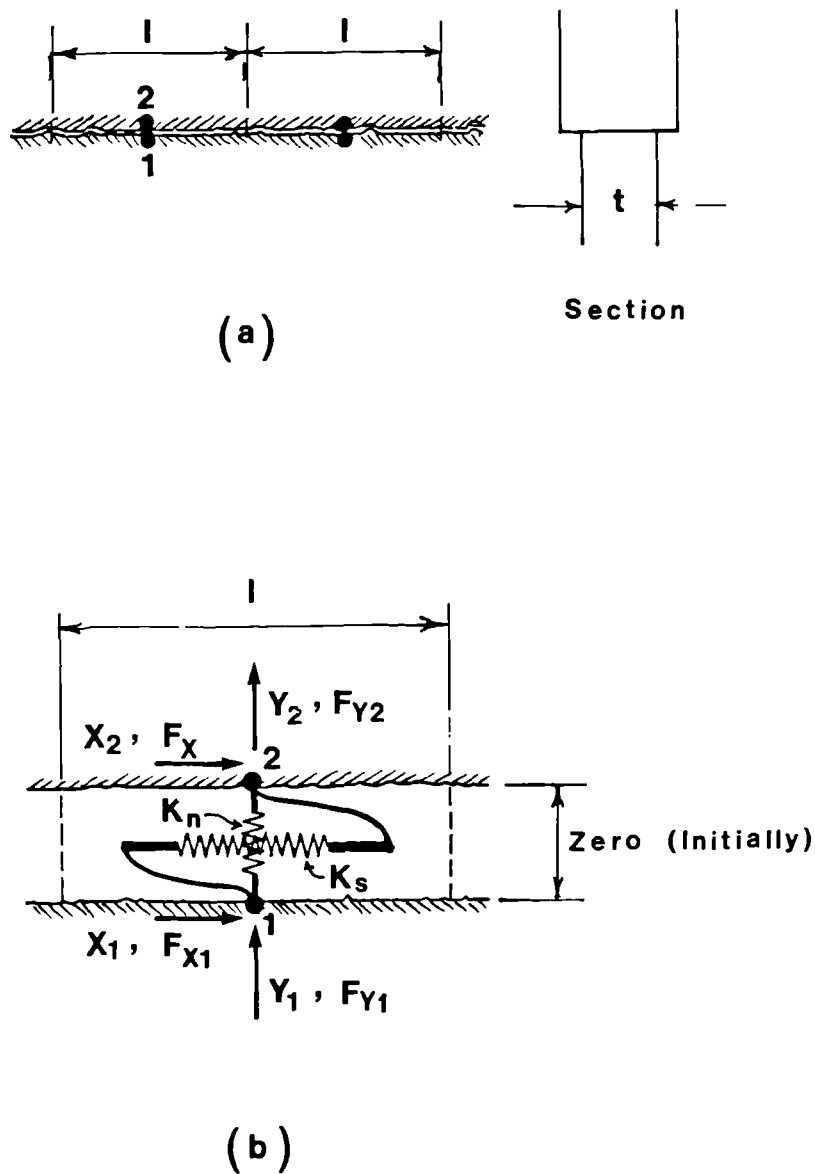


Figure 3.11 Modelling of an Interface by Linkage Elements

stresses uniformly distributed over this area. K_s and K_n are the tangential and normal stiffnesses of the interface expressed as Newtons per cubic millimeter (N/mm^3).

Substituting for the relative displacements, s and w , into Eqs 3.25, and 3.26, where:

$$s = X_2 - X_1 \quad \text{and} \quad w = Y_2 - Y_1$$

and equating these equations, gives:

$$(X_2 - X_1)(F_{x2} - F_{x1}) + (Y_2 - Y_1)(F_{y2} - F_{y1}) = A [K_s (X_2 - X_1)^2 + K_n (Y_2 - Y_1)^2]$$

Equating the independent terms from the both sides of the above equation leads to:

$$F_{x2} - F_{x1} = AK_s (X_2 - X_1)$$

$$F_{y2} - F_{y1} = AK_n (Y_2 - Y_1)$$

Allowing the external forces to act independently, the above equations result in:

$$F_{x1} = A(+K_s X_1 - K_s X_2)$$

$$F_{y1} = A(+K_n Y_1 - K_n Y_2)$$

$$F_{x2} = A(-K_s X_1 + K_s X_2)$$

$$F_{y2} = A(-K_n Y_1 + K_n Y_2)$$

which can be written in their matrix form as:

$$\begin{bmatrix} F_{x1} \\ F_{y1} \\ F_{x2} \\ F_{y2} \end{bmatrix} = A \begin{bmatrix} K_s & 0 & -K_s & 0 \\ 0 & K_n & 0 & -K_n \\ -K_s & 0 & K_s & 0 \\ 0 & -K_n & 0 & K_n \end{bmatrix} \begin{bmatrix} X_1 \\ Y_1 \\ X_2 \\ Y_2 \end{bmatrix}$$

$$\text{or: } \{F\} = [K]^e \{a\} \quad (3.27)$$

where $[K]^e$ denotes the stiffness matrix of the linkage element.

Since this linkage element permits only a uniform stress to develop over the area of the interface, a new interface element was developed as described in the following section.

3.10.3 Newly Developed Interface Element

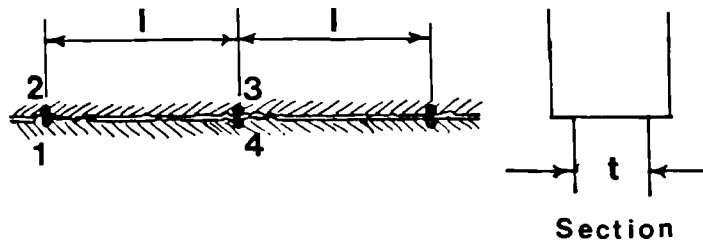
The stress and strain gradients along the length of contact between frame and the infill (especially within the regions close to the loaded corners) are significant. Therefore, a reasonably acceptable interface element should permit, at least, linearly variable relative displacements along the length of the element. Therefore a new interface element was developed to satisfy such requirement as described below.

Fig 3.12(a) shows a segment of a horizontal interface. This segment may be represented by a four node element and mapped into normalized co-ordinates with, originally, zero thickness as shown in Fig 3.12(b). Define s and w as the relative transversal and normal displacements of an arbitrary point along the interface. The proposed sign convention for s and w is given in Fig 3.12(c).

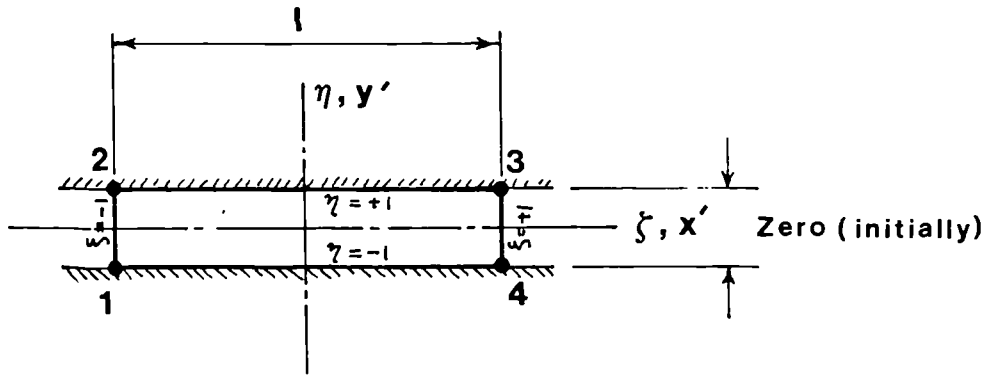
The relative displacements, s and w , may be related to the nodal displacements vector, $\{a\}$, as follows:

$$s = N_1X_1 + N_2X_2 + N_3X_3 + N_4X_4$$

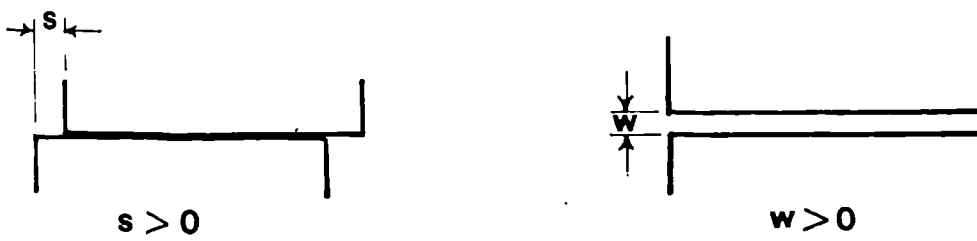
$$w = N_1Y_1 + N_2Y_2 + N_3Y_3 + N_4Y_4$$



(a)



(b)



(c)

Figure 3.12 Modelling of an Interface Segment by the Proposed 4-node Element; (a) actual geometry, (b) geometry of the proposed element, (c) sign convention

or:

$$\begin{bmatrix} s \\ w \end{bmatrix} = \begin{bmatrix} N_1 & 0 & N_2 & 0 & N_3 & 0 & N_4 & 0 \\ 0 & N_1 & 0 & N_2 & 0 & N_3 & 0 & N_4 \end{bmatrix} \begin{bmatrix} X_1 \\ Y_1 \\ X_2 \\ Y_2 \\ X_3 \\ Y_3 \\ X_4 \\ Y_4 \end{bmatrix}$$

or: $\{e\} = [N]\{a\}$ (3.28)

where N_1 to N_4 denote the relative displacement shape functions of node 1 to node 4 respectively, ie. N_i is the relative interface displacement at any point along the interface due to the nodal displacement of node i equals to unity. Since there are only two nodes on each side of the element, a set of linear shape functions best suit the relative displacements of the interface. Such shape functions are proposed as:

$$N_1 = -(1/2) (1-\xi)$$

$$N_2 = +(1/2) (1-\xi)$$

$$N_3 = +(1/2) (1+\xi)$$

$$N_4 = -(1/2) (1+\xi)$$

or generally expressed as only one equation:

$$N_i = (1/2)\eta_i(1+\xi\xi_i)$$
 (3.29)

where ξ_i and η_i are the normalized co-ordinates of node i .

The external work done by the nodal forces vector, $\{F\}$, can be written as:

$$W = (1/2)\{a\}^T\{F\}$$
 (3.30)

where:

$$\{a\}^T = \{x_1, y_1, x_2, y_2, x_3, y_3, x_4, y_4\}$$

and

$$\{F\}^T = \{F_{x1}, F_{y1}, F_{x2}, F_{y2}, F_{x3}, F_{y3}, F_{x4}, F_{y4}\}$$

The internal work done over the area of the interface can be written as:

$$U = (1/2) \int_A \{e\}^T \{\sigma\} dA$$

or:

$$U = (1/2) t \int_0^1 \{e\}^T \{\sigma\} dx \quad (3.31)$$

The stress vector, $\{\sigma\}$, is related to the relative displacements, Eq 4.172, as follows:

$$\{\sigma\} = \begin{bmatrix} \tau \\ \sigma_n \end{bmatrix} = \begin{bmatrix} K_s & 0 \\ 0 & K_n \end{bmatrix} \begin{bmatrix} s \\ w \end{bmatrix}$$

or:

$$\{\sigma\} = [D] \{e\} \quad (3.32)$$

Substituting for $\{\sigma\}$ from Eq 3.32 into Eq 3.31 and converting the integral into the normalized coordinates leads to:

$$U = (1/4) t \int_{-1}^{+1} \{e\}^T [D] \{e\} d\xi \quad (3.33)$$

Substituting for $\{e\}$ from Eq 3.28 and equating to Eq 3.30 gives:

$$(1/2) \{a\}^T \{F\} = (1/4) \{a\}^T \left[t \int_{-1}^{+1} [N]^T [D] [N] d\xi \right] \{a\}$$

or:

$$\{F\} = \left[(1/2) t \int_{-1}^{+1} [N]^T [D] [N] d\xi \right] \{a\}$$

Defining:

$$\{F\} = [K]^e \{a\}$$

and solving for $[K]^e$ leads to:

$$[K]^e = (1/2) t \int_{-1}^{+1} [N]^T [D] [N] d\xi \quad (3.34)$$

where $[K]^e$ denotes the element stiffness matrix of the proposed element. When small nodal displacements is involved, $[D]$ must be replaced by $[Dt]$. In the form of numerical integration, the expression 3.34 becomes:

$$[K]^e = (1/2) t \sum_{i=1}^{i=n} H_i [N_i]^T [D_i] [N_i] \quad (3.35)$$

where H_i signifies the weight of the i th sampling point.

Using the same energy approach the **equivalent** nodal forces, $\{q\}^e$, can be derived as:

$$\{q\}^e = t \int_{-1}^{+1} [N]^T \{\sigma\} d\xi$$

and the numerical integration leads to:

$$\{q\}^e = (1/2) \int_{-1}^1 \sum_{i=1}^{i=n} H_i [N_i]^T \{\sigma_i\} \quad (3.36)$$

It should be mentioned that if only one sampling point is assigned to this element, it becomes identical to the linkage element.

The proposed element permits as many Gaussian integration points as required to be allocated within each element. This feature allows partial slip and/or partial separation within only one element. As will be shown in Section 5.5.5, the proposed linear interface element significantly enhances the simulation of the mechanical behaviour of an interface.

3.11 Frame Discretization

3.11.1 General

A frame can be subdivided into its components; beams, columns, and connection blocks. These components are normally subjected to bending moment, axial and shear forces. In computer aided analyses mainly for design purposes, frame members are normally replaced by 2-node bending elements with allowance for only their bending flexibility⁽³⁶⁾. King et al⁽⁴²⁾ and Liauw et al⁽²⁴⁾ used this standard beam element in their finite element analyses of concrete infilled steel frames. For infilled frame structures, however, such an element may not be acceptable even if the effect of either or both the axial and shear forces are included into the element algorithm for

the following reasons:

- a) By ignoring the thickness of the members and the resulting corner blocks at the beam-column connections, the geometry may be significantly different from that of the actual structure and this may affect the frame-infill interaction behaviour and,
- b) Should the material become partially non-linear and/or plastic somewhere in the beam element, a numerical integration across the element cannot be carried out, because the integration is done algebraically over the depth of the element based on the assumptions of linear elasticity.

Therefore a planar element with finite thickness is needed so that the above requirements can be fulfilled.

An appropriate beam element may be sought within the family of isoparametric quadrilateral elements shown in Fig 3.5(b, c, d). Riddington⁽¹⁷⁾ used the 4-node linear elements packed into two rows as shown in Table 3.1. It has been shown⁽³⁶⁾ that such a simple element cannot simulate the curvature induced by bending, its deflection is 40% less and its bending and shear stresses are approximately four times greater than those resulting from beam theory⁽³⁸⁾, Table 3.1. Riddington ignored these discrepancies, perhaps, because he specifically concentrated on the axial deformation of the frame members.

The efficiency and accuracy of the results would, however, rapidly improve by using a more sophisticated element within the family of isoparametric quadrilateral

elements including some non-standard elements such as 6 and 10-node elements, whose shape functions can be derived with minor effort (36). This was investigated by carrying out a number of trial analyses with different elements. Table 3.1 compares the finite element analysis results of a cantilever beam subdivided into variety of such elements with the result obtained from the well known elasticity theory described by Timoshenko et al (38). Notice that this theory allows for the effects of shear deformation and the Poisson's ratio. Table 3.1 shows that 10-node element leads to fairly accurate results with allowance made for parabolic shear strain distribution across the beam. Its computation time, however is approximately 6 times greater than that of the 4-node element used by Riddington (17).

Attempts to develop an efficient beam element have led to:

- a) a 6-node non-conforming rectangular element developed by Wilson et al (44) in 1973 and
- b) the proposed 6-node element developed by the Author.

These are discussed in sections 3.11.2 and 3.11.3 respectively.

3.11.2 Non-Conforming Rectangular Element

Wilson et al (44) introduced two additional displacement shape functions to the linear quadrilateral element, as illustrated in Fig 3.13(b, c). The new element became a 6-node element with corner-node shape functions of:

$$N_i = (1/4) (1 + \eta \eta_i) (1 + \xi \xi_i) \quad (3.37)$$

and two imaginary internal independent nodes with the following shape functions.

$$N_5 = (1 - \xi^2) \quad (3.38)$$

$$N_6 = (1 - \eta^2) \quad (3.39)$$

Clearly, the deformations between the adjacent elements are non-conforming. Table 3.1 shows that by using this type of element, the computed deflections and stresses for the cantilever beam example considerably improves in comparison with the conforming linear 4-node element. The deflections are only 2% lower than the exact values calculated by beam theory.

Further tests on the above element showed⁽³⁶⁾ that when the cantilever beam is loaded in such a way that no shear force is produced in the beam, the computed deflection would become much closer to the exact value indicating that this element does not allow for shear deformation.

It is also worth mentioning that the parabolic shape functions N_5 and N_6 do not comply with the true bending curvature of that segment of the beam which contains a point of inflexion. Points of inflexion are always expected in frame members especially close to the loaded corners.

In order to ensure allowance for shear deformation and to maintain the true beam curvature, a new beam element was developed as described in the following section.

3.11.3 Proposed Rectangular Beam Element

Included in Table 3.1, is also a newly developed planar quadrilateral element with two internal independent nodes and eleven displacement degrees of freedom in total. The algorithm for this element is described in Appendix D.

As shown in Table 3.1, the proposed 6-node beam element is the most suitable element. Its computation time has proved to be about 4 times less than that of 10-node element which is almost equally sophisticated. Further, unlike the 10-node element the 6-node proposed beam element can readily handle more than two columns of gaussian integration points -reader may refer to Zienkiewicz⁽³⁶⁾ for the requirements concerning the optional number of gaussian points. This is of **great** significance in this particular study, since bending moments within the frame members, especially close to the loaded corners are highly variable. Therefore a greater number of gaussian points are needed so that the plastic hinges to occur in their right location and in the right time.

Flexibility of the proposed element in selecting the number of gaussian points permits the number of elements and consequently the computation time to be reduced dramatically. For example, the cantilever beam shown in Table 3.1 can be solved by only one beam element with 10 columns of gaussian points. However, in a non-linear elastoplastic analysis such a dramatic reduction in the number of elements is not recommended, because events such as occurrence of a plastic hinge or major local cracking or crushing produce abrupt changes in slope of the beam which

is not compatible with the continuous shape functions of the proposed beam element.

As will be shown in Chapter 5, a reasonable number of beam elements in the analysis of a reinforced concrete beam, loaded to destruction, will simulate the experimental behaviour.

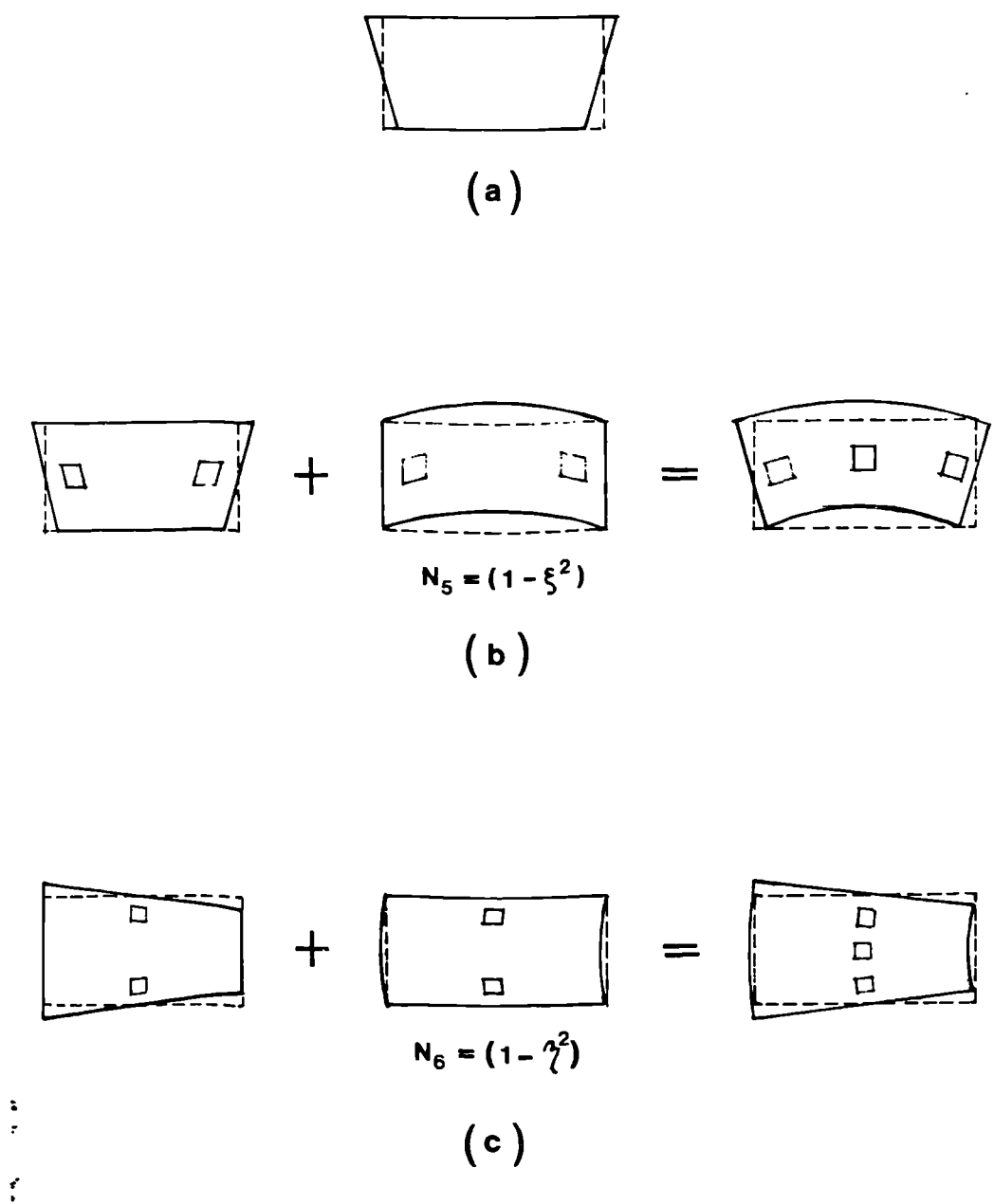

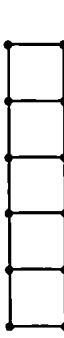
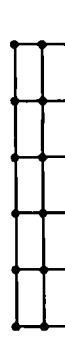


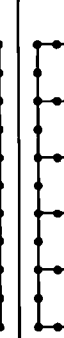

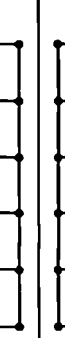


Figure 3.13 Wilson et al⁽⁴⁴⁾ Non-Conforming Beam Element; (a) 4-node linear element as a beam element and (b,c) converting into Wilson et al beam element

Table 3.1 Comparison of Different Types of Element as a Beam Element

Subdivision mesh pts.	Element Type	d	s	S.D.D	CP Time-index	Relevant No. of gauss
	Beam Theory	1.000	1.000	P		
	4-Node Linear	0.592	4.6	U	30	1X 2 (or more)
	4-Node (2 rows)	0.630	4.0	U	50	1X 1 (or more)
	6-Node	0.956	1.000	U	130	2X 2 (or more)
	8-Node	0.995	1.000	U	200	2X 2 (or more)
	10-Node	0.998	1.000	P	350	2X 3 (or more)
	6-Node Wilson (44)	0.985	1.000	U	130	2X 2 (or more)
	6-Node Proposed	1.000	1.000	P	100	2 (or more)X 3 (or more)

Notes: S.D.D =Shear Distribution Diagram, U =Uniform, P =Parabolic,
d =Deflection and
s =Average Shear Stress over the cross section of the beam

3.12 Choice Of Masonry Infilled Frame Subdivision

Blockwork infilling walls of single storey normally consist of at least 12 courses of blockwork. The exact subdivision of such a masonry panel into single block elements, when the masonry equivalent and interface elements described in Sections 3.9.6 and 3.9.8 are used, involve $12 \times 6 \times 12 = 864$ nodal displacements, added to which there are the nodal displacements of the boundary frame. Solution of such a high number of equations several times in a non-linear elastoplastic analysis is uneconomical.

The computation time of the problem can be reduced, however, by the choice of a subdivision mesh based on imaginary larger masonry units and proportionally thicker mortar joints and consequently lesser number of courses of blockwork, while keeping the size of the panel unchanged. This choice is acceptable provided that such a subdivision mesh is still fine enough to maintain a reasonable accuracy of stress distribution and also not to change the state and pattern of the cracks and the state of bed and head joints.

In order to select a suitable subdivision mesh some elastic finite element analyses were carried out on 12, 10, 8 and 4-course blockwork infills allowing for no joint failure. The results are plotted in Fig 3.14 comparing the stress distribution along the infill diagonal and the frame-infill boundary for the examples tested. As shown, the results of 12 and 10-course blockwork infills are identical showing that these meshes are sufficiently fine. The results of 8-course blockwork infill is in a fairly good agreement with

those of 12 and 10-course blockwork infills. However, a 4-course blockwork panel led to very poor results.

Although 8-course masonry infill subdivision is sufficiently fine as far as the degree of accuracy of stress distribution is concerned, its bed and head joints failure pattern leads to a slightly different pattern from that of the 12-course blockwork infill. Such a difference can be seen from Fig 3.15. As shown the difference is minor and does not affect any conclusion that one may come to.

The number of gaussian integration points had a slight effect on the computed stresses of the infill. However, in a non-linear elastoplastic analysis of such an infill, it is convenient to provide sufficient number of gaussian points within the elements that are likely to be subjected to plasticity, cracking or a high stress gradient.

The above examination showed that a single panel of 12-course blockwork can be scaled into an 8-course blockwork panel without any harmful effect. Having reduced the number of courses from 12 to 8 the computation time would decrease by about 6 times. Fig A.2 shows an 8-course masonry infill subdivision.

⋮
⋮
⋮

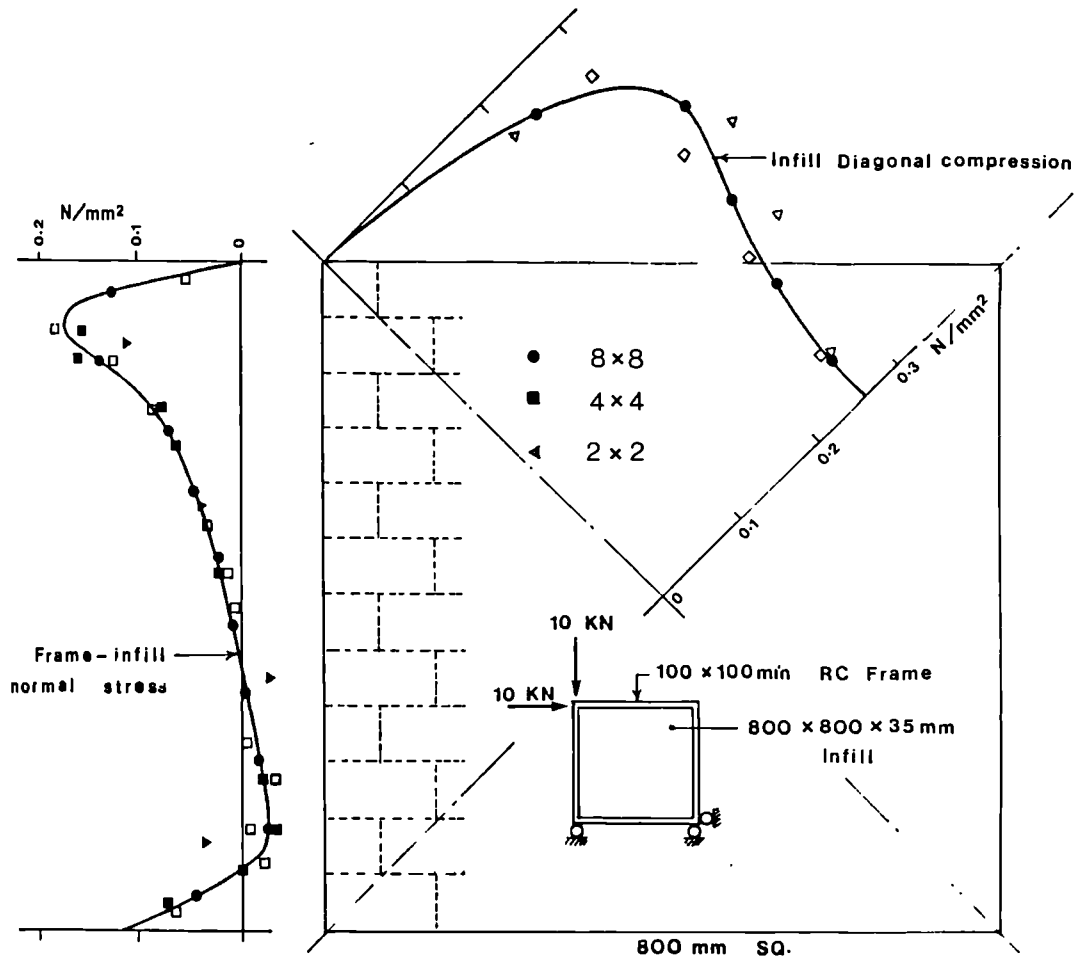


Figure 3.14 Linear Elastic Analysis of Infilled Frame with Various Subdivision Mesh

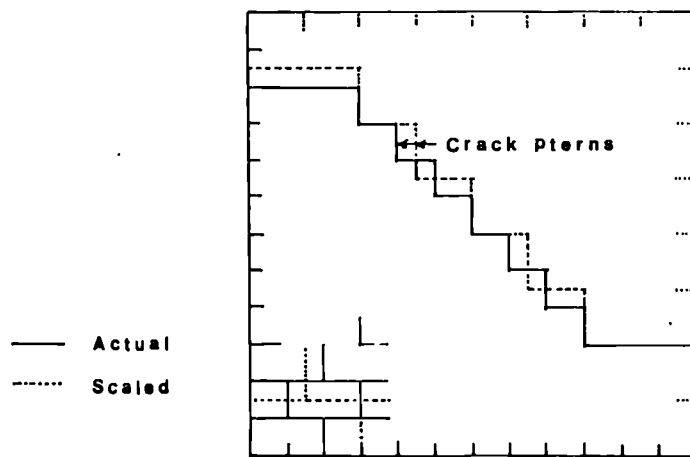


Figure 3.15 Effect of Scaling The Size of Masonry Elements on The Typical Infill Crack Pattern

3.13 Choices of Concrete Infilled Frame Subdivision

The same infill as studied in the previous section was examined for 4 and 8-node element subdivisions with different choices of gaussian integration points as listed in Table 3.2:

Table 3.2 Choices of Infill Subdivision

Division	Element	Gaussian pts.
8x8	4-node	1
8x8	4-node	2x2
4x4	8-node	2x2
2x2	8-node	2x2

The infill assumed **is** made of a uniform material with the same stiffness properties as those of the masonry infill discussed in section 3.12. The results of diagonal and vertical stresses are plotted in Fig 3.14 to compare with the results corresponding to the 12-course blockwork infill plotted in this Figure. As shown, the results of an 8x8 subdivision of 4-node element with 2x2 gaussian points gives the best results. However, the 4x4 subdivision of 8-node (parabolic) elements do not suit the high gradient double curvature stress diagrams near the loaded corners. An even more efficient mesh may be generated by allowing for finer elements in the vicinity of the loaded corners as shown in Fig A.4. The choice of concrete infill subdivision will, further, be studied in Section 5.5.5.

CHAPTER FOUR

Constitutive Formulation of Materials

4.1 General

The F.E formulation has been described in Chapter 3. Calculation of the incremental stress-strain relation matrix, $[D_t]$, and also the current stress vector, $[\sigma]$, in terms of the current strains and loading history are dependent on the mechanical behaviour of the materials which is discussed in this chapter.

The mechanical behaviour of the material normally used in infilled frames are non-linear and elastoplastic. The significance of the effect of non-linearity and plasticity of material in the analysis of infilled frames has been discussed in Chapter 2 and the various sources of non-linearity has been **outlined** in Table 2.2. It has also been concluded in Section 2.9, that an acceptable infilled frame analysis must be enhanced by a set of fairly accurate material models so as to simulate the elastoplastic behaviour of the constituents of the structure (frame and infill) as well as the interface between these constituents. Since different materials behaves differently, the commonly used materials may be categorized into the following groups;

- i) Brittle materials; concrete and masonry.
- ii) Ductile materials; steel
- iii) Interfaces; the joints between masonry units and the infill/frame interface.

Sections 4.2 to 4.8 deal with brittle materials and sections 4.9 and 4.10 deal with ductile materials and interfaces respectively.

4.2 The Existing Fracture Models

The several existing constitutive formulations can be categorized into six groups as shown in *Figs 4.1 to 4.5* as listed below;

- i) Linear elasticity theory (Fig 4.1)
- ii) Non-linear elasticity fracture model (Fig 4.2)
- iii) Elastic-perfect plasticity fracture model (Fig 4.3)
- iv) Elastic-work hardening plasticity fracture model (Fig 4.4)
- v) Endochronic plasticity theory
- vi) Representation of given experimental data using curve fitting method, interpolation or mathematical function, (Fig 4.5).

The existing theories based on the models of group (i) to (iv) are described in detail by Chen⁽³⁹⁾. The linear elasticity theory, Fig 4.1, is the most commonly used material model. This model ignores non-linearity and plasticity of the material and is normally used for analysis of the elements of the structure which are loaded within the range that would not undergo any plasticity or failure.

The models of groups (ii) to (iv), illustrated in Figs 4.2 to 4.4 respectively, are based on idealization of material by an elastic or plastic model. These models are neither exact nor impressively accurate but even so they may be rather complicated. Because of the idealization of the behaviour of the material, these models are discontinuous material models dividing the material responses into several stages. However, the actual behaviour of a non-cracked material is continuous. Further, such discontinuous models, while simplifying the problem, are the source of numerical difficulties⁽³⁹⁾. Nevertheless the elastic-perfect plasticity fracture model (for both tension and compression) suits steel material. This will be discussed in section 4.9.

The endochronic theory has received much attention in recent years because it is based on a continuous model. This model was originated by Valanis⁽⁴⁵⁾ (1971) for metal, based on the concept of "Etrinsic time." The theory does not require a specific definition of yielding. Bazant⁽⁴⁶⁾ (1976) extended the theory to describe the behaviour of brittle materials. For concrete, the formulation of the endochronic model is based on an extensive set of functions which fit nearly all the experimentally observed effects. However, "this model involves a rather high number of material parameters. Therefore further research in refining this theory is needed," Chen⁽³⁹⁾.

Since the aforesaid purely theoretical models involve extensive numerical work, in practice, either a simple uniaxial model is generalized to form a three-

dimensional model or one of the methods of group (vi) is used. The methods in this group are not related to any specific theory, but experimental observations and may therefore be expected to provide the best accuracy. These methods have mostly been developed for biaxial behaviour of material (plane stress problems). The most efficient method of this group seems to be the analytical method of Darwin and Pecknold⁽⁴⁷⁾, (1977), developed for concrete in plain stress problems. Fig 4.5 illustrates this model. In this method, the concept of equivalent uniaxial strain, described in section 4.6.2, is utilized. It is also assumed that concrete behaves as an orthotropic material with a variable Poisson's ratio. However the variation of Poisson's ratio under biaxial compression stress is ignored and the formulation involves a significant discrepancy between the proposed values of Poisson's ratio when the state of biaxial stress combination alters from compression-tension to compression-compression. Nevertheless Darwin and Pecknold's method reasonably predicts the actual behaviour of concrete under biaxial loading and a number of F.E. programs have been written using this method^(48,49). Because of the assumption of orthotropy, it is very difficult to expand this method for triaxial loading. In this project, however, it was decided to develop a new constitutive formulation for brittle materials using the concept of "Equivalent Uniaxial Strain", EUS. The proposed model allows for triaxial loading but ignores the orthotropy of uncracked materials. The new proposed model will be described later in this chapter.

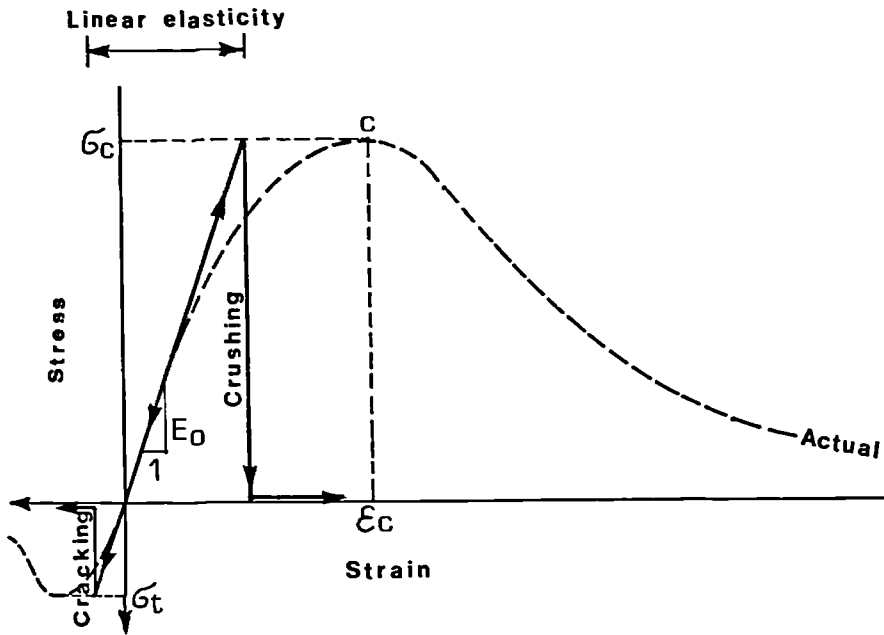


Figure 4.1 Linear Elasticity Fracture Model

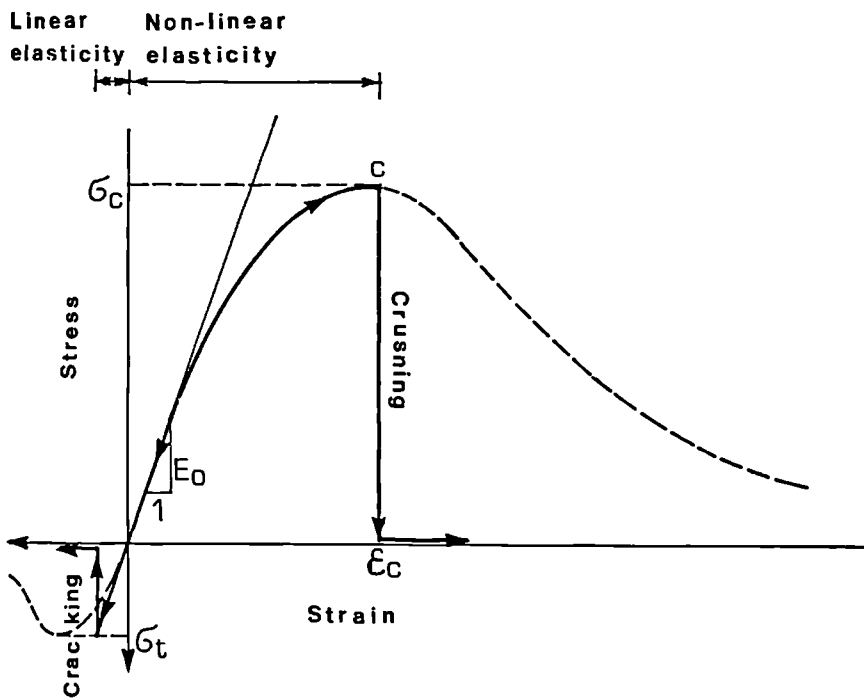


Figure 4.2 Non-Linear Elasticity Fracture Model

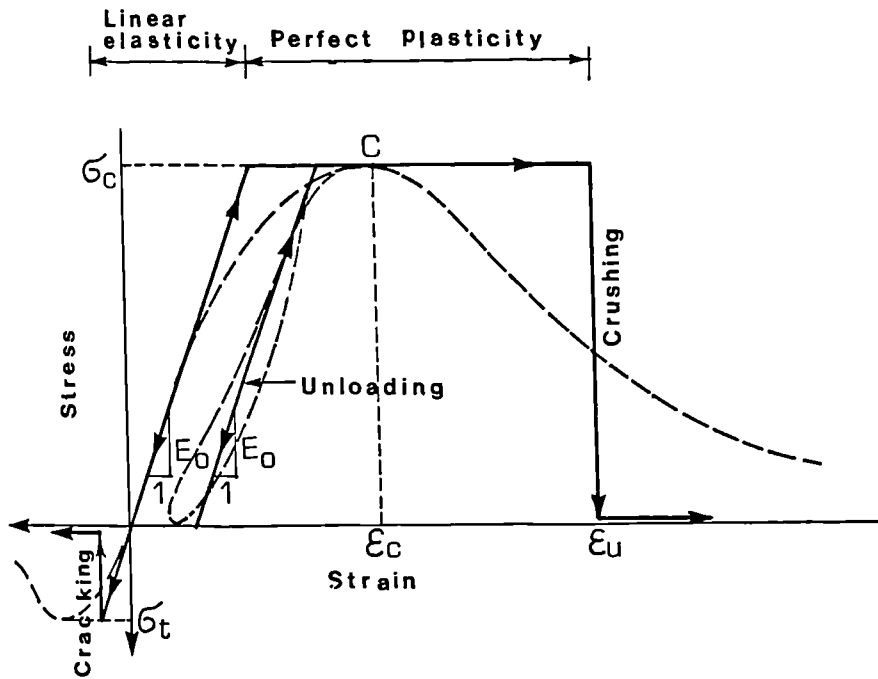


Figure 4.3 Elastic Perfect Plasticity Fracture Model

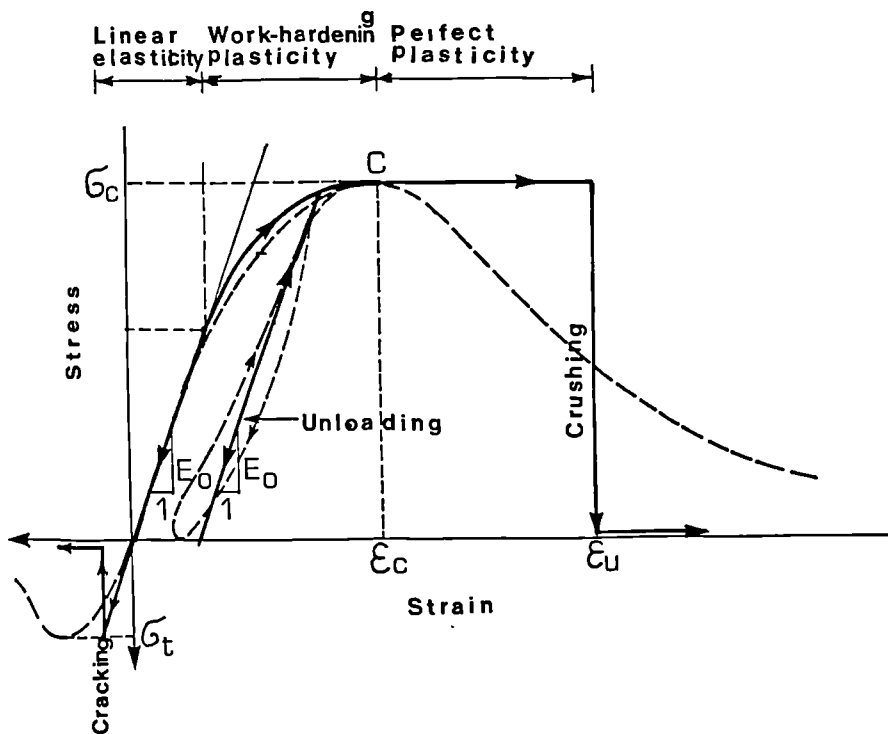


Figure 4.4 Elastic Work-Hardening Plasticity Fracture Model

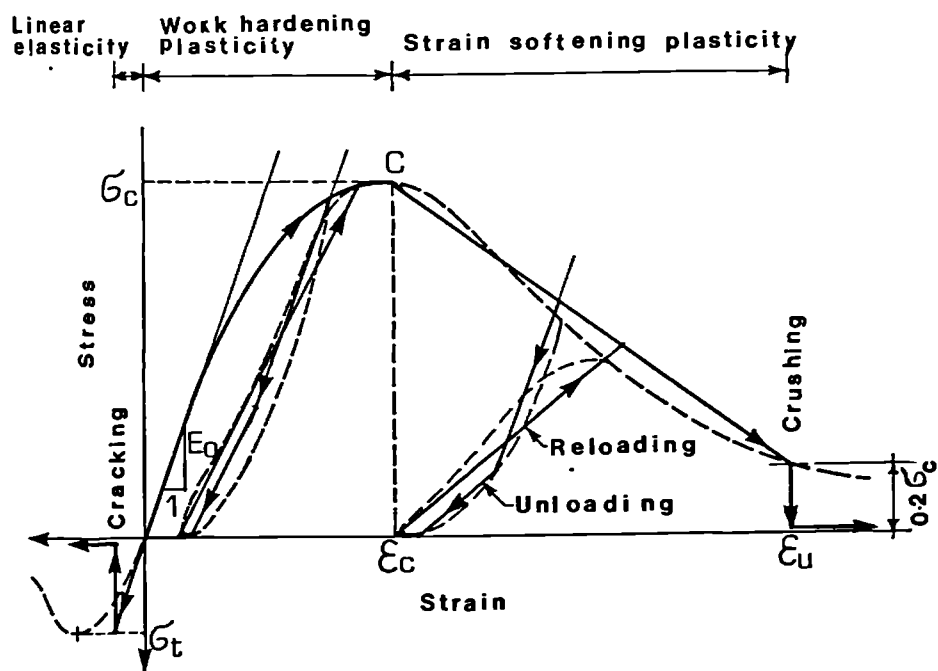


Figure 4.5 The Elastoplastic Fracture Model of Darwin and Pecknold(47)

4.3 Proposed Constitutive Formulation for Brittle Materials Under Uniaxial Compression

4.3.1 Stress-Strain Relation

The typical stress-strain relationship for concrete subjected to uniaxial compression is shown in Fig 4.6(a). Concrete has a nearly linear-elastic behaviour up to about 30 percent of its compressive strength σ_c . For stresses above this point the stress-strain curve shows a gradual increase in curvature up to the peak point, σ_c , due to extension of microcracks. Beyond this peak, the stress-strain curve has a falling branch until crushing failure occurs at some ultimate strain, ϵ_u .

Wischers⁽⁵⁰⁾ (1978) carried out a series of uniaxial loading tests on necked specimens in order to exclude the confinement effect of the end platens. The results of these tests are plotted in Fig 4.7. As shown the shape of the stress-strain curve is similar for concrete of low, medium and high strength. However, a high-strength concrete behaves in a more brittle manner, the stress dropping off more sharply than it does for concrete with lower strength.

For the rising branch of the stress-strain curves, the well known Saenz⁽⁵¹⁾ equation may be adopted as follows;

$$\sigma = E_0 \frac{\epsilon}{1 + \left(\frac{E_0}{E_c} - 2\right)\left(\frac{\epsilon}{\epsilon_c}\right) + \left(\frac{\epsilon}{\epsilon_c}\right)^2} \quad (4.1)$$

where σ and ϵ are the stress and strain and E_0 and E_c ($E_c = \sigma_c / \epsilon_c$) are the initial tangent and secant modulus at

peak respectively and ϵ_c is the strain at peak stress.

Eq 4.1 for $E_0/E_c < 2$ gives an unrealistic point of inflexion somewhere on the curve. The following proposed equation thus may be used when $E_0/E_c < 2$;

$$\sigma = E_0 \frac{\epsilon}{1 + \left(\frac{E_0}{E_c} - 1\right) \left(\frac{\epsilon}{\epsilon_c}\right)^g} \quad (4.2)$$

where

$$g = \frac{1}{1 - E_c/E_0} \quad \text{and} \quad \frac{E_0}{E_c} < 2 \quad (4.3)$$

It should be noted that for $E_0/E_c = 2$ equations 4.2 and 4.1 are identical, thus continuity between the two is maintained.

For the falling branch of the stress-strain curve, several observations and data (50 to 60) and especially the work of Wischers (50), Fig 4.7, were studied and compared, to derive the following proposed simple equation:

$$\sigma = \frac{\sigma_c}{1 + D \left(\frac{\epsilon}{\epsilon_c} - 1\right)^2} \quad (4.4)$$

where for concrete:

$$D = 10 \left(\frac{\sigma_c}{100}\right)^{2.15} \leq 0.25 \quad (4.5)$$

It should be mentioned that Eq 4.4 is independent of the initial stiffness of the material. The tangent value of the modulus of elasticity, E_t , may be derived by differentiation of Eqs 4.1, 4.2 and 4.3 in terms of ϵ for $E_0/E_c > 2$ as:

$$E_t = \frac{E_0 \left[1 - \left(\frac{\epsilon}{\epsilon_c} \right)^2 \right]}{\left[1 + \left(\frac{E_0}{E_c} - 2 \right) \left(\frac{\epsilon}{\epsilon_c} \right) + \left(\frac{\epsilon}{\epsilon_c} \right)^2 \right]^2} \quad (4.6)$$

and for $E_0/E_c < 2$ as:

$$E_t = \frac{E_0 \left[1 - \left(\frac{\epsilon}{\epsilon_c} \right)^g \right]}{\left[1 + \left(\frac{E_0}{E_c} - 1 \right) \left(\frac{\epsilon}{\epsilon_c} \right)^g \right]^2} \quad (4.7)$$

and for the falling branch as:

$$E_t = \frac{-2E_c D \left(\frac{\epsilon}{\epsilon_c} - 1 \right)}{\left[1 + D \left(\frac{\epsilon}{\epsilon_c} - 1 \right)^2 \right]^2} \quad (4.8)$$

As shown in Fig 4.7 the proposed Eqs 4.1 to 4.5 agree well with a wide range of possible concrete and mortar strengths. These equations were not examined for brittle materials other than concrete and mortar but it seems only Eq 4.5 needs some adjustments should a brittle material other than concrete be used.

The above formulation requires only the initial tangent modulus, E_0 , and the strain at peak, ϵ_c , and the unconfined uniaxial strength, σ_c , to be determined by test or any other means for the complete uniaxial stress-strain curve to be plotted.

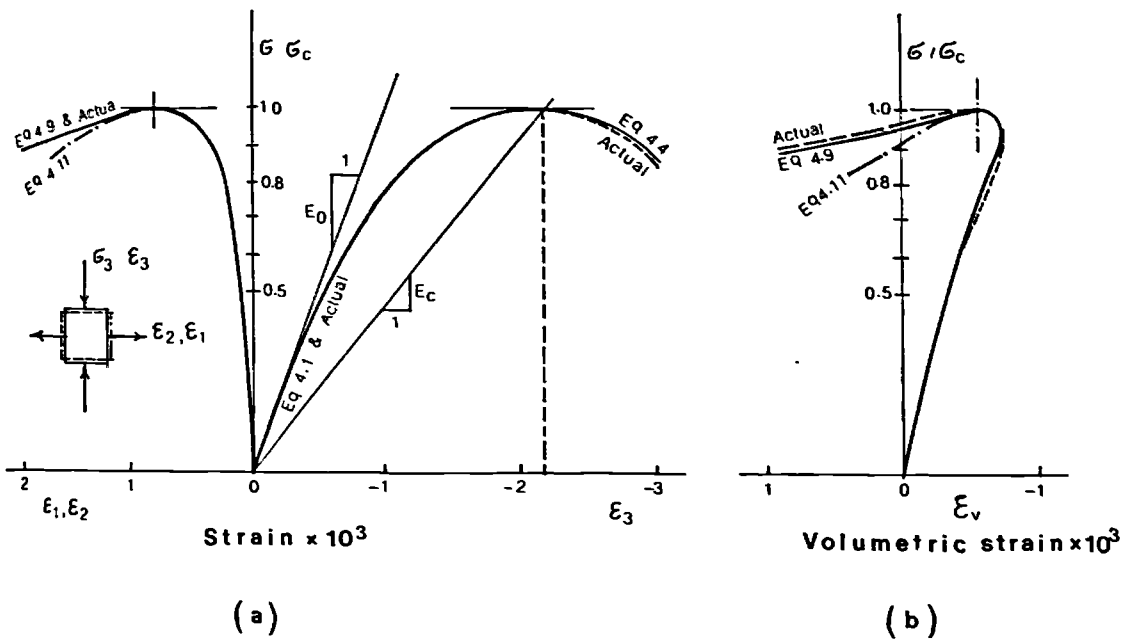


Figure 4.6 Comparison of the Proposed Formulation with experiments of Kupfer et al (55) for Concrete Under Uniaxial Stress;

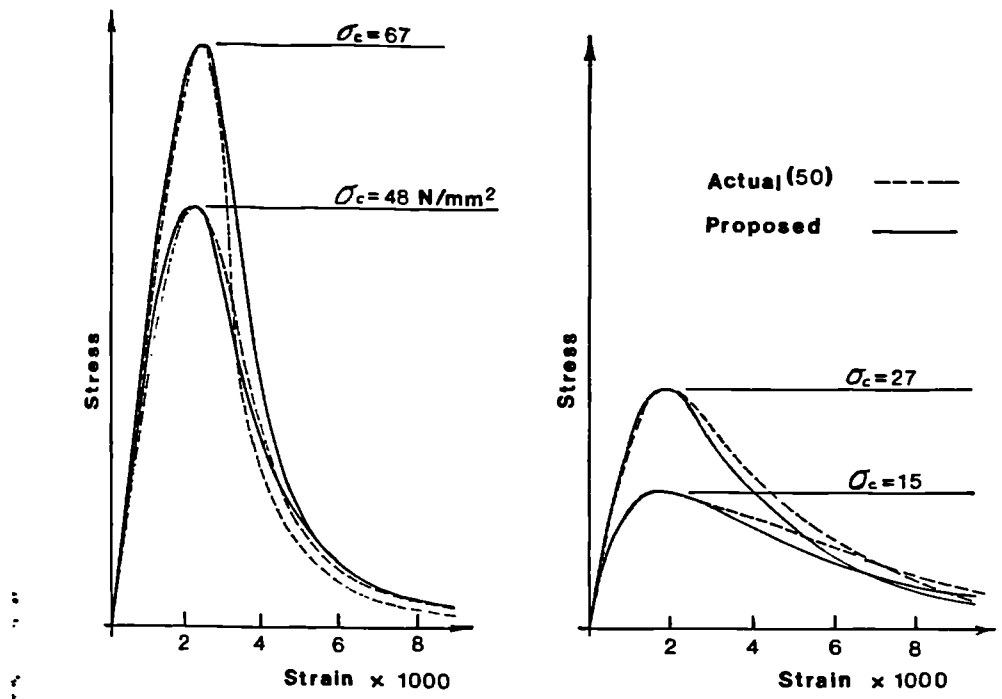


Figure 4.7 Comparison of Actual and Proposed Complete Stress-strain Curves of Concrete;

4.3.2 Poisson's Ratio

Poisson's ratio, ν , for concrete under uniaxial compression ranges from 0.15 to 0.22. The ratio ν remains constant until approximately 80 percent of σ_c or approximately $0.5\varepsilon_c$ at which stress (so called critical stress) the apparent Poisson's ratio begins to increase, Fig 4.6(a,b). At the peak stress, the Poisson's ratio increases up to about $2\nu_0$. Using the above experimental knowledge, the following formula was developed to represent the variation of Poisson's ratio in uniaxial loading;

$$\nu = \nu_0 \left[1 + k \left(\frac{\varepsilon}{\varepsilon_c} \right)^n \right] \quad (4.9)$$

Comparison of the experimental data of Kupfer et al(55) with Eq 4.9 led to $n = 3$ and $k = 0.85$ to obtain a good fit.

The incremental value of the Poisson's ratio may be derived as follows;

$$\nu^* = \frac{-d\varepsilon_r}{d\varepsilon} = \frac{d(\nu\varepsilon)}{d\varepsilon}$$

Substituting for ν from Eq 4.10 gives;

$$\nu^* = \nu_0 \left[1 + (n+1)k \left(\frac{\varepsilon}{\varepsilon_c} \right)^n \right] \quad (4.10)$$

where ε_r denotes the strain in the radial direction normal to the direction of the applied load.

Eq 4.10, beyond the peak load, gives a rather high value for the incremental Poisson's ratio. Although this is

evident in uniaxial compression test, in fact the apparent extensive volume expansion may be not so much due to yielding of the material as due to disintegration and lack of confinement. A small degree of confinement may greatly reduce the radial expansion of the specimen. Assuming a constant incremental Poisson's ratio beyond the peak stress, may be a realistic way to exclude the disintegration from the Poisson's effect. Therefore the following expressions replace Eqs 4.9 and 4.10 for ϵ/ϵ_c greater than unity.

$$v/v_c > 1.0 \quad \begin{cases} v^* = v_0 [1 + (n+1)k] \\ v = v_0 \left[1 + k \left(4 - 3 \left(\frac{\epsilon_c}{\epsilon} \right) \right) \right] \end{cases} \quad (4.11)$$

Fig 4.8 compares the equations 4.9 to 4.11 to the experimental results of Kupfer et al (55) showing a good agreement.

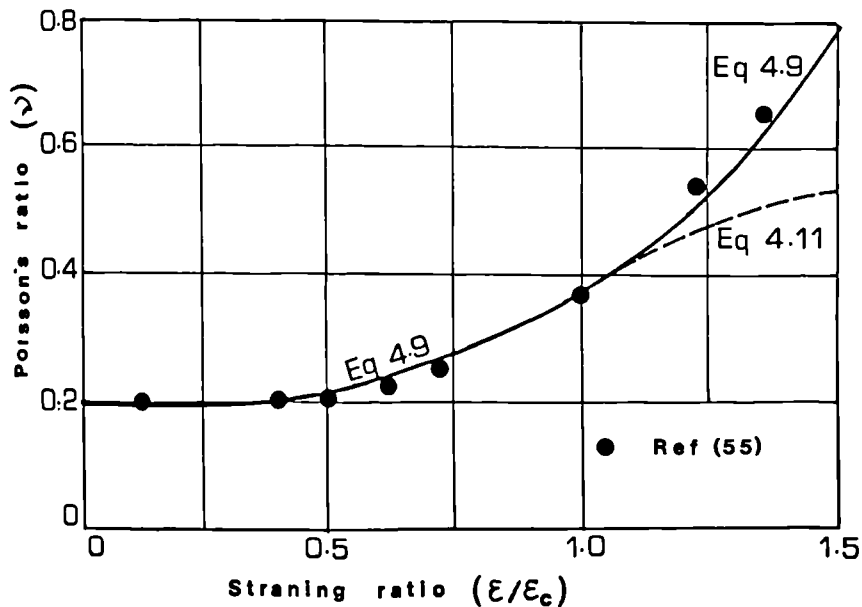


Figure 4.8 Comparison of the Proposed Poisson's Ratio with the Experimental Results of Kupfer et al (55)

4.3.3 Loading-Unloading-Reloading Behaviour

Previous work on this type of loading is limited to concrete and mortar under uniaxial load, (references 59 to 64). Work done by many investigators particularly Karsan and Jersa⁽⁶⁰⁾ led to the following information:-

- a) When a uniaxially loaded specimen of concrete is unloaded down to zero stress, the stress-strain diagram follows a curved line similar to **EP** in Fig 4.9. This induces some plastic residual strain, ϵ_p , as a result of energy dissipation and damage caused by preceding loading.
- b) When the specimen is reloaded, the stress-strain diagram follows a curve similar to **PR**. Where **R** is a point on the stress-strain curve beyond the unloading point, point **E**.
- c) The envelope of the stress-strain curve is not affected by any partial or complete previous unloading reloading cycle. Therefore the stress-strain curve in uniaxial monotonic loading is also called "The envelope curve" which is unique.

Karsan and Jersa⁽⁶⁰⁾ proposed the following equation to estimate the plastic residual strain induced after a full unloading.

$$\epsilon_p = \epsilon_c \left[0.145 \left(\frac{\epsilon_E}{\epsilon_c} \right)^2 + 0.127 \left(\frac{\epsilon_E}{\epsilon_c} \right) \right] \quad (4.12)$$

where ϵ_E is the strain corresponding to the point on the envelope curve at which strain unloading has been started.

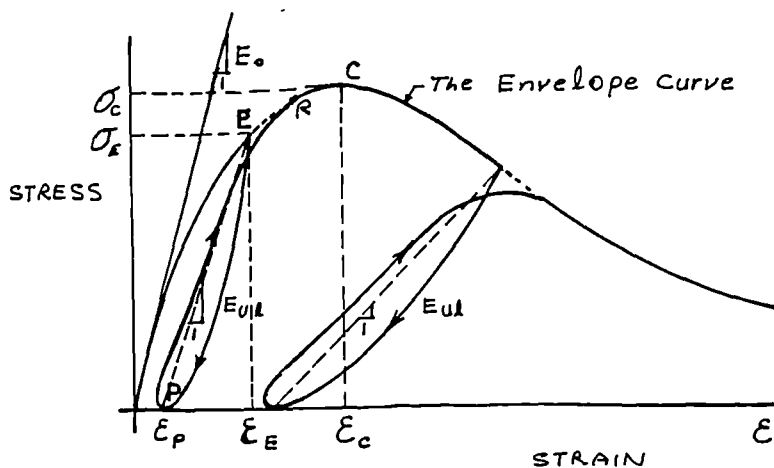


Figure 4.9 Concrete Under Unloading and Reloading

This equation agreed with the mean experimental results of concrete specimens with f'_c equal to 24.1 to 34.5 N/mm^2 .

The aforesaid assumption and Eq 4.12 were adopted by Darwin and Pecknold(49) and also Ghoneim, et al.(48) to develop a plane-stress and a three-dimensional F.E. analysis respectively. In these analyses, the unloading and reloading curves were simplified to multi-linear approximations as shown in Fig 4.5.

The unloading-reloading stress-strain diagram may also be idealized by the straight line of **EP** in Fig 4.9. The unloading and reloading modulus can thus be written as;

$$E_{ul} = \sigma / (\epsilon - \epsilon_p) \quad (4.13)$$

where σ and ϵ_p can be calculated from Eqs 4.1, 4.2, 4.4 and 4.12.

4.4 Brittle Materials Subjected to Uniaxial Tension

Concrete and other brittle materials behave in an almost linear-elastic fashion in tension. Therefore, in practice they are modeled by a linear-elastic-fracture model as shown in Fig 4.1. Previous work (55,64,65,66), however, shows that concrete under uniaxial tension undergoes some non-linearity and plasticity and the tensile stress-strain curve is similar to that for uniaxial compression. Eq 4.1 or 4.2 therefore, may also be used to represent the tensile stress-strain relationship provided that E_c and ϵ_c are replaced by E_{ct} and ϵ_{ct} respectively. Some experimental values for E_{ct}/E_0 are listed below from different sources;

Kupfer et al (55)	0.90
Tassuji et al (65)	0.65-0.70
Cook et al (64)	0.70-0.75
Evans et al (66)	0.40-0.60

These experimental values led to propose E_c as a value in between E_0 and E_c as follows:

$$\frac{1}{E_{ct}} = \frac{1}{2} \left(\frac{1}{E_0} + \frac{1}{E_c} \right) \quad (4.14)$$

For a medium strength concrete ($E_c \simeq 0.45E_0$), Eq 4.14 gives $E_{ct}/E_0 = 0.62$ which is the mean value of the last three of the above experimental data resulted from different test procedures. The strain corresponding to peak tensile stress, ϵ_{ct} , may now be calculated as follows:

$$\sigma_t$$

$$\epsilon_{ct} = \frac{\sigma_t}{E_{ct}} \quad (4.15)$$

Concrete and other brittle materials show little ductility in tension. The ultimate strain (the strain at the onset of cracking) is therefore, proposed to be limited to ϵ_{ct} beyond which strain concrete cracks in a plane normal to direction of the tensile stress and the tensile stress drops immediately to zero as shown in Fig 4.10.

Because of allowance for non-linearity, the above proposed model explains the cause of delay in cracking in the tensile region of the standard beams tested for determination of the modulus of rupture. The proposed model explains well the difference between the direct tensile strength and the modulus of rupture.

The Scanlon (67) model which is also shown in Fig 4.10, has received much attention in recent years for its ability to simulate the effect of tensile stiffening. But this model is unrealistic for unreinforced concrete.

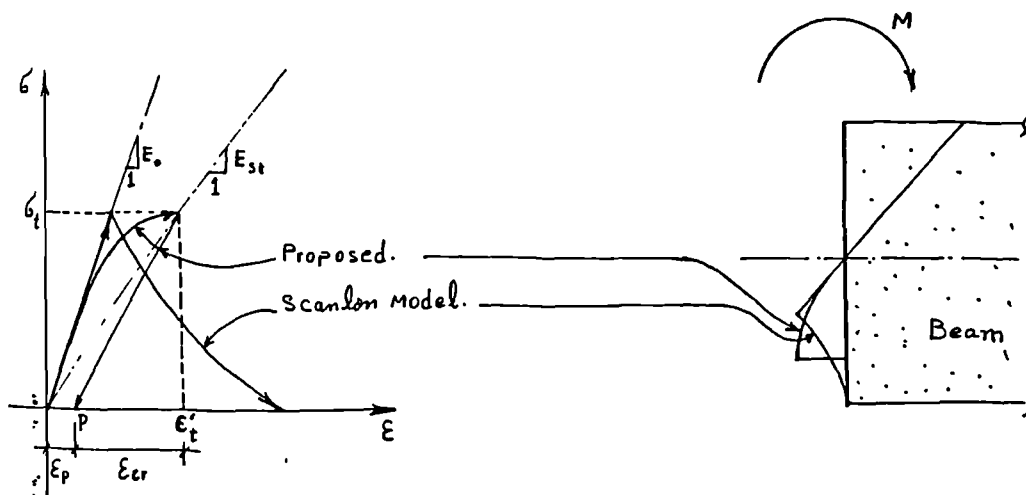


Figure 4.10 Stress strain Curve of Concrete in Tension

5 Failure Criteria

5.1 General

In formulating failure criteria for materials, a proper definition of failure must be defined. Criteria such as yielding, initiation of cracking, load-carrying capacity, and extent of deformation have been used to define failure. In this section failure is defined as the maximum load-carrying capacity of a test specimen or an element. The strength of materials under multiaxial stresses is a function of the state of stress and cannot be predicted by combination of simple compressive and shearing stresses independently of each other.

A failure criterion of isotropic materials based on state of stress must be an invariant function of the state of stress, ie, independent of the choice of the coordinate system by which stress is defined. One method of presenting such a function is to use the principal stresses ie,

$$f(\sigma_1, \sigma_2, \sigma_3) = K \quad (4.16)$$

indicate the general functional form of the failure criterion. It is known(39) that any invariant symmetric function of the state of stress can also be expressed in terms of the three stress invariants of I_1 , J_2 and J_3 or I_1 , J_2 and θ , where θ is the angle from the positive σ_1 axis which lies in the deviatoric plane, Chen(39). Thus one can replace Eq 4.16 by:

$$f(I_1, J_2, J_3) = K \quad (4.17)$$

or:

$$f(I_1, J_2, \theta) = K \quad (4.18)$$

where:

$$I_1 = \sigma_1 + \sigma_2 + \sigma_3 \quad (4.19)$$

$$J_2 = \frac{1}{6} \left[(\sigma_1 - \sigma_2)^2 + (\sigma_2 - \sigma_3)^2 + (\sigma_3 - \sigma_1)^2 \right] \quad (4.20)$$

$$J_3 = \frac{1}{3} (s_1^3 + s_2^3 + s_3^3) = s_1 s_2 s_3 \quad (4.21)$$

$$\theta = \cos^{-1} \left[\frac{2\sigma_1 - \sigma_2 - \sigma_3}{2\sqrt{3J_2}} \right], \quad \sigma_1 > \sigma_2 > \sigma_3 \quad (4.22)$$

$$\begin{aligned} s_1 &= \sigma_1 - \sigma_m & s_2 &= \sigma_2 - \sigma_m & s_3 &= \sigma_3 - \sigma_m \\ \sigma_m &= 1/3(\sigma_1 + \sigma_2 + \sigma_3) = I_1/3 \end{aligned} \quad (4.23)$$

Chen (39) has described several failure criteria developed by various investigators. The most commonly used ones are illustrated in Figs 4.11 and 4.12. These are algebraically expressed as follows:

i) Von Mises yield criterion;

$$f = 3J_2 - \sigma_y^2 = 0 \quad (4.24)$$

:

ii) Tresca yield criterion;

$$f = 2\sqrt{J_2} \sin(\theta + \pi/3) - \sigma_y = 0 \quad (4.25)$$

iii) Mohr-Coulomb failure criterion;

$$f = \frac{1}{3} I_1 \sin\phi + \sqrt{J_2} \sin(\theta + \pi/3) + \frac{\sqrt{J_2}}{\sqrt{3}} \cos(\theta + \pi/3) \sin\phi - c \cos\phi = 0 \quad (4.26)$$

where the material parameters of ϕ and c are the angle of friction and cohesion of the material respectively.

iv) Drucker-Prager failure criterion;

$$f = \alpha I_1 + \sqrt{J_2} - K = 0 \quad (4.27)$$

where:

$$\alpha = \frac{2 \sin\phi}{\sqrt{3}(3 - \sin\phi)} \quad \text{and} \quad K = \frac{6c \cos\phi}{\sqrt{3}(3 - \sin\phi)} \quad (4.28)$$

The Von Mises and Tresca yield criterion are well verified in metal plasticity. In this project the Von Mises criterion is adopted for steel frame members. For concrete and other frictional materials the Mohr-Coulomb and its approximation, Drucker-Prager failure criteria are frequently used in practice. In this project, however, since the above criteria are particular to concrete only, it was decided to develop new failure criteria for various stress combinations. The parameters involved in the proposed criteria are adjustable so as to suit the different brittle materials under consideration such as concrete, ^{and} blockwork mortar. These criteria are described in the following section.

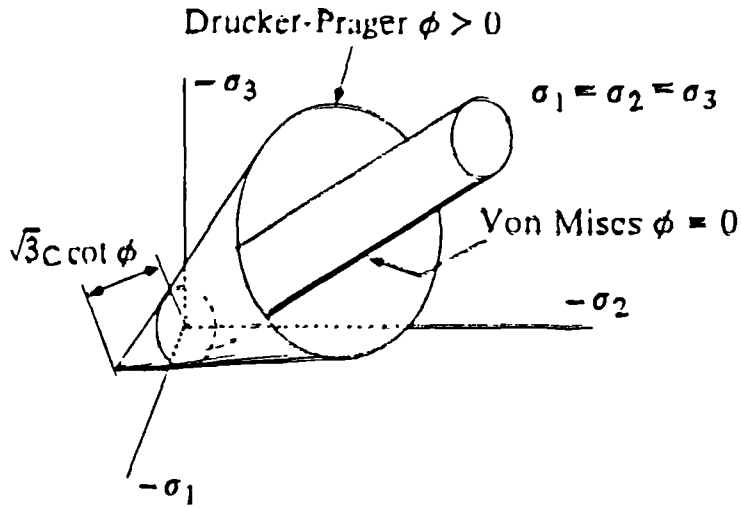


Figure 4.11 Drucker-Prager and Von Mises Yield Surface in Principal Stress Space (after Zienkiewicz (36))

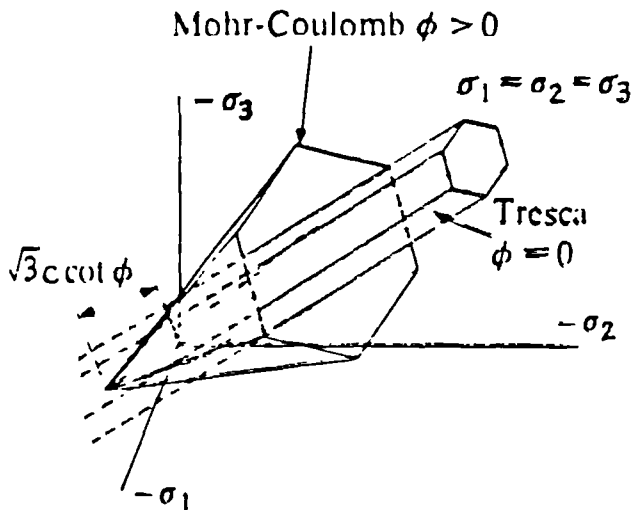


Figure 4.12 Mohr-Coulomb and Tresca Yield Surface in Principal Stress Space (after Zienkiewicz (36))

4.5.2 Proposed Failure Criterion of Brittle Materials under Triaxial Compression

Using the principal stresses, σ_1 , σ_2 and σ_3 while:

$$0 > \sigma_1 > \sigma_2 > \sigma_3 \quad (\text{comp. -ve})$$

The following stress function is proposed in order to incorporate the variation in material types;

$$f = \frac{(\sigma_3 - \sigma_2)^2}{\left[1 + c \left(\frac{\sigma_1}{\sigma_c}\right)^q\right]^2} + \frac{(\sigma_3 - \sigma_1)(\sigma_2 - \sigma_1)}{\bar{f}_{bc}^2 \left[1 + kc \left(\frac{\sigma_1}{\sigma_c}\right)^q\right]^2} - \sigma_c^2 = 0 \quad (4.29)$$

where $\bar{f}_{bc} = f_{bc}/\sigma_c$ denotes the ratio of equal-biaxial compressive strength to the unconfined uniaxial compressive strength. q is a material constant value controlling the curvature of the failure surface in the tensile and compressive meridians (Fig 4.14). c is the slope of the compressive meridian at $\sigma_1 = \sigma_c$ and k is a constant relating the tensile meridian to the compressive meridian. These constant values may be adjusted to suit any brittle material using the following approach.

a) Biaxial Compression

When σ_1 becomes zero, Eq. 4.29 reduces to:

$$f = \sigma_3^2 + \sigma_2^2 - (2 - 1/\bar{f}_{bc}^2)\sigma_2\sigma_3 - \sigma_c^2 = 0 \quad (4.30)$$

In the condition when $\sigma_2 = \sigma_3$ the criterion leads to

$$\sigma_3 = \sigma_2 = \bar{f}_{bc} \sigma_c$$

Values of 1.14 to 1.18 can be concluded for \bar{f}_{bc} by Kupfer et al(55). Fig 4.13 compares the proposed biaxial yield function Eq 4.30, to the experimental data (55). The agreement is good when $\bar{f}_{bc} = 1.17$ is used. Notice that, as shown in Fig 4.13, an even better agreement can be achieved by adapting the biaxial stress function to:

$$f = (\sigma_3/\sigma_c) + 0.26(1.66\sigma_2/\sigma_3 - 1)^2 - 1.26 = 0 \quad (4.31)$$

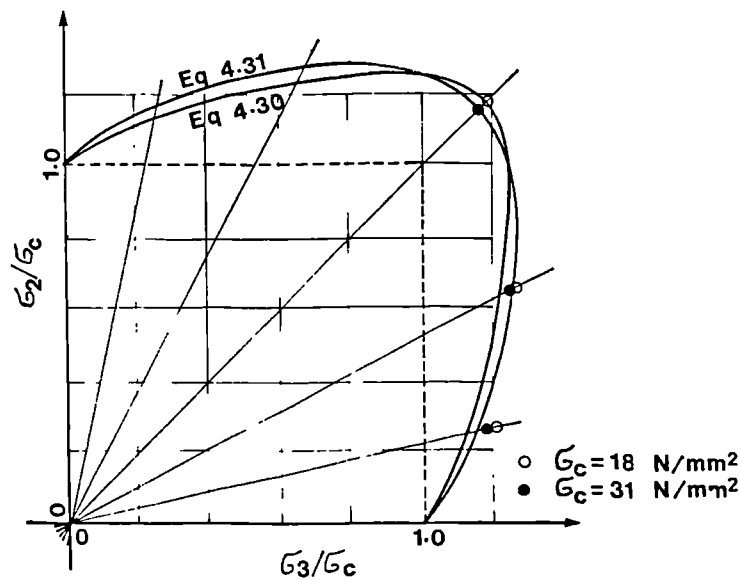


Figure 4.13 Comparison of the Proposed Failure Criteria for Concrete under Biaxial Compression with the Experimental Results of Kupfer et al(55)

b) Triaxial Tests at Compressive Meridian ($0 > \sigma_1 = \sigma_2 > \sigma_3$)

Equating σ_1 and σ_2 in order to meet the load combination shown in Fig 4.14(a), Eq 4.29 becomes:

$$f = \sigma_3/\sigma_c - \sigma_1/\sigma_c - c(\sigma_1/\sigma_c)^q - 1 = 0 \quad (4.32)$$

which is the failure criterion at the compressive meridian. The tests carried out (70,71) on normal concrete led to the adoption of $c=3.6$ and $q=0.8$.

c) Triaxial Tests at Tensile Meridian ($0 > \sigma_1 > \sigma_2 = \sigma_3$)

In order to have the failure criterion at the tensile meridian (Fig 4.14(b)) one may set σ_2 equal to σ_3 in Eq 4.29 to get:

$$f = \sigma_3/\sigma_c - \sigma_1/\sigma_c - \bar{f}_{bc} [1 + kc(\sigma_1/\sigma_c)^q] = 0 \quad (4.33)$$

Examination of results of the tests carried out on normal concrete led to the adoption of $k = 0.68$.

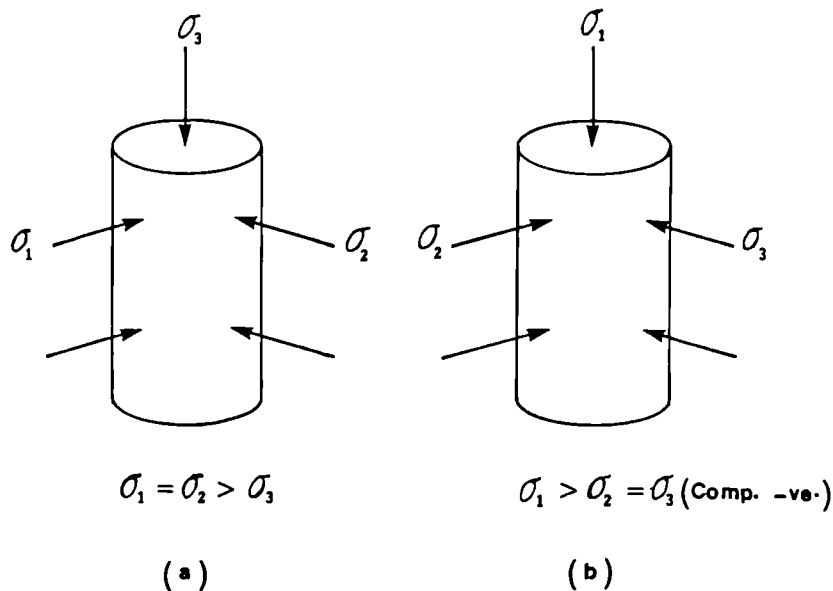


Figure 4.14 Typical Triaxial Test Arrangements; (a) at compressive meridian and (b) at tensile meridian.

By the same procedure as followed in this section for normal concrete the constant parameters \bar{f}_{bc} , q , c and k can be determined for any other brittle materials. While k and \bar{f}_{bc} are expected to have only small variations for different brittle materials, q and c are expected to vary considerably. The experimental results of Khoo and Hendry (72) suggest $c=1.91$ and $q=0.73$ for the mortar types commonly used in masonry.

4.5.3 Proposed Failure Criterion for Brittle Materials under Triaxial Compression-Tension

Using the principal stresses, while:

$$\sigma_3 < \sigma_2 < 0 < \sigma_1 \quad (\text{comp. -ve})$$

the failure surface function is proposed as follows:

$$f = (\sigma_3 - \sigma_2)^2 + (\alpha \sigma_1)^2 + A(\alpha \sigma_1)(\sigma_3 + \sigma_2) + (1/\bar{f}_{bc}^2)\sigma_2\sigma_3 - \sigma_c^2 = 0 \quad (4.34)$$

Where α denotes the ratio of unconfined uniaxial compressive strength, σ_c , to direct tensile strength, σ_t , and A is a constant controlling the curvature of the failure surface in biaxial compression-tension. This constant is highly variable and can be adjusted for any brittle material as will be discussed later. The above criterion may be examined using the available test results as follows:

a) Biaxial Compression ($\sigma_1=0$)

When σ_1 equals zero, Eq 4.34 becomes identical to Eq 4.30. This proves the continuity of Eq 4.34 and Eq 4.29.

b) Zero Intermediate Stress ($\sigma_2=0$)

Eq 4.34 with $\sigma_2=0$ becomes:

$$f = \sigma_3^2 + (\alpha\sigma_1)^2 + A\alpha\sigma_1\sigma_3 - \sigma_c^2 = 0 \quad (4.35)$$

The experimental results of the tests carried out by Kupfer et al⁽⁵⁵⁾ on normal concrete of various strength were compared with Eq 4.35 to determine the value of **A**. This examination led to the following proposed relation.

$$A = 0.25 + 0.0006(|\sigma_c|-10)^2 \quad (4.36)$$

The value of **A** may be determined by the same procedure as given above for any brittle material. The experimental results of Khoo and Hendry⁽⁷²⁾ may be used to give **A**=5.0 for fired clay brick. Fig 4.15 compares the biaxial compression-tension failure criterion, Eq 4.35, to the experimental results of Kupfer et al⁽⁵⁵⁾ and shows a good agreement.

c) Equal-Compression Tension ($\sigma_2=\sigma_3$)

When $\sigma_2=\sigma_3$, Eq 4.34 leads to:

$$f = \sigma_3^2/\bar{f}_{bc}^2 + (\alpha\sigma_1)^2 + 2A(\alpha\sigma_1)\sigma_3 - \sigma_c^2 = 0 \quad (4.37)$$

There is little experimental data for concrete under such stress combination, but it is known that the intermediate stress, σ_2 , has little effect on the total strength⁽⁵⁷⁾.

4.5.4 Proposed Failure Criterion for Brittle Materials Under Tension-Compression

A very limited number of experimental data in this zone ($\sigma_3 < 0 < \sigma_2 < \sigma_1$), have been reported by Hobbs et al (57). They suggest that the effect of σ_2 is insignificant. Therefore Eq 4.35 may also be used for this stress combination while σ_2 may take any value between σ_1 and zero.

4.5.5 Proposed Failure Criterion for Brittle Materials Under Triaxial Tension

It is believed (57,55) that the failure of brittle material under triaxial tension ($\sigma_1 > \sigma_2 > \sigma_3 > 0$) is governed by only the most tensile principal stress, σ_1 . The criterion thus reduces to:

$$\sigma_1 - \sigma_t = 0 \quad (4.38)$$

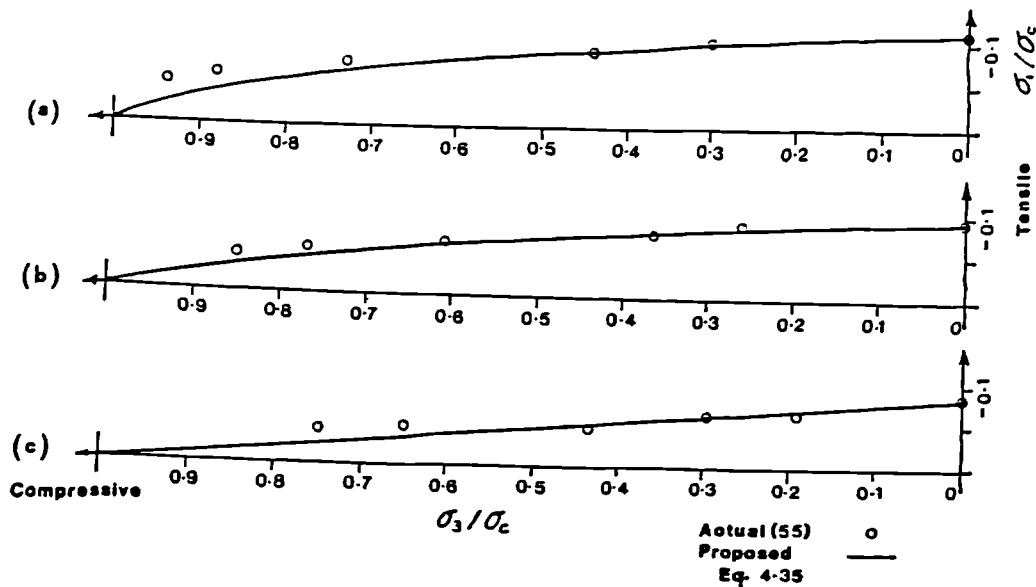


Figure 4.15 Comparison of Proposed Failure Criteria with Experimental Results of Kupfer et al (55) for Concrete Under Combined Tension and Compression (a) $\sigma_c = 18.6$, (b) $\sigma_c = 30.9$, (c) $\sigma_c = 57.9$ N/mm²

4.6 Proposed Constitutive Formulation for Brittle Materials Under Multiaxial Stresses

4.6.1 General

The behaviour of concrete under multiaxial loads has been studied by several investigators (47, 55, 56, 57, 65, 73, 74). The manner of loading in the laboratory is normally monotonic and proportional in consistent principal directions. For such loading and assuming the concrete material remains isotropic up to cracking stage, the stress-strain relationship according to the Hooke's Law is given as follows:

$$\begin{bmatrix} \epsilon_1 \\ \epsilon_2 \\ \epsilon_3 \end{bmatrix} = \frac{1}{E} \begin{bmatrix} 1 & -\nu_{12} & -\nu_{13} \\ -\nu_{21} & 1 & -\nu_{23} \\ -\nu_{31} & -\nu_{32} & 1 \end{bmatrix} \begin{bmatrix} \sigma_1 \\ \sigma_2 \\ \sigma_3 \end{bmatrix}$$

or:

$$\{\epsilon\} = \frac{1}{E} [C] \{\sigma\}$$

and

$$\{\sigma\} = E [C]^{-1} \{\epsilon\}$$

$$\{\sigma\} = [D] \{\epsilon\} \quad (4.39)$$

Where E signifies the secant elastoplastic modulus and ν values denotes the secant Poisson's ratios in directions shown by their indices. In order to keep the $[D]$ matrix symmetric the following relations must be satisfied:

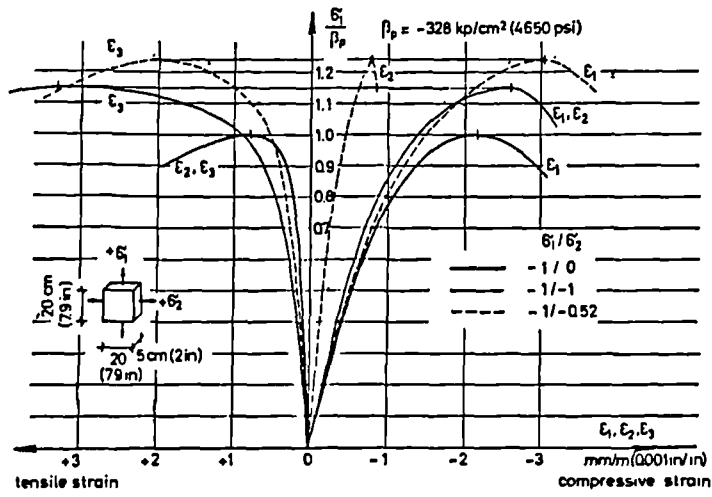
$$v_{12}=v_{21} , \quad v_{13}=v_{31} , \quad v_{23}=v_{32} \quad (4.40)$$

Since the material behaves in a non-linear and elastoplastic fashion, the solution involves four material properties; E , v_{12} , v_{23} and v_{31} which are all functions of stress or strain level. These values can be formulated using the available experimental data.

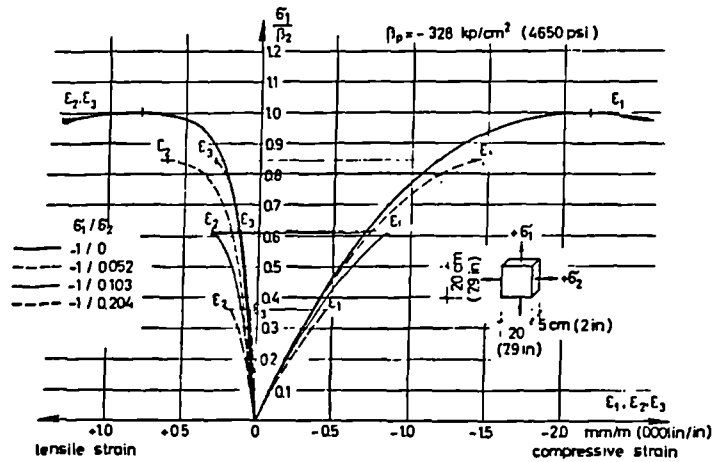
Fig 4.16 shows the stress-strain curves plotted by Kupfer et al (55) from biaxial loading tests. These curves are widely referred to as a set of reliable experimental data which can be used together with some other experimental data in other areas of loading, eg. the experiments reported by Hobbs et al (57), to formulate the above mentioned material properties.

Such data cannot be easily utilized for this purpose since, for each stress combination, the stress-strain curves for the three principal directions are quite dissimilar. Instead it is convenient to define the "equivalent uniaxial strain" vector (**EUS**) described in the following section, so that the formulation can be developed step by step, initially excluding the effect of Poisson's ratio from the actual strains.

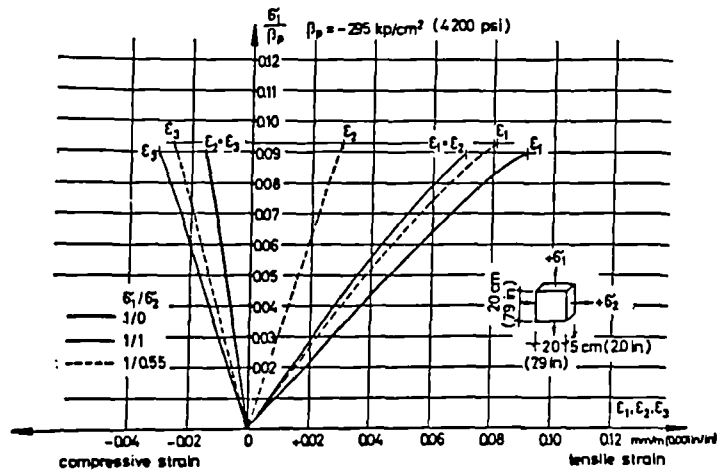
It will be seen later in section 4.6.4 that the **EUS** can be simply transformed to the real strains and finally the theoretical stress-strain curves can be plotted. Comparison of the proposed model and the experimental results is given in section 4.6.4 , Fig 4.20 and Fig 4.21.



(a)



(b)



(c)

Figure 4.16 Experimental Stress-strain Relationship of Concrete under Biaxial Loading;
 (a) compression-compression,
 (b) tension-compression and
 (c) tension-tension (after Kupfer et al (55))

4.6.2 Equivalent Uniaxial Strains (EUS)

The **EUS** vector is defined as follows:

$$\{\epsilon_u\} = \frac{1}{E} \{\sigma\}$$

or:

$$\begin{bmatrix} \epsilon_{1u} \\ \epsilon_{2u} \\ \epsilon_{3u} \end{bmatrix} = \frac{1}{E} \begin{bmatrix} 1 & 0 & 0 \\ 0 & 1 & 0 \\ 0 & 0 & 1 \end{bmatrix} \begin{bmatrix} \sigma_1 \\ \sigma_2 \\ \sigma_3 \end{bmatrix} \quad (4.41)$$

and

$$\{\sigma\} = E\{\epsilon_u\}$$

The **EUS** comprise only that part of the strains that result from application of each stress component and occur in the same direction as that of the stress itself. i.e., the strains due to the Poisson's ratios are excluded.

Comparison of Eq 4.39 and Eq 4.41 leads to:

$$\{\epsilon\} = [C]\{\epsilon_u\}$$

or

$$\{\epsilon_u\} = [C]^{-1}\{\epsilon\} \quad (4.42)$$

which relate the real strains to EUS or vice-versa. The **[C]** matrix is given in Eq 4.39.

4.6.3 Proposed Stress-EUS Relationship Formulation

Eqs 4.41 imply that in a monotonic proportional loading EUS are proportional to their corresponding stresses at any particular stress level. i.e;

$$\alpha_i = \frac{\sigma_i}{\sigma_3} = \frac{\epsilon_{iu}}{\epsilon_{3u}} = \frac{\epsilon_{iuc}}{\epsilon_{3uc}} = \frac{\sigma_i'}{\sigma_3'} \quad (4.43)$$

Where σ_i' and ϵ_{iuc} denote the material strength and its corresponding **EUS** in i th principal direction and α_i denotes the ratio of the principal stress component in i direction to the stress of the most compressive principal direction. The stress ratios remain constant throughout the loading process, because a proportional loading is assumed.

The proportionality of the **EUS** implies also that the three principal stress-**EUS** curves are proportional as shown typically in Fig 4.17, such that the magnitude of σ_i and ϵ_{iu} are reduced by the corresponding stress ratio α_i . This similarity reduces the task to that of formulating only σ_3 in terms of ϵ_{3u} which are the most compressive principal stress and **EUS** respectively.

As will be seen later in Section 4.6.5 the stress-**EUS** curves are parabolic-like and are smooth with an initial modulus of elasticity of E_0 , such that the same formulas as for uniaxial loading (Eq 4.1 to 4.5) can be proposed with new notations as follows:

$$E_0/E_s > 2;$$

$$\sigma_i = E_0 \frac{\epsilon_{iu}}{1 + \left(\frac{E_0}{E_s} - 2\right)\left(\frac{\epsilon_{iu}}{\epsilon_{iuc}}\right) + \left(\frac{\epsilon_{iu}}{\epsilon_{iuc}}\right)^2} \quad (4.44)$$

$$E_0/E_s < 2;$$

$$\sigma_i = E_0 \frac{\epsilon_{iu}}{1 + \left(\frac{E_0}{E_s} - 1\right)\left(\frac{\epsilon_{iu}}{\epsilon_{iuc}}\right)^g} \quad (4.45)$$

where:

$$g = 1/(1-E_s/E_0) \quad (4.46)$$

and for the falling branch:

$$\sigma_i = \frac{\sigma_i'}{1 + D \left(\frac{\epsilon_{iu}}{\epsilon_{iuc}} - 1 \right)^2} \quad (4.47)$$

Where $E_s = \sigma_i' / \epsilon_{iuc}$ denotes the secant modulus at peak stress and ϵ_{iuc} signifies the EUS corresponding to the peak stress.

The above equations are convenient to be written in their normalized form so as to represent all the three curves shown in Fig 4.17 as given below:

$$E_0/E_s > 2;$$

$$s = \left(\frac{E_0}{E_s} \right) \frac{e}{1 + (E_0/E_s - 2)e + e^2} \quad (4.48)$$

$$E_0/E_s < 2;$$

$$s = \left(\frac{E_0}{E_s} \right) \frac{e}{1 + (E_0/E_s - 1)e^g} \quad (4.49)$$

and for the falling branch:

$$s = \frac{1}{1 + D(e-1)^2} \quad (4.50)$$

where:

$$S = \sigma_i / \sigma_i' \quad \text{and} \quad e = \epsilon_{iu} / \epsilon_{iuc}$$

The stress-EUS relationship given by Eq 4.44 to 4.47 depend on the values of σ_i' and ϵ_{iuc} , ($i = 1, 2, 3$) or σ_3' and ϵ_{3uc} and the stress ratios α_1 and α_2 . The values of peak stresses were discussed in Section 4.5 under "Failure Criteria". ϵ_{3uc} is formulated in the following Section.

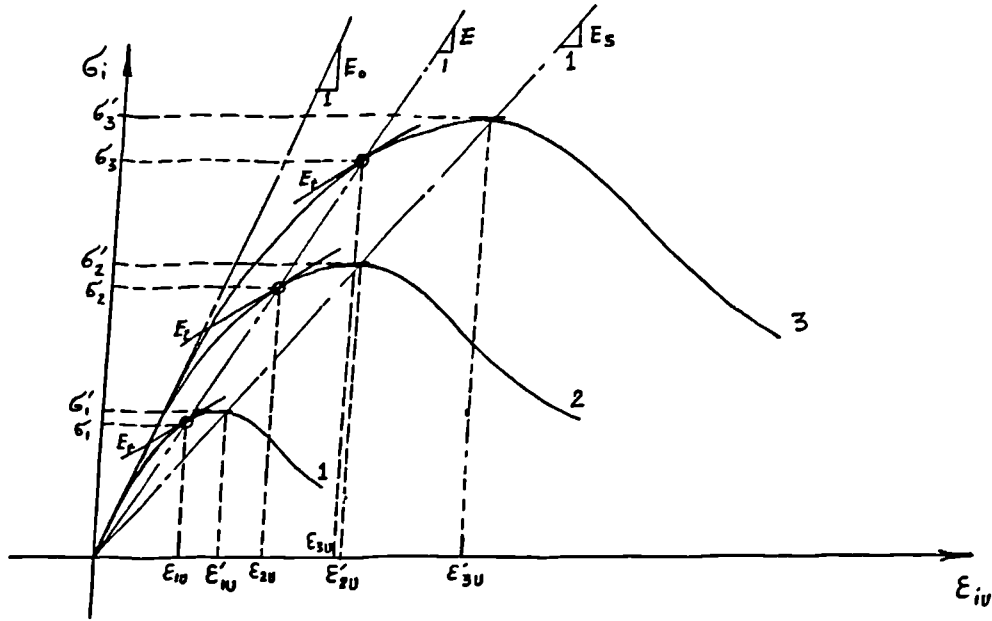


Figure 4.17 Equivalent Uniaxial Stress-strain Curves

4.6.4 EUS at Peak Load

Determination of ϵ_{3u} may be formulated using the available experimental data. In order to accommodate such formulation, the relation between ϵ_{3u} and the real strains is derived below for both biaxial and triaxial loading.

In a proportional biaxial loading where $\sigma_i=0$, ie. $\alpha_i=0$ and $\epsilon_{iu}=0$, combination of Eqs 4.42 and 4.43 leads to:

$$\begin{bmatrix} \epsilon_i \\ \epsilon_j \\ \epsilon_k \end{bmatrix} = \begin{bmatrix} -v_{ij} & -v_{ik} \\ 1 & -v_{jk} \\ -v_{kj} & 1 \end{bmatrix} \begin{bmatrix} \alpha_j \epsilon_{3u} \\ \alpha_k \epsilon_{3u} \end{bmatrix} \quad (4.51)$$

Because of the condition of isotropy and symmetry discussed in section 4.6.1, $v_{jk}=v_{kj}$ and the second and third of

Eqs 4.51 can be solved for v_{jk} and ϵ_{3u} to give;

$$v_{jk} = v_{kj} = \frac{\alpha_k \epsilon_j - \alpha_j \epsilon_k}{\alpha_j \epsilon_j - \alpha_k \epsilon_k} \quad (4.52)$$

$$\epsilon_{3u} = \frac{\alpha_k \epsilon_k - \alpha_j \epsilon_j}{\alpha_k^2 - \alpha_j^2} \quad (4.53)$$

Triaxial loading tests are normally carried out at one of the meridians. i.e. $\sigma_k \neq \sigma_i = \sigma_j$. As a result of such a multiaxial stress combination, Eq 4.42 reduces to:

$$\begin{bmatrix} \epsilon_i \\ \epsilon_k \end{bmatrix} = \begin{bmatrix} 1 & -v_{ij} & -v_{ik} \\ -v_{ki} & -v_{kj} & 1 \end{bmatrix} \begin{bmatrix} \alpha_i \epsilon_{3u} \\ \alpha_j \epsilon_{3u} \\ \alpha_k \epsilon_{3u} \end{bmatrix} \quad (4.54)$$

Because of the equality of σ_i and σ_j no relative plasticity is expected between the two principal directions of i and j requiring that $v_{ij} = v_0$. Also because of the condition of isotropy and symmetry discussed in section 4.6.1:

$$v_{kj} = v_{jk} = v_{ik} = v_{ki} = v \neq v_0$$

Now the two equations of 4.54 can be solved for ϵ_{3u} and v to give:

$$v = \frac{1}{\alpha_k} \left[\epsilon_i \frac{(1-v_0)(\alpha_i^2 + \alpha_j^2)}{\alpha_k \epsilon_k - \alpha_i \epsilon_i - \alpha_j \epsilon_j} + \alpha_i - v_0 \alpha_j \right] \quad (4.55)$$

$$\epsilon_{3u} = \frac{\alpha_k \epsilon_k - \alpha_i \epsilon_i - \alpha_j \epsilon_j}{\alpha_k^2 - (1-v_0)(\alpha_i^2 + \alpha_j^2)} \quad (4.56)$$

Eqs 4.53 and 4.56 were used to calculate ϵ_{3uc} with the aid of the experimental data ($\epsilon_1, \epsilon_2, \epsilon_3, \alpha_1$ and α_2) of Kupfer et al(55), Hobbs et al(57) and Tassuji et al(65). These values were entered into a nondimensional coordinate system of σ_3'/σ_c versus ϵ_{3u}/ϵ_c as shown in Fig 4.18. Also are plotted in this figure, the following relations proposed to calculate $\epsilon_{3uc}/\epsilon_c$.

For $\sigma_3' < \sigma_c$: (comp. -ve)

$$\frac{\epsilon_{3uc}}{\epsilon_c} = \frac{\sigma_3'}{\sigma_c} + R \left(\frac{\sigma_3'}{\sigma_c} - 1 \right) \left(1 - \frac{E_c}{E_0} \right) \quad (4.57)$$

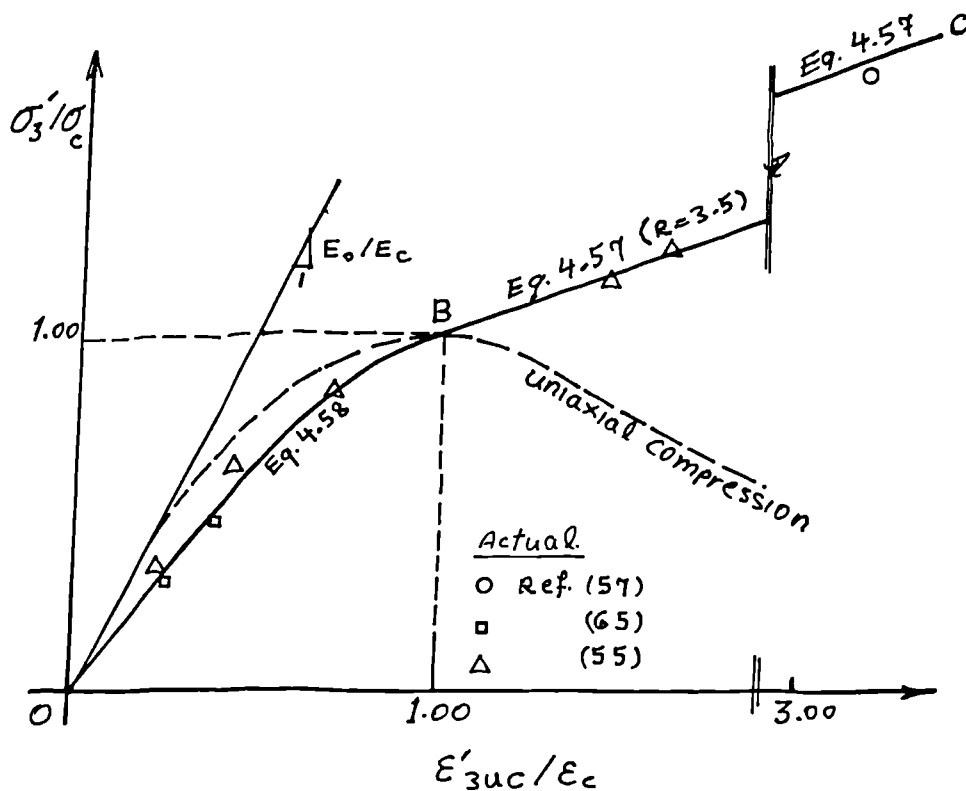


Figure 4.18 Comparison of The Proposed Analytical Prediction of Equivalent Uniaxial Strains at Peak Load with Some Experimental Data

For $0 > \sigma_3' > \sigma_c$:

$$\left(\frac{\epsilon_{3uc}}{\epsilon_c}\right) = 0.5 \left(\frac{\sigma_3'}{\sigma_c}\right) \left[\left(1 + \frac{E_c}{E_0}\right) + \left(1 - \frac{E_c}{E_0}\right) \left(\frac{\sigma_3'}{\sigma_c}\right)^{2R} \right] \quad (4.58)$$

and for $\sigma_3' > 0$

$$\frac{\epsilon_{3uc}}{\epsilon_c} = 0.5 \left(1 + \frac{E_c}{E_0}\right) \frac{\sigma_3'}{\sigma_c} \quad (4.59)$$

where R is a material constant. R=3.5 suits normal concrete.

4.6.5 Transformation of EUS to Real Strains and Vice-versa

EUS and real strains can be converted to each other using Eqs 4.42. These equations involve the [c] matrix defined in section 4.6.1. In a multiaxially and proportionally loaded isotropic material, this matrix involves 3 independent Poisson's ratios as follows:

$$v_{12}=v_{21}, \quad v_{23}=v_{32} \quad \text{and} \quad v_{13}=v_{31}$$

The Poisson's ratios can be formulated according to the available experimental data. Eqs 4.52 and 4.55 relate the Poisson's ratios at any stress level to the strains of a biaxially and triaxially loaded material respectively. Examination of the experimental results of Kupfer et al (55) led to an expansion of Eq 4.9 (proposed for uniaxial loading) to account for biaxial and multiaxial loading as follows:

$$v_{ji} = v_{ij} = v_0 \left[1 + k f_{ij} (\epsilon)^n \right] \quad (4.60)$$

where \mathbf{e} denotes the straining ratio i.e. $\mathbf{e} = \epsilon_{iu}/\epsilon_{iuc}$
 and \mathbf{k} and \mathbf{n} are material constants. $\mathbf{k} = 0.85$ and $\mathbf{n} = 3$
 suits normal concrete. \mathbf{f}_{ij} is proposed as follows:

For $\sigma_1' < 0$: (comp. -ve)

$$\mathbf{f}_{ij} = \frac{|(\sigma_i' - \sigma_j')/\sigma_c|}{1 + c \left(\frac{\sigma_1'}{\sigma_c}\right)^q} \quad (4.61)$$

For $\sigma_1' > 0$:

$$\mathbf{f}_{ij} = |(\sigma_i' - \sigma_j')/\sigma_c| - 2|\sigma_1'/\sigma_c| \quad (4.62)$$

where \mathbf{c} and \mathbf{q} are defined in section 4.5.2 and σ_1' denotes the most tensile stress at the peak. These formulas agree well with the experimental results of Kupfer et al (55) at peak loads as shown in Fig 4.19. Eq 4.60 covers all the possible states of load combination.

The incremental and secant values of Poisson's ratios are related as follows:

$$\bar{v}_{ij} d\epsilon_j = d(v_{ij}\epsilon_{ij})$$

where \bar{v}_{ij} and v_{ij} are the incremental and secant Poisson's ratios respectively for calculating the strain in the i th principal direction induced by the strain in the j th principal direction. From the above relation the incremental and secant values of Poisson's ratios can be calculated in terms of each other as follows:

$$\bar{v}_{ij} = \frac{d(v_{ij} \cdot \mathbf{e})}{d\mathbf{e}}$$

$$v_{ij} = \frac{\int \bar{v}_{ij} \cdot e}{e} \quad (4.63)$$

These equations can now be used to develop the tangent and post peak stress Poisson's ratios as follows:

$$v_{ij} = v_0 [1 + (n+1)k f_{ij} e^n] \quad (4.64)$$

where \bar{v}_{ij} denotes the incremental Poisson's ratio between i th and j th principal directions and,

$$\bar{v}_{ij} = v_0 [1 + (n+1)k f_{ij}] \quad (4.65)$$

$$v_{ij} = v_0 [1 + k f_{ij} (4-3/e)]$$

where the strains has past the strains corresponding to the peak stresses i.e, $e = \epsilon_{iu}/\epsilon_{iuc} > 1.0$. Eqs 4.60, 4.64 and 4.65 are valid only when the increment of stresses are proportional to the current stresses.

Having formulated the Poisson's ratios, the real strains ($\epsilon_1, \epsilon_2, \epsilon_3$) can be calculated from Eq 4.42. The proposed constitutive formulation and failure criteria (sections 4.5 and 4.6) are compared with the experimental results of Kupfer et al (55) in Figs 4.20 and 4.21 and good agreement can be seen.

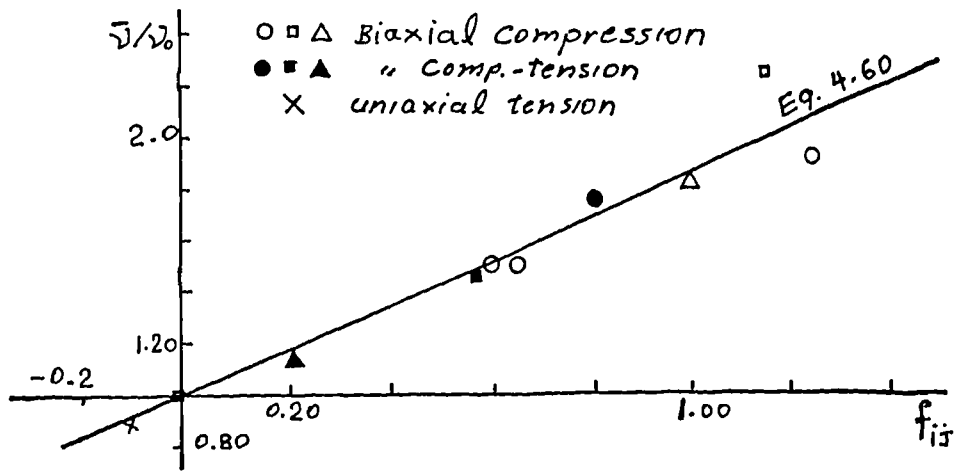


Figure 4.19 Comparison of the Proposed Prediction of The Poisson's Ratio at Peak Stress, with Experimental Results of Kupfer et al (55)

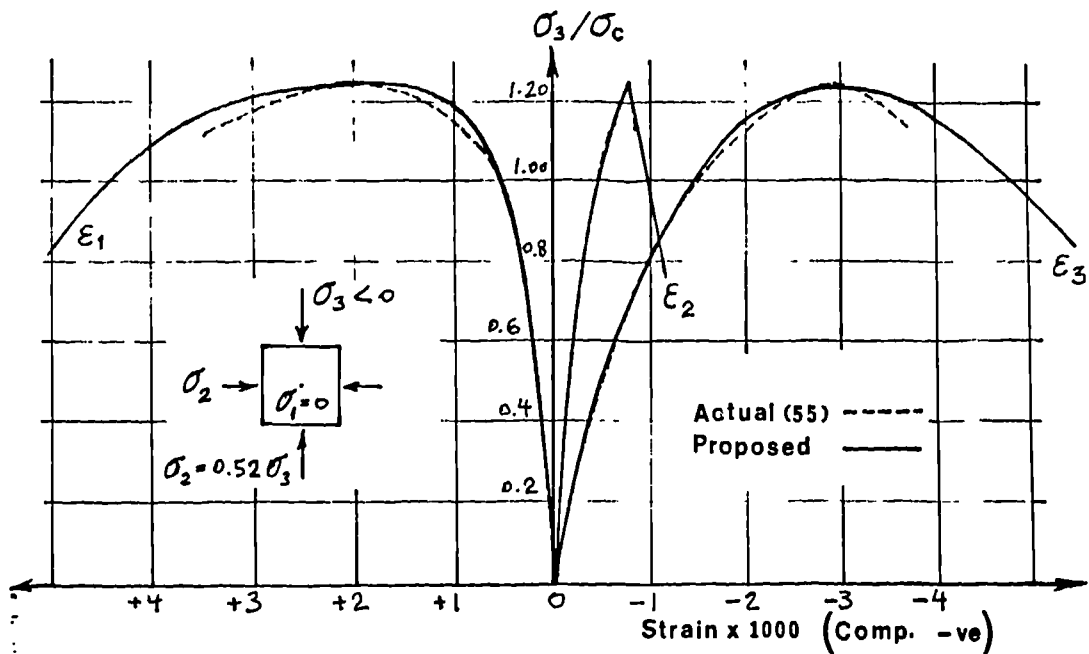


Figure 4.20 Comparison of the predicted and actual Stress-strain Diagrams for concrete under biaxial Compression; $\sigma_1=0$, $\sigma_2/\sigma_3=0.52$

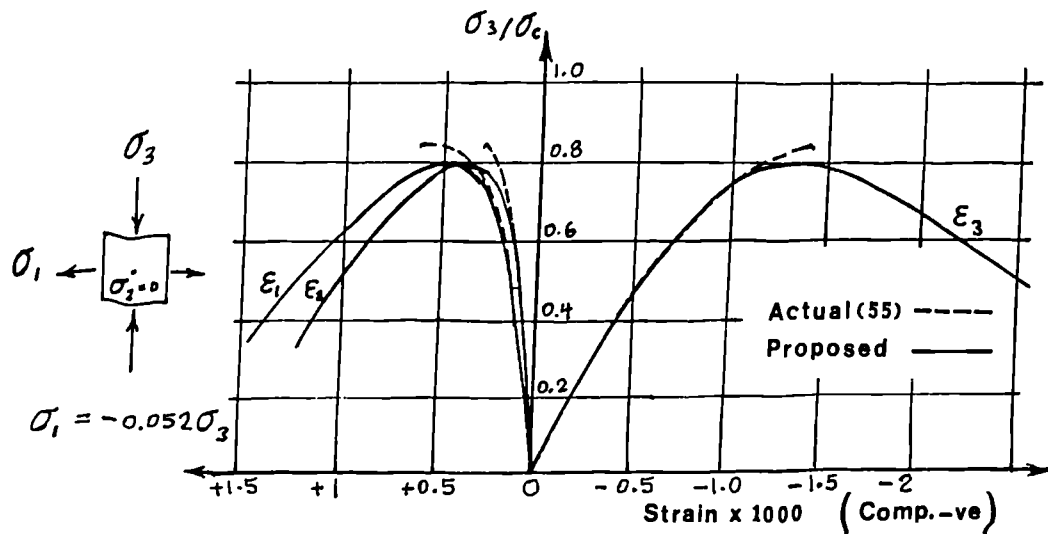


Figure 4.21 Comparison of the predicted and actual Stress-strain Diagrams for concrete under Biaxial Compression and tension; $\sigma_2=0$, $\sigma_1/\sigma_2=-0.052$

4.6.6 Proportional Unloading and Reloading

The unloading-reloading behaviour of uniaxially loaded concrete has been studied in detail (59,64). This has been discussed in section 4.3.3, where the stress-strain relationship for a cycle of unloading and reloading was modeled by a straight line, **EP**, as shown in Fig 4.9. Unlike the uniaxial case there is no experimental data available for unloading-reloading behaviour of concrete under biaxial and multiaxial loading. Therefore, in this project the basic principles of parts (a) to (c) of section 4.3.3 were generalized to include concrete under multiaxial loading. Accordingly the proposed linear model of unloading-reloading was generalized into stress-**EUS** curves as shown in Fig 4.22.

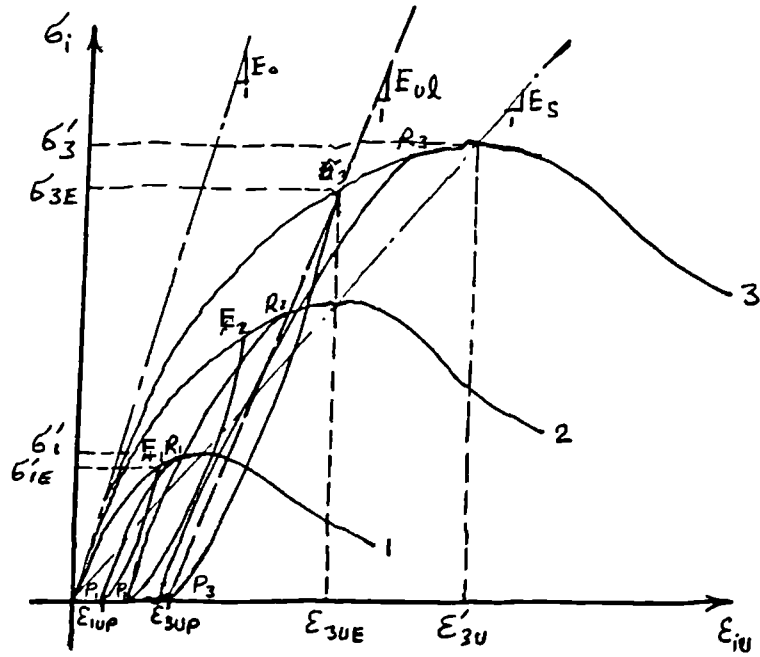


Figure 4.22 Stress and Equivalent Uniaxial Strain Relationship of Concrete under Proportional Multiaxial Unloading and Reloading

The generalized linear unloading-reloading behaviour implies that no plasticity takes place during a complete or partial unloading-reloading cycle. Therefore, the material can be treated as linear elastic with constant modulus of elasticity, E_{ul} , and constant poisson's ratio, ν_0 , in any direction within the material.

For the sake of simplicity, taking advantage of the stress proportionality, the three stress-EUS envelope curves may be mapped into one non-dimensional envelope curve, Fig 4.23 where s and e denote the stressing and straining ratios respectively defined as follows:

$$\left. \begin{aligned} e &= \epsilon_{iu} / \epsilon_{iuc} \\ s &= \sigma_i / \sigma_i' \end{aligned} \right\} \quad (4.66)$$

For $e_E < 1.0$;

$$\frac{E_{ul}}{E_0} = \frac{2}{2 + (E_0/E_s - 1)e_E^{1.5g}} \quad (4.67)$$

For $e_E > 1.0$;

$$\frac{E_{ul}}{E_0} = \frac{1}{(1 + E_0/E_s)(0.5 + 0.3m + 0.8m^2)} \quad (4.68)$$

where g and m are to be calculated as:

$$m = (e_E - 1) \sqrt{D} \quad (4.69)$$

$$D = \left(\frac{|\sigma_c|}{100} \right)^{2.15} > 0.25 \quad (\text{for concrete}) \quad (4.70)$$

$$g = \frac{E_0/E_s}{E_0/E_s - 1} \quad (4.71)$$

The residual plastic EUS after a full unloading in its normalized form, $e_p = \epsilon_{iup}/\epsilon_{iuc}$, can be derived using Fig 4.23 as follows:

$$\frac{E_{ul}}{E_s} = \frac{s_E}{e_E - e_p}$$

Solving for e_p leads to:

$$e_p = e_E - \frac{s_E}{E_{us}/E_0} \cdot \frac{1}{E_0/E_s} \quad (4.72)$$

where s_E and e_E denote the stressing and straining ratios

corresponding to the point on the normalized stress-strain envelope curve at which the unloading started. Fig 4.24 shows the variation of E_{ul}/E_0 against straining ratio, e_E , and also a wide range of E_0/E_s ratio. Also shown in this figure is the plot of E_{ul}/E_0 against e_E calculated from the Karsan and Jersa⁽⁶⁰⁾ proposed formula, (Eq 4.12), in comparison with the proposed Eqs 4.67 and 4.68. Although these curves agree well over most of the length of the curves, the Karsan and Jersa⁽⁶⁰⁾ formula gives E_{ul} larger than E_0 at the beginning of the envelope curve and this is a source of numerical problems. Another numerical problem with the Karsan and Jersa formula will be encountered by having a negative E_{ul} when e_E is high, Fig 4.24.

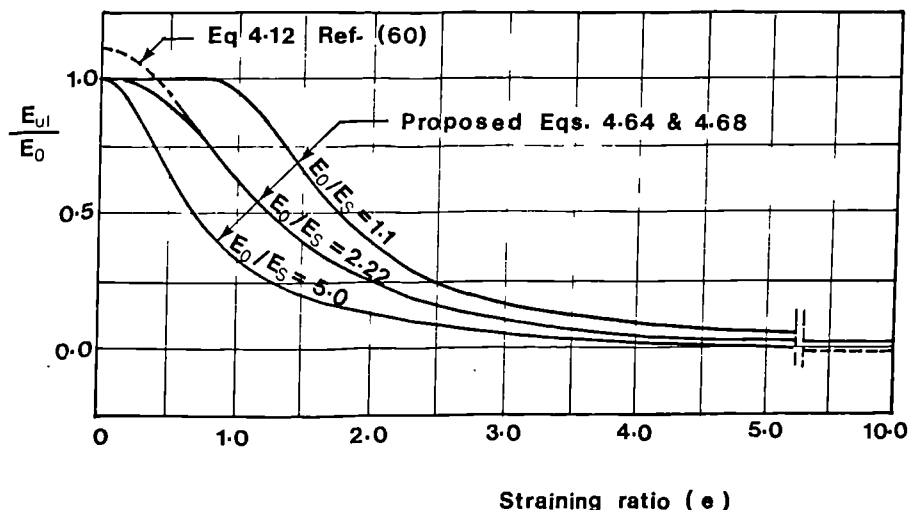


Figure 4.24 Comparison of the proposed Prediction of Unloading Modulus of Elasticity with Karsan and Jersa⁽⁶⁰⁾ Formula. Note: the straining ratio 'e' refers to the unloading point on the envelope curve

4.6.7 Proposed Incremental Stress-strain Relationship

In a non-linear elastoplastic but monotonic and proportional loading the principal directions are consistent. Under such loading the incremental stress-strain relation matrix $[D_t]$, can be formed using Eq 4.39 and including the terms for shear stresses and strains and also the incremental values of modulus of elasticity and poisson's ratios as follows:

For biaxial loading and in the principal directions of stress Eq 4.39 becomes:

$$\begin{bmatrix} d\sigma_1 \\ d\sigma_2 \\ d\tau_{12} \end{bmatrix} = E_t \begin{bmatrix} 1/\phi & \nu_{12}/\phi & 0 \\ \nu_{12}/\phi & 1/\phi & 0 \\ 0 & 0 & \frac{1}{2(1+\nu_{12})} \end{bmatrix} \begin{bmatrix} d\varepsilon_1 \\ d\varepsilon_2 \\ d\gamma_{12} \end{bmatrix} \quad (4.73)$$

$$\phi = 1 - \nu_{12}^2$$

and for multiaxial loading and in the principal directions of stress leads to:

$$\begin{bmatrix} d\sigma_1 \\ d\sigma_2 \\ d\sigma_3 \\ d\tau_{12} \\ d\tau_{23} \\ d\tau_{31} \end{bmatrix} = \begin{bmatrix} D_{11} & D_{12} & D_{13} & 0 & 0 & 0 \\ & D_{22} & D_{23} & 0 & 0 & 0 \\ & & D_{33} & 0 & 0 & 0 \\ & & & D_{44} & 0 & 0 \\ & & & & D_{55} & 0 \\ \text{Symmetry} & & & & & D_{66} \end{bmatrix} \begin{bmatrix} d\varepsilon_1 \\ d\varepsilon_2 \\ d\varepsilon_3 \\ d\gamma_{12} \\ d\gamma_{23} \\ d\gamma_{31} \end{bmatrix} \quad (4.74)$$

where:

$$\begin{aligned}
 D_{11} &= (1-\nu \cdot 23^2)/\phi & D_{33} &= (1-\nu \cdot 12^2)/\phi \\
 D_{12} &= (\nu 31 \nu 23 + \nu \cdot 12)/\phi & D_{44} &= E_t/[2(1+\nu \cdot 12)] \\
 D_{13} &= (\nu 12 \nu 23 + \nu \cdot 31)/\phi & D_{55} &= E_t/[2(1+\nu \cdot 23)] \\
 D_{22} &= (1-\nu \cdot 31^2)/\phi & D_{66} &= E_t/[2(1+\nu \cdot 31)] \\
 D_{23} &= (\nu \cdot 12 \nu \cdot 31 + \nu \cdot 23)/\phi \\
 \phi &= [1-\nu \cdot 12^2-\nu \cdot 23^2-\nu \cdot 31^2-2\nu \cdot 12 \nu \cdot 23 \nu \cdot 31]/E_t
 \end{aligned}$$

The incremental poisson's ratios, ν_{12} , ν_{23} , ν_{31} , are given by Eqs 4.64 and 4.65. E_t denotes the incremental modulus shown in Figs 4.17 and 4.23. E_t can be calculated by differentiation of the stress against strain using Eqs 4.44 to 4.47. i.e,

$$E_t = \frac{d\sigma_i}{d\varepsilon_{iu}}$$

When the material is subjected to unloading or reloading (Line **EP** on Fig 4.23), behaves in an isotropic and elastic manner as described in section 4.6.6, i.e:

$$E_t = E_{u1}$$

$$\nu_t = \nu_0$$

E_{u1} is calculated as described in section 4.6.6 and ν_0 denotes the initial tangent poisson's ratio which is uniform in all directions. The tangent elasticity matrix, $[D_t]$, for unloading and reloading can be adapted from Eqs 4.150 and 4.151 for plane stress and 3-D loading respectively with replacing E_0 by E_{u1} .

$[D_t]$ may be transformed into the global coordinates as follows:

$$\begin{matrix} [D_t] & = & [T]^T [D_t] [T] & (4.75) \\ \text{(Global)} & & \text{(Principal)} & \end{matrix}$$

where $[T]$ denotes the strain transformation matrix which transforms the strains from the global co-ordinates to the principal directions as follows:

$$\begin{matrix} \{d\varepsilon\} & = & [T] & \{d\varepsilon\} & (4.76) \\ \text{Global} & & \theta & \text{Principal} & \end{matrix}$$

θ is the angle from the principal directions to the global co-ordinates measured anticlockwise.

The transformation matrix $[T]$ for plane stress problems is written⁽³⁹⁾ as:

$$[T] = \begin{bmatrix} \cos^2\theta & \sin^2\theta & \sin\theta\cos\theta \\ \sin^2\theta & \cos^2\theta & -\sin\theta\cos\theta \\ -2\sin\theta\cos\theta & 2\sin\theta\cos\theta & \cos^2\theta - \sin^2\theta \end{bmatrix} \quad (4.77)$$

This matrix for 3-D problems when the old and the new out of plane coordinate directions coincide, becomes;

$$[T] = \begin{bmatrix} \cos^2\theta & \sin^2\theta & 0 & \sin\theta\cos\theta & 0 & 0 \\ \sin^2\theta & \cos^2\theta & 0 & -\sin\theta\cos\theta & 0 & 0 \\ 0 & 0 & 1 & 0 & 0 & 0 \\ -2\sin\theta\cos\theta & 2\sin\theta\cos\theta & 0 & \cos^2\theta - \sin^2\theta & 0 & 0 \\ 0 & 0 & 0 & 0 & \cos\theta & -\sin\theta \\ 0 & 0 & 0 & 0 & \sin\theta & \cos\theta \end{bmatrix} \quad (4.78)$$

Based on the proposed model, when the material is subjected to unloading or reloading the transformed $[D_t]$ becomes identical to the original one because the poisson's ratio is uniform in all directions and no variation in the mechanical properties can be imagined for changing the coordinate directios.

4.7 Non-proportional Loading

4.7.1 Stress-strain Relationship

The model described in sections 4.6.1 to 4.6.7 is proposed for proportional loading. But the behaviour and deformation of an infilled frame are associated with some discontinuities and non-proportionalities as a result of lack of fit, plasticity and also the following events:

- occurrence of plastic hinges in frame members.
- shear failure or slip at joints
- cracking in either frame or infill materials.
- local crushing especially at the loaded corners of panel

These events induce some stress redistributions which are not necessarily proportional to the current stresses. As a result, the principal directions may rotate and in some regions the material may be subject to unloading while the external loads have not changed.

In order to account for such non-proportional changes, the following approach has been employed to determine the true path in the stress-strain co-ordinate system.

Assume a particle subjected to a set of multiaxial strains and stresses represented by point E_1 on the most compressive stress-EUS envelope curve shown in Fig 4.25. When this particle is further loaded on line E_1R up to the new strain and stress levels, point R , such a load increment might not be proportional to the previous one. Therefore it is convenient to assume that the particle is, first, unloaded down to the zero stress level, line E_1P . In this unloading, the material behaves in a purely elastic and linear manner as described in section 4.6.6. The plastic equivalent uniaxial strain, O_1P , and the modulus of elasticity of the material E_{ul} , remain unchanged.

Now the effective equivalent uniaxial strains, ϵ_{ue} (PR' in Fig 4.25), can be calculated using the total and the residual plastic strains, $\{\epsilon_p\}$ (O_1P in fig 4.25), from Eq 4.42 as follows:

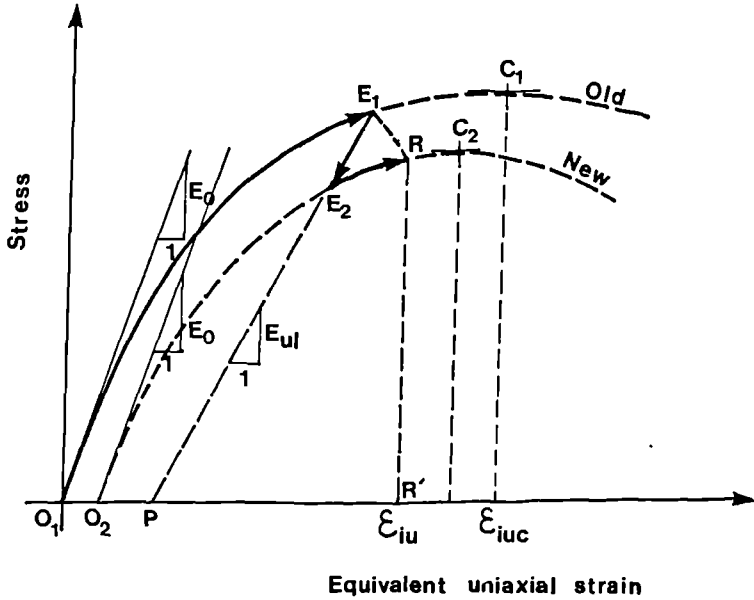


Figure 4.25 Proposed Model for Non-proportional Triaxial Load Increment

$$\{\epsilon_{ue}\} = [C]^{-1}\{\epsilon - \epsilon_p\} \quad (4.79)$$

Where $[C]$ involves the secant Poisson's ratios discussed in Section 4.6.2.

The effective **EUS** values permit the new stress proportions to be calculated and the new stress-**EUS** envelope curve, $O_2E_2C_2$, to be drawn such that the unloading line (corresponding to the current unloading modulus, E_{u1} or E_2P in Fig 4.25) matches the unloading line of the old envelope curve, E_1P . This permits the material to be reloaded on the unloading line up to point E_2 on the new envelope curve while undergoing the new stress proportions.

The loading is further continued with the same stress proportion as that of the reloading up to point R where the total effective **EUS** is met.

4.7.2 Poisson's Ratios under Non-proportional Loading

The Secant Poisson's ratios can be calculated from Eq 4.63 which involves an integration. The integral must be carried out over the whole path of the stress-**EUS** curve. As shown in Fig 4.25, a non-proportional loading can be converted into a linear elastic branch, line PE_2 , with a constant tangential poisson's ratio equal to the initial poisson's ratio, ν_0 , and a non-linear elastoplastic branch, curve E_2R , with variable poisson's ratio as given by Eqs 4.64 and 4.65. For the case when e_R is less than unity the integral can be split into the linear and non-linear parts. ie;

$$v_{ij} = \frac{1}{e_R} \left[\int_0^{e_E} v_0 de + \int_{e_E}^{e_R} v_{ij} de \right] \quad (4.80)$$

Substituting for v_{ij} from Eq 4.64 and executing the integrals leads to:

$$v_{ij} = v_0 \left[1 + k f_{ij} (e_R^n - e_E^{n+1}) / e_R \right] \quad (4.81)$$

The k and f_{ij} values are given in section 4.6.5.

4.7.3 Proposed Incremental Stress-strain Relationship for Non-proportional Load Increment

As shown in Fig 4.25 the stress and strain increments follow the path E_1R which is neither tangent to the old nor to the new envelope curves. An accurately derived incremental stress-strain relationship has not been attempted by the author, but numerical examination of some practical examples showed that the proportional incremental stress-strain relationship developed in section 4.6.7 can successfully be used in the practical examples whose orientation of principal directions and principal stress proportions remain nearly consistent in two successive load increments. If however, such a solution is not successful for some reason, the unloading elasticity matrix, $[D_t]$, formed by the overestimated values for stiffness as discussed in Section 4.6.7, i.e. $E_t = E_{u1}$ and $v = v_0$, leads to a secured but rather slow convergence.

4.8 Cracking and Cracked Materials

4.8.1 Cracking

Cracking of concrete material is generally modeled by a linear-elastic fracture relationship, Fig 4.1. Two fracture criteria are commonly used, the maximum principal-stress criterion and the maximum principal-strain criterion, Fig 4.26. When a principal stress or strain exceeds its limiting value, a crack is assumed to occur in a plane normal to the direction of the offending principal stress or strain. A more elaborate and realistic criterion is the proposed strength criterion based on the results of Kupfer et al (55) described in section 4.5. The proposed criterion is compared with the two fracture criteria in Fig 4.26.

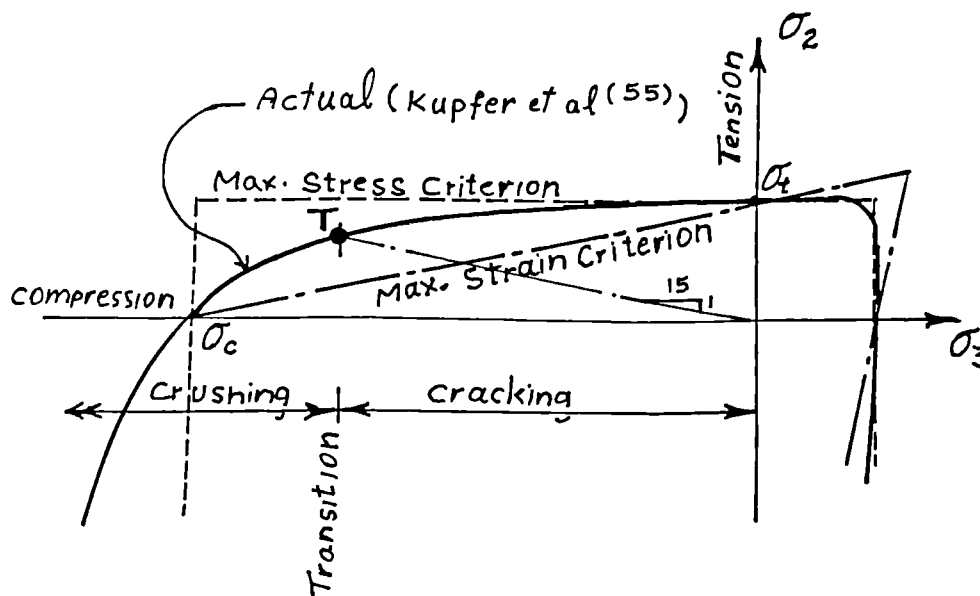


Figure 4.26 Different Fracture Criteria for Concrete in Tension

According to the experiment of Kupfer et al⁽⁵⁵⁾, at the biaxial failure surface, when the absolute value of the ratio of tensile to compressive principal stresses exceeds approximately 1/15, the mode of failure is tension cut off at the peak stress. Otherwise the material fails by a gradual crushing. In this project, the above specified tensile/compressive stress ratio, 1/15, was generalized to multiaxial loading as the transition between the tensile and compressive failure modes while the effect of intermediate principal stress on this transition was ignored.

4.8.2 Cracked Material

Once a crack has formed, it is generally assumed that no tensile stress can be supported across the crack. However, material parallel to the crack is still capable of carrying stress according to the uniaxial or biaxial conditions prevailing parallel to the crack. On increased loading, further cracks are allowed to occur.

In reinforced concrete cracks are more frequent and therefore, the crack width is less than in unreinforced concrete. The following effects proved to have a major influence on the behaviour of a cracked reinforced concrete element (39):

- i) tensile stiffening
- ii) aggregate interlock
- iii) dowel action

The tensile stiffening effect is usually accounted for indirectly as follows:

- a) By assuming that the loss of tensile strength in concrete appears gradually.
- b) By increasing the stiffness of steel.

The former choice was first introduced by Scanlon(67) as shown in Fig 4.10 and is more popular, but the latter choice seems to be more convenient for infilled frame structures composed of different materials, including concrete blocks and mortar which are not necessarily reinforced and for which the Scanlon model may lead to unrealistic results.

The aggregate interlock is usually accounted for by assuming a perfect or partial shearing stiffness for crack surfaces(39). In this project, however, the interlocking behaviour is accounted for by a proposed new approach to crack modeling given in the following sections.

The dowelling action effect is either ignored or allowed for by increasing the shearing stiffness at crack surfaces.

Cracks in a cracked material may close and open again in later stages of the loading. Opening and closing of cracks is measured by crack strain, ϵ_{cr} , which is assumed to be distributed uniformly within the material. In the following sections the mechanical behaviour of a cracked material is modeled for plane stress condition. This model also deals with double sets of cracks in different orientations.

4.8.3 Proposed Slip-dilatancy Crack Model

4.8.3.1 General Concept

Consider a particle of brittle material under biaxial stresses loaded to failure. When the criteria outlined in section 4.8.1 are met, the material fails in a tensile manner i.e. the particle would crack through one or more planes perpendicular to the most tensile principal stress direction, Fig 4.27(a). The surface of such cracks within the material is irregular and rough, Fig 4.27(b).

If normal stress across the crack is constant, any relative tangential displacement, s , or slip, between the opposite surfaces of the crack, is always accompanied by a relative normal displacement, w , or crack width. This is called "crack dilatancy". Based on this phenomenon the shape of the crack surface may be idealized as a regular trapezoidal shape as shown in Fig 4.27(c) with a dilatancy angle of α where:

$$\beta = \text{Tan}\alpha = \frac{w}{s} \quad (4.82)$$

denotes the dilatancy ratio. The value of β can be adjusted by changing the angle α in order to agree with the experiments on the material in question.

A crack may either be closed, interlocked or open as shown in Fig 4.27. The state of the crack can be determined as described in Sections 4.8.3.3 to 4.8.3.5. The following section deals with the stress-strain relationship of a cracked material under plane stress conditions.

4.8.3.2 Stress-strain Relationship for Cracked Materials under Plane-stress Conditions

Consider the cracked element shown in Fig 4.27 (a). The effective strains are the source of the biaxial stresses. The effective strains can be obtained by excluding

- a) the residual strains resulting from shrinkage, temperature effect and plasticity of the material and,
- b) the crack strains resulting from crack opening or crack interlocking.

The procedure is, therefore, to exclude the strain of group (a) from the total strains, and then to transform them into the crack directions, x' and y' , as shown in Fig 4.27 (a). The effective strains vector, ϵ_e , may then be calculated as follows:

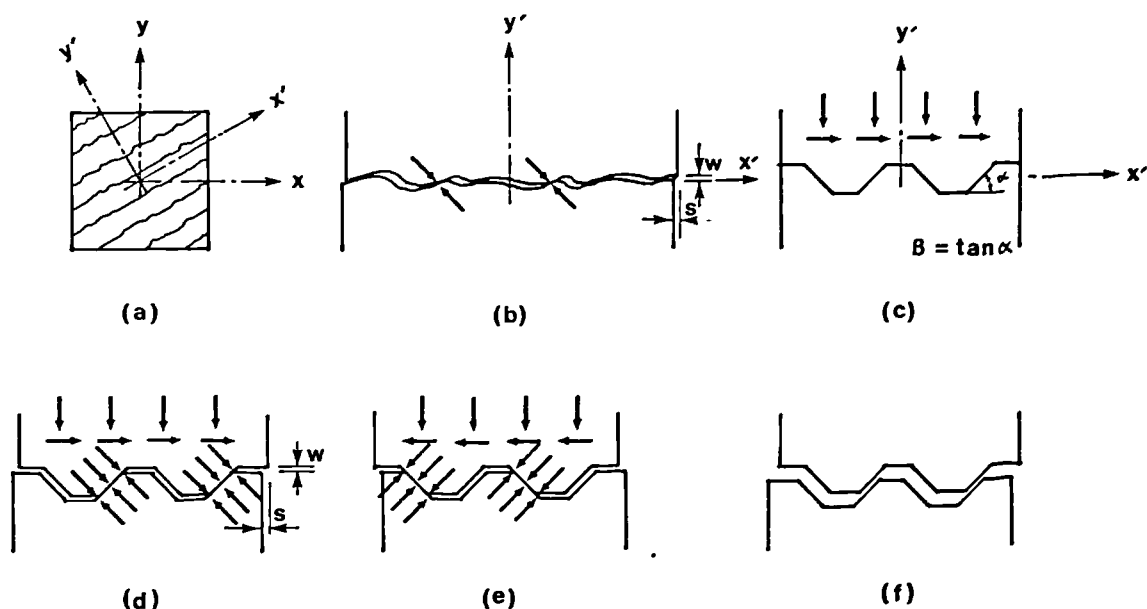


Figure 4.27 Crack Modelling; (a) orientation, (b) geometry, (c) idealization of the crack geometry, (d) interlocked crack (+ve shear), (e) interlocked crack (-ve shear) and (f) open

$$\epsilon_{x'e} = \epsilon_{x'} \quad (4.83)$$

$$\epsilon_{y'e} = \epsilon_{y'} - \epsilon_{sp} \quad (4.84)$$

$$\gamma_{x'y'} = \gamma_{x'y'} - \epsilon_{sl} \quad (4.85)$$

where ϵ_{sl} and ϵ_{sp} are the strain-equivalent values for the tangential and normal relative displacements respectively at the crack surfaces where:

$$\epsilon_{sl} = s/d_{cr} \quad (\text{slip strain}) \quad (4.86)$$

$$\epsilon_{sp} = w/d_{cr} \quad (\text{separation strain}) \quad (4.87)$$

and d_{cr} denotes the cracks spacing.

Now the secant stress-strain relation can be written as:

$$\{\sigma\} = [D]\{\epsilon_e\}$$

where:

$$[D] = \frac{E}{1-\nu^2} \begin{bmatrix} 1 & \nu & 0 \\ \nu & 1 & 0 \\ 0 & 0 & (1-\nu)/2 \end{bmatrix}$$

and ν signifies the Poisson's ratio derived for principal directions of stress. $[D]$ is independent of co-ordinate directions because its transformed terms are identical to its original terms. Therefore the secant stress-strain relation in crack directions can be written as:

$$\begin{bmatrix} \sigma_{x'} \\ \sigma_{y'} \\ \tau_{x'y'} \end{bmatrix} = \frac{E}{1-\nu^2} \begin{bmatrix} 1 & \nu & 0 \\ \nu & 1 & 0 \\ 0 & 0 & (1-\nu)/2 \end{bmatrix} \begin{bmatrix} \epsilon_{x'} \\ \epsilon_{y'} - \epsilon_{sp} \\ \gamma_{x'y'} - \epsilon_{sl} \end{bmatrix} \quad (4.88)$$

ϵ_{sp} and ϵ_{sl} are to be calculated as described in the following sections.

4.8.3.3 Material with Open Cracks

When cracks are open, the shear and normal stresses, $\sigma_{y'}$ and $\tau_{x'y'}$, equal zero. Setting these in Eq 4.88 gives:

$$\epsilon_{sp} = \epsilon_{y'} + \nu\epsilon_{x'} \quad (4.89)$$

$$\epsilon_{sl} = \gamma_{x'y'} \quad (4.90)$$

As can be seen from Fig 4.27 the geometry of the crack interface requires that for an open crack;

$$\frac{w}{|s|} > \beta \quad (4.91)$$

combining the above with Eqs 4.86 and 4.87 gives:

$$|\epsilon_{sl}| = < \frac{\epsilon_{sp}}{\beta} \quad (4.92)$$

Substituting for ϵ_{sp} and ϵ_{sl} from Eqs 4.89 and 4.90 into Eq 4.92 leads to the necessary and sufficient condition for an open-cracked material expressed as follows:

$$Y + \nu X > \beta \quad (4.93)$$

where:

$$X = \frac{\epsilon_{x'}}{|\gamma_{x'y'}|} \quad \text{and} \quad Y = \frac{\epsilon_{y'}}{|\gamma_{x'y'}|} \quad (4.94)$$

When cracks are open the separation and slip strain can be calculated from Eqs 4.89 and 4.90 respectively.

4.8.3.4 Material with Closed Cracks

When cracks are closed, no relative displacement prevails at the crack surfaces i.e: $s = w = 0$. It may, thus, be concluded from Eqs 4.86 and 4.87 that $\epsilon_{s1} = \epsilon_{sp} = 0$.

The frictional resistance at a crack may be assumed to be mainly due to the geometry of the surface, which was idealized as a trapezoidal shape in Fig 4.27 (c). Therefore the surface friction over the parts of the crack surface in contact, may be ignored and it may be assumed that the forces are transferred normal to these parts as shown in Fig 4.27(d) or 4.27(e). The above assumptions lead to the conclusion that should a crack remains closed, the following inequality must be satisfied:

$$|\tau_{x'y'}| < -\beta\sigma_{y'} \quad (4.95)$$

Substituting for $\sigma_{y'}$ and $\tau_{x'y'}$ from Eq 4.88 (while equating ϵ_{s1} and ϵ_{sp} to zero) into Eq 4.95, leads to:

$$y + vx < -\frac{1-\nu}{2\beta} \quad (4.96)$$

which is the necessary and sufficient condition to ensure the cracks are closed.

4.8.3.5 Material with Interlocked Cracks

When neither of the conditions of Eq 4.93 and 4.96 are satisfied, the cracks are interlocked. The interactive forces, are therefore transferred normal to the surfaces in contact as shown in Fig 4.27(d) and (e) and the following relations can be derived:

$$|\tau_{x'y'}| = -\beta\sigma_{y'} \quad (4.97)$$

$$|\epsilon_{s1}| = \epsilon_{sp}/\beta \quad (4.98)$$

Substituting the normal and shear stresses, $\sigma_{y'}$ and $\tau_{x'y'}$, from Eq 4.88 into Eq 4.97 and combining with Eq 4.98 leads to the separation and slip strains as follows:

$$\epsilon_{sp} = \frac{\beta [(1-\nu) |\gamma_{x'y'}| + 2\beta(\nu\epsilon_{x'} + \epsilon_{y'})]}{1-\nu+2\beta^2} \quad (4.99)$$

and,

$$\epsilon_{s1} = \frac{R}{\beta} \epsilon_{sp} \quad (4.100)$$

where: $R = \gamma_{x'y'} / |\gamma_{x'y'}| \quad (4.101)$

The criteria outlined in sections 4.8.3.2 to 4.8.3.4 are represented in Fig 4.28, where the strain space is divided into three zones each associated with either states of open, interlocked or closed cracks. A cracked material may develop another set of cracks. This is discussed in section 4.8.5

4.8.4 Proposed Incremental Stress-strain Relationship for Cracked Materials

As described in Section 4.8.3.1 a cracked material may have open, interlocked or closed cracks. When cracks are closed the incremental stress-strain relationship can be established as for a non-cracked material as discussed in section 4.6.7. When cracks are open the material is under uniaxial stress parallel to the cracks. Therefore the stress-strain relation can be written as:

$$\{d\sigma\} = [D_t]\{d\varepsilon\} \quad (4.102)$$

where:

$$[D_t] = E_t \begin{bmatrix} 1 & 0 & 0 \\ 0 & 0 & 0 \\ 0 & 0 & 0 \end{bmatrix} \quad (4.103)$$

E_t is the tangent modulus of the material described in section 4.3.1. $[D_t]$ must be transformed into the global co-ordinates, \mathbf{x} and \mathbf{y} , using Eq 4.75.

When cracks are interlocked the elasticity matrix may be derived taking into account the relative displacements at the interlocking interfaces. The mathematical work has been avoided by adopting the $[D_t]$ matrix derived by Bazant et al⁽⁷⁵⁾ for a cracked material with interlocked cracks.

This $[D_t]$ matrix is a nonsymmetric matrix involving the co-efficient of friction, k , and dilatancy ratio, β . The author's proposed model requires that $k=\beta$. This condition causes the Bazant et al $[D_t]$ matrix to become symmetric. This is given below in a different format and notations so as to match the notation used in this text:

$$[D_t] = \frac{E_t}{\phi} \begin{bmatrix} 1+2\beta^2/(1-\nu) & \nu & -R\nu\beta \\ \nu & 1 & -R\beta \\ -R\nu\beta & -R\beta & \beta^2 \end{bmatrix} \quad (4.104)$$

where:

$$\phi = 1-\nu^2+2\beta^2/(1-\nu) \quad \text{and} \quad R = \gamma_{x'y'} / |\gamma_{x'y'}|$$

Note that the first and second rows and columns of the Bazant et al proposed $[D_t]$ matrix had to be interchanged to correspond to the proposed crack directions. The proposed

[D_t] matrix can be transformed into global co-ordinate directions using Eq 4.75. Fig 4.29 compares the actual K and β values (76) and the proposed approximation based on K=β For two different normal stress levels.

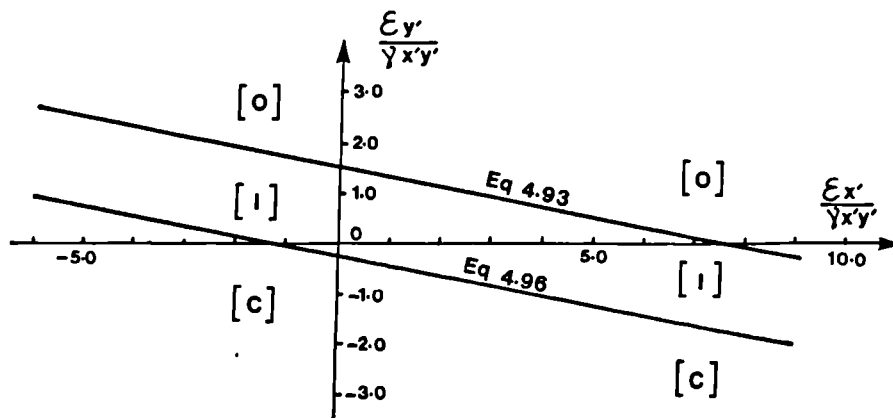


Figure 4.28 Possible States of a Single Cracked material.
 Note: The diagram is plotted for $\nu=0.2$ and $\beta=1.5$,
 O=open, I=interlocked and C=closed

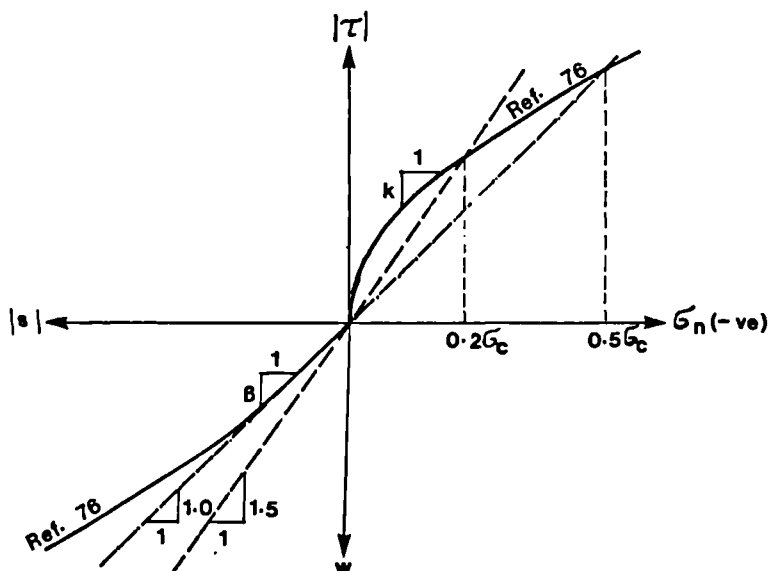


Figure 4.29 Determination of One Co-efficient for Both Crack Dilatancy, β , and Crack Friction, K , for Different Normal Stress Levels

4.8.5 Proposed Model for Double Sets of Cracks

4.8.5.1 General Concept and Definitions

While the primary cracks of a material in a plane stress structure are either closed or interlocked, the material is subjected to biaxial stresses and another set of cracks may develop normal to the most tensile principal stress direction provided that the criteria of tensile failure outlined in section 4.5 are violated.

As shown in Fig 4.30 the new cracks may develop at an angle γ_2 to the first crack set where $-\pi/2 < \gamma_2 < \pi/2$. As the surface of the new cracks are rough, the same model as proposed for the first crack set described in section 4.8.3 could also be applied for the new crack set. But since these lately developed secondary cracks are less likely to become interlocked they may for simplicity be assumed smooth or frictionless while separated and perfectly rough while closed. These cracks hereinafter will be called minor cracks. The minor cracks can be either open or closed only. The six major and minor crack state combinations shown in Table 4.1 are thus the only possible major and minor crack state combinations. These will be discussed in the following sections.

Note that a more sophisticated model permitting the minor cracks to become interlocked will improve the method and may accommodate a faster convergence. Such a complicated model was not attempted by the author.

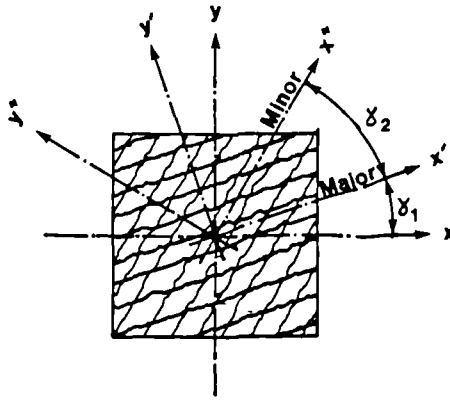


Figure 4.30 Double Cracked Material

Table 4.1 The Possible Major and Minor Crack State Combinations

	Major Cracks	Minor Cracks	Code
1	Open	Open	OO
2	Open	Closed	OC
3	Interlocked	Open	IO
4	Interlocked	Closed	IC
5	Closed	Open	CO
6	Closed	Closed	CC

4.8.5.2 Material with Closed Minor Cracks

When the minor cracks are closed the same procedure as for single cracked materials described in Section 4.8.3 can be applied to determine the state of the major cracks. While examining the major cracks the normal stress at minor cracks must also be examined to see whether it is compressive, ie. contact at the minor cracks is secured. The rest of this section, therefore, deals with development of the criteria to ensure $\sigma_{y''} < 0$. The

effective strains in major crack directions (x' and y') can be transformed into the minor crack directions (x'' and y'') using the transformation matrix of Eq 4.77 as follows:

$$\begin{Bmatrix} \epsilon_e \\ (x'', y'') \end{Bmatrix} = [T] \begin{Bmatrix} \epsilon_e \\ (x', y') \end{Bmatrix} \quad (4.105)$$

where γ_2 denotes the angle of minor to major crack directions and $\{\epsilon_e\} (x', y')$ is given by Eq 4.83 to 4.85.

The secant stress-effective strain relationship in minor crack directions can be worked out by the same procedure as was used to derive Eq 4.88 as follows:

$$\begin{Bmatrix} \sigma \\ (x'', y'') \end{Bmatrix} = [D] \begin{Bmatrix} \epsilon_e \\ (x'', y'') \end{Bmatrix} \quad (4.106)$$

Where $[D] (x'', y'')$ is given by Eq 4.88. Substituting for $\{\epsilon_e\} (x'', y'')$ from Eq 4.105 into Eq 4.106 leads to:

$$\begin{Bmatrix} \sigma \\ (x'', y'') \end{Bmatrix} = [D] \begin{Bmatrix} [T] \\ (x'', y'') \end{Bmatrix} \begin{Bmatrix} \epsilon_e \\ (x', y') \end{Bmatrix} \quad (4.107)$$

From Eq 4.107, $\sigma_{y''}$ can, now, be written in terms of the effective strains as follows:

$$\sigma_{y''} = \phi_2 \left[(K^2 + \nu) \epsilon_{x'} + (1 + \nu K^2) (\epsilon_{y'} - \epsilon_{sp}) - K(1 - \nu) (\gamma_{x' y'} - \epsilon_{s1}) \right] \quad (4.108)$$

Where $\phi_2 = E / [(1 - \nu^2) (1 + K^2)]$

and $K = \tan \gamma_2$

The value of $\sigma_{y''}$ can now be determined for various major crack states as follows:

a) Major cracks open:

σ_{sp} and σ_{s1} must, therefore, be substituted from Eq 4.89 and 4.90 respectively into Eq 4.108 to give:

$$\sigma_{y''} = \frac{\kappa^2}{1+\kappa^2} E \epsilon_{x'}$$

or: $\sigma_{y''} = \phi_3 \epsilon_{x'}$ (4.109)

where:

$$\phi_3 = \frac{\kappa^2}{1+\kappa^2} E$$

b) Major cracks closed:

ϵ_{sp} and ϵ_{s1} are both zero and Eq 4.108 becomes:

$$\sigma_{y''} = \phi_2 \left[(\kappa^2 + \nu) \epsilon_{x'} + (1 + \nu \kappa^2) \epsilon_{y'} - \kappa(1 - \nu) \gamma_{x'y'} \right] \quad (4.110)$$

c) Major cracks interlocked:

ϵ_{sp} and ϵ_{s1} should be substituted from Eq 4.99 and 4.100 into Eq 4.108 to give $\sigma_{y''}$.

Fig 4.31 gives a graphical representation for the criteria established to determine the state of cracks of a double cracked material within a normalized strain space defined by:

$$X = \epsilon_{x'} / |\gamma_{x'y'}| \quad \text{and} \quad Y = \epsilon_{y'} / |\gamma_{x'y'}|$$

Fig 4.31(a) is for the case when $\gamma_2 = -45$ and Fig 4.31(b) is for $\gamma_2 = +45$. The thick solid line in each graph indicates the transition between the states of closed and open minor cracks as discussed in this section.

When minor cracks are closed the separation and slip strains can be calculated from Eqs 4.89 and 4.90 or Eqs 4.99 and 4.100 when the major cracks are open or interlocked respectively.

4.8.5.3 Materials with Open Minor Cracks

As proposed in section 4.8.5.1 the minor cracks are assumed to be rough when they are closed and perfectly smooth when they are open.

At an open minor crack, stresses are as follows:

$$\left. \begin{aligned} \sigma_x'' &= E\varepsilon_x''e \\ \sigma_y'' &= 0 \\ \tau_{x''y''} &= 0 \end{aligned} \right\} (4.111)$$

where $\varepsilon_x''e$ denotes the effective strain parallel to the minor cracks which is independent of the separation and slip strains of these cracks. $\varepsilon_x''e$ can be calculated in terms of effective strains in the major crack directions using the transformation matrix given by Eq 4.77 as follows:

$$\varepsilon_x''e = \cos^2\gamma_2\varepsilon_{x'}e + \sin^2\gamma_2\varepsilon_{y'}e + \sin\gamma_2\cos\gamma_2\gamma_{x'y'}e \quad (4.112)$$

The only non-zero stress component, σ_x'' , may be transformed into major crack directions as follows:

$$\begin{aligned} \sigma_{x'} &= \cos^2\gamma_2(E\varepsilon_x''e) \\ \sigma_{y'} &= \sin^2\gamma_2(E\varepsilon_x''e) \\ \tau_{x'y'} &= \sin\gamma_2\cos\gamma_2(E\varepsilon_x''e) \end{aligned} \quad (4.113)$$

Having derived these stress components the state

of the major cracks can thence be verified as described below:

a) Major cracks interlocked (IO):

From Eq 4.97 the necessary condition for equilibrium of stresses at major cracks can be written as:

$$R\tau_{x'y'} = -\beta\sigma_{y'} \quad (4.114)$$

Substituting for $\tau_{x'y'}$ and $\sigma_{y'}$ from Eq 4.113 leads to:

$$K = \text{Tan}\gamma_2 = - \frac{R}{\beta} \quad (4.115)$$

Eq 4.115 is the only condition for an open-minor-crack material to become interlocked at its major cracks. This condition is independent of the effective strains, but it depends on the angle of the minor cracks to the major ones, γ_2 . Any arbitrary major crack separation strain, ϵ_{sp} , leads to a unique ϵ_{xe} which is the only non-zero stress component. This will be further verified below.

We may define an arbitrary major crack separation strain, ϵ_{sp} , and its corresponding slip strain, ϵ_{s1} , and write Eq 4.112 in terms of the total strains as follows:

$$\epsilon_{xe} = \text{Cos}^2\gamma_2\epsilon_{x'} + \text{Sin}^2\gamma_2(\epsilon_{y'} - \epsilon_{sp}) + \text{Sin}\gamma_2\text{Cos}\gamma_2(\gamma_{x'y'} - \epsilon_{s1})$$

Substituting for ϵ_{s1} as given by Eq 4.100 leads to:

⋮

$$\epsilon_{xe} = \text{Cos}^2\gamma_2\epsilon_{x'} + \text{Sin}^2\gamma_2\epsilon_{y'} + \text{Sin}\gamma_2\text{Cos}\gamma_2\gamma_{x'y'} - \epsilon_{s1}(\text{Sin}^2\gamma_2 + (R/\beta)\text{Sin}\gamma_2\text{Cos}\gamma_2)$$

Substituting the value of R/β from Eq 4.115, the 4th term of the above equation vanishes showing that the values of major crack strains do not affect the value of $\epsilon_x''_e$ and subsequently the values of the stresses of Eq 4.113 have no influence on $\epsilon_x''_e$.

The above conclusion proves that the state of interlocked-open, IO, may occur only when the angle of minor to major cracks takes a certain value given by Eq 4.115 and it is only a mechanism by which material can alter from IO to CO state without any influence on the existing stresses. Therefore the IO state may be substituted by its alternative state, CO, without any harming effect.

b) Major cracks closed (CO):

When the stress normal to the major cracks is compressive, the state of these cracks is either interlocked or closed. Since with open minor cracks any interlocked major cracks can alter into closed major cracks, as discussed in the preceding subsection, the condition of $\sigma_y' < 0$ is the necessary and sufficient condition in an open-minor-crack material for its major cracks remain closed. Considering Eq 4.113, such a condition can be written as:

$$\epsilon_x''_e < 0 \quad (4.116)$$

Since major cracks are closed, $\epsilon_x''_e = \epsilon_x''$ and the above condition can be written as:

$$\epsilon_x'' < 0 \quad (4.117)$$

Using the transformation matrix of Eq 4.87, Eq 4.117 can be written in terms of the major crack direction strains as:

$$\cos^2\gamma_2 \varepsilon_{x'} + \sin^2\gamma_2 \varepsilon_{y'} + \sin\gamma_2 \cos\gamma_2 \gamma_{x'y'} < 0$$

or:

$$\frac{1}{K^2} \varepsilon_{x'} + \varepsilon_{y'} + \frac{1}{K} \gamma_{x'y'} < 0 \quad (4.118)$$

Eq 4.118 is the necessary and sufficient condition for an open-minor-crack material to have closed major cracks.

The minor crack separation and slip strains, ε_{sp2} and ε_{s12} , may now be calculated. Allowing for zero stresses at minor cracks, Eq 4.106 leads to:

$$\begin{aligned} \nu \varepsilon_{x''} + (\varepsilon_{y''} - \varepsilon_{sp2}) &= 0 \\ \gamma_{x''y''} - \varepsilon_{s12} &= 0 \end{aligned} \quad (4.119)$$

The values of the total strains in minor crack directions can be written in terms of the strains in the major crack directions using the transformation matrix of Eq 4.371 as follows:

$$\begin{Bmatrix} \varepsilon \\ \gamma \end{Bmatrix}_{(x'', y'')} = [T] \begin{Bmatrix} \varepsilon \\ \gamma \end{Bmatrix}_{(x', y')} \quad (4.120)$$

Substituting for $\begin{Bmatrix} \varepsilon \\ \gamma \end{Bmatrix}_{(x'', y'')}$ from Eq 4.120 into Eq 4.119 and solving for ε_{s12} and ε_{sp2} leads to:

$$\varepsilon_{sp2} = \frac{1}{1+K^2} \left[(\nu+K^2) \varepsilon_{x'} + (\nu K^2+1) \varepsilon_{y'} - K(1-\nu) \gamma_{x'y'} \right] \quad (4.121)$$

$$\varepsilon_{s12} = \frac{1}{1+\kappa^2} [2\kappa(\varepsilon_{y'} - \varepsilon_{x'}) + (1-\kappa^2)\gamma_{x'y'}] \quad (4.122)$$

c) Major cracks open (OO):

A material with open minor cracks may also have open major cracks. The double crack combination states are graphically represented in Fig 4.31.

4.8.6 Proposed Incremental Stress-strain Relationship for Double Cracked Materials

The incremental stress-strain relationship of a double cracked material can be determined using a similar approach to that given in Section 4.8.4 as follows:

a) Either major or minor cracks open (OC or CO):

$[D_t]$ must be taken the same as in Eq 4.103, but it must be written for the directions of the open cracks.

b) The both crack sets open (OO):

The material has no stiffness; $[D_t] = 0$.

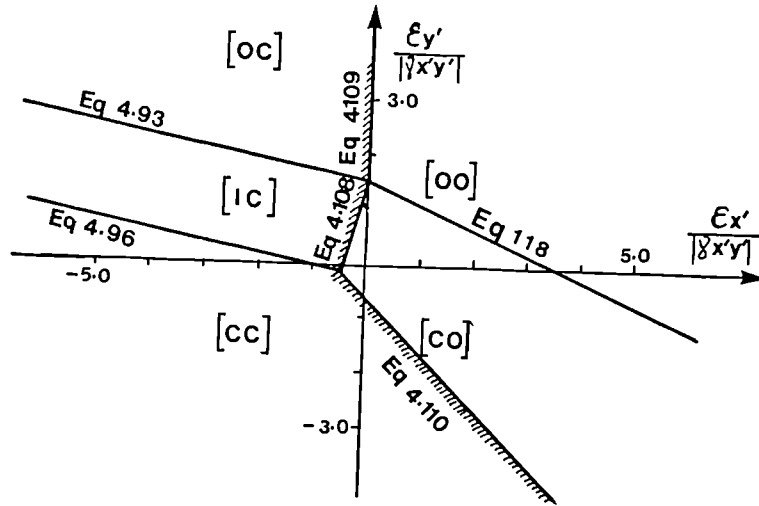
c) Interlocked-closed (IC):

$[D_t]$ is to be formed as given by Eq 4.104

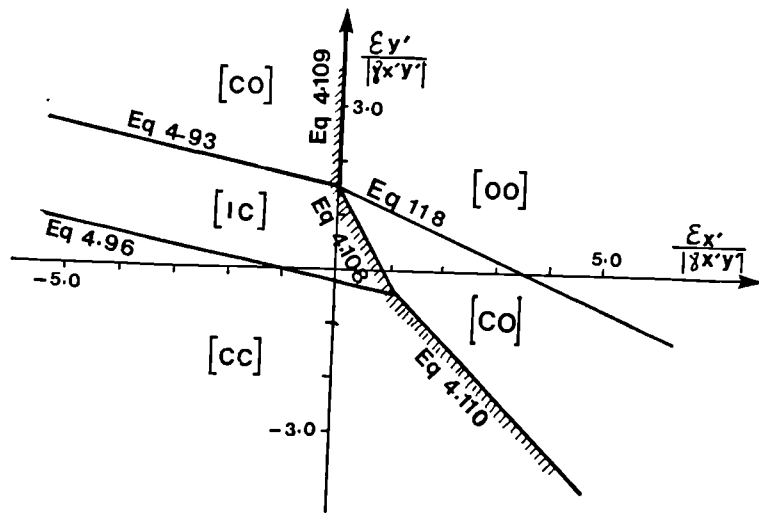
d) Closed-closed (CC):

$[D_t]$ is to be formed as if no crack exists.

The above calculated $[D_t]$ must be transformed into the global co-ordinates using Eq 4.75.



(a) $\delta_2 = -45^\circ, \nu = 0.2, \beta = 1.5$



(b) $\delta_2 = 45^\circ, \nu = 0.2, \beta = 1.5$

Figure 4.31 Possible States of Double Cracked Materials.
 Note: O=open, I=interlocked and C=closed
 Note: CO (closed-open state) is not valid for (b) above

4.9 Constitutive Formulation for Steel

4.9.1 General Characteristics of Steel

The general characteristics of steel are described in the standard text books, eg. Chen⁽³⁹⁾. Only a brief description is given here in order to establish the basis and notations upon which the constitutive formulation for steel is structured.

Fig 4.32 shows some typical stress-strain curves for different qualities of steel. The stress-strain curves for steel grades 40, 50 and 60 which are normally used in steel structures, are characterized normally by the following general features:

- i) An initial linear-elastic part up to (σ_y, ϵ_y) ;
- ii) a yield plateau from ϵ_y to ϵ_{st} (the typical ratio of ϵ_{st}/ϵ_y is 8 to 15),
- iii) a strain-hardening part from ϵ_{st} to the ultimate strain, ϵ_u , then a strain softening part (ϵ_u to ϵ_f),
- iv) an ultimate strength of 1.55 times the yield strength,

As the strength of the steel increases, its capacity for inelastic deformation, or ductility decreases. As shown in Fig 4.32, for grade 75 and higher the yield plateau in the stress-strain curve disappears.

The stress-strain curves for steel are generally assumed to be identical in tension and compression. The stress-strain relationship for steel subjected to unloading and reloading is approximately linear-elastic with a stiffness equal to the initial modulus of elasticity of steel, Fig 4.32 (b).

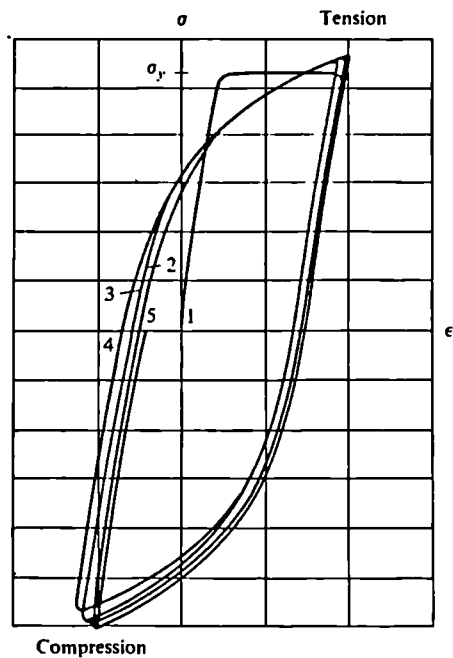
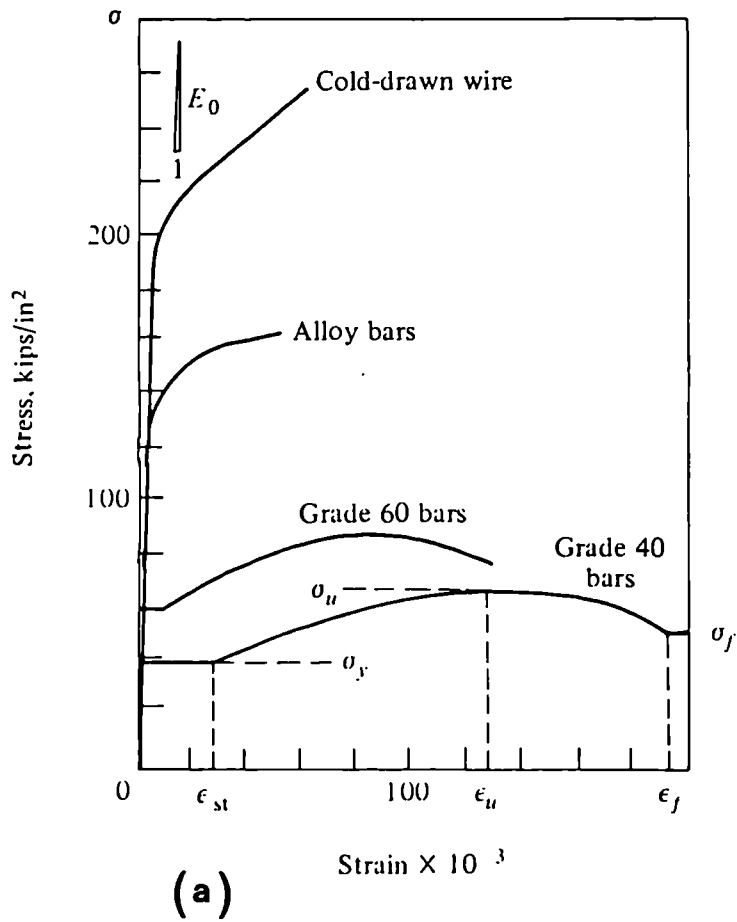


Figure 4.32 Stress-strain Curves for Steel(after Chen⁽³⁹⁾);
 (a) typical curves for reinforcement under
 monotonic loading and (b) typical curves for
 cyclic loading

4.9.2 Proposed Model for Stress-Strain Relationship of Steel Material under Uniaxial Stress

The uniaxial stress-strain relationship of steel is normally simplified into a multilinear model which can be adjusted to suit the experimental results. This is typically shown in Fig 4.32(a).

In this project a trilinear elastic-work hardening plasticity fracture model defined in section 4.2 is proposed. Fig 4.33(a) illustrates the model in more detail. As shown it is well adjustable to the experimental results of high strength steel bars normally used in RC elements. If however the steel material is of a low grade, the work hardening plasticity of the model, line **AB** in Fig 4.33(b), can be eliminated such that the horizontal part of the model, line **BC**, represents the plateau normally occurring immediately after the yield point, point **A**. Such a model, thus, is a linear-elastic perfect-plastic model which has already been introduced in section 4.2. Initially the unloading and reloading stress-strain curves are straight lines with slope equal to the initial modulus of the material so as to satisfy the typical steel behaviour, Fig 4.32(b). As the material is loaded beyond the yield point, Point **A** in Fig 4.33(b), it gains plastic strain such that after a full unloading to the zero stress the residual strain, would be considered as the total plastic strain gained during the preceding loading and unloading. The new yield point is thus the point at which strain unloading has started (point **R** in Fig 4.33) and the new

stress-strain curve is **PRC** in the bilinear model and **PRBC** in the trilinear model as shown in Fig 4.33(a) and 4.33(b) respectively.

4.9.3 Failure Criteria of Steel

Strength of steel material under multiaxial stresses is different from the uniaxial strength normally recorded by standard tests. As discussed in section 4.5.1 Von Mises and Tresca yield criteria are well verified in metal plasticity. The graphical representation of these yield surfaces are given in Fig 4.11 in 3-D space. In this project the popular Von Mises yield criterion is used. The general form of this criterion is given as:

$$f = 3J_2 = \sigma_y^2 \quad (4.123)$$

where J_2 is defined as the second invariant of the deviatoric stress tensor and is given(39) as follows:

$$J_2 = \frac{1}{6} \left[(\sigma_x - \sigma_y)^2 + (\sigma_y - \sigma_z)^2 + (\sigma_z - \sigma_x)^2 + \tau_{xy}^2 + \tau_{yz}^2 + \tau_{zx}^2 \right] \quad (4.124)$$

For plane stress problems the Von Mises criterion becomes:

$$f = \sigma_x^2 + \sigma_y^2 - \sigma_x \sigma_y + 3\tau_{xy}^2 = \sigma_y^2 \quad (\text{global}) \quad (4.125)$$

and

$$f = \sigma_1^2 + \sigma_2^2 - \sigma_1 \sigma_2 = \sigma_y^2 \quad (\text{principal}) \quad (4.126)$$

This elliptic biaxial yield criterion is plotted in Fig 4.34

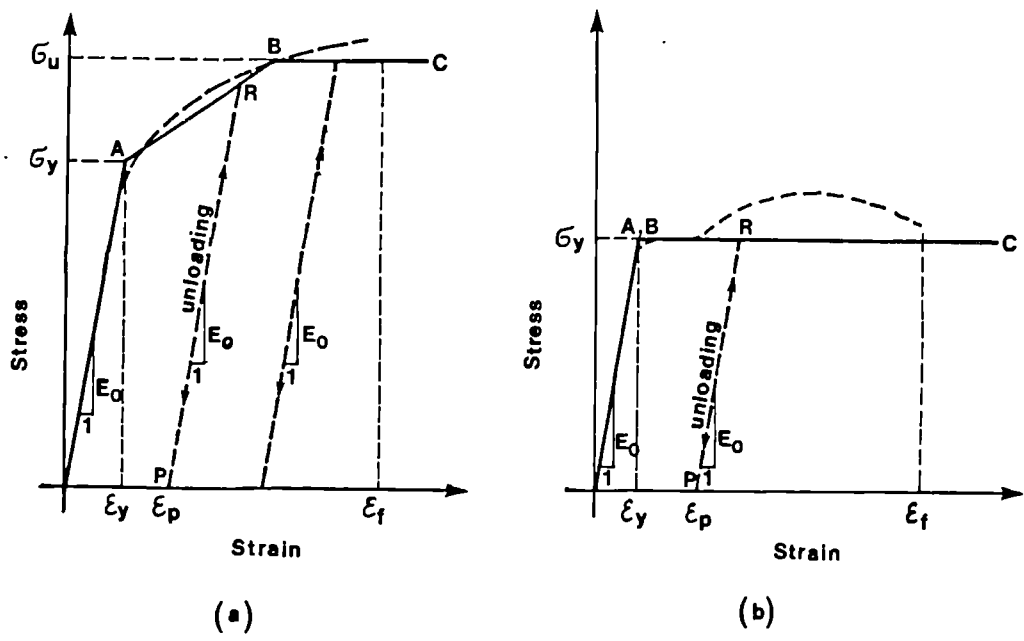


Figure 4.33 Proposed Stress-strain Relationship Model for Steel; (a) high strength steel and (b) low and medium strength steel

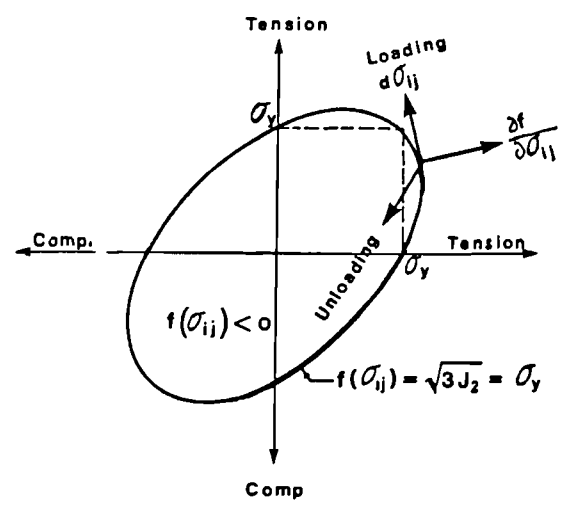


Figure 4.34 Von Mises Yield Criterion on The Co-ordinate Plane $\sigma_3=0$

4.9.4 Stress-strain Relationship of Ductile Material

4.9.4.1 Definitions and Basis of Elastic-Perfect Plasticity Theory

The uniaxial stress-strain relation discussed in section 4.9.2 led to a linear elastic-Perfect plasticity fracture model as shown in Fig 4.33. A similar model may be adopted for multiaxially loaded material. The general behaviour under a complex stress state can be defined by the following statements (39).

The material is elastic until it reaches the yield limit i.e, until a function of the stress components reaches a certain value. This is known as the yield function, yield surface or yield criterion. Such a function, as discussed in section 4.5.1, is generally given as follows:

$$f(\sigma_{ij}) = K \quad (4.127)$$

In the Von Mises criterion the yield surface is given as:

$$f(\sigma_{ij}) = \sqrt{3J_2} = \sigma_y$$

or

$$f(\sigma_{ij}) = J_2 = \frac{1}{3} \sigma_y^2 = k^2 \quad (4.128)$$

Then plastic deformation takes place without limit. For the plastic flow to continue, the state of stress must remain on the yield surface. This is known as the criterion for loading or consistency condition (39).

$$df = \frac{\partial f}{\partial \sigma_{ij}} d\sigma_{ij} = 0 \quad (4.129)$$

This flow strain is permanent; i.e. it remains when the stresses are removed or when the stress intensity drops below the yield value. This is known as the criterion for unloading algebraically expressed as:

$$df = \frac{\partial f}{\partial \sigma_{ij}} d\sigma_{ij} < 0 \quad (4.130)$$

In general the yield function, Eq 4.128, represents a six dimensional stress space. Only a 2-D representation of this function is shown in Fig. 4.34. The stress point cannot go outside the yield surface and plastic flow occurs when the stress point is on the yield surface and the additional loading $d\sigma_{ij}$ must lie in the tangent plane as shown in Fig 4.34.

It is not obvious whether there exists a necessary connection between f and the plastic strain-increment vector $d\varepsilon_{ij}(p)$. In general, we can introduce the concept of plastic-potential function $g(\sigma_{ij})$, which enables us to write the equations of plastic flow in the form

$$d\varepsilon_{ij}(p) = d\lambda \frac{\partial g}{\partial \sigma_{ij}} \quad (4.131)$$

Where $d\lambda$ is a positive scalar factor of proportionality.

It is normally acceptable in metal plasticity to assume that the yield function and plastic potential coincide; i.e. $f = g$. Thus,

$$d\varepsilon_{ij}(p) = d\lambda \frac{\partial f}{\partial \sigma_{ij}} \quad (4.132)$$

and plastic flow develops along the normal to the yield surface. Relation 4.132 is called the associated flow rule (39).

4.9.4.2 Stress-Strain Relationship under Multiaxial Stress Conditions

Based on the particulars of the elastic-perfect plasticity theory outlined in Section 4.9.4.1, the overall stress-strain relation has been developed as follows:

When a particle of a ductile material is loaded to the yield surface, it is actually forced to a new strain level which includes plastic strains such that:

$$\{\epsilon\} = \{\epsilon_e\} + \{\epsilon_p\} + \{\Delta\epsilon_p\} \quad (4.133)$$

where $\{\epsilon\}$ and $\{\epsilon_e\}$ denote the total elastoplastic strain and the total elastic strain vector respectively. $\{\epsilon_p\}$ signifies the accumulated plastic strain vector not including the plastic strains, $\{\Delta\epsilon_p\}$, achieved during the current load increment.

The stresses are directly related to the elastic strains as given in Eq 4.73 or 4.74 for 2 and 3 dimensional stress space respectively. These relations may generally be written as:

$$\begin{aligned} \{\sigma\} &= [D_e]\{\epsilon_e\} \\ \{\epsilon_e\} &= [N_e]\{\sigma\} \end{aligned} \quad (4.134)$$

The secant form of the elasticity matrix, $[D_e]$, and its inverse matrix, $[N_e]$, are formed by the elastic poisson's ratio ν_0 and the initial tangent elasticity modulus, E_0 .

Substituting for $\{\epsilon_e\}$ from Eq 4.134 into Eq 4.133 leads to:

$$\{\epsilon'\} = \{\epsilon - \epsilon_p\} = [N]\{\sigma\} + \{\Delta\epsilon_p\} \quad (4.135)$$

A stress-strain relation may be established from Eq 4.135 only when $\{\Delta\epsilon_p\}$ can be related to the current stress vector $\{\sigma\}$. This may be achieved by writing Eq 4.132 for the Von Mises yield criterion as follows:

$$f = J_2 ; \quad \text{as given by Eq 4.128}$$

$$\Delta\epsilon_{ij(p)} = \Delta\lambda \frac{\partial J_2}{\partial \sigma_{ij}}$$

Substituting for J_2 from Eq 4.124 leads to:

$$\Delta\epsilon_{ij(p)} = \Delta\lambda s_{ij}$$

where s_{ij} denotes the deviatoric stresses. For principal directions, the above relation leads to:

$$\Delta\epsilon_{ij(p)} = \Delta\lambda (\sigma_i - \sigma_m) \quad (4.136)$$

where σ_m is the hydrostatic stress defined as:

$$\sigma_m = \frac{1}{3} (\sigma_1 + \sigma_2 + \sigma_3) \quad (4.137)$$

Substituting for σ_m from Eqs 4.137, Eq 4.136 can be written in matrix form as:

$$\{\Delta\epsilon_p\} = \frac{1}{3} \Delta\lambda \begin{bmatrix} 2 & -1 & -1 \\ -1 & 2 & -1 \\ -1 & -1 & 2 \end{bmatrix} \{\sigma\} \quad (4.138)$$

or

$$\{\Delta\epsilon_p\} = [C]\{\sigma\} \quad (4.139)$$

Substituting for $\{\Delta\epsilon_p\}$ from Eq 4.139 into Eq 4.135, for principal directions, leads to:

$$\{\epsilon'\} = [N+C]\{\sigma\} \quad (4.140)$$

Solution of Eq 4.140 leads to the elastoplastic secant stress-strain relation as follows:

$$\{\sigma\} = [D_{ep}]\{\epsilon'\} \quad (4.141)$$

where

$$[D_{ep}] = \frac{E_0}{\phi} \begin{bmatrix} a & b & b \\ b & a & b \\ b & b & a \end{bmatrix}$$

$$\phi = (1-2\nu_0)(1+\nu_0+E_0\Delta\lambda)$$

$$a = (1/3)E_0\Delta\lambda+1-\nu_0$$

$$b = (1/3)E_0\Delta\lambda+\nu_0$$

Combining Eq 4.141 and the yield function, Eq 4.128, and solving for $\Delta\lambda$ leads to:

$$\Delta\lambda = \frac{1}{\sqrt{2}\sigma_y} \sqrt{[(\epsilon_1' - \epsilon_2')^2 + (\epsilon_2' - \epsilon_3')^2 + (\epsilon_3' - \epsilon_1')^2]} - \frac{1+\nu}{E_0} \quad (4.142)$$

where $\{\epsilon'\}$ denotes the effective strain defined as given in Eq 4.135. When $\Delta\lambda$ becomes negative or zero, it indicates that no plastic flow has taken place. In such a case the value of $\Delta\lambda$ must be taken as zero and $[D_{ep}]$ (Eq 4.141) reduces to the standard elastic matrix, $[D]$, Eq 4.74.

The above model of plasticity based on the Von Mises yield criterion and its associated flow rule is

known as the Prandtl-Reuss material which is the most widely used model (39)

Eq 4.136 states that:

- 1) The increment of plastic strains is proportional to the state of the deviatoric stresses.
- 2) The principal axes of stress and of plastic strain increment tensors coincide.
- 3) No plastic volume change can occur during plastic flow.
- 4) The ratios of plastic strain increments in the different directions are specified, but the actual magnitudes of the increments are determined by the magnitude of the actual increment in the work of plastic deformation dW_p . This is simply expressed (39) as:

$$\Delta W_p = \sigma_{ij} d\varepsilon_{ij}(p) = \Delta\lambda \sigma_{ij} s_{ij} = 2\Delta\lambda J_2$$

or:

$$\Delta W_p = (2/3)\Delta\lambda \sigma_y^2$$

4.9.4.3 Stress-Strain Relationship for Plane Stress Loading

The stress-strain relationship for multiaxial loading derived in section 4.9.4.2 led to Eqs 4.141 and 4.142. If the structure is subjected to plane stresses; ie:

$$\sigma_3 = 0 \tag{4.143}$$

The principal effective strain in this direction, ε_3' , is unknown. ε_3' can however be derived by combining Eq 4.143

and 4.141 leading to:

$$\epsilon_3' = - \frac{(\nu + (1/3)E_0\Delta\lambda)(\epsilon_1' + \epsilon_2')}{1 - \nu + (1/3)E_0\Delta\lambda} \quad (4.144)$$

$\Delta\lambda$ and ϵ_3' may now be calculated from Eq 4.144 and 4.142 using an iterative numerical method.

4.9.5 Incremental Stress-Strain Relationship for Ductile Materials

4.9.5.1 In Elastic State

The incremental stress-strain relation for an isotropic material loaded within the elastic range can be formed with the aid of the Hooke's "Elasticity Law" and use of "Indicial Notation" convention described by standard text books(39), as follows:

$$d\sigma_{ij} = K \cdot d\epsilon_{kk} \cdot \delta_{ij} + 2G \cdot d\epsilon_{ij} \quad (4.145)$$

$$d\epsilon_{ij} = \frac{1}{9K} \sigma_{kk} \cdot \delta_{ij} + \frac{1}{2G} s_{ij}$$

The first of the above can be written in the preferable form

$$d\sigma_{ij} = D_{ijmn}(\mathbf{e}) \cdot d\epsilon_{mn} \quad (4.146)$$

where:

$$D_{ijmn}(\mathbf{e}) = 2G \cdot \delta_{im} \cdot \delta_{jn} + (K - (2/3)G) \cdot \delta_{ij} \cdot \delta_{mn} \quad (4.147)$$

In the above relations, $d\sigma_{ij}$ and $d\epsilon_{mn}$ denote the incremental stress and strain tensors respectively. $d\epsilon_{ij}$ signifies the incremental deviatoric strain tensor and $D_{ijmn}(\mathbf{e})$ denotes

the incremental elasticity matrix $[D_e]$. The symbol δ is a special matrix (Kronecker Delta) written as:

$$\delta = \begin{bmatrix} 1 & 0 & 0 \\ 0 & 1 & 0 \\ 0 & 0 & 1 \end{bmatrix} \quad (4.148)$$

The components of this matrix, δ_{ij} , are unity if $i=j$ and zero if $i \neq j$. The shear and bulk modulus, G and K , are defined as:

$$G = \frac{E_0}{2(1+\nu)} \quad \text{and} \quad K = \frac{E_0}{3(1-2\nu)} \quad (4.149)$$

The above standard incremental stress-strain matrix for plane stress condition becomes:

$$\begin{bmatrix} d\sigma_x \\ d\sigma_y \\ d\sigma_{xy} \end{bmatrix} = \frac{E_0}{1-\nu^2} \begin{bmatrix} 1 & \nu & 0 \\ \nu & 1 & 0 \\ 0 & 0 & (1-\nu)/2 \end{bmatrix} \begin{bmatrix} d\epsilon_x \\ d\epsilon_y \\ d\gamma_{xy} \end{bmatrix} \quad (4.150)$$

and for multiaxial stress condition leads to:

$$\begin{bmatrix} d\sigma_x \\ d\sigma_y \\ d\sigma_z \\ d\tau_{xy} \\ d\tau_{yz} \\ d\tau_{zx} \end{bmatrix} = \phi \begin{bmatrix} a & \nu & \nu & 0 & 0 & 0 \\ & a & \nu & 0 & 0 & 0 \\ & & a & 0 & 0 & 0 \\ & & & b & 0 & 0 \\ \text{symmetry} & & & & b & 0 \\ & & & & & b \end{bmatrix} \begin{bmatrix} d\epsilon_x \\ d\epsilon_y \\ d\epsilon_z \\ d\gamma_{xy} \\ d\gamma_{yz} \\ d\gamma_{zx} \end{bmatrix} \quad (4.151)$$

where:

$$\phi = \frac{E_0}{(1+\nu)(1-2\nu)}, \quad a = 1-\nu \quad \text{and} \quad b = \frac{1-2\nu}{2}$$

4.9.5.2 In Elastoplastic State

When the material has shown some plasticity and the criterion of loading, Eq 4.129, has been met at the end of the previous iteration, the material will undergo elastoplasticity; i.e:

$$\{d\epsilon\} = \{d\epsilon_e\} + \{d\epsilon_p\} \quad (4.152)$$

Substituting for $\{d\epsilon_e\}$ and $\{d\epsilon_p\}$ from Eq 4.145 and 4.132 respectively leads to:

$$d\epsilon_{ij} = \frac{1}{9K} d\sigma_{kk} \cdot \delta_{ij} + \frac{1}{2G} ds_{ij} + d\lambda \frac{\partial f}{\partial \sigma_{ij}} \quad (4.153)$$

Combining the above with the consistency condition, Eq 4.129, and the Von Mises criterion, Eq 4.128 leads to:

$$d\sigma_{ij} = K \cdot d\epsilon_{kk} \cdot \delta_{ij} + 2G \cdot d\epsilon_{ij} - \frac{G}{K^2} s_{mn} \cdot d\epsilon_{mn} s_{ij} \quad (4.154)$$

Derivation of Eq 4.154 is given in detail elsewhere (39). This equation may be written in its preferable form as:

$$d\sigma_{ij} = D_{ijmn}(ep) \cdot d\epsilon_{mn} \quad (4.155)$$

$$\text{where: } D_{ijmn}(ep) = D_{ijmn}(e) + D_{ijmn}(p) \quad (4.156)$$

Substituting for $D_{ijmn}(e)$ from Eq 4.147 Eq 4.156 leads to:

$$D_{ijmn}(p) = - \frac{G}{K^2} s_{mn} \cdot s_{ij} \quad (4.157)$$

where k^2 is defined by Eq 4.128 and $D_{ijmn}(e)$ denotes the elasticity matrix given by Eq 4.151. The matrix $D_{ijmn}(ep)$ is referred to as the elastoplastic constitutive matrix(39).

Notice that if the incremental stresses are determined in the principal directions, no shear stress exists in these directions and s_{mn} or s_{ij} is zero for $m \neq n$ or $i \neq j$ respectively, indicating that for such cases $D_{ijmn}(p)=0$ and Eq 4.157 for its non-zero terms, leads to

$$D_{ijmn}(p) = D_{im}(p) = - \frac{G}{k^2} s_i \cdot s_m \quad (4.158)$$

where i and m denote the order number of the principal directions. Therefore Eq 4.156 reduces to:

$$[D_{ep}]_{6 \times 6} = [D_e]_{6 \times 6} + [D_p]_{3 \times 3} \quad (4.159)$$

where:

$$[D_p] = \frac{G}{k^2} \begin{bmatrix} s_1^2 & s_1 s_2 & s_1 s_3 \\ s_2 s_1 & s_2^2 & s_2 s_3 \\ s_3 s_1 & s_3 s_2 & s_3^2 \end{bmatrix} \quad (4.160)$$

and

$$s_i = \sigma_i - \frac{\sigma_1 + \sigma_2 + \sigma_3}{3}$$

where $k^2 = (1/3)\sigma_y^2$ and σ_1, σ_2 and σ_3 denote the current principal stresses which satisfy the Von Mises yield criterion, Eq 4.128. The resultant $[D_{ep}]$ matrix formed for the principal direction must be transformed into global coordinates by the transformation rule, Eq 4.75

4.9.5.3 Under Plane Stresses and in Elastoplastic State

Most of the problems encountered in practice and research work are concerned with plane stress loading. The steel frames used in infilled frame construction fall into this category. When the material in question is subjected to plane stresses the following is the only extra condition to satisfy:

$$d\sigma_3 = 0 \quad (4.161)$$

The elastoplastic constitutive matrix is, thus, a 3 x 3 matrix derived by the author as described below.

The stress components in 3-D principal directions can be written as:

$$d\sigma_1 = D_{11}d\epsilon_1 + D_{12}d\epsilon_2 + D_{13}d\epsilon_3 \quad (4.162)$$

$$d\sigma_2 = D_{21}d\epsilon_1 + D_{22}d\epsilon_2 + D_{23}d\epsilon_3 \quad (4.163)$$

$$d\sigma_3 = D_{31}d\epsilon_1 + D_{32}d\epsilon_2 + D_{33}d\epsilon_3 \quad (4.164)$$

where the terms D_{im} denote the elastoplastic incremental stress-strain matrix terms whereas the "ep" identifier has been dropped for simplicity.

Combining Eq 4.164 and 4.161 and solving for $d\epsilon_3$ gives:

$$d\epsilon_3 = - \frac{D_{31}}{D_{33}} d\epsilon_1 - \frac{D_{32}}{D_{33}} d\epsilon_2 \quad (4.165)$$

Substituting $d\epsilon_3$ from Eq 4.165 into Eqs 4.162 and 4.163 leads to:

$$d\sigma_1 = \left(D_{11} - \frac{D_{13}^2}{D_{33}} \right) d\varepsilon_1 + \left(D_{12} - \frac{D_{13}D_{23}}{D_{33}} \right) d\varepsilon_2$$

$$d\sigma_2 = \left(D_{21} - \frac{D_{23}D_{13}}{D_{33}} \right) d\varepsilon_1 + \left(D_{22} - \frac{D_{23}^2}{D_{33}} \right) d\varepsilon_2$$

These relations lead to the plane stress incremental stress-strain relation matrix as follows:

$$\{d\sigma\} = [D_{ep}]\{d\varepsilon\}$$

where:

$$[D_{ep}] = \begin{bmatrix} D_{11} & D_{12} & 0 \\ D_{21} & D_{22} & 0 \\ 0 & 0 & D_{33} \end{bmatrix} \quad (4.166)$$

where:,

$$D_{iJ} = D_{iJ} - \frac{D_{i3}D_{J3}}{D_{33}}$$

$$D_{33} = D_{44}$$

In these matrices D terms denote the corresponding terms of 3-D elastoplastic constitutive matrix as per Eq 4.159.

4.9.6 Stress-Strain Relationship for Reinforcement

Steel bars may be modeled as anisotropic steel layer or as single bars as described in sections 3.7.2 and 3.7.3 respectively. Since in the both cases the steel material is under uniaxial stress, the stress-strain relation matrix becomes;

for horizontally extended bars:

$$[D_{si}] = \begin{bmatrix} E_{si}r_{si} & 0 & 0 \\ 0 & 0 & 0 \\ 0 & 0 & 0 \end{bmatrix} \quad (4.167a)$$

and for vertically extended bars:

$$[D_{si}] = \begin{bmatrix} 0 & 0 & 0 \\ 0 & E_{si}r_{si} & 0 \\ 0 & 0 & 0 \end{bmatrix} \quad (4.167b)$$

where E_{si} and r_{si} denote the incremental modulus of elasticity and the ratio of the group i steel bars respectively, within the integration zone under consideration. For an inclined group of bars, $[D_{si}]$ may be computed by transforming Eq 4.167a into the appropriate angle using Eq 4.77.

4.10 Constitutive Formulation for Mechanical Behaviour of Interfaces and Joints

4.10.1 General

The step by step development of the F.E representation of interfaces has been discussed in detail in Chapter 3, leading to the new proposed interface element described in section 3.10.3. While the geometrical formulation was accomplished by introducing the proposed shape functions, the mechanical behaviour of interfaces is yet to be modelled. This constitutes the following:

- i) The criteria under which yielding, slip and/or separation occur.

- ii) The strain-relative displacement relationship of the interfaces both for the incremental changes and for the overall values.

These are discussed in the following sections.

4.10.2 Yielding, Slip and Separation Criteria

The shear strength and behaviour of interfaces and joints has been studied by many investigators (76 to 81). The shear strength of a bonded interface is generally considered as comprising:

- i) bond shear strength of the interface
- ii) the frictional resistance of the interface

The frictional resistance of the interface is normally calculated as the product of the normal stress σ_n and the coefficient of friction, μ , where μ is normally assumed to be constant for all normal stress levels. These lead to the "bond shear failure criterion" of the interface expressed algebraically as follows:

$$\begin{aligned} \text{or:} \quad |\tau| &= \sigma_{bs} - \mu\sigma_n \\ R\tau &= \sigma_{bs} - \mu\sigma_n \end{aligned} \quad (4.168)$$

where R is assigned either +1 or -1 when τ is positive or negative respectively and the sign of σ_n is considered to be $-ve$. for compression.

When the interface is not bonded or it has totally debonded in the course of loading, the first term in the

above function vanishes and Eq 4.168 becomes the "slip criterion" of the interface written as:

$$\tau = -\mu\sigma_n \quad (4.169)$$

These criteria (Eq 4.168 and 4.169) are graphically shown in Fig 4.35 by lines BC and OD respectively.

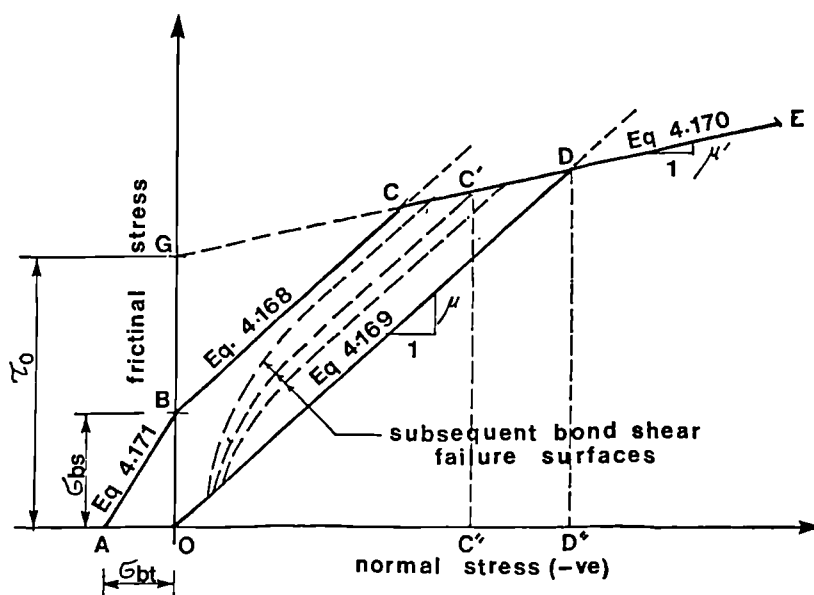


Figure 4.35 Criteria for Inelastic Behaviour of an Interface

When the interface constitutes a thin layer of a relatively soft material, like mortar in the bed joints of masonry structures, another effect may become the source of the permanent shear displacement by mean of plastic shear deformation or yielding of the confined joint material. This has been studied by Page (79) and Hegemier (81) for the bed joints of brick and grouted hollow concrete block masonry respectively. Such a criterion may be idealized by a straight line (line **GE**) with μ' slope. As shown in Fig 4.35 the joint "yielding criterion" can be algebraically expressed as:

$$R\tau = \tau_0 - \mu' \sigma_n \quad (4.170)$$

Fig 4.35 also shows the proposed "bond tensile failure criterion", represented by line **AB** to specify the normal tension and frictional shear stresses causing this type of failure. The function to represent the bond tensile failure criterion is, thus, written as:

$$\frac{R\tau}{\sigma_{bs}} + \frac{\sigma_n}{\sigma_{bt}} = 1 \quad (4.171)$$

where σ_{bs} and σ_{bt} denote bond shear and tensile strength of the interface respectively.

Table 4.2 lists some experimentally recorded values of the mechanical properties of interfaces and joints dealt with in practice.

Table 4.2 Experimental Data for Interfaces, Joints and Cracks

Type of Interface or joint	Ref	Bond Strength		μ, μ'	K_{sru} N/mm ³
		Tensile N/mm ²	Shear N/mm ²		
Interfaces:					
Steel on Concrete	77		0.38	0.65	1500
	24			0.41	145
	42			0.41	0.65
Mortar on Steel	42			0.44	0.76
Brick on Steel	42			0.5	0.67
Brick on Concrete	42			.62	0.52
Mortar on Concrete	42			0.42	0.54
Concrete on Concrete	42			0.44	0.63
Masonry bed Joints:					
Wire Cut Clay	78		0.30	0.50	
Solid Sand-lime	78		0.20	0.84	
Clay brick ($\tau_0 = 1.91$)	79	0.29	0.19	0.87, 0.11	18.01
Hollow block (net area)	80	0.40	0.52	1.07	
Hollow grouted block ($\tau_0 = 0.70$)	81	0.55	0.55	0.68	1.80
Lightweight Block	8	0.15	0.25	0.76	
Concrete Cracks	76				53.00

Notes:

μ = slope of the slipping criterion

μ' = slope of yielding criterion

K_{sru} = tangential stiffness of the interface after debonding

4.10.3 Stress-Displacement Relationship of Interfaces

4.10.3.1 General

The general relationship between stresses and relative displacements of the opposite surfaces of an interface is given by Eq 3.32. It is numerically convenient to write Eq 3.32 in terms of the effective relative displacements $\{e_e\}$, as follows:

$$\{\sigma\} = [D]\{e_e\} \quad (4.172)$$

where:

$$\{e_e\} = \begin{bmatrix} s_e \\ w_e \end{bmatrix} = \begin{bmatrix} s - s_0 \\ w - w_0 \end{bmatrix}, \quad \{\sigma\} = \begin{bmatrix} \tau \\ \sigma_n \end{bmatrix} \quad (4.173)$$

s_0 and w_0 are the total tangential and normal residual relative displacements. They comprise the lack of fit, yielding, slip and the separation effects (if any). s and w are the total tangential and normal relative displacements respectively. $[D]$ denotes the secant stiffness matrix of the interface corresponding to the current $\{e_e\}$. The effective relative displacement vector is purely elastic and there is no cross effect between its components. The shear and normal stresses are, therefore, independent of each other such that $[D]$ can be written as:

$$[D] = \begin{bmatrix} K_s & 0 \\ 0 & K_n \end{bmatrix} \quad (4.174)$$

In the following sections the values of K_s and K_n will be discussed for all the possible states of an interface.

4.10.3.2 Proposed Model Based on Experimental Observations

Fig 4.36(a) shows a number of shear-tangential displacement curves resulting from tests of concrete on steel carried out by King et al⁽⁴²⁾ using a shear box at different normal stress level. King et al idealized these curves by bilinear diagrams shown in Fig 4.36(b). The steep and straight line shows the elastic behaviour of the interface with a fairly high shear stiffness, K_{sru} , and the horizontal lines characterize the slip occurring under constant normal and shear stresses. This behaviour is exactly the same as that of the elastic-perfect plastic fracture model discussed for ductile materials. Such a simplification seems to be a fair idealization provided the interface has no bond resistance.

If however the interface is initially bonded, the shear stress-tangential displacement diagram must show an additional shearing resistance. This is in fact evident as shown in the tests carried out by Hegemier⁽⁸¹⁾ on bed-joints of a prototype concrete blockwork, Fig 4.37. These experiments also indicate that the event of bond shear failure is gradual and the higher is the absolute value of normal/shear stress ratio the more gradual the debonding process becomes.

All the above experimental observations may be put together to obtain a typical shear stress-relative displacement diagram as shown in Fig 4.38(a). The curves shown by dotted line up to yielding, represent the shear stress-tangential displacement relation provided the bond

shear failure and slip have been prevented.

From these experimental observations the shear stress-relative tangential displacement relation can be idealized as shown in Fig 4.38(b). The trilinear diagram **OABE** in this figure constitutes three distinct behaviours as follows:

- i) The linear elastic behaviour for bonded interface (Line **OA** with a very steep slope, K_s)
- ii) The gradual debonding (Line **AB**), i.e. gradual decrease in the shear stiffness from K_s to K_{sru}
- iii) The plateau characterizing slip while the shear and normal stresses and the shear stiffness, K_{sru} , remain unchanged.

The proposed debonding model, Line **AB**, requires that an unloading at Point **D**, Fig 4.38(b), follows line **DO** with slope K_{sr} and the subsequent reloading follows the same line up to point **D**, as shown in Fig 4.38(b). In such a case, the interface can be called a partially bonded interface with a subsequent bond shear failure criterion, Line **OC'** as shown in Fig. 4.35.

No experiment with recorded stiffness data is available (to the knowledge of the author) for bonded interfaces under tensile normal stress. Nevertheless, as it is evident, Fig 4.37, that for interfaces under a low compressive normal stress, the event of debonding is rather brittle, interfaces under tensile stress may be expected to behave in a similar brittle fashion. i.e, immediately following a linear elastic deformation up to the peak

stress, Point **F** in Fig 4.38(b), the interface loses all its bond strength and the shear stress suddenly drops down to $-\mu\sigma_n$ (Point **F''** as shown in Fig 4.38(b)).

Some experimental data obtained from different sources are listed in table 4.2. As shown in this table, a very high discrepancy can be noticed between the values of k_{sru} reported by different researchers. This may be attributed to either the unit conversion error (eg. taking N/mm^2 instead of N/mm^3) or the difficulties associated with refining and measuring a relatively high interface stiffness while the other materials conforming the interface demonstrate relatively much higher flexibility. Such a discrepancy becomes more obvious as different workers used different test approaches.

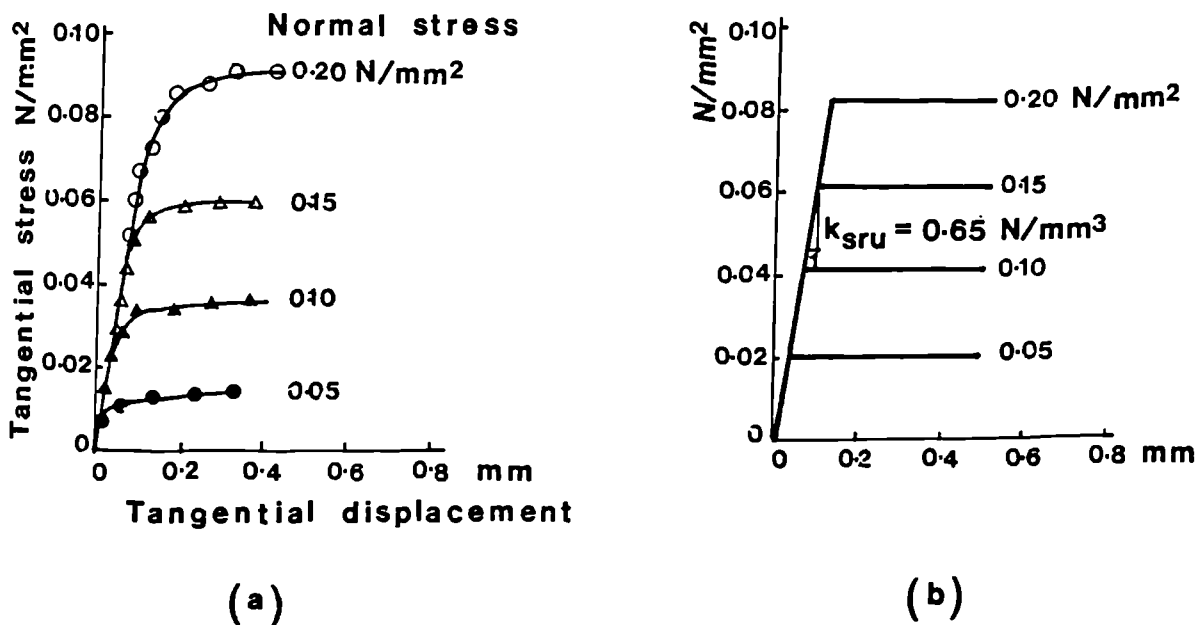
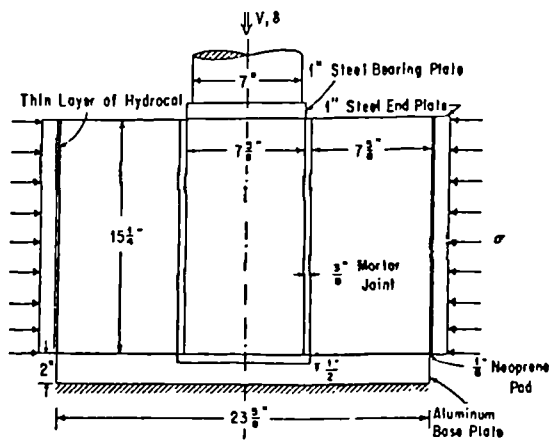
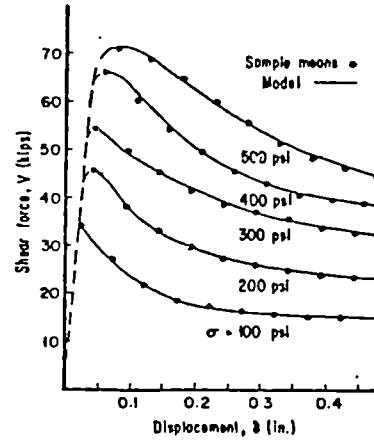


Figure 4.36 Concrete-on-steel Shear-relative Displacement Relationship; (a) actual and (b) idealized (after King and Pandy(42))

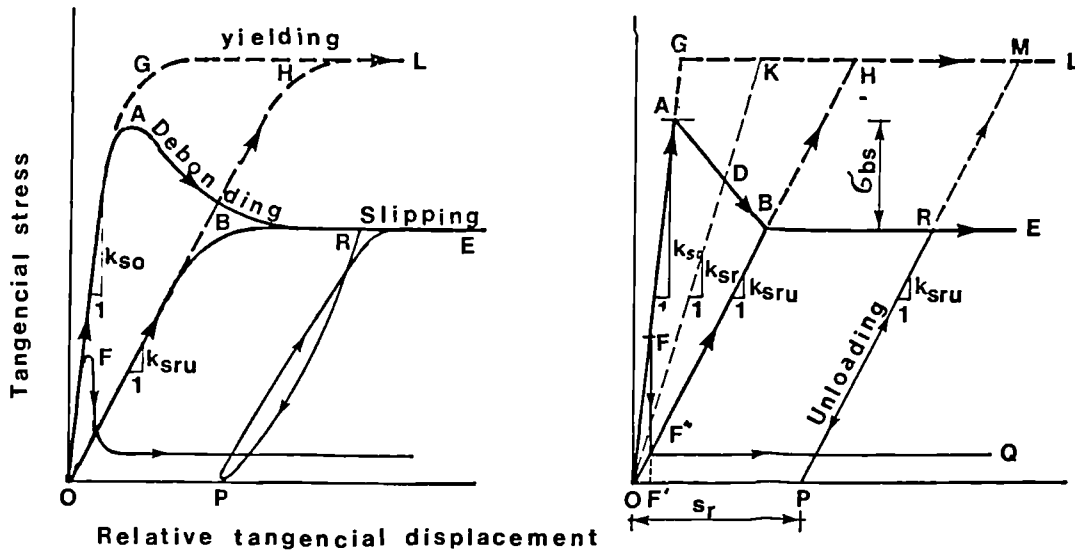


(a)



(b)

Figure 4.37 Behaviour of Bed Joints of Grouted Concrete Block Masonry under Precompression; (a) test set up and (b) shear-displacement curves



(a)

(b)

Figure 4.38 Typical Shear Stress-Tangential Displacement Curves for Interfaces under Constant Normal Stress; (a) actual (b) idealized model.

No experimental data is available for shear and normal stiffness of a fully bonded interface. Theoretically, they must be set to very high values. When the interface has a finite thickness (bed and head-joints in masonry), the above discussed values of stiffness must also include the additional flexibility induced by the finite thickness and presumably soft mortar joints. This will be discussed later in Section 4.11

4.10.4 Determination of the State of an Interface

4.10.4.1 General

Assume \mathbf{s} and \mathbf{w} are the tangential and normal relative displacements at a gaussian point within an interface from which the previously acquired yielding and slip, and also the initially specified lack of fit, are excluded. Further assume that the interface inelastic behaviour (yielding, debonding, slipping and separation) during the current iteration is somehow prevented. i.e. $\mathbf{s}_0 = \mathbf{w}_0 = 0$. Using \mathbf{s} and \mathbf{w} from Eq 4.172 and the latest values of the shearing stiffness, \mathbf{K}_{sr} , the shear and normal stresses may then be calculated. These stresses can be coupled with the criteria by which the interface would possibly undergo one of the inelastic events as shown in Figs 4.39 to 4.41.

As shown in these figures the calculated stresses simply indicate that what is going to happen to the interface as a result of the current changes in the relative displacements. This permits the changes to the inelastic relative displacements to be calculated and the new state of

the interface to be determined as discussed in the following sections.

4.10.4.2 New State of a Previously Fully Bonded Interface

As shown in Fig 4.39 (b) Lines **EF**, **FC** and **CG** divide the stress space into 4 zones indicating whether the interface is subjected to debonding leading to separation, debonding possibly leading to slip, yielding or resuming the elastic state. These lines have already been defined in Section 4.10.2 by Eqs 4.171, 4.168 and 4.170 as bond tensile failure; bond shear failure, and the interface (Joint) yielding criteria respectively. If point **P** (the point representing the shear and normal stresses calculated in the manner described in Section 4.10.4.1) takes a position above one of these lines the indicated inelastic event would take place. The induced inelastic displacements and the subsequent stresses can be calculated as follows:

a) Debonding Interface Leading to Separation

The graphical representation of this state is shown for point **P4** on Fig 4.39. In a separated interface no shear and normal stress develops. Therefore:

$$\text{new slip} = s_{s1} = s \text{ and separation} = w_{sp} = w \quad (4.175)$$

and $\sigma_n = \tau = 0 \quad (4.176)$

b) Debonding Interface Leading to Partial Debonding

Allow the interface to debond gradually until

point P_1 drops down to P_1' on the appropriate subsequent debonding surface as shown in Fig 4.39. Clearly, such a drop is possible by assuming a partially debonded interface with shear stiffness of K_{sr} rather than that of the fully bonded interface, K_{s0} . The new stiffness, K_{sr} , may also be used to specify the rate of debonding as shown in Fig 4.39(a). K_{sr} can be calculated as follows:

Line AB in Fig 4.39(a) can be formulated using the co-ordinates of points A and B i.e.

$$\frac{y - y_A}{x - x_A} = \frac{y - y_B}{x - x_B} \quad (4.177)$$

where

$$A \left| \begin{array}{l} \frac{\sigma_{bs} - \mu\sigma_n}{K_{s0}} \\ \sigma_{bs} - \mu\sigma_n \end{array} \right. \quad \text{and} \quad B \left| \begin{array}{l} -\mu\sigma_n \\ K_{sru} \\ -\mu\sigma_n \end{array} \right.$$

using the unknown partially debonded shearing stiffness, K_{sr} , Line OP_1' can be written as:

$$y = K_{sr}x \quad (4.178)$$

Elimination of y from these two equations leads to K_{sr} in terms of the absolute value of the shear displacement R_{s1} (the x co-ordinate of intercept of the two lines) as follows.

$$K_{sr} = \frac{1}{R_s} \left[-\mu\sigma_n + \sigma_{bs} \frac{\mu\sigma_n/K_{sru} + R_s}{\mu\sigma_n/K_{sru} + (\sigma_{bs} - \mu\sigma_n)/K_{s0}} \right] \quad (4.179)$$

The stresses may now be calculated as:

$$\sigma_n = wK_n \quad \text{and} \quad \tau = sK_{sr} \quad (4.180)$$

Since the interface is still partially bonded no separation or slip can occur. R takes the value either +1 or -1 so as to make R_s always positive.

c) **Debonding Interface Leading to Total Debonding**

For point P_3 in Fig 4.39, the absolute value of shear displacement, Rs_3 , may exceed s_b indicating that the interface has totally debonded and some slip has taken place. This case will be discussed in Section 4.10.4.4 (b)

d) **Fully Bonded Interface Undergoing Yielding**

Allow for a prescribed residual yielding displacement, s_y , for point P_2 as shown in Fig 4.39(a) so that the new position of this point, P_2' , meets the yielding criterion, Line CG . Then s_y can be calculated from Fig 4.39(a) as:

$$s_y = s - \frac{-\mu' \sigma_n + \tau_0}{RK_{s0}} \quad (4.181)$$

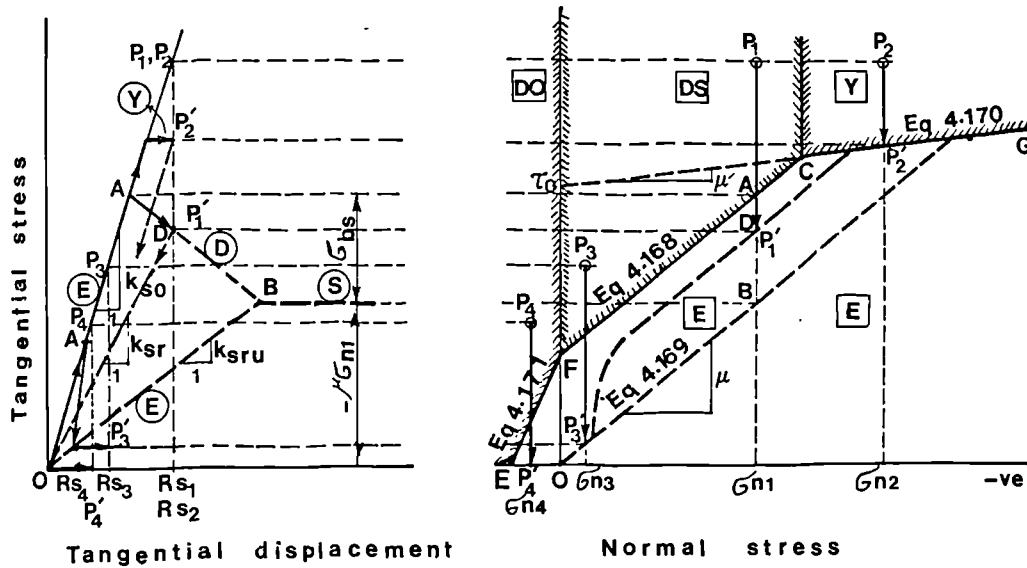
and

$$\tau = K_{s0}(s - s_y) \quad \text{and} \quad \sigma_n = K_n w \quad (4.182)$$

e) **Fully Bonded Interface Resuming Elastic State**

No separation or slip has occurred and the already calculated elastic stresses are the true values. ie,

$$\tau = sK_{s0} \quad \text{and} \quad \sigma_n = wK_n \quad (4.183)$$



(a) (b)

Figure 4.39 Proposed Constitutive Model for Fully bonded Interfaces; (a) shear stress-shear displacement curves, (b) criteria for the inelastic events
 Note: D=debonding, E=linear elastic, O=open, S=slipping and Y=yielding

4.10.4.3 New State of a Previously Partially Bonded Interface

Fig 4.40 shows the zones and criteria of all the possible states for a partially bonded interface in terms of the new displacements. Calculation of the inelastic displacements and the true stresses are given in the following sections.

a) Debonding Interface Leading to Separation

As discussed in part (a) of Section 4.10.4.2

b) Debonding Interface Undergoing Partial Debonding

The debonding criterion of a partially bonded interface, Fig 4.40 (b), has not yet been developed. But The

same approach as used in part (b) of Section 4.10.4.2 may be employed. For the value of current σ_n and previous value of K_{sr} and from Fig 4.40(a), the value of $R\tau_d$ can be calculated for point D on the debonding criterion (Line AB) as follows:

$$R\tau_d = -\mu\sigma_n + \sigma_{bs} \frac{1 - \beta}{1 - \beta \frac{\sigma_{bs}}{\mu\sigma_n}} \quad (4.184)$$

where

$$\beta = \frac{K_{s0}/K_{sr} - 1}{K_{s0}/K_{sru} - 1} \quad (4.185)$$

K_{sr} is the shear stiffness of the interface at the end of the previous iteration. Now if the absolute value of shear (say for point P₁) is higher than $R\tau_d$, the interface is subjected to further debonding and the procedure to calculate the new value of K_{sr} and stresses is exactly the same as given in part (b) of Section 4.10.4.2. Note the location of point C' calculated in Clause (d) of this section.

c) **Debonding Interface Leading to Total Debonding**

This will be discussed in Section 4.10.4.4(b)

d) **Partially Bonded Interface Undergoing Yielding**

Permit a residual yielding shear displacement, s_y , and proceed as described in part (d) of Section 4.10.4.2 leading to:

$$s_y = s - \frac{-\mu'\sigma_n + \tau_0}{RK_{sr}} \quad (4.186)$$

$$\tau = K_{sr}(s - s_y) \tag{4.187}$$

$$\sigma_n = K_n w$$

Note that the abscissa of point **C'** can be derived by combining Eqs 4.170 and 4.184 to give:

$$OC'' = \frac{1}{\mu - \mu'} \left[\tau_0 - \sigma_{bs} \frac{1 - \beta}{1 - \beta \frac{\sigma_{bs}}{\mu(OC'')}} \right] \tag{4.188}$$

where β is calculated from Eq 4.185 using the previous value of K_{sr} . Eq 4.188 may be calculated for OC'' numerically by trial and error approach. The graphical representation of yielding is given for point **P2** in Fig 4.40.

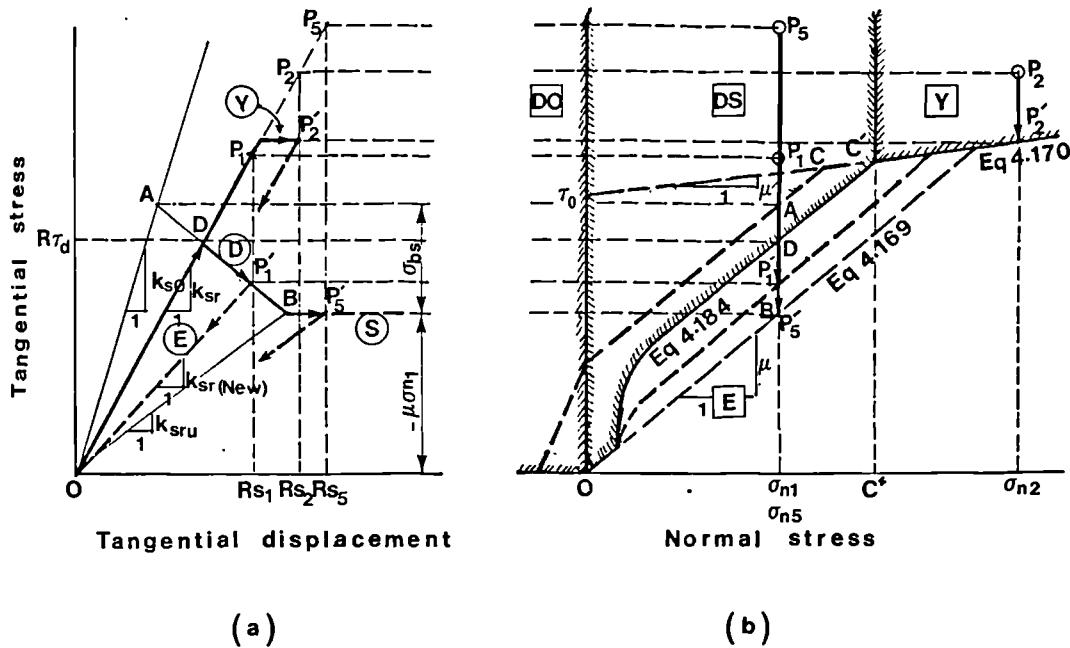


Figure 4.40 Proposed Constitutive Model for Partially Bonded Interface; (a) shear stress-shear displacement curves and (b) criteria for the inelastic events.
 Note: D=debonding, E=linear elastic, O=open, S=slipping and Y=yielding

e) **Partially Bonded Interface Resuming Elastic State**

As concluded in Clause (e) of Section 4.10.4.2:

$$\tau = sK_{sr} \quad \text{and} \quad \sigma_n = wK_n$$

4.10.4.4 **New State of a Totally Debonded Interface**

Fig 4.41 shows the zones and criteria of all possible states for a debonded interface in terms of the new displacements. Calculation of the inelastic displacements and the true stresses are given in the following sections.

a) **Separated Interface**

proceed as discussed in Section 4.10.4.2(a)

b) **Slipping Interface**

The graphical presentation of slip is given in Fig 4.41 for point **P1**. As shown slip can be derived by coupling the slip criterion and the frictional stress-tangential displacement relationship formulation as follows:

$$s_{s1} = s + \frac{\mu\sigma_n}{RK_{sru}} \quad (4.189)$$

and

$$\begin{aligned} \sigma_n &= wK_n \\ \tau &= (s - s_{s1}) K_{sru} \end{aligned} \quad (4.190)$$

The above formulation can also be used for a previously bonded interface leading to complete debonding.

4.10.4.5 Proposed Incremental [D] Matrix

The incremental stress-relative displacement relation in its general form can be written as:

$$\begin{bmatrix} d\tau \\ d\sigma_n \end{bmatrix} = [D_t] \begin{bmatrix} ds \\ dw \end{bmatrix} \quad (4.194)$$

When the interface is separated, no stress will be transferred through the interface requiring, thus, the $[D_t]$ matrix to be a null matrix.

If the incremental changes have not produced any gradual inelastic changes, such as yielding, debonding or contacted slip, the shear and normal components of the incremental stresses and displacements are independent of each other. Therefore Eqs 4.194 can be written as:

$$\begin{bmatrix} d\tau \\ d\sigma_n \end{bmatrix} = \begin{bmatrix} K_s & 0 \\ 0 & K_n \end{bmatrix} \begin{bmatrix} ds \\ dw \end{bmatrix} \quad (4.195)$$

where K_s is the current elastic shear stiffness of the interface taking values of K_{s0} , K_{sr} or K_{sru} for a fully bonded, partially bonded or a totally debonded interface respectively, Figs 4.39 to 4.41.

If however one of the gradual inelastic events occurs during the incremental displacements, a precise tangent elasticity matrix $[D_t]$ can be derived by differentiation of the stress components, τ and σ_n , from the formulation provided in Sections 4.10.4.2 to 4.10.4.4 as follows:

i) Differentiation of τ and σ_n from Eq 4.190 with respect to \mathbf{s} and \mathbf{w} leads to a non-symmetrical $[D_t]$ for a slipping interface as follows:

$$[D_t] = \begin{bmatrix} 0 & -R\mu K_n \\ 0 & K_n \end{bmatrix} \quad (4.196)$$

ii) Differentiation of τ and σ_n from either of Eqs. 4.182, 4.187 or Eq 4.191 with respect to \mathbf{s} and \mathbf{w} gives a non-symmetrical $[D_t]$ for a yielding interface as follows:

$$[D_t] = \begin{bmatrix} 0 & -R\mu' K_n \\ 0 & K_n \end{bmatrix} \quad (4.197)$$

Notice that if μ' is sufficiently small it can be neglected and, thus, the second term of the first row becomes zero and, therefore $[D_t]$ becomes symmetric.

iii) Similar differentiations as in (i) and (ii) above can be conducted to derive $[D_t]$ for a debonding interface using Eq 4.180. Such a $[D_t]$ is again non-symmetric as follows:

$$[D_t] = \begin{bmatrix} D_{11} & D_{12} \\ 0 & D_{22} \end{bmatrix} \quad (4.198)$$

It must be noted that these non-symmetrical $[D_t]$ matrices are not compatible with the standard F.E. programs which require, for the sake of economy, an overall symmetric stiffness matrix. A straightforward and safe solution is to adopt the overstiff unloading shear stiffness as shown by

the heavy dotted lines in Figs. 4.39 to 4.41. Even so it causes a slow convergence. Therefore Eq 4.195 may be considered as the general incremental stress-displacement relationship, unless a solution of unsymmetric equations is incorporated with the F.E program. Such a solution is included with the program "NEPAL".

4.11 Constitutive Formulation for Masonry

The finite element representation of masonry has briefly been discussed in Section 3.9. Of the element types studied, the 4-node element made of the proposed plane-stress equivalent material, representing both the units and the joints, separated by interface elements, Fig 3.9, was found to be the most economical, practical and simplest available choice. The proposed 2-D material facilitates the possibility of simulating the masonry behaviour beyond its peak stress. Such a representation constitutes two distinct stiffness and strength contributors as follows:

- i) The proposed plane-stress masonry equivalent material which must (on the basis of plane stress-strain constitutive relationship) simulate the combined 3-D mechanical behaviour of masonry units and mortar joints while assuming the interface of the equivalent material elements remain intact.
- ii) The interfaces of the proposed equivalent material elements. These line elements are assumed to pass through the midplane of the bed and head joints. Such interfaces must simulate all the inelastic behaviour of the joints such as debonding, slip and separation.

The strength and stiffness of these contributors can be determined experimentally. Analytical approaches are also available which are rather complicated. A new approach has also been developed by the author to calculate the mechanical properties of masonry. Since these approaches were not actually used in the finite element analysis, they will be described in Appendix F.

CHAPTER FIVE

Numerical Implementation and Programming

5.1 General

This chapter deals with the numerical implementation of the finite element technique described in Chapter 3, using the material constitutive formulations developed in Chapters 4. The numerical analyses are incorporated into the finite element computer program "NEPAL" developed by the author. This program may be used for plane stress problems in general and for infilled frame structure in particular. A guide to running program NEPAL is given in Appendix A followed by a number of notes and examples. Appendix B describes the structure of the program and lists the variable names involved.

5.2 Characteristics of Program NEPAL

Table 2.2 lists The characteristics that are incorporated into the computer program NEPAL. As seen this program accounts for almost all the desirable features listed in the table. It is also possible with this program to account for the weight of the structure and lack of fit of the infill. However implementation of masonry as a single material has ^{been} not yet accomplished. But masonry regarded as a composition of the units and the joints, can

be analysed as described in Section 4.11. The analytical study of Appendix F may further advanced^{be} in the future to lead to a theory for calculating the properties of masonry as a single material.

The post peak stress behaviour of materials has a significant effect on the overall behaviour of structure. This is particularly important for infilled frame structures in which it is not yet certain whether the infill or the frame material starts yielding first. As described in Chapter 4, such effects are all incorporated into the program.

Some convergence difficulties may arise for structures in which discontinuities such as cracking, joint debonding and/or slip occur. This has been overcome as discussed in Sections 5.3 and 5.4.

5.3 Loading Procedure

As described in Section 3.3, the non-linear equations of displacements are solved by the Newton-Raphson method based on application of load increments. When the load reaches its peak value, this solution may not be further carried on because no further increase in load is possible. In this project, however, the complete load deflection curve of the structure is desired to be computed. Such a curve must include rising and falling branches and also a plateau, if any, indicating the ultimate plastic strength of the structure.

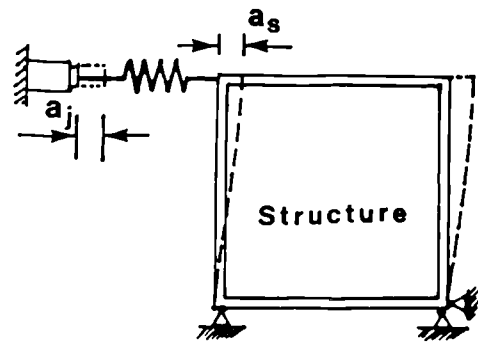
A popular method to avoid the above problem consists of prescribing an incremental value of displacement

component at the loaded node and evaluate the corresponding force reaction. Only one variable load is applicable. This technique was first described by Argyris(91).

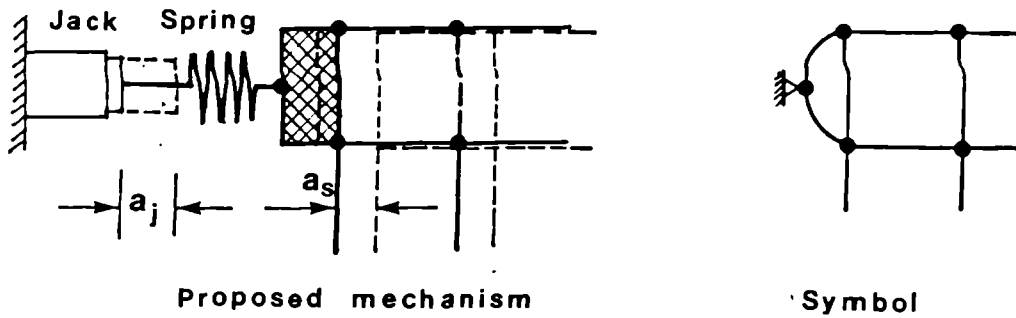
Another alternative for eliminating the problem has been suggested by Sharifi et al(92). This method introduces fictitious springs to keep the slope of the load deflection curve of the combined structure positive throughout the load deflection curve. For a single load and only one spring this method is straightforward and easy to apply. The method cannot, however, be easily justified, when several springs are added to the system, due to difficulty of deriving suitable spring constants.

A method similar to the second of the above has been used in this project by introducing a fictitious jack combined with a spring. This combination may be called the "Load increment adjusting element." This element can be coupled with the structure at the point and direction of the applied load, Fig 5.1(a,b). The load-deflection diagram and the convergence strategy for such a coupled structure are shown in Fig 5.1(c).

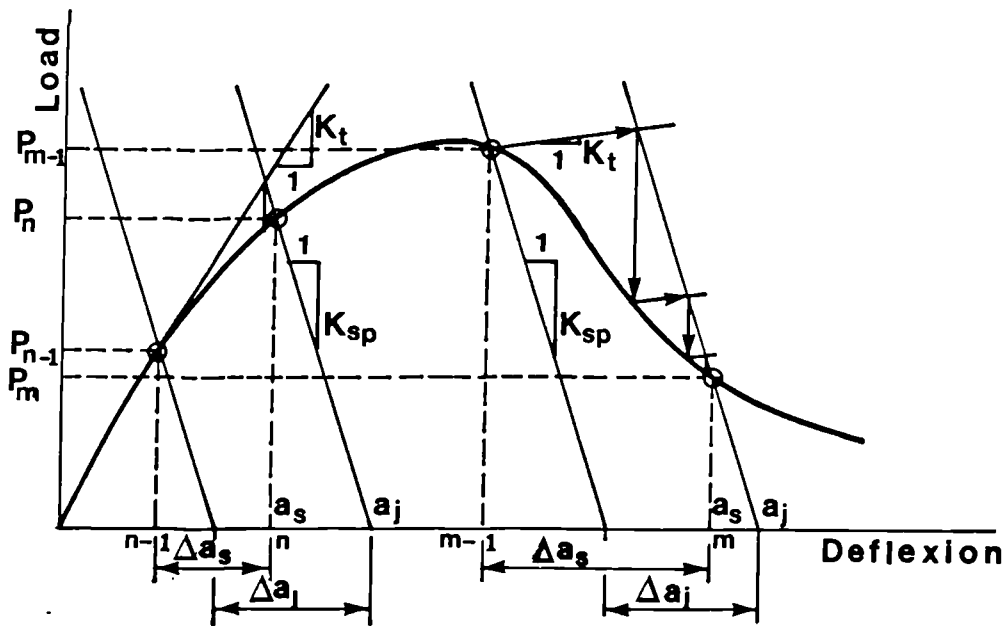
As shown, the structure is loaded by deflection increments, Δa_{jk} , applied by the jack. These applied deflection increments will be taken by the spring, Δa_{sg} , and the structure, Δa_s , in proportion to their flexibilities. If the stiffness of the spring, K_{sg} , is taken as a very high value, relative to the stiffness of the structure, K_t , the system will be equivalent to the deflection increment method described by Argyris(91). It is desirable to take a reasonably low stiffness value for the



(a)



(b)



(c)

Figure 5.1 Proposed Load Application: (a) load application (b) flexible loading jack (load increment adjusting element) and (c) convergence strategy

spring so that the structure undergoes a gradual increase in the load and deflection, in a similar fashion to the behaviour of a real structure. If a very stiff spring is used the behaviour will simulate a displacement control load in which some unloading may occur.

5.4 Criteria for Convergence

The iteration must continue until the convergence criteria are met. To examine the convergence of the iteration, basically, three solution variables can be used: the incremental displacements, the out-of-balance forces and the incremental internal energy⁽⁴⁰⁾. Since the incremental approach used in this project is based on nearly uniform deflection increments, the first of the above variables was found to be most convenient. Therefore the convergence was based on the examination of the nodal displacement vector as follows.

The solution for the corrections to the nodal displacements is said to be converged when the maximum of the absolute value of these corrections (so called the maximum norm) becomes smaller than a prescribed displacement tolerance. This can be expressed as:

$$\epsilon = \frac{\Delta a (\max)}{REF} < \gamma \quad (5.1)$$

$\Delta a (\max)$ = The maximum of the absolute value of change in the nodal displacements.

REF= A reference value related to the deflection increments which is normally taken as the current deflection increment but in this project it is defined as:

$$\text{REF} = 1/2(\Delta_{\text{max}} + \Delta_{\text{min}}) \quad (5.2)$$

so as to maintain a uniform precision throughout the analysis.

Δ_{max} and Δ_{min} = the specified maximum and minimum allowed deflection increments.

γ = A prescribed displacement tolerance taking a value of order 10^{-3} to 10^{-6} , Bergan et al(93).

For this particular type of structure (infilled frames) $\gamma=2 \times 10^{-3}$ was found to give results not more than 1% different from that of $\gamma= 10^{-6}$. A high value for γ is tempting from the view point of economy, but it may lead to severe inaccuracy and divergence.

The iterative scheme described previously would converge only if the non-linearities occurring in the current step are sufficiently small. The more severe the non-linearities are, or the greater the number of discontinuity events is, the smaller the step that must be taken to ensure convergence. In practice, the magnitude of the next load or deflection increment will be decided using the magnitude of the previous step and the number of iterations taken to get into convergence. In order to keep the number of iterations close to the desired number of

iterations, **DITR**, Crisfield⁽⁹⁴⁾ suggested a very simple formula to calculate the length of the next incremental step as follows:

$$\Delta(i) = \Delta(i-1) \frac{\text{DITR}}{\text{ITR}(i-1)} \quad (5.3)$$

$\Delta(i-1)$ = The value of the previous load increment

$\text{ITR}(i-1)$ = The number of iterations taken in the previous step

Program NEPAL, however, uses a newly proposed formula as follows:

$$\Delta(i) = 1.67 \left[1 - \frac{\text{EITR}(i-1)}{\text{DITR}} \right] \text{REF} + \Delta(i-1) \quad (5.4)$$

where **DITR** denotes the specified desired number of iterations within each increment and **EITR(i-1)** denotes the effective number of iterations.

This formula was found to suit better the analysis of infilled frames involving so many discontinuity events such as: cracking, crushing, interfaces or joints debonding or slip, which demand a greater number of iterations in order to deal with the sudden changes in the course of convergence. The effective number of iterations is to be calculated as follows:

$$\begin{array}{l} \vdots \\ \vdots \\ \text{EITR}(i-1) = \text{ITR}(i-1) - \mathbf{I} \\ \vdots \\ \vdots \end{array} \quad (5.5)$$

where **I** equals to the number of iterations within the last

increment during which at least one damaging event (cracking, crushing or debonding) has taken place. The total number of iterations within each load or deflection increment may be restricted to a prescribed number, **MAXITR** so as to prevent a possible divergence.

No straightforward rule is available to determine the values of **DITR**, **MAXITR**, Δ_{\max} and Δ_{\min} so that a guaranteed convergence and a reasonable accuracy can be ensured. The following guideline has however been established by the author after several examinations on highly non-linear problems including infilled frames:

Δ_{\min} = 1/20 to 1/40 of the expected deflection at the peak load.

Δ_{\max} = 2 x Δ_{\min}

DITR = 4 to 6

MAXITR = 2 x **DITR**

5.5 Examination of The Proposed F.E Analysis

5.5.1 General

In Chapter 3 a number of examinations were carried out to test the performance of the proposed elements and the proposed subdivision layouts using the standard elastic material model. In the following sections the intention is to further examine those elements and also examine the performance of the proposed non-linear and elastoplastic finite element analysis approach, ie. Program NEPAL, in

predicting the strength, stiffness and the mode of failure and distortion of the structures. The following sections discuss such examinations carried out on two reinforced concrete beams, a model steel frame with micro-concrete infill.

5.5.2 R.C. Beam Without Shear Reinforcement

Fig 5.2 compares the experimental and the finite element analysis results of a reinforced concrete beam with no shear reinforcement tested by Bresler et al (95). The analytical predictions of the strength, stiffness and the mode of failure are in a good agreement with the experimental results. The following observations are, however, worth mentioning.

The load-deflection curve from the finite element analysis, Fig 5.2(c), remains below the experimental one after the flexural tensile cracks develop. This is obvious as the tensile stiffening due to cracked concrete is ignored. If, however, this effect was accounted for by increasing the modulus of elasticity of the tensile steel bars, the two curves would have agreed much better.

As shown in Fig 5.2, the 6-node beam element proved to be advantageous over the 10-node isoparametric element.

Variation of the interlocking factor, β , described in Section 4.8.3.5, between 1.0 and 1.5 does not affect the results indicating the fact that a crack would be unlikely to become interlocked when no reinforcement crosses it.

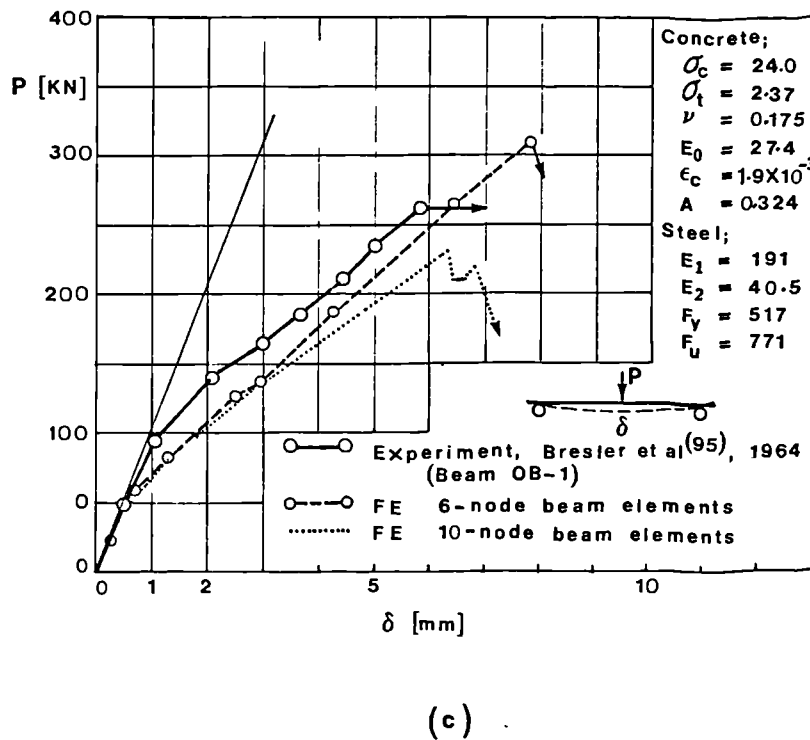
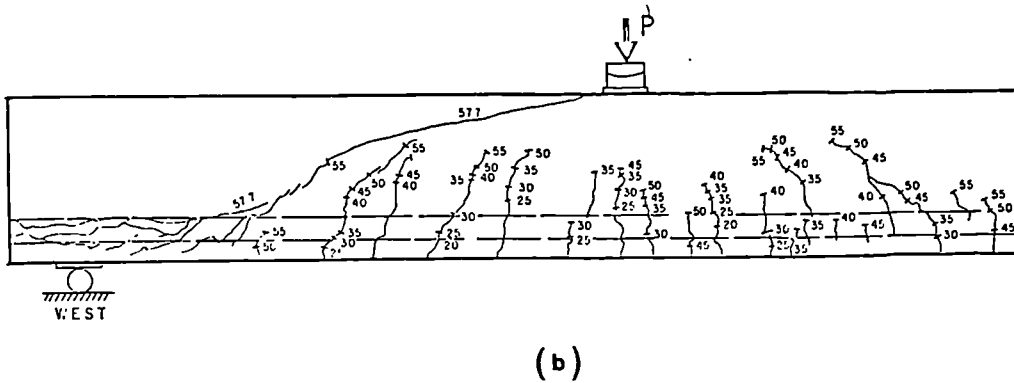
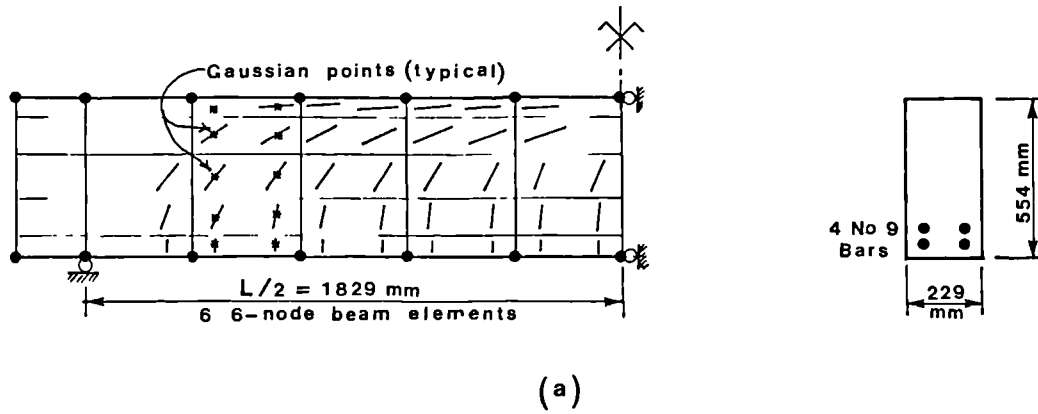


Figure 5.2 finite element Analysis of R.C Beam under Centre Point Load; (a) analytical prediction of the crack pattern, (b) experimental crack pattern (95) and, (c) load-deflection diagrams
 Note: The interlocking factor, β , has been set to unity.

Failure occurs finally due to fracture of concrete at the top-most part of the beam where concrete is under compression tension principal stresses. This type of failure is very sensitive to factor λ described in Section 4.5.3. A small adjustment of this material constant would reduce the peak load down to the experimental value. The comparatively high analytical strength maybe, partly, because of the assumption of continuously distribution of shear deformation over the area of the elements which extended over the entire depth of the beam. This is not true in a diagonally cracked beam. Therefore it may be concluded that although the large sophisticated elements are significantly economic and accurate but they might not **be a** relevant choices for a careful non-linear analysis involving brittle materials that are supposed to carry load well beyond the onset of cracking. Nevertheless, considering the variation of material in the test, the proposed beam element has led to results that are fairly close to the actual values.

5.5.3 R.C. Beam with Shear Reinforcement

Fig 5.3 compares the finite element analysis and the experimental results of almost the same beam, as discussed in Section 5.5.1, with the inclusion of link bars.

The following points (in addition to the ones made for the beam without shear reinforcement) are worth mentioning.

The interlocking factor, β , affects the behaviour only when the cracks that are developed due to diagonal tension have well developed and, thus, the link bars have

become effective.

The abrupt drop in the applied load at the occurrence of the major diagonal cracks could not have been recorded by the loading machine, with no control on deflection, used by Bresler et al (95). This reasoning would explain the experimental curve with no such an abrupt load decrease. The same conclusions as drawn for the beam without link bars also apply this case.

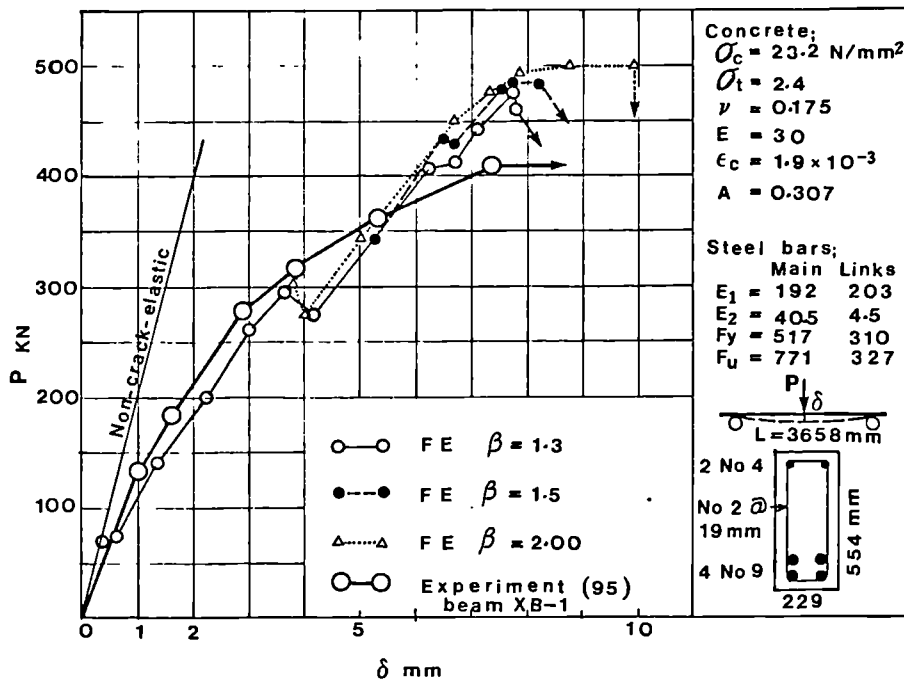


Figure 5.3 Comparison of The finite element Analysis of Reinforced Concrete Beam (With Shear reinforcement) under Centre Point Load with Experimental results of Bresler et al (95)

5.5.4 Square Steel Frame Subjected to Racking

Fig 5.4 compares the finite element analysis results of an open steel frame with experimental results recorded by the author (29). As shown they agree well, indicating that both the proposed beam element and the adopted ductile material model would well simulate the geometry and the mechanical behaviour of the structure. Nevertheless, the following points are worth mentioning.

Apparently the modulus of elasticity of the frame material, steel, must have been slightly lower than reported in the experiment. It seems only 5 percent reduction in the modulus of elasticity would bring the first part of the two curves together.

The analytical load deflection curve looks like a multi-linear line. This may be due to the stepwise numerical integration approximation over the plastic regions at the vicinity of the corners. Increasing the number of Gaussian points in both horizontal and the vertical directions within the elements attached to the corners will improve the analytical curve so as to look more natural and smooth. But such an upgrading involves extra computation time.

The ultimate strength of steel must have been more than the experimentally recorded value. This can be adjusted by increasing the value of F_u of steel by only 2%.

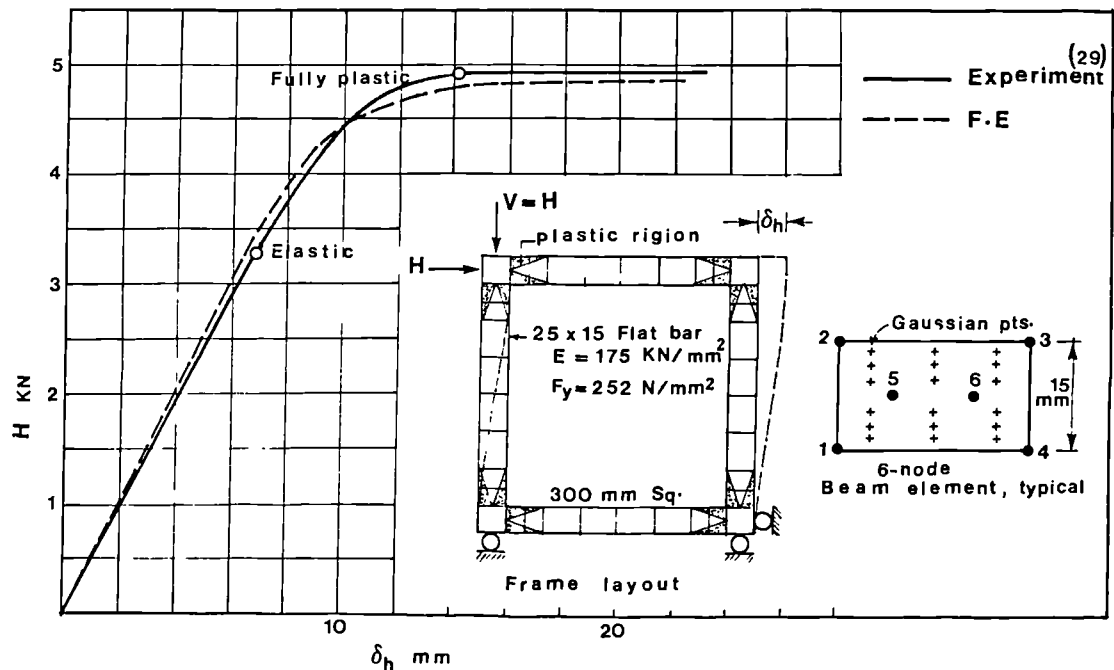


Figure 5.4 Comparison of The Finite Element Analysis of an Open Steel Frame under Racking to the Experiments (29)

5.5.5 Micro-concrete infilled Steel Frame Subjected to Racking

In order to examine the performance of the proposed interface element and also further examine the proposed beam element in a zone with a high bending moment gradient, the model steel micro-concrete-infilled frames (Frame series No. 5) tested by Saneinejad (29), were analyzed under the same type of loading as used in the experiment (Fig 5.5). The reason that this particular experiment was selected for examination of program NEPAL was because the test had been carried on well beyond the peak load up to an obvious

plateau shown in the load deflection curve, indicating formation of a mechanism and thus plastic distortion. The mechanical properties of the materials related to this frame are listed in Table 5.1.

As shown in Fig 5.5, the load-deflection curve resulting from the finite element analysis falls between the two experimental curves recorded from two almost identical infilled frames (Frames No. 105 and 205). The analytical plastic load capacity (plateau) is, however, somewhat higher than those of the experimental ones. This difference may be attributed to development of rather extensive damage to the structure as a result of release of the energy stored within both the structure and the elements of the testing machine immediately after the peak load has reached. Such a damage could have been partly prevented by using a displacement-controlled testing machine.

Figs 5.6 to 5.9 diagrammatically show the frame forces and distortion modes and the interface and the infill stress distributions at the marked stations. These figures show that the proposed finite element analysis predictions of the strength, stiffness and the mode of failure of infilled frames agree well with the actual behaviour of these structures.

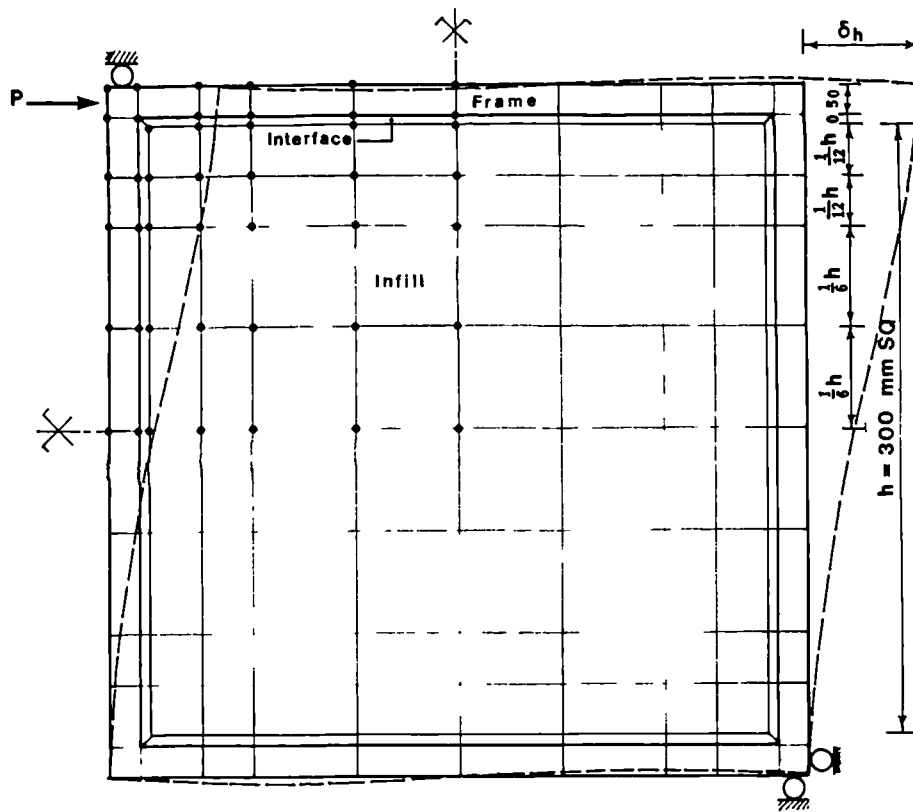
It is worth mentioning that with the aid of the proposed beam and interface elements accurate and finely detailed frame forces and interface stress distribution are numerically established with the use of a substantially low computation time compared to the existing equivalent choices. It is still possible to further increase the

accuracy of the analysis by simply increasing the number of gaussian points within the zones at the vicinity of the loaded corners. Alternatively, the size of the corner elements may further be reduced without increasing the total number of elements and nodes and gaussian points. This choice would be efficient for infilled frames with a strong infill in which the diagonal stresses would concentrate within tiny zones at the loaded corners.

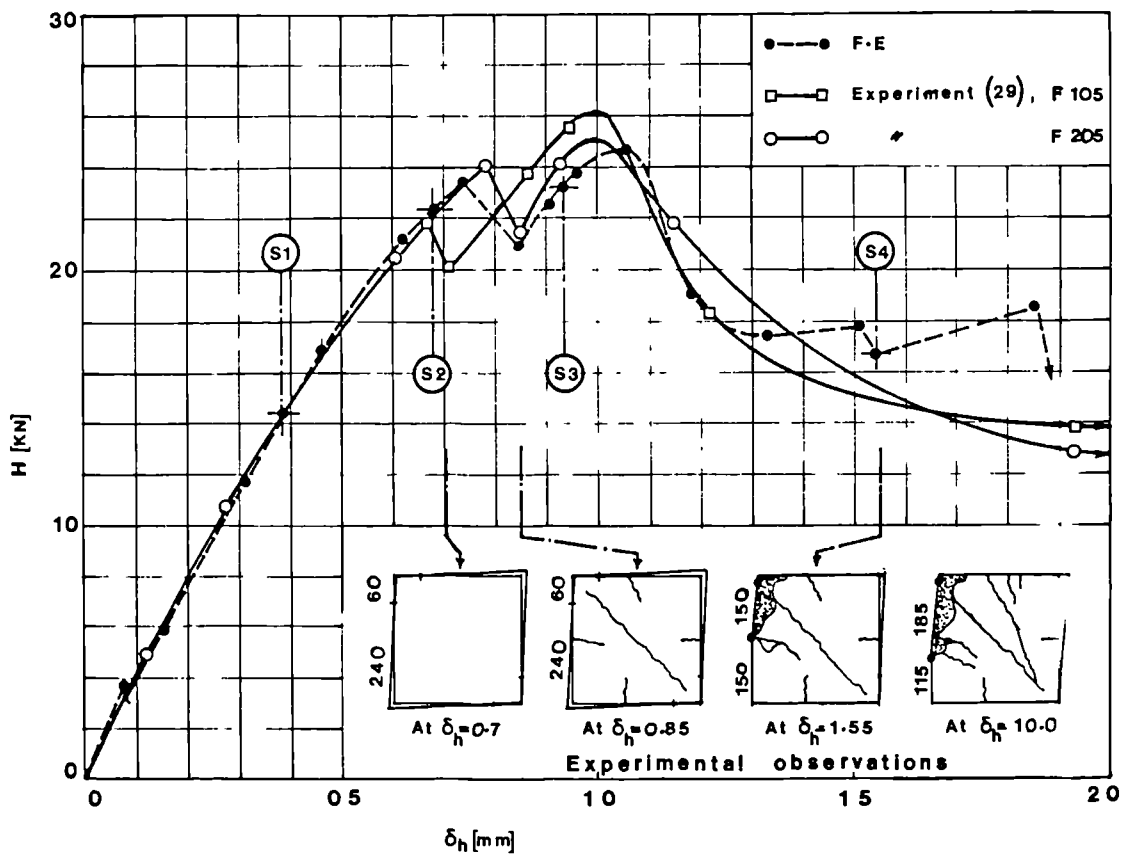
The actual final mode of distortion at station 5 shown in Fig 5.5, indicates that because of non-uniformity in the geometry and material of both the frame and the infill at the loaded corners, the infill normally crushes at only one loaded corner and the frame presumably becomes plastic only at the crushed corner. The numerical analysis, however, treats both the loaded corners the same because of the exact symmetry assumed for the structure, material and the loading. It is believed that the actual behaviour may be simulated by changing, slightly, the thickness of the infill at one of the loaded corners.

Table 5.1 Properties of The materials related to Fig 5.5

Frame	Infill	Interface
$E = 175 \text{ KN/mm}^2$ $\nu = 0.25$ $F_y = 252 \text{ N/mm}^2$	$E = 25 \text{ KN/mm}^2$ $\nu = 0.175$ $\sigma_t = 4.0 \text{ N/mm}^2$ $\sigma_c = 35 \text{ N/mm}^2$ $\epsilon_c = 2.1 \times 10^{-3}$ $\beta = 2.0$	$K_n = 1000 \text{ KN/mm}^3$ $K_s = 500 \text{ KN/mm}^3$ $\sigma_{tb} = 0.0$ $\sigma_{sb} = 0.0$ $K_{sru} = 0.5 \text{ KN/mm}^3$ $\mu = 0.6$

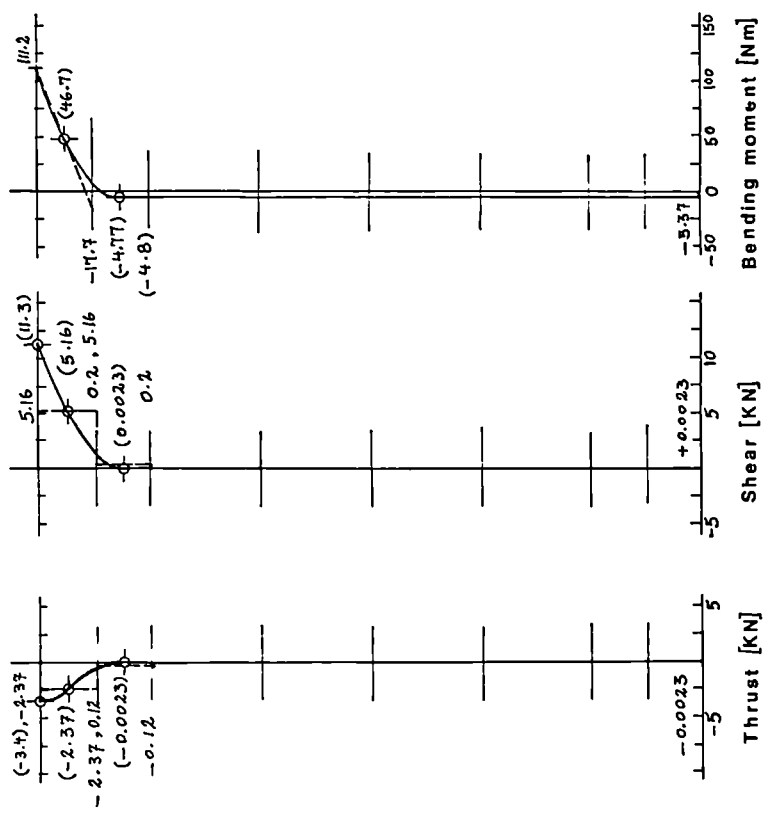
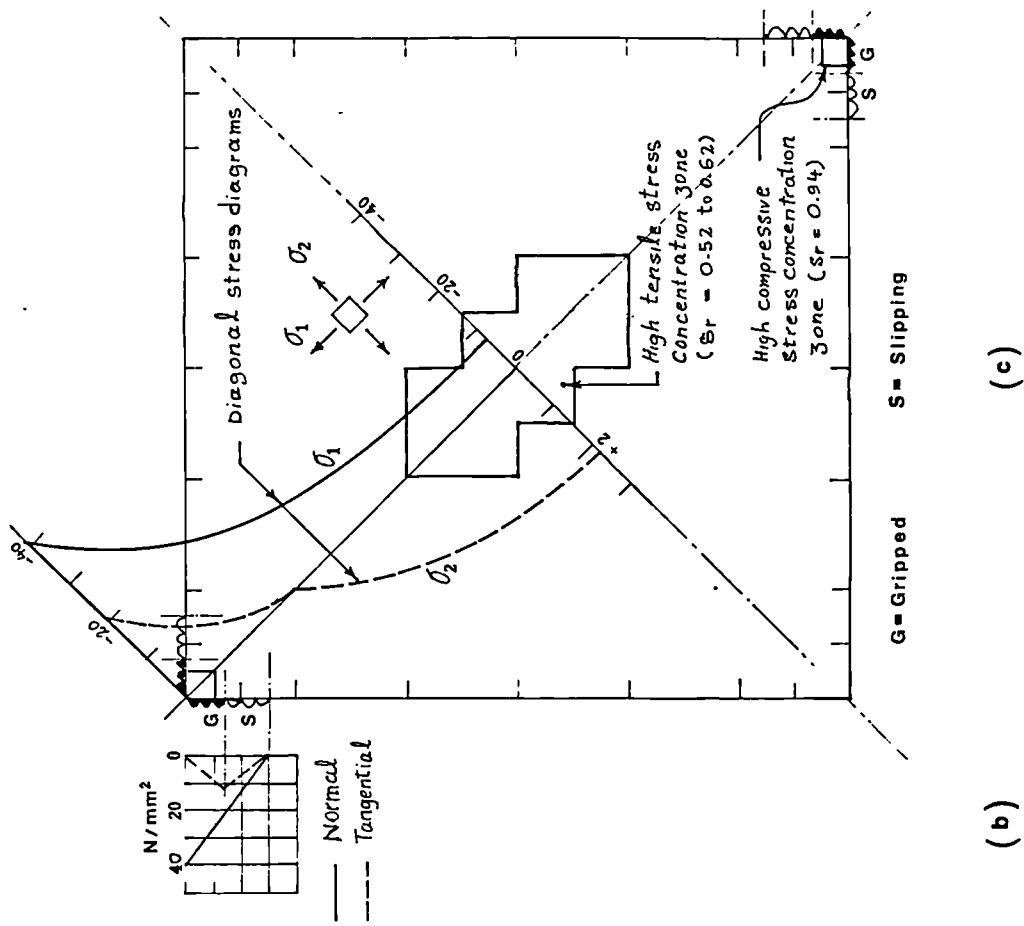


(a)



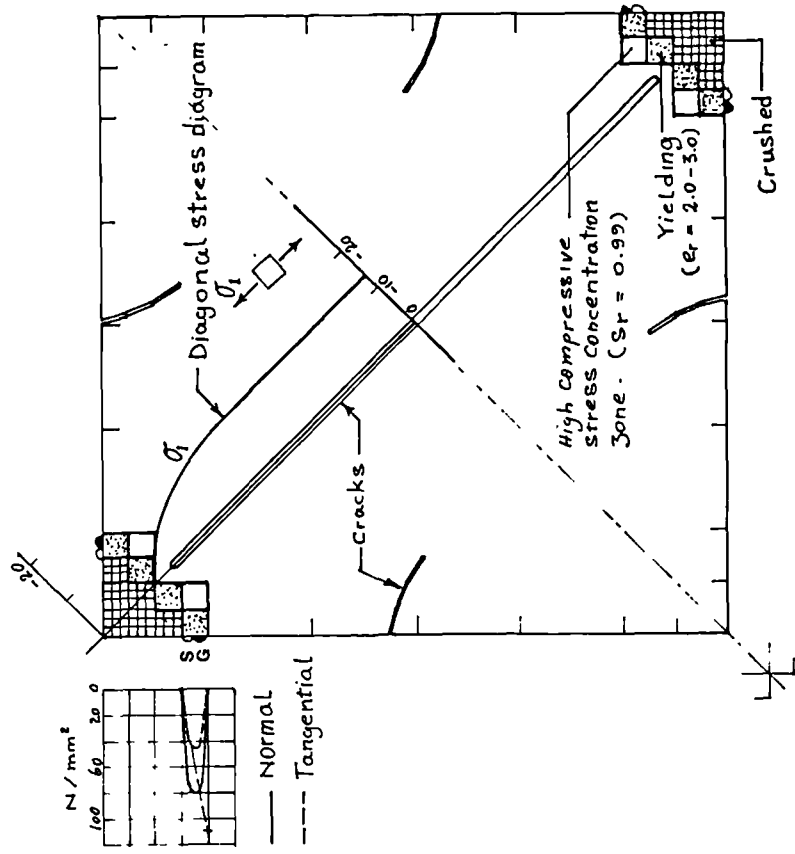
(b)

Figure 5.5 Comparison of The Finite Element Analysis of Model Steel Concrete Infilled Frame With Experimental results(29); (a) Subdivision layout, (b) load-deflection diagrams

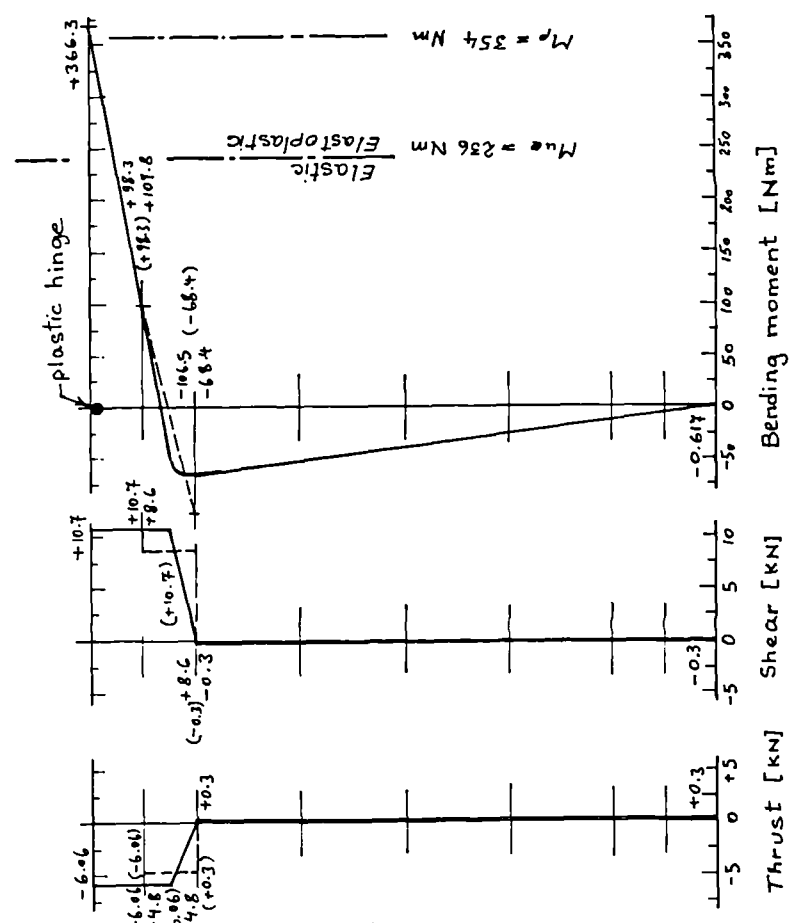


(a) (b) (c)

Figure 5.6 Finite Element Results at Station 1, $\Delta h=0.382\text{mm}$. (a) Frame, (b) interface and (c) infill



(a)



(b)

(c)

Figure 5.9 Finite Element Results at Station 4, $\Delta h = 1.54\text{mm}$; (a) Frame, (b) interface and (c) infill

5.6 Conclusions

The finite element analysis tests carried out in this chapter assisted to examine the computer program "NEPAL" against the requirements outlined in table 2.2. The results also led to the following conclusions:

- 1) The proposed material and interface models simulated, closely, the behaviour of the structures at the peak and beyond the peak load.
- 2) The proposed incremental $[D]_{ep}$ matrix developed for ductile material (steel) subjected to plane stress condition, Eq 4.166, performs excellently.
- 3) Although significantly economic, the choice of large elements with sophisticated shape functions is not the most accurate choice for a non-linear analysis involving materials subjected to discontinuous displacements such as a cracked concrete carrying load well beyond the onset of cracking.
- 4) Considering the variation of material in the test, the proposed beam element leads to results that are fairly close to the actual values.
- 5) The effect of tensile stiffening on the stiffness of r.c. beams is significant. This can be accounted for by increasing the modulus of elasticity of the tensile steel bars after the tensile cracks, caused by flexure, are developed.

- 6) The crack interlocking affects the results of strength and stiffness only when the cracks are intercepted by reinforcing bars. These reinforcements become effective after the cracks have well developed.
- 7) The proposed crack interlocking model well simulated the behaviour of r.c beams with shear reinforcement subjected to high shear force.
- 8) the proposed crack modeling well simulated occurrence of the secondary cracks. These cracks develop only after the primary cracks become interlocked and are under a high shear stress.
- 9) The proposed interface element together with the proposed interface mechanics model, well simulates the behaviour of the interfaces resulting in smooth and fairly accurate stress distribution diagrams involving four possible states of bonded (intact), gripped, slipping and open.
- 10) The proposed deflection increment approach assists preventing the errors such as unnecessary cracking of the material, and debonding and/or over-slipping the interfaces.
- 11) The proposed finite element analysis can be extended successfully well beyond the peak load with satisfactory convergence. However for structures subjected to a sudden failure such as a beam subjected to shear failure, the analysis may not be continued much beyond the peak load.